Addis Ababa University

Addis Ababa Institute of Technology

African Railway Center of Excellence

THERMOMECHANICAL MODELING AND ANALYSIS OF RAIL VEHICLES DISC BRAKE WITH NON-AXISYMMETRIC FINITE ELEMENT METHOD

A Dissertation Submitted to Addis Ababa University

Addis Ababa Institute of Technology

In Partial Fulfillment of the Requirement for the Degree of Doctor of Philosophy (Ph.D.) in Railway Engineering and management (Rolling Stock)

By: Kejela Temesgen Deressa

Supervisor: Dr. Ing Demiss Alemu Ambie (Associate professor)

June 27, 2024
Addis Ababa, Ethiopia

Addis Ababa University

Addis Ababa Institute of Technology

African Railway Center of Excellence

THERMOMECHANICAL MODELING AND ANALYSIS OF RAIL VEHICLES DISC BRAKE WITH NON-AXISYMMETRIC FINITE ELEMENT METHOD

By: Kejela Temesgen Deressa

Approved by the board of Examiners

Mr. Zewdie Moges	_____	_____
Chairman, Department Graduate Committee	Signature	Date
Dr. Ing Demiss Alemu	_____	_____
Supervisor	Signature	Date
Dr. Addisu Asmelash	_____	_____
External Examiner	Signature	Date
Dr. Bisrat Yosef	_____	_____
Internal Examiner	Signature	Date
Dr. Sosina Mengistu	_____	_____
Post Graduate Director	Signature	Date

DECLARATION

I confirm that "Thermomechanical Modeling and Analysis of Rail Vehicles Disc Brake with Non-Axisymmetric Finite Element Method " is my original concept and has never been submitted as part of any institute's graduation requirements. Through referencing, I have given credit to every source I have used. This essay is being submitted to Addis Abeba University in part fulfillment of the criteria for the degree of Doctor of Philosophy in Railway Engineering and Management (Rolling stock).

_____ _____

Kejela Temesgen Deressa Date

This is to certify that the above declaration made by the candidate is correct to the best of my knowledge

_____ _____

Dr. Ing Demiss Alemu Ambie (Associate Professor) Date

ACKNOWLEDGMENT

My first and foremost thanks go to the Almighty God for his protection up to this point and for giving me the confidence to finish my dissertation. Next, I am immensely grateful to World Bank Group for sponsoring me with the tuition fees and supporting me in the financial aspect.

My appreciation also extends to Dr. Ing. Demiss Alemu, my supervisor and associate professor, for his outstanding assistance and support throughout my stay in the Ph.D. program. His astute advice, steadfast support, constant availability to help, and extraordinary efforts on this study project make him one of a kind. I can therefore think of myself as one of the privileged employees who get to work under his direction.

Additionally, I would like to express my sincere gratitude to Ethiopian Rail Corporation and Addis Ababa Rail Transit for providing me with useful disc brake data. I'm fortunate to be able to express my gratitude to the African Railway Center of Excellence for allowing me to enroll. I am very appreciative of the School of Mechanical and Industrial Engineering for their support and encouragement during my program of study.

My special thanks go to all my family members who have always encouraged me, who have been an unstinting source of support, and shown me patience. Last but not least, I would like to thank each of my dear office comrades for their continuous support and guidance.

ABSTRACT

THERMOMECHANICAL MODELING AND ANALYSIS OF RAIL VEHICLES DISC BRAKE WITH NON-AXISYMMETRIC FINITE ELEMENT METHOD

Braking could have unfavorable consequences, including disc thickness variations, thermal judder, crack, fade, surface wear, and limited service life as a result of thermal fatigue. To counteract such damaging consequences, accurate prediction or determination of temperature is fundamental in the design stage and during operation and maintenance. Eventually, several FE (finite element) models have been attempted to assess the temperature, stress, and fatigue life prediction of disc brakes. Despite this, the spatial variations of heat input load and boundary conditions are not adequately taken into account in these models. Hence, accurate detection of failure in the design stage and during preventive maintenance is a key problem. In this dissertation, an FE-based non-axisymmetric moving heat source (NAMHS) algorithm that takes into account the temporal and spatial change of thermal load and boundary conditions is developed, and implemented in disc brake geometry and material selection, as well as in evaluating the effect of braking energy. All input geometric parameters and braking conditions implemented in thermomechanical modeling are extracted from the trailer and motor bogie of Addis Ababa Light Rail Transit (AALRT). ANSYS parametric design language (APDL) is implemented in coding the variations in thermal loads and the corresponding boundary conditions, both spatially and timely. The model constitutes three separate analyses: thermal, mechanical (stress assessment) and fatigue life. To consider space and time variation in heat input and boundary condition, NAMHS is executed by the APDL programming model, similar to FORTRAN written commands. Once the model is seen successful in disc brake analysis, its applicability in other research areas is tested in three ways: comparative analysis geometry selection, examining the effect of braking energy, and disc material comparative analysis. The consideration of radial distance in the NAMHS model algorithm showed surface temperature variation as high as 10% and 60% compared to traditional FE models of moving heat source and axisymmetric, respectively. Besides, the partition of friction surface area into the heat input and convection in NAMHS resulted in maximum circumferential variations of temperature, von Mise stress, and fatigue life prediction as high as 49°C, 46MPa, and 2000 life (braking times), respectively. Moreover, the friction surface is exposed to radial stress variations from tensile stress of 20MPa to compressive stress of -125MPa. Stress variation between the leading and trailing edge of the pad trace due to deceleration is illustrated 5^{o}C and 3MPa on late-braking times, respectively. The applicability test of the NAMHS model algorithm revealed

encouraging outcomes. Although the maximum friction surface temperature seems similar, its variation is highlighted higher in the original disc geometry, compared to the modified. Unexpectedly, the original disc's stress is found more than twice the stress found in modified disc geometry. Besides, the braking energy variation prevailed in emergency braking of the motor bogie revealed twice the strain range in the motor bogie, compared to the service brake in the trailer bogie. And, its applications in material selection displayed cooling times as the main factor. Finally, the NAMHS model algorithm is applied to experimentally and analytically studied solid disc brakes, and successfully validated. Therefore, this finding has drawn our attention to the significance of considering the spatial variation of heat source in a modeling disc brake, which couldn't have been supported in traditional models. The results reported here suggest that the NAMHS model algorithm could provide convincing evidence and a reliable estimate of where a maximum temperature and stress were observed, and where a crack could be initiated.

Hence, this study provides a first step towards a realistic and comprehensive representation of FE modeling, which could be implemented in failure prediction. Hence, this NAMHS finding will help us to predict thermal fatigue life in a better way, compared to any traditional modeling. And, the model should find a broad range of applications in conducting comparative analysis of geometries and materials under any braking type. We hope that our finding could influence disc brake manufacturers, researchers, and maintenance personnel in disc brake damage investigation. Furthermore, the proposed model could be easily implemented and suitable in the area of linear or tangential sliding frictions in addition to disc brakes. These might include, but not limited to thermal and stress analysis of tread brakes, drum brakes, engine piston-cylinder, and camshafts are just to cite a few of its application areas.

Keywords: ANSYS APDL, Disc brake, finite element, spatial temperature variation, moving heat source, thermal stress, thermal fatigue, geometry and material comparative analysis

TABLE OF CONTENTS

Contents

LISTS OF FIGURES

LISTS OF TABLES

NOMENCLATURE

A	Pad-disc contact area (mm^2)	R_r	The stress ratio
a	Deceleration(m/s^2)	R	External radius (m)
A_d	Full disc friction surface area(m^2)	r	The total number of substeps within the cooling time
A_p	Pad-disc interface area (m^2)	Re	Friction surface Reynold number
A_c	Vane mid-point cross-sectional area (m^2)	R_{edh}	Hydraulic Reynold number
A_{in}	Vane inlet area(m^2)	r	Internal radius (m)
A_{out}	Vane outlet area(m^2)	r_j	Radius variation from pad internal radius to external radius
b'	Fatigue strength exponent	r_m	Disc effective radius (m)
C	Specific heat capacity(J/Kg °C)	R_w	Wheel radius (m)
c	The substep variations within cooling time	r_{int}	Disc internal radius (m)
c'	fatigue-ductility exponent	r_{ext}	Disc external radius (m)
D	External diameter (m)	r_m	Effective radius of disc (m)
D_{ext}	Disc external diameter (m)	Rw	Wheel radius (m)
D_{int}	Disc internal diameter in (m)	Re	Reynold number along friction surface
E	Young's modulus (GPa)	Re_{dh}	Reynold's number along vane
d_h	Hydraulic diameter (m)	S_X	Circumferential stress (MPa)
d	Internal diameter in (m)	S_Z	Radial stress (MPa)
F_{disc}	Friction force on disc (N)	S_Y	Axial stress (MPa)
f_N	The volume fraction of void nucleation	S_N	The standard deviation of mean stress for nucleation
f_c	Critical porosity	T_a	Ambient temperature
f_o	Initial porosity	t	Instant time (s)
f_F	Failure porosity	t_i	Time increment (s)
h_s	Friction surface convection (w/m^2k)	t_b,	Braking time (s)
h_f	Fin surface convection (w/m^2k)	t_c	Cooling time (s)
h_R	Surface convection coefficient (w/m^2k)	t_{ls}	Load step time (s)
k_a	Air thermal conductivity (w/mk)	v	Air kinematic viscosity (m^2/s)
K	Thermal conductivity (W/(m°C))	v_{avg}	Vanes air average velocity (m/s)
l	Cooling vane length (m)	$v_{disc}(t)$	Disc instant velocity (m/s)
M	Vehicle mass (kg)	v_{input}	Vent speed at inlet of rotor (m/s)
N	Disc revolutions per minute (rpm)	v_o	Initial speed (kph)
N_r	Ramberg-Osgood hardening exponent	u_x, u_y, u_z	Displacement boundary conditions along x, y and z

NOMENCLATURE (CONTINUED)

n	Total number of heat source circumferential variation	v_{output}	Vent speed at exit of rotor (m/s)
$P(t)$	Braking power (watt)	w	Open distance between two consecutive fins (m)
$q(t)$	Heat flux (w/m^2)	Z_D	Related to the cyclic J integral
q_1	First tvergaard constant	w	Open distance between two consecutive fins (m)
q_2	Second tvergaard constant		
q_3	Third tvergaard constant		

Greek letters

α	Angular deceleration (rad/s^2)	θ_n, θ_{tot}	Heat source total rotation angle (°)
γ	Heat partition coefficient	ρ	Density (kg/m^3)
$\Delta\theta$	Heat distance increment (°)	$\omega(t)$	Instant disc angular velocity (rad/s)
θ_m	The highest multiple of pad cover angle (°)	ω_o	Initial angular velocity (rad/s)
θ_o	Pad cover angle (°)	$\delta_{d,f}$	Disc and fin thickness
ω_0	Initial angular velocity (rad/s)	θ_{tot}	Total pad displacement (°)
α	Angular deceleration (rad/s^2)	σ_N	Mean stress for nucleation (MPa)
σ_u	Ultimate stress (MPa)	σ_y	Yield strength (MPa)
$\Delta\sigma, \Delta\varepsilon$	The stress and strain range, resp.	v	Kinematic viscosity of air (m^2/s)
μ	Disc/pad friction coefficient	μ'	Shear modulus
λ	Lame's first parameter	α_T	thermal expansion coefficient (1/°C)
ε_{tot}	Total strain	ε_{th}	Thermal strain
$\Delta\varepsilon_e$	Elastic strain range	$\Delta\varepsilon_p$	Plastic strain range
ε'_p	Fatigue ductility coefficient	σ'_f	fatigue strength coefficient

Subscripts

p	Pad	d	Disc
i	The load step variations within braking time	k	The load step variations within structural analysis

NOMENCLATURE (CONTINUED)

f	fin	s	Disc surface
n	Maximum braking time increment	i	braking time increment
r	Maximum cooling time increment	c	Cooling time increment
v	Maximum structural analysis time increment		

ABBREVIATIONS

AALRT	Addis Ababa light rail transit
ERC	Ethiopian railway corporation
APDL	ANSYS parametric design language
BC	Boundary condition
CFD	Computational fluid dynamics
CGI	Compacted graphite iron
CI	Cast iron
CM	Coffin Manson
CMB	Coffin Manson Basquin
CMC	ceramic matrix composite
CPU	Central processing unit
CRGE	Climate resilient green growth of Ethiopia
CRH	Chinese high-speed train
FE	Finite element
FEM	Finite element method
FGM	Functionally graded materials
FGI	Flake graphite iron
GTN	Gurson-Tvergaard-Needleman
HI	Heat input
ICE	InterCity Express
LCF	Low cycle fatigue
MHS	Moving heat source
MMC	Metal matrix composite
M-T-M	Motor-Trailer-Motor configuration of AALRT train
NAMHS	Non-axisymmetric moving heat source
PRISMA	preferred reporting items for systematic reviews and meta-analyses
SGI	Spheroidal graphite iron
SWT	Smith-Watson-Topper
VPM	Virtual-node polygonal finite element method
VP-XFEM	virtual node polygonal Extended finite element method
XFEM	Extended finite element method

LIST OF APENDICES

CHAPTER 1: INTRODUCTION

1.1 Background

Transportation is one of the leading areas that play an important role in accomplishing shortage eradication and sustainable development. The inception of railway technology as a mode of transportation can be traced back to the coal mining industries in Great Britain around 1630 [1]. Since then, it has emerged as a dominant ground transportation means, exemplified by the Japanese shinkansen since 1964, as well as the French TGV, German ICE, and Chinese CRH [2]. This might be due to its safety, mass transportation, environmental friendliness (minimum or no CO_2 emission), and low energy consumption (due to the low adhesion coefficient between wheel and rail, compared to tier and road). Hence, the railway is attracting the attention of many nations throughout the world, and become a research hotspot all over the world. However, the long braking distance from the maximum running speed to the full stop remained unanswered [3].

Braking in railway vehicles is the conversion of kinetic energy to thermal energy. The rotating discs are sandwiched between hydraulically pressurized stationary pads (Figure 1.1), resulting in high thermal energy from the mechanical motion (kinetic energy) of the train [4]. And this thermal energy is responsible for the disc brake failures emanating from the temperature, thermal stress, and surface cracks. To counteract such negative impacts, realistic and accurate FE (Finite element) thermomechanical modeling is essential.

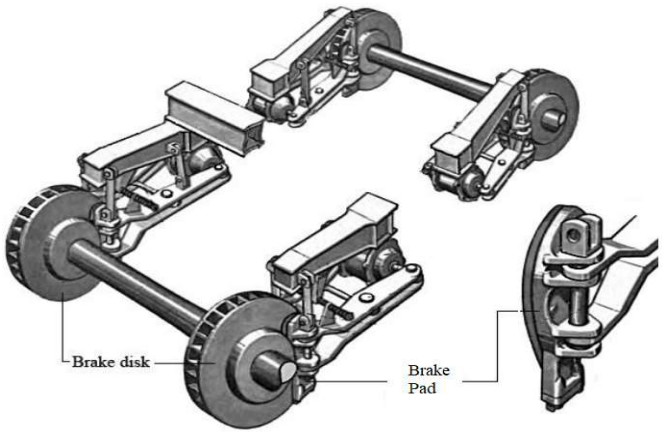

Figure 1.1 Disc brakes and pads installed on rolling stock bogie [5]

Since the development of railway disc brakes, three severe braking conditions have inspired great interest among researchers: repeated or frequent service braking [6], emergency braking [7], and long drag or continuous braking [8]. In these braking conditions, precise prediction of

failure parameters (temperature, stress, crack initiation life, and cracked site) requires a reliable FE model. If these parameters are not determined precisely, the on-time response seems difficult in preventive maintenance and brake design. Moreover, disc brake design and development with inappropriate models misleads manufacturers, and maintenance personnel, even inappropriate models mislead, and cause accidents on human life and waste of materials.

Repeated service braking is operated at normal or designed baking conditions. If the number of braking times per hour is high, the disc is vulnerable to damage, due to storage of temperature at each braking station [9]. This type of braking is observed in passenger trains serving in the cities, including trams, metros, and Addis Ababa Light Tail Transit (hereinafter abbreviated to AALRT). Besides, emergency brake applications from maximum speeds are widely seen to prevent accidents occurring on railway tracks due to external body interventions: pedestrian, animal, or other modes of transportation. Eventually, the friction surface is vulnerable to thermal stress and related cracks [10]. Finally, long drag braking is conducted due to the rail track's long gradient, which is manifested over a long distance, resulting in huge heat storage in the disc. This extreme condition is further worsened when combined with repeated braking [11] and emergency braking [12].

Huge amount of temperature could lead to undesirable effects on the performance and lifespan of the friction pairs: The brake fade phenomenon [13][14], modification of the pad/disc materials' behavior [15][12], rapid wear [16] and poor braking performance [17]. The negative consequence of temperature on pad-disc is not limited to the aforementioned ones. But also reduction in yield strength of the material [18], radial cracks initiation (Figure 1.2. c) on the friction surface [19], the rise in maintenance cost and accident [20] are few of them. Therefore, to mitigate these effects, a suitable FE failure prediction model is essential. Furthermore, it also has a direct impact on ride comfort (vibration) and brake squeal (noise) [21] [22], disc thickness variation[23], coning [24] due to high temperature. To counteract such damaging consequences due to temperature, again precise temperature prediction is significant for temperature and stress estimation [25].

1.2 Existing FE Models and Their Draw Backs

Overall, modeling involves constructing representations of a real-world system or process that help us to understand, analyze, and make predictions about various phenomena in different fields. In the context of FE, modeling is concerned with creating a representation of heat input and boundary condition applications in disc brake thermomechanical analysis. Hence, a review

conducted in this study (Chapter 2) has identified four types of FE modeling on railway disc brake thermomechanical analysis [26]: axisymmetric, uncoupled thermomechanical, coupled thermomechanical, and non-axisymmetric moving heat source.

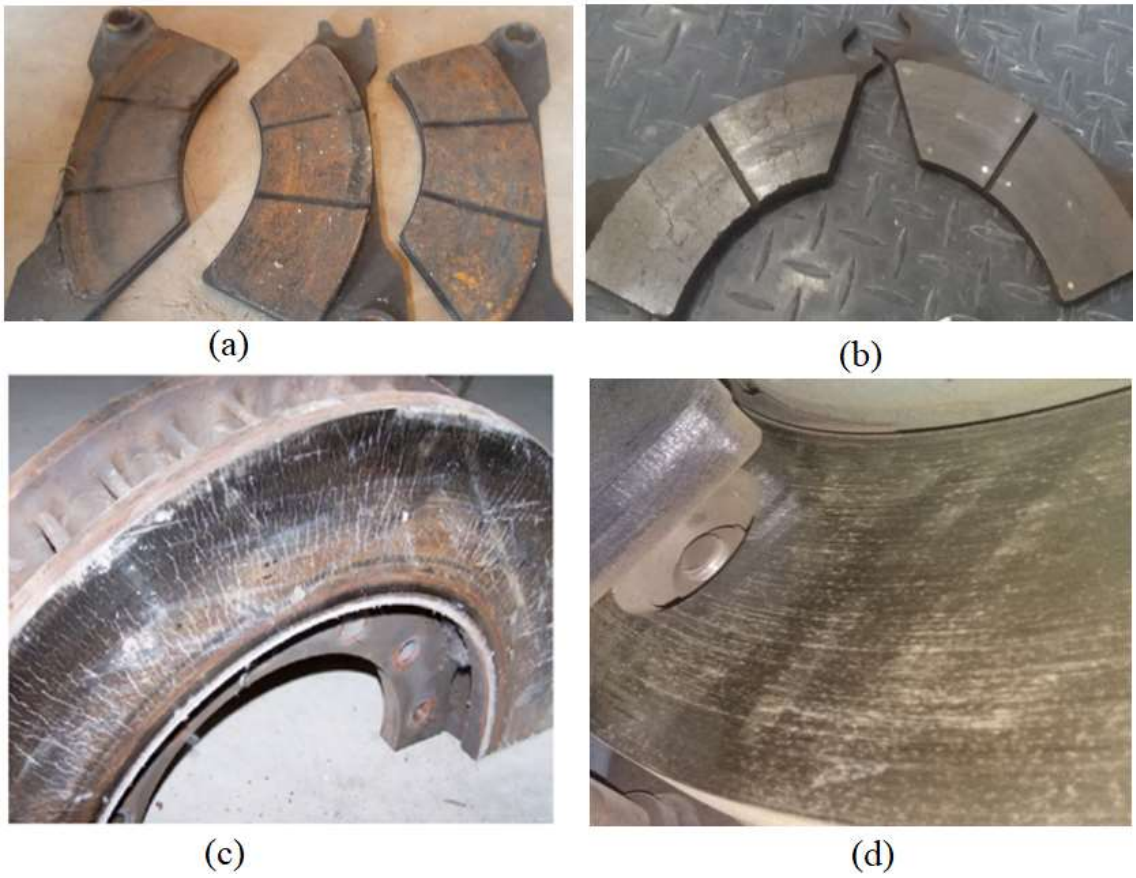

Figure 1.2 Damaged friction surface due to thermal stress: (a) two radial grooves, (b) one radial groove, both from AALRT and (c) hub-bolted disc [20] (d) AALRT disc

Comparatively, a large volume of studies has been published on axisymmetric modeling (45%), because computational problems (convergence, computational time) have been easily improved [26]. Although the disc brake is a three-dimensional model, it assumes the disc as a two-dimensional geometry, in which the 360^{o} of the disc contact surface is covered by the brake pads [27]. In spite of these achievements, axisymmetric modeling displayed three main drawbacks.

Firstly, the assumption is not coincident with the actual braking condition. Besides, it assumes the whole friction surface to receive heat at the same time. Secondly, according to Dufrénoy, Bodovillé, and Degallaix, 2002 [28], the amount of symmetric disc geometry taken (in degrees) can affect the number of hot spots created on the friction surface [28]. Thus, crude results

owing to the random selection of symmetry by different researchers are undeniable. The third and major pitfall in axisymmetric assumption is the incapability of the model to predict the position of crack initiation, as it assumes equal temperature and thermal stress along the circumference and radial direction of the friction surface. Hence, the question related to determining the spatial location of failure on friction surfaces remained unknown.

In contrast, uncoupled thermomechanical modeling has been performed by determining interface pressure calculation, from which heat flux is calculated for thermal analysis [29]. Hence, this type of modeling appeared to suffer from a long simulation time and convergence problems. And finally, coupled thermomechanical modeling appears realistic in considering the spatial variation of heat input [30]. In spite of that, both coupled and uncoupled models are vulnerable to convergence problems due to massive CPU computational efforts, high computational costs, and higher computer memory usage (huge data storage) [30]. Consequently, both are limited to short braking times: 4 sec in [29] and 3.5 sec in [7].

Due to the problems raised in previous models, non-axisymmetric thermal modeling of disc brakes expressed in moving heat sources has emerged, attracting the attention of many investigators [29][7]. Because, variations of heat input and boundary conditions with space and time variables are easily managed by programs written in many software codes, including APDL [7], ABAQUS [31], and COMSOL Multiphysics [6]. Despite its effectiveness in managing spatially varying heat and convergence problems, there has been very little research conducted on the non-axisymmetric moving heat sources (9.8%), and still, the question of spatial and temporal variation of heat has not been fully answered.

To sum up, no previous model has fully addressed the presence of spatially varying thermomechanical analysis of railway vehicles' disc brakes, within feasible computational time and accuracy. Previous studies have failed to demonstrate any convincing evidence of variation in heat input and boundary conditions according to the space on the disc surface and braking time variation. Many designs and developments of disc brakes have been performed, in which disc and pad geometry and materials are optimized by different FE models aforementioned. However, what is not yet known is the extent to which these models accommodate the actual braking conditions.

This study proposes a new non-axisymmetric moving heat source (hereinafter abbreviated to NAMHS) FE modeling that accounts for spatial and temporal variation of heat, with feasible computational time and computer storage. Secondly, this study set out to assess the

effectiveness of the proposed model in managing temperature spatial and temporal variation, by comparing it with two traditional models used as a reference: axisymmetric and non-axisymmetric moving heat source of Pan and Cai,2018 [31]. Finally, this dissertation examines the applicability of the proposed model in comparative analysis of material and geometry selection.

Data for this study are collected from Addis Ababa Light Rail Transit by direct measurement and from technical and operational manuals, including geometry, material, and braking conditions [32]. ANSYS parametric design language (APDL) is the utilized FE software to code or program commands and operators in defining spatial and timely varying heat input and boundary conditions.

1.3 Addis Ababa Light Rail Transit (AALRT)

The Ethiopian Railways Corporation (ERC) provided AALRT passenger transport services since 2015. Additionally, Ethio-Djibout Railways (EDR) opened in 2018 for passenger and freight transport services. AALRT is a 70% low-floor vehicle manufactured by CNR-CRC (Chinese railway corporation), and it can transport 60,000 passengers per hour through two lines connecting the city on a North-South line of 16.9 km and an East-West line of 17.35 km (Figure 1.3.a). Besides, a single train consists of three cars and three bogies. These bogies are made up of two motor bogies (Figure 1.3.b) and one trailer bogie. Motor bogie has two discs, and trailer bogie has four disc brakes (two discs per axle). The East-West line route has 21 stations (braking point) with a maximum running speed of 65kph and 15 trips per day. These data suggest that the brakes play an important role in train operation from one corner of the city to the other.

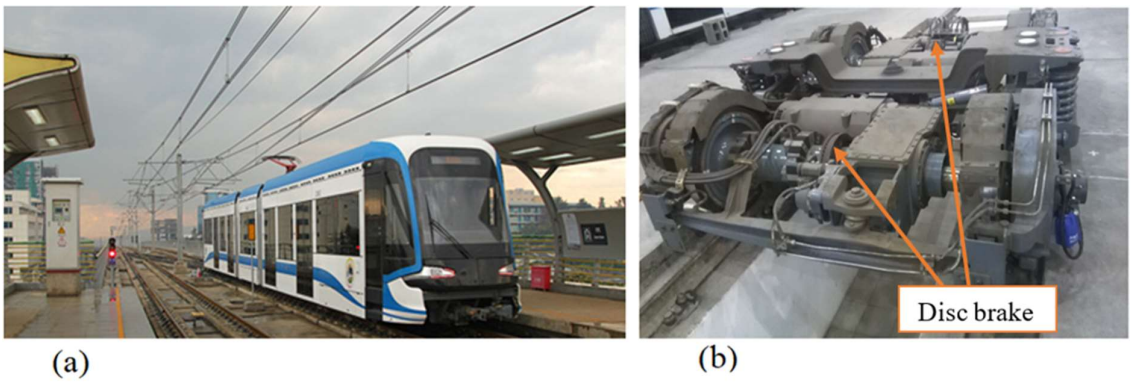

Figure 1.3 (a) AALRT train and (b) its motor bogie with disc brake [camera view taken by the author]

1.4 Statement of the Problem

Computational efficiency and realistic modeling have been the two contradicting interests in the FE thermomechanical modeling of disc brakes. Gaining the two advantages simultaneously has remained the battle field among researchers. The former is related to a convergence-free analysis modeling within a minimum computational time. Meanwhile, the latter is associated with the actual position of the disc (and the associated heat) within the instant of time, relative to stationary pads. This is further interpreted with the spatial (radial and circumferential) and temporal variation of heat generated between the pad and disc. Based on these cases, the review of literature has identified four types of FE modeling on railway disc brake thermomechanical analysis [26]: uncoupled thermomechanical, coupled thermomechanical, axisymmetric, and non-axisymmetric moving heat source. The first two of the thermomechanical modeling were identified as computationally not feasible (convergence problem) and took a long simulation time. consequently, the volumes of published literature on disc brake thermomechanical with these models were comparatively reported low.

In contrast, the axisymmetric model (circumferentially two -dimensional disc geometry assumption) has successfully solved the challenges in the convergence problems and long computational time. Eventually, the review in this study has shown the implementation of the model in almost half of the studies (45%) [26]. However, the critical observation of the model reveals the main drawbacks in the reality of the modeling, compared to the actual braking condition. The assumption of heating the full friction surface (360^{o}) at the same time with constant heat magnitude violates the actual braking condition, leading to non-realistic modeling. This argument agrees well with other studies [29], which confirmed the presence of spatial (radial and circumferential) temperature variation.

Due to the problems raised in the aforementioned models, a non-axisymmetric moving heat source has emerged, attracting the attention of many investigators [6][29] [33] [34]. Because, variations in heat input and boundary conditions with space and time variables are easily managed by programs written in many software codes. Despite its effectiveness in managing spatially varying heat and convergence problems, there has been very little research conducted on non-axisymmetric moving heat sources, and still, the question of spatial and temporal variation in heat has not been fully addressed.

Due to the abovementioned reasons, a novel non-axisymmetric modeling is mandatory to overcome the problems in spatial (radial and tangential) and temporal variation of heat input

and boundary conditions. Because, each and every space on the friction surface is expected to have varying heat input, radially and circumferentially. So that the resulting temperature, stress, and fatigue life for friction surface is expected to vary. Eventually, a non-axisymmetric moving heat source can precisely determine the crack initiation site and crack coalescence direction successfully.

Furthermore, various disc geometries have been developed or designed by FE thermomechanical modeling [35][36][17][37]. Moreover, various disc brake material selections have been performed, implementing FE models [33][38][39][40]. However, the low precisions of temperature, stress, and fatigue life prediction could mislead us in the developed geometries and selected materials. Because, according to THOMAS et al. 2004 [41], an error of 10% in temperature prediction could lead to a factor of 2 on the fatigue life estimation. Therefore, the advantage of a precise FE element model is not only limited to the exact determination of thermal-related parameters (temperature, thermal stress and thermal fatigue). But geometry and material comparative analysis are also another crucial benefit.

The AALRT train consists of three cars per train (Figure 1.3.a) arranged in an M-T-M configuration, where M represents the motor bogie and T represents the trailer bogie. Each car is supported by a single bogie, and the train has a maximum load-carrying capacity of 66220kg. Each motor bogie is equipped with two discs (one per axle), while a trailer bogie has four discs (two discs per axle). Due to the presence of traction equipment (motor and transmission) in the motor bogie, there is no additional space available for extra disc brakes. Consequently, during emergency braking without dynamic braking, a significant amount of braking energy is absorbed by the motor bogie disc, as compared to the trailer bogie disc. This discrepancy in the mass supported per disc between the trailer and motor bogie, and variation in braking conditions (service, emergency, drag braking) results in braking energy variations between disc brakes. Therefore, a reliable finite element (FE) model is necessary to precisely investigate the effects of this braking energy.

Therefore, the lack of efficient FE modeling of thermal, structural, and fatigue life could intensify negative consequences due to severe braking conditions. And, the ongoing and future research directions related to disc brake design development, in terms of comparative analysis in material and geometry selection remained unanswered. Brake component failure information could be poorly understood by maintenance personnel in preventive maintenance,

particularly when braking energy varies between motor and trailer bogies. These problems motivated the authors to conduct this investigation.

1.5 Objective of the Study

The main objective of this study is to develop a novel FE modeling of a non-axisymmetric moving heat source (NAMHS) that considers the spatial and temporal variation of thermomechanical load, leading to the spatially varying temperature, thermal stress, and fatigue life.

The specific objectives are:

- To develop the NAMHS model that executes the FE model of the disc brake, and solves thermal analysis
- To evaluate the effectiveness of the newly developed NAMHS model in managing spatial and temporal variation of temperature, compared to selected traditional models
- To extend the NAMHS thermal analysis model to the structural thermal stress analysis, for the friction surface spatial and temporal stress study
- Employing the NAMHS model algorithm to predict disc brake life before crack propagation
- To examine the success of the newly developed model (NAMHS) in investigating the effects of braking energy variation
- To assess the effectiveness of the developed model in comparative analysis disc material, pad geometry, and disc geometry

1.6 Significance of the Study

- This is the first model to fill a gap in the spatial (circumferential, radial) and temporal (early, middle, and late braking) variations of heat input, boundary conditions, and their consequences: temperature, stress, crack, and life prediction. Understanding the link between space and time will help us to generate fresh insight into the actual or realistic braking conditions in the real world of train operations
- It is hoped that this study will contribute to understanding, identifying, and evaluating the factors responsible for spatially and timely varying heat inputs. And, this enhances the identification of critical positions on friction surfaces precisely, where temperature hot spots, stress concentrations, crack initiation site and its direction of propagation, and where short service life is found.

- This study offers a fresh perspective to predict the precise temperature and stress concentration areas during the design and development stage of disc brakes for various severe braking conditions, which is not dealt within previous studies. This provides the opportunity to introduce design modifications in terms of material and dimensions until the best design is achieved in the early design stage.
- It will also shed light on the potential benefits for all railway stakeholders, including manufacturers, customers, maintenance personnel, and train operators in providing exact failure information so that, an on-time response is taken.
- The proposed technique could be easily implemented and suitable in the area of linear or tangential sliding frictions in addition to disc brakes. These might include, but not limited to thermal and stress analysis of tread brakes, drum brakes, engine piston-cylinder, and camshafts are just to cite a few of its application areas.
- The model developed in this investigation contributes to the growing area of research in pad geometry, disc geometry and disc material comparative analysis.

1.7 Scope and Delimitation

This study focuses on a novel NAMHS FE model algorithm that takes into account the spatial and temporal change of heat input and the resulting output in temperature, stress, and fatigue life prediction. Then further investigation of structural analysis (stress and fatigue life evaluation) is conducted by the NAMHS algorithm. To evaluate the model's application for future study in other research areas, comparative analysis of materials and geometries are performed.

The implementation of the model in material comparative analysis is focused on three cast iron families: flake graphite iron (FGI), compacted graphite iron (CGI), and spheroidal graphite iron (SGI), because of the research gap identified in mechanical and thermal properties of these materials. Further investigation on disc brake and pad materials including steel and composite materials is beyond the scope of this study. It is believed that if the NAMHS model is successful in selected materials, it is assumed effective in other materials also.

Furthermore, comparative analysis of geometry involves both pad and disc. Only pad geometry with composite type is selected, and sintered type is beyond the scope of this study. Composite type geometry selection is based on radial and tangential variation of grooves, varying in number up to two for each. Further increase in the number of grooves is not included in this work, because, to test the application of the NAMHS model, this number is believed to be

enough. In contrast, comparative analysis of the disc geometry is limited to disc friction surface conditions: friction surface-bolted (Figure 1.2.d, the original design) and its modified geometry (hub-bolted).

Moreover, mechanical loading due to inlet hydraulic pressure applied on the disc surface through the pad surface area is taken insignificant [42]. Eventually, it is excluded in disc brake failure thermomechanical analysis. Besides, for all studies included in this study, none of them is seen to include the mechanical load. The thermomechanical solicitation due to thermal diffusion is generally considered to be predominant. Furthermore, the model algorithm developed in this study is unable to encompass wear analysis of disc brake, though it is possible to conduct it using analytical formula and the result outputted from the model developed. This assumption is conducted based on insignificant material removal for disc brake, compared to pad material [24]. Besides, its effect is low compared to friction heat generation [7].

Finally, this study deals only with the modeling, without experimental investigation. Instead, the validation of the model is conducted mainly by comparison of NAMHS temperature results with experimentally investigated disc brakes through thermocouples and thermocamera images. The validation is biased toward temperature, compared to thermal stress and thermal fatigue, because, temperature is input for both stress and thermal fatigue.

1.8 Novelty of the Study

The research novelty starting from model development and its applications in the comparative analysis of geometry and material is summarized below.

- The reasons behind the spatial variation in heat input are identified as pad-disc discontinuity, deceleration, radius, grooves, and hydraulic pressure
- Consideration of radial distance in the NAMHS model revealed surface temperature variation as high as 10% and 60% in other moving heat sources [31] and axisymmetric, respectively.
- The variation in heat flux within the pad cover angle and the distribution of the friction surface area between the heat source and convection in the NAMHS model led to a significant difference in circumferential surface temperature, reaching a maximum of 49°C at the mean radius during mid-braking.
- Increasing the axle load per disc (braking energy) on the motor bogie resulted in a twofold increase in stress and strain levels when emergency braking was applied,

compared to the service brake in the trailer bogie. And, the sudden fall of fatigue life reported for nodes close to the bolt holes also proved this effect.

- The model could be easily utilized by any user with little knowledge of ANSYS software.

1.9 Dissertation Outline/Organization

The remaining part of the dissertation has been proceeded in the following way. The second section of this study will examine a comprehensive review of the literature on different FE modeling and their applications on comparative analysis of material and geometry. Chapter thee introduces the methods followed in conducting the investigations. It describes the FE approach and its input geometries, materials, and braking conditions extracted from AALRT, and from the literature. Chapter four provides a brief description of the NAMHS model algorithm development on temperature spatial variation modeling for service brake application. To test its efficiency, thermal simulation is also conducted in parallel with axisymmetric and moving heat source modeling. This chapter also summarizes the main findings of temperature spatial investigations, in friction surface-bolted and hub-bolted types of disc. In chapter five, we extended the application of the NAMHS model algorithm in handling radial, circumferential, and axial variation of thermal stress and fatigue life predictions. This section also draws together the key findings of stress-strain hysteresis loops, for both braking types, and for both disc geometry types. Fatigue life prediction is additionally conducted here for critical points on disc surfaces, for emergency braking of motor bogie. Finally, chapter six evaluates the application of the newly developed model in comparative analysis of geometry and material, and ties together conclusions, and recommendations, and identifies areas for further research.

CHAPTER 2: LITERATURE REVIEW

2.1 Introduction

FE thermomechanical model of disc brake has been developed since the beginning of its application in braking operation. Eventually, all FE models are extracted from the literature, and their pros and cons are evaluated in terms of heat input, boundary conditions, and their spatial variations. As railway braking differs substantially from automotive or aircraft braking, the current review is focused on the published literature concerning the modeling of railway axle mount and wheel mount disc brakes. However, to present the complete picture of the state-of-the-art, studies related to frictional heating topics are also discussed, mainly from automotive disc brakes.

In parallel to examining modeling types, the application of these models in material non-linearity, optimum disc material and geometry selection, and optimum pad geometry selection are also reviewed. Because FE modeling involves the way heat and boundary conditions are applied, the way geometry is modeled, and the types of material implemented. Finally, concluding remarks, the future direction of the study, and research gaps are discussed. Before these presentations, rolling stock brake types are presented next.

2.2 Rolling Stock Disc Brake Classifications

Disc brakes were first developed in England in the 1890s, and the first patent for a brake disc for road vehicles was submitted by Frederick William Lanchester in 19022 and became popular in the 1950s [43]. In the mid-nineties the SABWABCO (UK) Ltd. company, developed an axle-mounted ventilated disc brake for high-speed trains [44]. At the end of the 19th century, in the wake of railway transportation and the beginning of automotive vehicle production, new technology-based materials became necessary for the manufacture of brake systems to provide safer and more effective braking of vehicles transporting heavy loads at higher speeds [45].

To provide a highly reliable railway safety systems, various braking types have been developed over time based on construction, design and operation, running speed, axle load, rolling stock type, structure and technical features of the vehicles, traffic situations, and braking conditions (emergency, drag, service), etc. Generally, two broad classifications are known: adhesion and non-adhesion braking (aerodynamic and magnetic), which are further divided into subcategories [3]. The former is further classified as friction brakes (in which friction force between two rubbing components plays a key role in deceleration), and dynamic brakes (in which braking force is obtained from train kinetic energy conversion to electric energy is

applied in the opposite rotation direction of the wheels, and supports other friction brakes up to a certain speed). Consequently, wear in friction brakes is reduced, achieving considerable economy).

Even if dynamic braking systems are often largely used in normal service braking, their performances are not sufficient to ensure emergency braking at high speed. Then, friction braking systems are important safety systems, which have to match severe criteria dictated by the security rules, in terms of stopping distance associated with a maximum average deceleration, under all environmental conditions. As an example, in the case of an emergency braking at 300 km/h of the TGV, the maximum stopping distance is 3500 m with an average deceleration of 1 m/s^2 and a braking time of 80 s, corresponding to a dissipated energy of 14 MJ per braking disc [46][47].

Friction-type braking is operated when the rotary component is compressed between two stationary components (Figure 2.1). While operating in such a way, the transformation of kinetic energy due to vehicle speed to thermal energy is performed through friction force at the sliding surface. This energy might be stored in brake components, dissipated to the atmosphere, or conducted to other brake components, based on brake type, geometry, and material.

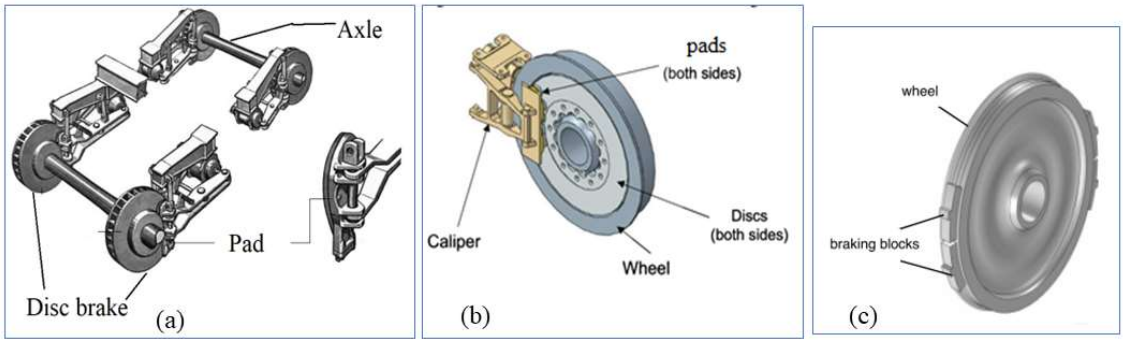

Figure 2.1(a) axle mount disc [5], (b) wheel mount disc [48], (c) Tread/block brake [49]

There are two well-known types of friction brakes currently used in railway vehicles: disc brakes (Figure 2.1a-b) and tread brakes (Figure 2.1.c) [36] [50]. In the former, the friction pair consists of the rotary (disc) and stationary (pads) components [51]. In the latter, it comprises the wheel tread and the brake shoe. Several advantages of brake discs over shoe brakes are reported (Table 2.1), including better stopping performance (disc cooled readily), easy-to-control (not self-applying), and less susceptibility to brake fade, which largely contributed to their popularity [1][52]. These are the primary reasons why its range of application varies from low-speed to high-speed passenger rail vehicles.

Table 2.1 Table Tread and disc brake comparisons [3][51][11][36][50][53]

Friction brake type	Advantage	Disadvantage
Tread/block brake	• Installed when there is limited space in freight wagons and motor bogies of metro rolling stock • Simple in design, cost, and mass saving as no rotating parts	• Higher thermal loads resulting in poor braking performance • High wheel tread wear and accelerated wheel damage • Noise generated at the wheel-rail interface
Disc brake	• Allows to perform high-power brake applications without inducing thermal stresses in wheels • Smooth operations, low noise levels, low maintenance costs • Symmetrical thermal loading leads to better performance in axle-mounted	• Rotation resistance due to drag force (in the case of ventilated type)

Relatively disc brakes are more advantageous than tread brakes in allowing high braking power application [54], better cooling performance, easily controlled, and little susceptibility to fade [55][56]. Based on its connection with the bogie, it is either friction surface-bolted (Figure 2.3), or hub-bolted (Figure 2.4). And, based on the space availability in the bogie, it is classified as wheel-mounted and axle-mounted [47][50], also presented in Figure 2.2.

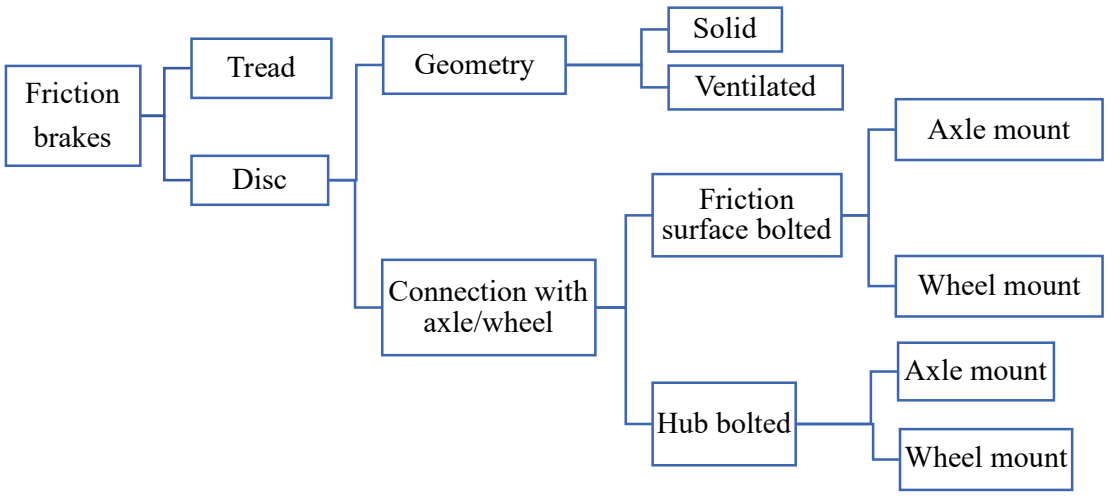

Figure 2.2 Friction brakes classifications [11][56][57][58][59][60]

On powered (motor) bogies, power transmission components (gearbox) occupy considerable space, usually leaving insufficient space for more number of disc brake installations. It is either

impossible to install axle-mounted disc brakes or, at best, only one disc per axle can be accommodated (e.g. AALRT motor bogie Figure 1.3.b). Hence, wheel-mounted brake discs are quite often installed on locomotives and power bogies of multiple units (Figure 2.4. c-d), whereas axle-mounted brake discs are installed on trailer bogies of multiple units (Figure 2.4. a-b). Requirements for service friction braking are normally reduced in powered axles, as dynamic braking can be substantial. However, in the case of dynamic brake failure, emergency braking imposes much higher demands on the powered axles' friction brakes [51][36].

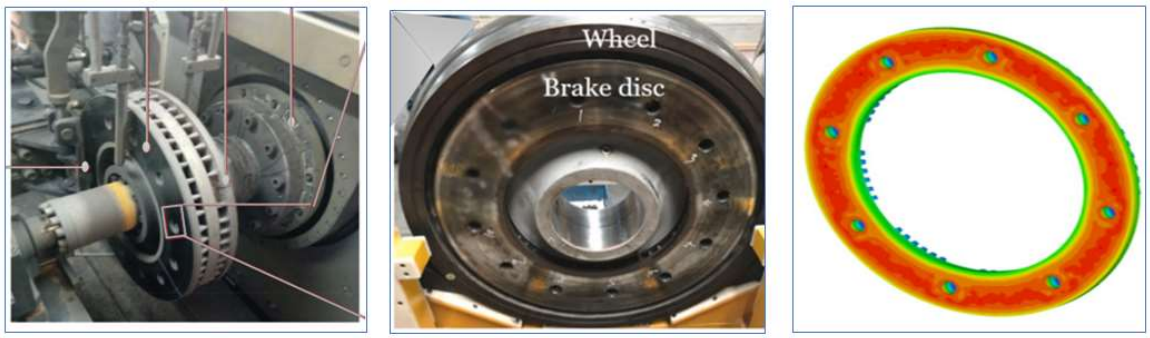

Figure 2.3 Friction surface-bolted disc brakes: (a) axle mount [30], (b) web-bolted wheel mount [19], (c) web-bolted wheel mount 3D FE model [57][56]

Wheel-mounted discs are suitable for vehicles with small wheel diameters (offering space for a relatively large disc and good ground clearance) and large wheel diameters when space on top of the axle is required (shared bogies etc.). That makes them very attractive not only for power car axles but also for trailer car axles of passenger and freight vehicles. Designs and applications of wheel-mounted discs vary, from low-speed passenger and freight vehicles to passenger cars with maximum speed, in the range of around 200 km/h [36]. Likewise, the advantages and disadvantages of other types of dsic design are summarized in Table 2.2.

Wheel-mounted discs are specific to railway vehicles. In most cases, the designs consist of two separate rings (split), each attached to one side of the wheel (Figure 2.3. b,c). For some designs (such as wheel web-mounted), disc rings can be continuous (360^{o}) or two separate rings (split annulus), in two 180^{o} sections, to facilitate replacement of the brake discs. Based on the connection between the disc and wheel, wheel-mount disc brake is further classified as web-bolted (Figure 2.3.b-c) and Hub-bolted disc brakes (Figure 2.4. c-d). In the former one, the disc friction surface has holes through which it is tightened to the wheel web with bolts. Meanwhile, in the latter one, the friction surface is free from the hole, and the disc is tightened to the wheel by its hub to the wheel hub.

Table 2.2 Disc brake types and their advantages and disadvantages [36][11][53][50][3][51]

Disc brake type	Advantage	Disadvantage
Axle-mount ventilated disc	• Allows free air entry and exit leading to better performance • Symmetrical thermal loading leads to better performance	• High air resistance to rotation due to drag in the channel
Wheel-mount ventilated disc	• Offers more space around the axle • Easily installed	• Insufficient air in ventilation channels • Lower braking performance • Increased wheel mechanical and thermal load • Asymmetrical thermal loading leading to coning (distortion)
Axle-mount solid disc	• No air resistance to rotation due to lack of cooling channel • High level of structural integrity	• Poor cooling performance

Similarly, based on the connection between the disc and the axle, axle-mount disc brakes are classified into two design geometries: friction surface-bolted type (Figure 2.3.a-c) and hub-bolted type (Figure 2.4.a-b). In light of the reduced disc friction surface area in the former case, it becomes crucial to thoroughly investigate the potential impact on the spatial distribution of temperature, stress, and fatigue life. It is impossible to judge optimum disc geometry from the two, before conducting thermomechanical analysis. Firstly, the reduction in mass on the friction surface-bolted disc may be counterbalanced by the removal of reinforcing structures around the fins in the hub-bolted disc. Secondly, the presence or the absence of bolt holes on the friction surface may affect the temperature and stress evolution, positively or negatively.

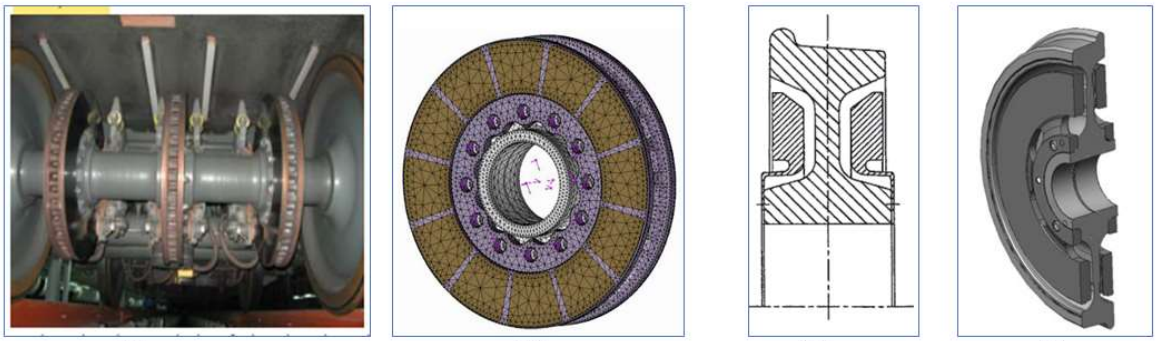

Figure 2.4 Hub-bolted disc brakes: axle mount (a) [58], (b) [59]), wheel mount (c) [11], (d) [60])

Therefore, this investigation is necessary to understand how the disc design geometry may influence failure analysis in terms of spatial factors. By examining the disc's design elements, such as its shape, size, and material properties, we can gain insights into how these factors interact with the reduced friction surface area and contribute to changes in temperature distribution, stress concentration, and ultimately, the fatigue life of the disc. Such an analysis will provide valuable information for optimizing the disc design and ensuring its long-term reliability and performance.

2.3. Heat Input and Boundary Conditions Modeling in Temperature, Stress, and Fatigue Analysis.

Even though realistic heat input and boundary conditions are compulsory, the FE models in which the heat input and boundary conditions have been calculated, and applied were revealed highly diversified among researchers. Besides, they were full of assumptions and simplifications [61]. However, Afzal & Abdul Mujeebu, 2019 [61] revealed assumptions taken for simplifying boundary conditions were seen far from actual braking conditions. And, Tirovic & Sarwar, 2004 [24] stated that actual boundary conditions modeling has to be accessible to get a guarantee in FE results.

As shown in Table 2.3, FE modeling of energy transformation from mechanical to thermal during the braking process has two approaches to estimating temperature [62]. In the first, the pad and disc are heated separately with known heat flux intensity (known a priori), based on friction power, energy conversion, and heat partition coefficient. Furthermore, the application of such heat input on the disc surface was seen as having two approaches: axisymmetric, fixed, or stationary heat flux [40] and moving or rotating heat flux with the speed of the disc [33].

These types of modeling have been used in analytical formulas relating train speed and friction force for heat input (flux) estimation, particularly, uncoupled FE analysis such as uniform wear [63] (Eq. 2.1& 2.2) and uniform pressure [64] (Eq. 2.3), or both [65].

Table 2.3 Methods of heat flux input

Heat input type	Heat input methods	ANSYS	ABAQUS	Others
1. Unknown priori (thermoelastic)	1.1 Uncoupled TM[1]	[66] [17] [28] [42] [63] [67] [68]	[24] [35]	[5]
	1.2 Coupled TM[1] (disc rotation)	[38]	[8] [69][70] [71]	[72]
2. Known priori	2.1 Axisymmetric Or Stationary or fixed BC[2]	[73][74] [75] [56] [64] [76] [77] [78] [79]	[36] [11] [80] [60] [10] [81] [82]	[83] [39] [84] [37] [85] [40] [59]
	2.2 Moving HS[3]	[9][33]	[30]	[6] [86]
Others		[87] [44] [58] [50]	[88] [89] [90]	-----

$$E = \frac{1}{2} m V_o^2 \tag{2.1}$$

$$q_d = mV_o^2 \frac{t_b - t}{A_d t_b^2} \tag{2.2}$$

$$q_d = \frac{\xi\mu\left(\frac{F_p}{A_p}\Delta A_p\right)v_r}{\Delta A_d} \tag{2.3}$$

$$\xi_d = \frac{1}{1+\left(\frac{k_d\rho_d c_d}{k_p\rho_p c_p}\right)} \tag{2.4}$$

Where ξ *and* μ are respectively, the heat partition coefficient (Eq. 2.4) and friction coefficient between disc and pad, q_d is the amount of heat input to disc (W/m^2), E is braking energy (MJ), v_r is the relative velocity between the disc and the pads (m/s) where the radius is r (m). Besides, m is vehicle mass per disc (kg), t_b is braking time, V_o is initial velocity (m/s), F_p is the total

[1] Thermomechanical
[2] Boundary condition
[3] Heat source

clamp force between the disc and the pad (in N), and A_p *and* A_d are pad and disc friction surface areas (m^2), respectively. Also, ΔAp and ΔAd are pad and disc infinitesimal areas, respectively. And finally, the heat partition coefficient is expressed by material properties, including thermal conductivity k (W/(m·K)), density ρ (kg/m^3), and specific heat capacity c (J/kg.K), for corresponding pads (p as subscript) and disc (d as subscript).

In the second approach, heat flux is unknown a priori, but found from solution of thermal contact analysis. Again, the application of such heat input was seen of two types: uncoupled thermomechanical (TM) [63] and coupled thermomechanical (disc rotation against fixed pads) [8]. The uncoupled thermomechanical analysis involves FE calculation of contact pressure distribution first, which is later used for heat input calculation [66][42]. While, the coupled thermomechanical model involves rotation of the disc against stationary pads, accompanied by thermal structural coupled elements [38].

2.3.1 Uncoupled thermomechanical modeling in temperature and stress analysis

Local interface pressure distribution strongly affects the generation and distribution of heat at the mating surface of the friction brake based on its type: uniform or non-uniform. Motivated by this impact of interface pressure, uncoupled thermomechanical simulation was developed by Dufrénoy and Weichert, 1995 [66]. The same authors utilized the model in Disc brake fracture mechanism investigation [42]. Besides, the same model is implemented in railway disc brake pads design optimization by Benseddiq et al., 1996 [17]. Disc structural distortion and material removal due to the wear was reported periodically updated based on time increment $t+\Delta t$ (Figure 2.5).

The same uncoupled thermomechanical model was applied by Dufrénoy, Bodovillé, & Degallaix, 2002 [28], in the study of disc brake crack investigation. Based on a series of seven consecutive stop braking simulations, the authors took two assumptions: uniform pressure distribution and non-uniform (presence of macroscopic hot spots). The former led to uniform heat flux on the disc surface. However, the latter was recommended to consider the contact surface and its variation accompanied by the wear model. Maximum thermal results registered on the disc surface at the mid-braking time were 485°C, -579MPa, and -1.41×10^{-2}%, for temperature, circumferential stress, and strain, respectively.

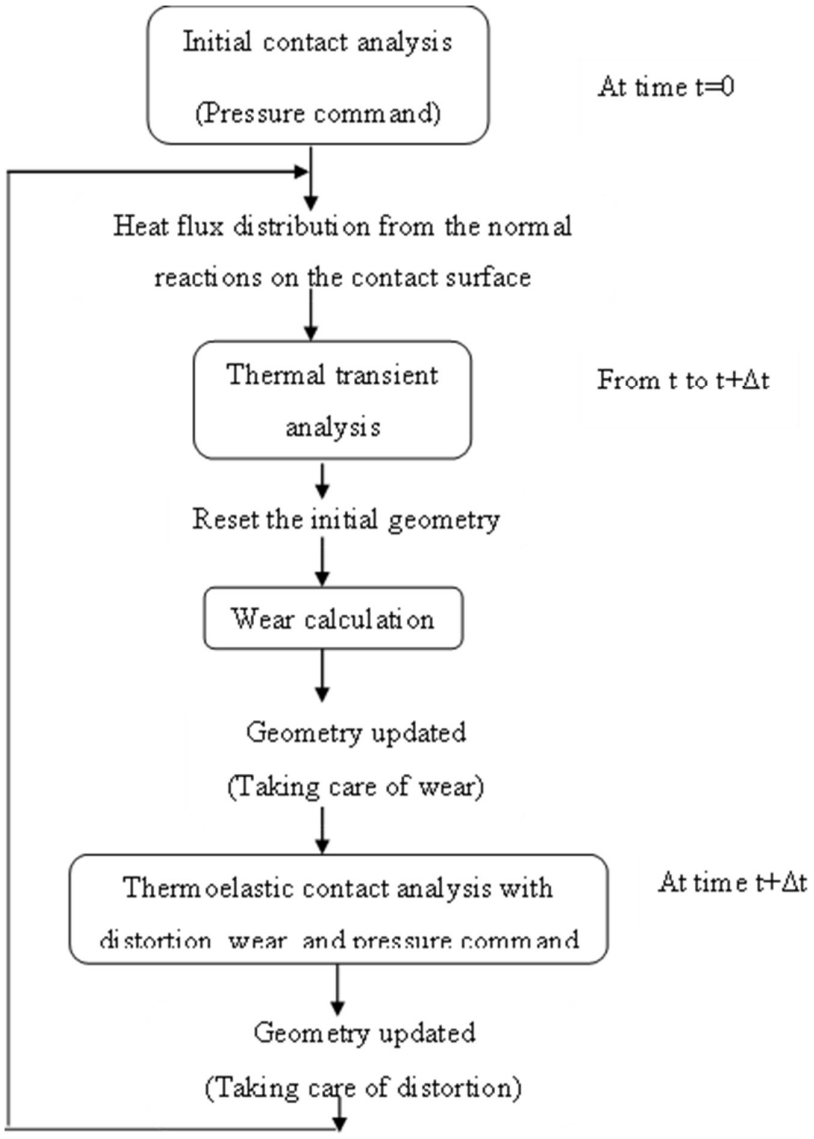

Figure 2.5 Uncoupled thermomechanical algorithm [66]

In contrast, Tirovic and Sarwar 2004 [24] modeled different uncoupled thermomechanical analysis, based on calculation of heat distribution from interface pressure and heat flux calculated and stored in a database called heat flux distribution database (HFDD). Detail algorithms are presented in and Figure 2.6. From data base, heat flux was immediately used in a subsequent thermomechanical (coning) prediction with relatively small time increments ($t=t+\Delta t$) analysis. The applicability of the model in further research investigation was tested by disc geometry optimization performed by the same authors in [35]. The level of complexity and its scope was seen wider, compared to the model developed in [66].

Relatively uncoupled thermomechanical model enabled to simulate wear, temperature, and disc optimization for the large braking time, effectively. For example, the analysis was seen performed for 62s [17][66], 80s [28], and 76s [24]. However, such advantages were with the cost of non-realistic two dimensional or 3D sector disc geometries. This means, the model developed so far were limited to two-dimensional disc geometries, or a sector of three-dimensional disc geometries, to alleviate long computational time and convergence problems. Eventually, it is inconvenient in predicting the disc's tangential temperature gradients.

Motivated by this shortcoming, Dufrénoy 2004 [63] developed a hybrid two-/three-dimensional uncoupled thermomechanical model in order to provide a compromise between limitations of a non-realistic two-dimensional model and massive computational requirements of a full three-dimensional approach (Figure 2.7). Despite that, his model consideration of spatial temperature distribution was limited to radial only.

In such uncoupled themomechanical algorithm, contact pressure variations due to wear and distortions were seen calculated and updated at the consecutive time steps, and then, pressure at each time step was seen utilized for calculating heat flux in thermal analysis. Although the complexity of uncoupled thermomechanical modeling algorithm varies among studies, what they have in common is structural analysis (in which interface pressure is calculated), heat flux calculation from previous structural analysis, thermal analysis (temperature results), wear analysis and structural analysis (in which stress and strain are estimated). Besides, the model was seen successfully implemented in the effect of pressure on the disc thermal stress [68], evaluation of disc brake structural, thermal, and wear phenomena [5], and in the surface contact pressure and stress analysis [90].

Compared to the railways, few uncoupled thermomechanical investigations has been conducted in automotive disc brakes. Gao and Lin, 2002 [29] carried out uncoupled thermoelastic contact analysis that enabled them to account for radial and time variables. The same authors modified this modeling to uncoupled thermoelastic contact analysis in determining the source of the thermal fatigue under residual stress analysis in [7]. The main advantage of the models were their presentation of a radial temperature and thermal stress gradient, although the extent to which they vary circumferentially remained unclear (Figure 2.8). Furthermore, the model's application was limited to short braking time (less than 3.5s), due to convergence problems in uncoupled thermomechanical (thermoelastic) analysis.

Besides, the geometry upon which the model was applied was also simplified (not complicated geometry in actual disc), just to reduce computational time and convergence problems.

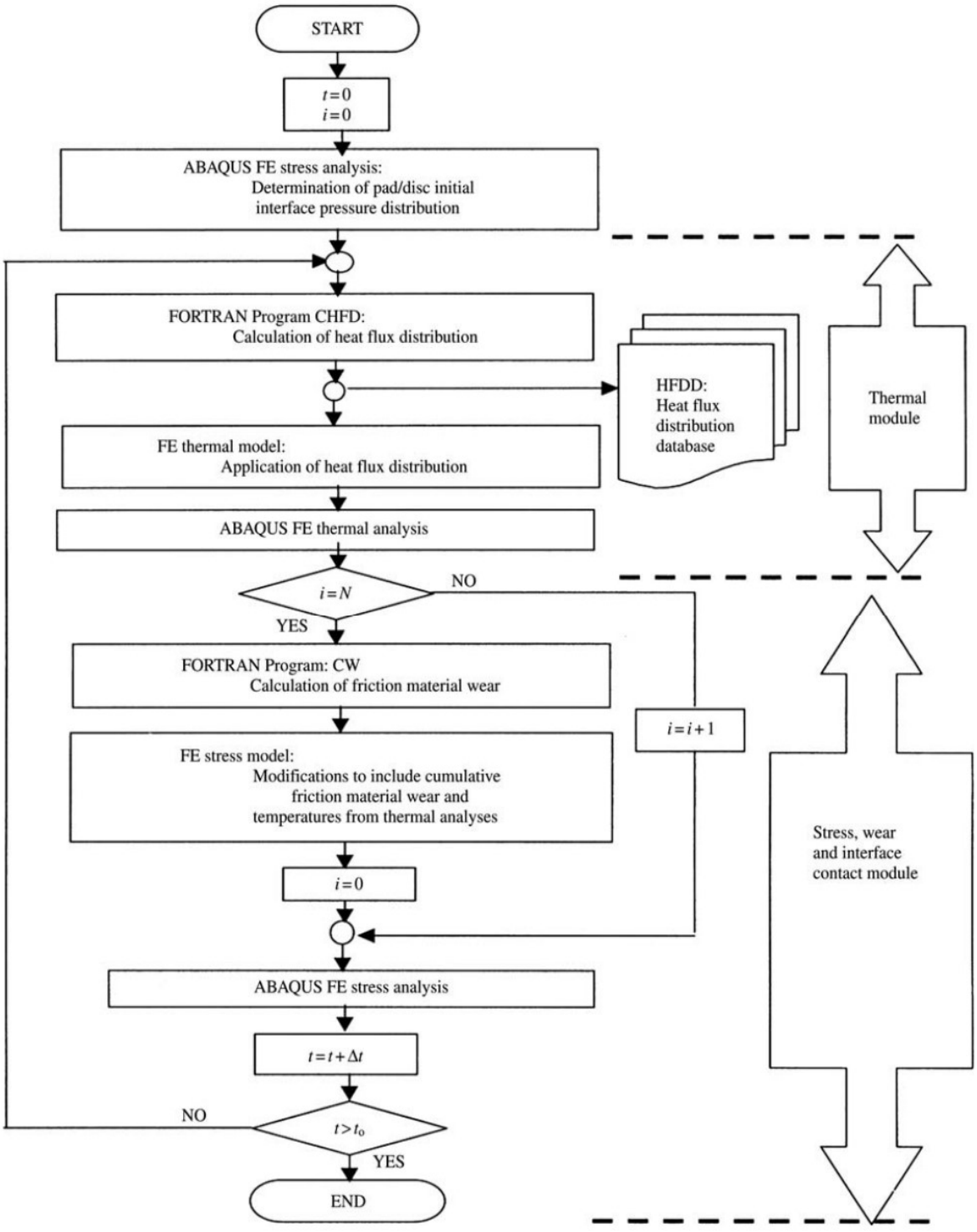

Figure 2.6 Uncoupled thermomechanical algorithm [24]

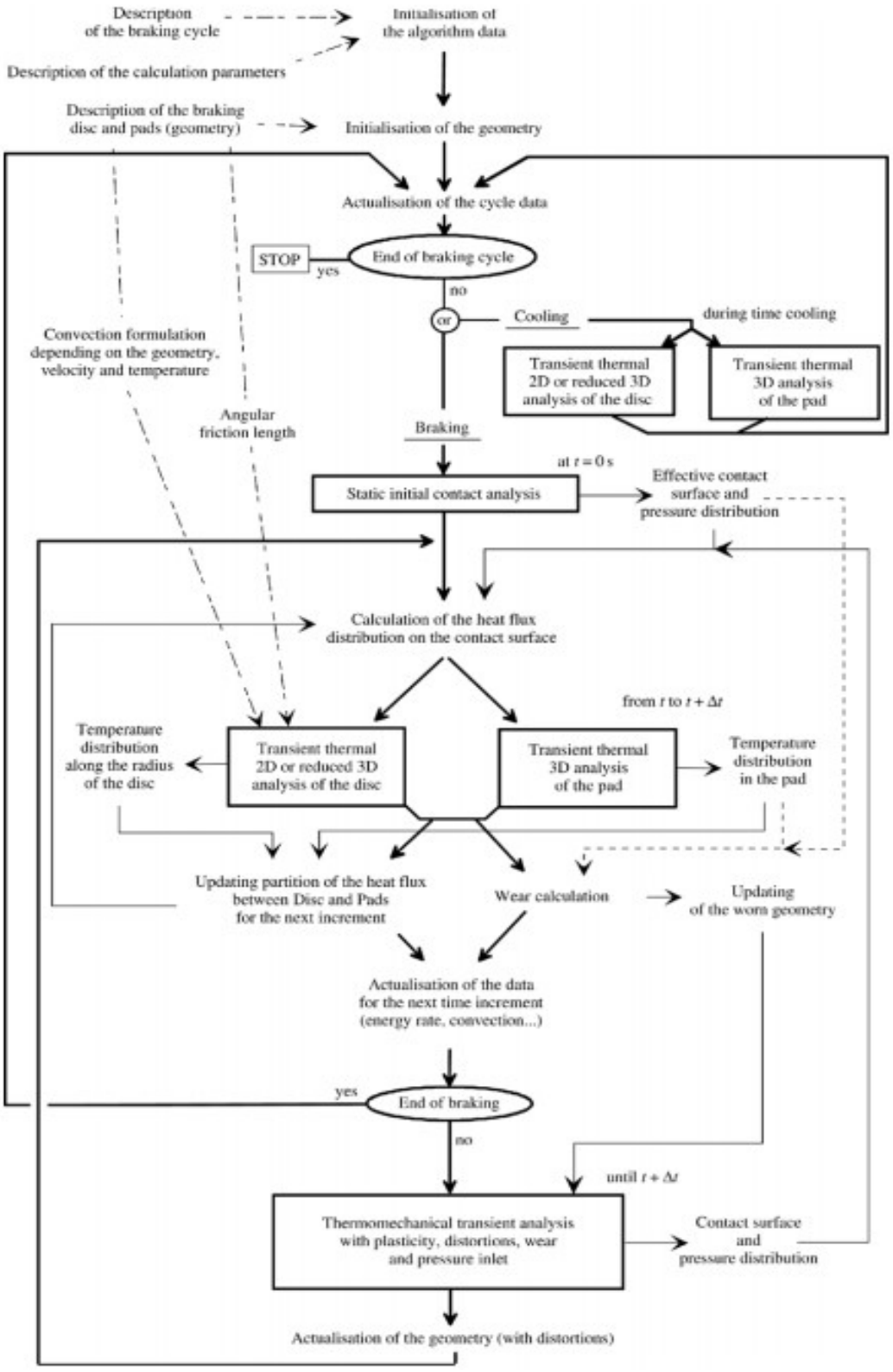

Figure 2.7 A hybrid two/three-dimensional uncoupled thermomechanical model algorithm [63]

2.3.2 Coupled thermomechanical modeling in temperature and stress analysis

On the contrary, saw-toothed (Zigzagged) types of temperature distribution on disc brakes were revealed earlier in the automotive industry [29] than in railways. For the first time, it was investigated in railways by Wang, Fu, and Zhao, 2011 [8], who performed coupled thermomechanical (disc rotation against stationary pads) heat input method in studying temperature distribution along circumferential, radial and axial (thickness) directions of the brake disc. The problem in computation time was successfully relieved by disregarding wear, implementing simple disc geometry and coarse mesh. Besides, convergence problem in structural analysis was not reported, since only temperature was simulated. Despite their first attempt, predicted results accommodated spatial and time variations of temperature, with a maximum of 44°C on the friction surface.

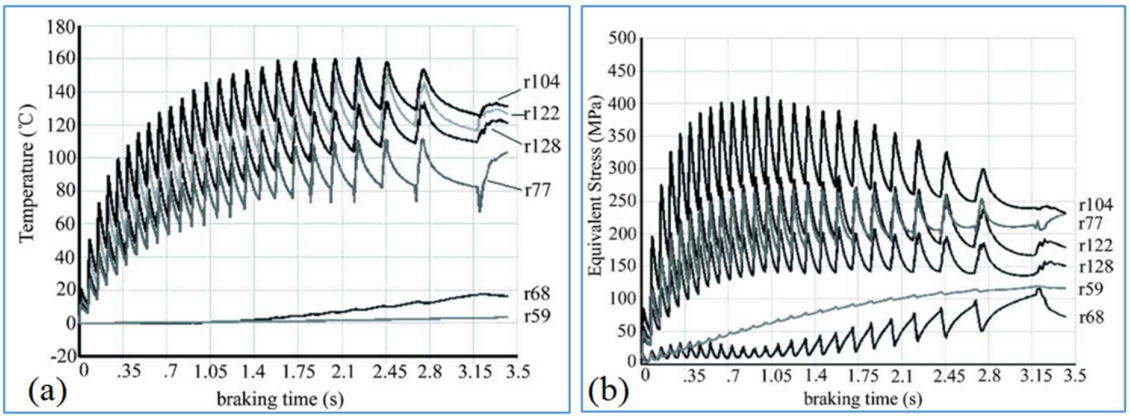

Figure 2.8 Surface temperature and von Mise stress versus time, at 0° [7]

Likewise, Tang and Wang, 2012 [69] analyzed the temperature field of the disc using the rotation of the disc against stationary pads. Hot band and hot spot temperature distribution were observed on the surface, with the saw-toothed thermal gradient in the radial, circumferential, and axial directions (Figure 2.9). This was due to the fact that the disc surface node entered and exited the contact region periodically, resulting in a rise and fall in temperature. In spite of its disregarding wear, the method was also observed in predicting thermal cracking [70], in fatigue life initiation and propagation [71], in the effect of FGM grading index changing [38], and in finding factors affecting thermal stress [72]. Also, various means of heat flux input and applications, including thermomechanical are shown in Table 2.3 as a summary, in which, other means of software (SOLIDWORKS and COMSOL), and other means of heat input (unspecified) are also identified.

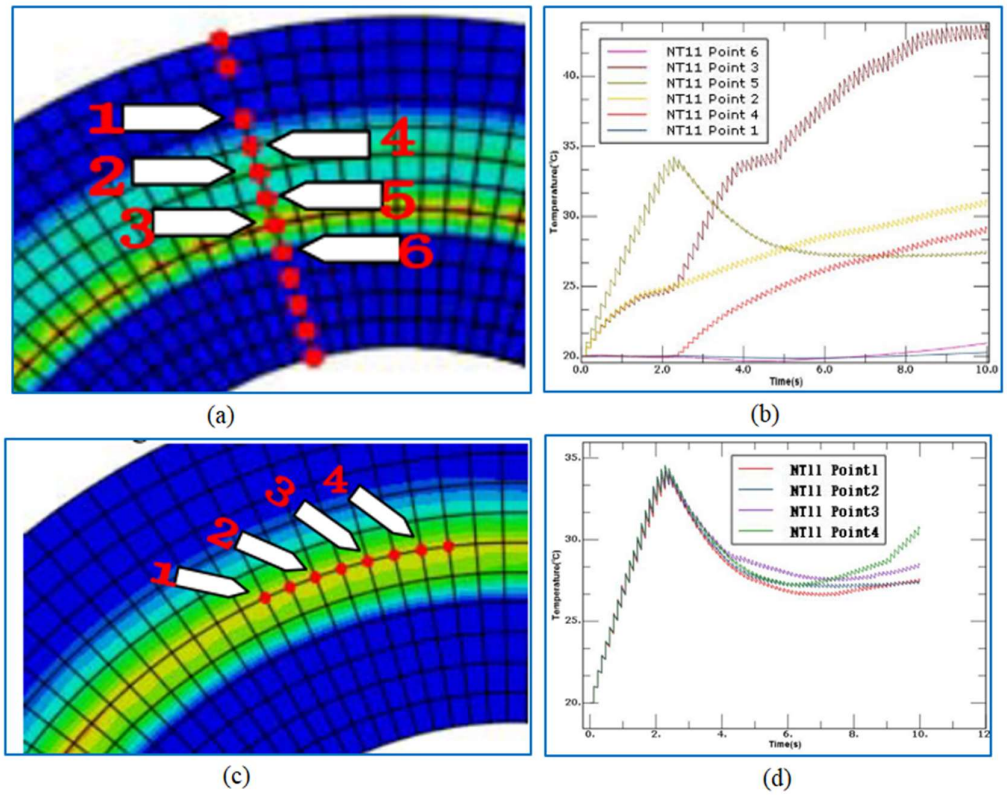

Figure 2.9 Spatial temperature investigations: (a,c) selected positions, (b) radial, (d) circumferential [69]

2.3.3 Axisymmetric/stationary modeling in temperature and stress analysis

Axisymmetric or stationary (fixed) heat input is the widely used and well-known heat input method in thermal analysis. It was used in the study performed by Ghadimi, Kowsary, & Khorami, 2013 [56], in which FLUENT CFD software was highlighted to estimate convection. Based on imported convection, the higher temperature was seen on top of ventilation fins (Figure 2.10.a), compared to areas between fins (Figure 2.10.b), which were elaborated by the formation of stagnation and wake region created on the top of fins that reduced heat transfer coefficient and increased temperature. It was also seen that the lagging of the fins' temperature resulted from the absence of cooling at early braking and maximum temperature in the middle of the braking process.

Moreover, stationary heat input was conducted by Luo & Zuo, 2014 [64] to optimize the heat dissipation performance of the ventilated disc in two ways: reducing disc wall thickness and improving the thermal conductivity of disc material. Boundary conditions were seen derived based on timely varying heat flux and boundary condition, inlet velocity wind speed, and dynamic mesh movement using the FLUENT user-defined function (UDF) file. By doing so,

the researchers successfully improved the heat transfer rate by 10% and 30%, respectively in the improved thermal conductivity and in the reduced wall thickness.

Table 2.4 Means of inputting convection boundary condition

Convection input methods	Authors
CFD[1]/ANSYS	[87] [75] [56] [64] [50]
CFD/Other[2]	[44] [39] [40] [59]
Empirical Formula	[66] [17] [58] [37] [33] [10] [81] [70] [78] [30]
Literature value	[83] [74] [42] [63] [24] [35] [68] [67] [88] [89] [85] [6] [82] [86]
Not specified	[36] [11] [28] [90] [76] [77] [73] [9]
Convection not used	[80] [8] [84] [38] [79] [71] [60] [69] [5] [72]

In addition, Wu, Zhu, & Zuo, 2014 [77] developed APDL/ANSYS Visual Basic 6.0 to calculate the temperature and stress field of disc brake under the stationary heat input method. Users were required only to choose and fill in parameter values, and the system will automatically call the calculation program of ANSYS to conduct meshing, loading, and solving analysis. It was enabled to perform maximum temperature and stress results of 293.2°C on the surface and 135MPa at cooling ribs, respectively. As a result of stationary boundary conditions used, it was concluded that the computation efficiency was enhanced, under specified load conditions.

Furthermore, the numerical and experimental analysis of a railway brake disc temperature studied by Grzes et al., 2016 [85] used analytically estimated stationary heat flux. Constant convective heat transfer coefficient was used on COMSOL Multiphysics, due to the short braking duration. The temperature gradient was seen along the radius, approximately proportional to the distance from the axis of rotation, except in the middle of the rubbing path. Because no contact area between the pad and disc due to the groove on the pad. Moreover, radiation was shown the only boundary condition excluded from analysis, undermining its contribution.

[1] Computational fluid dynamics
[2] Software different from ANSYS

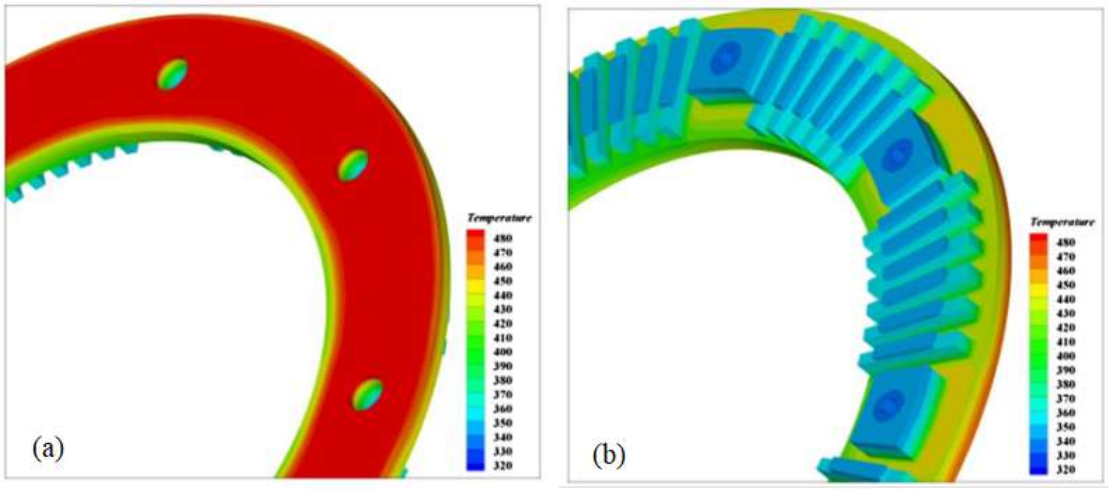

Figure 2.10 Axisymmetric model temperature (°C) distributions of the brake disc at 24s [56]: (a) friction surface, (b) fin surface

Goo, 2018 [81] also observed radial profiles of temperature and thermal stress for the same total amount of stationary heat flux, but varying in the distribution along the radial direction. Four different distributions of heat flux functions investigated were: uniform distribution, linearly increasing, quadratic and quartic distributions. It was revealed that the effect of the boundary condition change revealed a 10% variation in thermal stress. As a summary, the means of convection input and heat transfer modes used in each study are listed in Table 2.4 and Table 2.5, respectively.

Table 2.5 Mode of heat transfer used and corresponding software implemented

Heat transfer mode used	**ANSYS**	**ABACUS**	**Other**
All	[66] [17] [42] [63] [50][73]	[24] [35] [89] [10] [30]	[39] [37] [86]
Conduction and	[74] [28] [68] [67] [58] [75]	[36] [11] [88][81] [70]	[83] [85] [6] [40]
Convection	[56] [64] [76] [77] [33] [78] [9]	[82]	[59]
Conduction only	[38] [79]	[80] [8] [90] [71] [60] [69]	[84] [5] [72]
Convection only	[87] [44]	----	---

Although many studies have clearly identified heat input methods, few studies have an unspecified method. Tirovic & Galindo-Lopez, 2008 [87], for instance, studied characteristics

of disc convective heat dissipation performed by computational fluid dynamics, with an unidentified heat input method. The assembly was rotated in still air using a frame of reference about the wheel axis, with a large enough air domain more improved by boundaries of the open types. The solution method employed was the κ-ε model with scalable wall function and sequential load steps of 400rpm and 550rpm, leading to turbulent flow. The disc friction face displayed quite uniform distribution of convective heat dissipation coefficient, while the vent face of the disc demonstrated a very different and complex distribution.

Table 2.6 Heat flux spatial variation on the disc surface

Heat Flux Location Variation	**Heat input types/methods**				
	TM[1] (Uncoupled)	**TM (Coupled)**	**Axisymmetric Stationary/Fixed**	**MHS[2]**	**Others[3]**
Vary (R[4]&T[5])	[28] [42] [67]	[8] [70] [71] [69] [72]	---	---	[90]
Constant (R&T)	---	---	[36] [83] [11] [74] [39] [84] [75] [56] [77] [37] [10] [40] [59] [79] [82] [60] [73]	[33]	[88] [89] [58] [50]
Constant (R) & vary (T)	---	---	---	[76][6] [30][9] [86]	---
Vary (R) & Constant (T)	[17] [66] [63] [24] [35] [68] [5]	[38]	[80] [64] [85] [78] [81]	---	---
Others	---	---	---	---	[87] [44]

Also, Wu, Zuo, & Wu, 2012 [58] developed a new convection coefficient equation, in which the heat input method was not specified, to improve the limitation in using constant convection value. It considered the impact of wind speed on the disc surface. The newly developed convection coefficient equation was shown to vary both radially and tangentially along the disc surface. The maximum temperature revealed was seen as higher (529.058℃) for the new

[1] Thermomechanical
[2] Moving Heat Source Model
[3] Other types of heat input methods, including unspecified methods
[4] Radially
[5] Tangentially

convection equation than the simplified method. Likewise, heat flux location variation in radial and circumferential directions, versus heat input methods are summarized in Table 2.6, in which others unspecified heat flux and input types are also included. Furthermore, timely varied heat flux and convection coefficient are also displayed in Table 2.7 for the rest of the studies.

2.3.4 Moving heat source (MHS) modeling in temperature and stress analysis

Due to the problems raised in previous models, non-axisymmetric thermal modeling of disc brakes expressed in moving heat source has emerged, attracting attention of many investigators [29]. Because, variations in heat input and boundary conditions with space and time variables are easily managed by programs written in many software codes, including APDL [7], ABAQUS [31] and COMSOL Multiphysics [6]. Despite its effectiveness in managing spatially varying heat and convergence problem, there has been very few researches conducted on non-axisymmetric moving heat source, and still question of spatial and temporal variation in heat has not been fully answered.

Yang et al. 2013 [9] modeled the concept of moving heat input, using timely varying heat flux values on the disc friction surface. The exterior of the friction surface was shown subjected to periodic tensile and compressive circumferential stresses, leading to fatigue crack initiation and propagation. The model was shown successful in predicting the depth of crack initiation and propagetion site. However, the implementation of the model in determining the spatial variation of these cracked site require further development of the model

Besides, the moving heat source based on COMSOL Multiphysics was conducted by Yevtushenko et al. 2017 [6] to determine the transient temperature field in the ventilated disc brake. The stationary pads and the rotating disc were represented by analytically estimated moving heat source of arbitrary shape with velocity $\omega(t)$ over the stationary disc. Although FE model, analytical method and experimental method were seen to agree well, the common behavior of moving heat source model (saw-toothed temperature profile) was not revealed. Furthermore, the model didn't consider the spatial (radial and tangential) variations of heat input and temperature results.

After four years, advanced and recent moving heat source FE model approach was presented by the same authors [86] on the comparative analysis of temperature fields between solid and ventilated brake, adapted in COMSOL Multiphysics. Comparisons were also reported for the stationary disc and rotating disc. Rotational motion of the disc was carried out by assigning a

variable velocity field at each point of the disc area againest a fixed pad (heat source). But this was seen possible only for solid disc geometry, and not applicable in ventilated disc, due to alternating fins/ribs circumferentially. And this challenge was seen solved by in-house program code written in the Python programming and scripting language. The rotational motion of the disc speed was described by coordinate transformation equations that could manage heat flux variations for each element on the rubbing area.

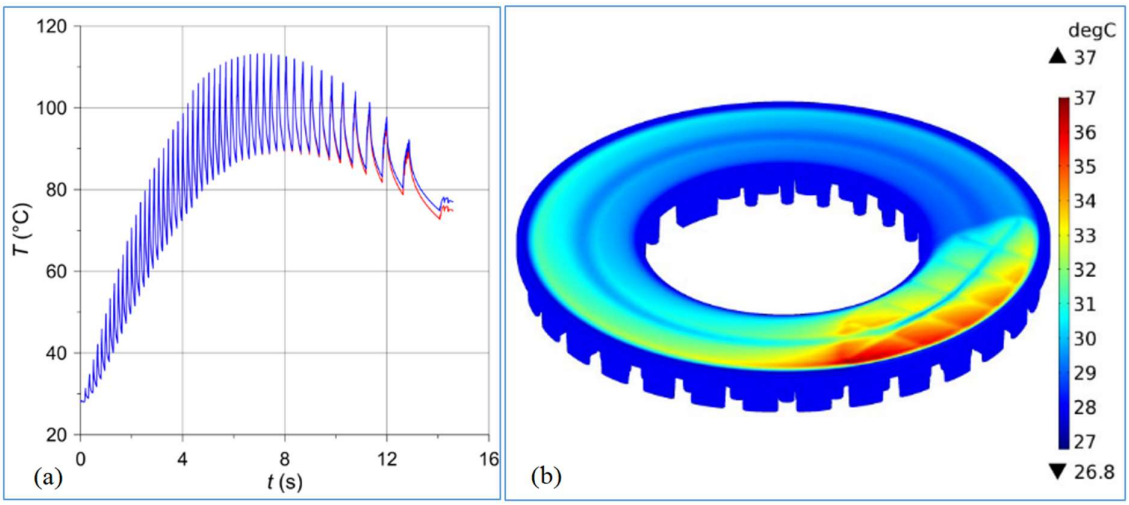

Figure 2.11 (a) Temperature for the solid (red lines) and the ventilated (blue lines) brake discs (b) ventilated disc brake temperature at 0.4s [86]

Though the model contributed a significant drop in computational time, the model developed (written program) was not flexible in variations related to pad geometry (pad grooves), disc geometry (surface-bolt holes) and hydraulic pressure variations during braking time. Besides, programs written for mathematical equations implemented in coordinate transformation was utilized only for contact area (heat source). The friction surface area free from contact, and which is exposed to convection in actual braking condition was not considered. Eventually, a clear border between heat source and heat dissipative convection was not identified (Figure 2.11)

In the same years, Yuan et al. 2021 [30] modeled modified heat flux with cosine functions, to consider its discontinuity at friction surface. Still, the model lacked spatial variation of heat flux at the pad-disc interface, due to pad and disc geometry, and the absence of convective heat dissipation on the discontinuous area of the friction surface. Consequently, the results obtained by the model were seen to oscillate about the axisymmetric model.

Table 2.7 Heat input and boundary condition time variation

BC[1] time variation	Authors
Flux & convection (V[2])	[75] [56] [64] [76] [33] [10] [40] [70] [59]
Flux (C[3]) & convection (V)	[30][36] [83] [28] [68][80][90][86]
Flux (V) & convection (C)	[66] [17] [42] [63] [24] [35] [88] [89] [39] [58] [77] [37] [85] [6] [81] [78]
Time independent convection and flux[4]	[11] [87] [44] [8] [38] [50][67] [73] [69] [5]
Unspecified flux	[87] [44]
unspecified convection	[9]
Disregarded convection	[74] [84] [79] [71] [60] [5] [72]

Furthermore, a non-axisymmetric moving heat source was modeled by Adamowicz and Grzes 2011 [34] for assessing the influence of the convective mode of heat dissipation, for drag type of braking. Similar modeling was also performed by Mahmoudi et al. 2015 [33], on functionally graded brake disk material. In both studies, one rotation time of the disc brake was shared between the heating time and cooling time, according to the proportion of the pad cover angle (60°) to the disc angle (360°). The full disc surface was seen heated or cooled alternatively by their corresponding timeshare within different load steps. Although the radial variation of heat input was considered in [34] (but not in [33]), the method was still axisymmetric for each load step.

Compared to the railway, a moving heat source has been utilized in automotive disc brake investigations [31][91]. Baron Saiz et al., 2015 [91] studied the thermomechanical performance of disc brakes with different geometries using a moving heat source. Even though it was revealed successful in selecting the best shape of the brake rotor, using spatially constant heat flux at the pad-disc interface, and using time-independent heat flux application for a single wheel rotation were areas requiring further improvement. Besides, the moving heat source was modeled by Pan and Cai, 2018 [31] to investigate the temperature and stress analysis of the automotive disc brake. It was reported that the model had better engineering value compared to other axisymmetric and fully coupled modeling. The simulation time ratio comparison

[1] Boundary condition
[2] Varying
[3] Constant
[4] For drag braking only

between coupled thermomechanical and uniformly distributed heat sources (axisymmetric model) was highlighted as 665.61 times higher in the former modeling [31].

Table 2.8 Quantitative analysis of results from different FE modeling

Input calculation methods		Energy per disc (MJ)	Maximum results, their locations & braking times (Temperature and Stress)	Ref.
Heat	Convection			
TM[1]	Empirical	10	694.8 °C by TM (Pressure) & 329.5 °C by stationary, on the mid-surface of the disc at mid-braking time	[66]
TM	Empirical	10	1100 °C for 1 pad groove b/n grooves & edge at early braking time	[17]
Stationary	Literature	3.71	915 °C and 0.8 MPa at mid-braking time on mid-surface	[83]
TM	Literature	13.9	910 °C&736 MPa at early braking on mid-surface	[42]
TM	Literature	2.62	159 °C, and 100MPa mid-surface in variable pressure,	[68]
			151 °C, and 103 MPa at the inner radius for uniform pressure on mid-braking time	
Stationary	CFD[2]	11	359 °C and 461 °C on the surface, with and without consideration of airflow cooling, respectively	[39]
			164 and 269 MPa on the surface with and without consideration of airflow cooling	
			at the ends of the braking	
Stationary	Convection not used	11	373 °C and 415 °C for the new and worn disc, respectively on the surface at mid-braking time	[84]
			237 MPa and 113 MPa for the new and worn discs, respectively, on cooling ribs at the mid-braking time	
Stationary	CFD	5.14	226 °C on the disc surface	[56]
Stationary	CFD	14	600 °C at the outer surface on mid-braking time	[64]
Moving BC[3]	Empirical	5	234.5 °C and 160 MPa on the surface at mid-braking,	[33]
Stationary	Literature	2.7	186 °C on the mid surface at mid-braking time	[85]
Moving BC	Literature	2.5	197.6 °C on the surface at mid-braking time	[6]
Stationary	Empirical	14	278 °C and 378 MPa on the surface at early braking time	[81]
Stationary	CFD	21	517 °C on the surface and 192 MPa around bolt holes at early braking time	[59]
Stationary	Literature	14	298 °C on mid-surface and 201 MPa on fixing teeth at early braking	[82]
Stationary	Convection not used	7.5	410 °C on the surface & 170 MPa on the bolt hole, at mid-braking time	[60]
TM	Convection not used	12	340 °C and 420 MPa on the outer radius surface at the mid-braking	[72]

[1] Thermomechanical (pressure)
[2] Computational Fluid Dynamics
[3] Boundary Condition

Besides, in Pan and Cai, 2018 [31] model, the actual physical movement or rotation of heat on the friction surface was seen obviously, compared to other types of moving heat source modeling. Despite that, spatially uniform thermal results illustrated at the pad-disc interface required further improvement. Furthermore, pad groove and convective coefficient effects on friction surface were fully excluded from the modeling. To the best of the authors' knowledge, no model revealed in the literature, to accounting the spatial (radial and circumferential) and time variations of heat input and boundary conditions simultaneously.

As a summary, FEM thermal modeling of railway disc brakes in terms of heat input and boundary condition were listed in Table 2.8, along with maximum results (temperature and stress) and their corresponding locations and braking time. The studies were portrayed for the only representative studies having specified energy dissipated per disc [66], or calculated from specified mass per disc [17], using equation 2.1.

2.4 Heat Input and Boundary Conditions Modeling in Fatigue Life Prediction

In thermal cycling, the expansion and contraction caused by temperature changes are limited by the uneven distribution of temperature and its interaction with nearby components. This interaction creates local stresses and strains that can have two types of effects on brakes [25]: i) overall thermal effects, such as deformation known as coning, and ii) localized effects, such as thermal cracks. When a brake disc experiences localized overheating and thermal stress, it can undergo changes in its material structure, develop cracks, and suffer other forms of degradation that reduce its lifespan. Therefore, having an accurate model to estimate temperature, stress, and fatigue life is essential for timely response.

Ensuring the safe operation of brake discs throughout their fatigue lifetimes requires numerous expensive and time-consuming dynamometer test techniques [9][76]. However, this validation process is both time-consuming and costly. As a result, there has been a growing demand for robust Finite Element (FE) modeling that can accurately determine the stress and lifetime of disc brakes. While the FE approach is practical, it relies on comprehensive and realistic input, including thermal, mechanical, and fatigue loading and material properties [92]. The quality of the FE modeling heavily relies on the accuracy of heat input, boundary condition application, and material constitutive models. According to Thomas et al. 2004 [41], a 10% error in temperature can result in a twofold difference in fatigue life. Therefore, it is crucial to have reliable temperature forecasting models for precise stress and fatigue life prediction.

The application of axisymmetric modeling was studied by Zhang et al., 2009 [73] in determining thermal fatigue, based on semi-ellipsoid imperfection due to manufacturing. Three imperfection parameters were prepared based on the dimensions of the crack axis, crack depth, and crack direction (radial and circumferential). The imperfections directions were not observed to influence the extent of the stress concentration. Ruther, geometrical structures like crack axis and depth were seen to impact stress concentration.

Besides, Wu, Zhang, and Xu 2016 [10] implemented an axisymmetric model with the application of a novel extended finite element method (XFEM) and crack tip region meshing refinement to carry out the thermal fatigue crack growth under consecutive emergency braking (Figure 2.12). Experimental determination of thermo-physical mechanical properties, fracture parameters, and fatigue crack growth rate curve (da/dN) of the material was performed. It was reported that a total of about 2.77 x 10^5 times single emergency braking or 5.06 years of safe operation was guaranteed. A similar methodology was also applied in the study of Xie et al. 2021 [19]. Despite its successful life prediction, heat input was seen evenly distributed on the rubbing surface (axisymmetric), although the spatial variation of results was seen reported, which might be due to disc geometry.

Likewise, Gigan et al. 2019 [93] implemented an axisymmetric model in evaluating fatigue life predicting model, on an automotive disc brakess. The authors utilized SWT (Eq. 2.5), CMB (Eq. 2.9), and Mechanism-based D_{TMF}-model (Eq. 2.6).

$$\sigma_{\max}\frac{\Delta\varepsilon^{m}}{2}=I_{SWT}\left(N_{f}\right)^{S_{SWT}} \tag{2.5}$$

$$N_{f}=\frac{A}{\left(D_{TMF}\right)^{B}} \tag{2.6}$$

Where σ_{max} is maximum stress, I_{SWT} and S_{SWT} are Smith-Watson-Topper constants (1.82 and 20.25, respectively), ε^m principal mechanical strain range, and N_f is life. For the Mechanism-based D_{TMF} model, A and B are constants to be fit to experimental values.

In contrast, Yang et al., 2013) [9] used rotating (moving) heat input to determine temperature, stress, and fatigue crack initiation and propagation using ANSYS. FE was modeled as applying a timely varying moving heat source with a pad-disc contact zone. Change in the location of the contact area between the disc and pad was determined by the relative position of the disc and pad at a different time step, considering the deceleration rate of the train. The same authors

used this type of modeling in determining the effect of braking energy on fatigue crack propagations for various types of initial braking speeds [76]. This type of simulation resulted from circumferentially varying temperature and stress distribution, with localized maximum temperature (750°C) and stress (675Mpa) in the middle of the friction surface. Yet, spatial consideration of temperature and stress reports did not consider variation within pad-disc contact, along the radial direction. Furthermore, stress results were not seen to predict fatigue life before crack initiation.

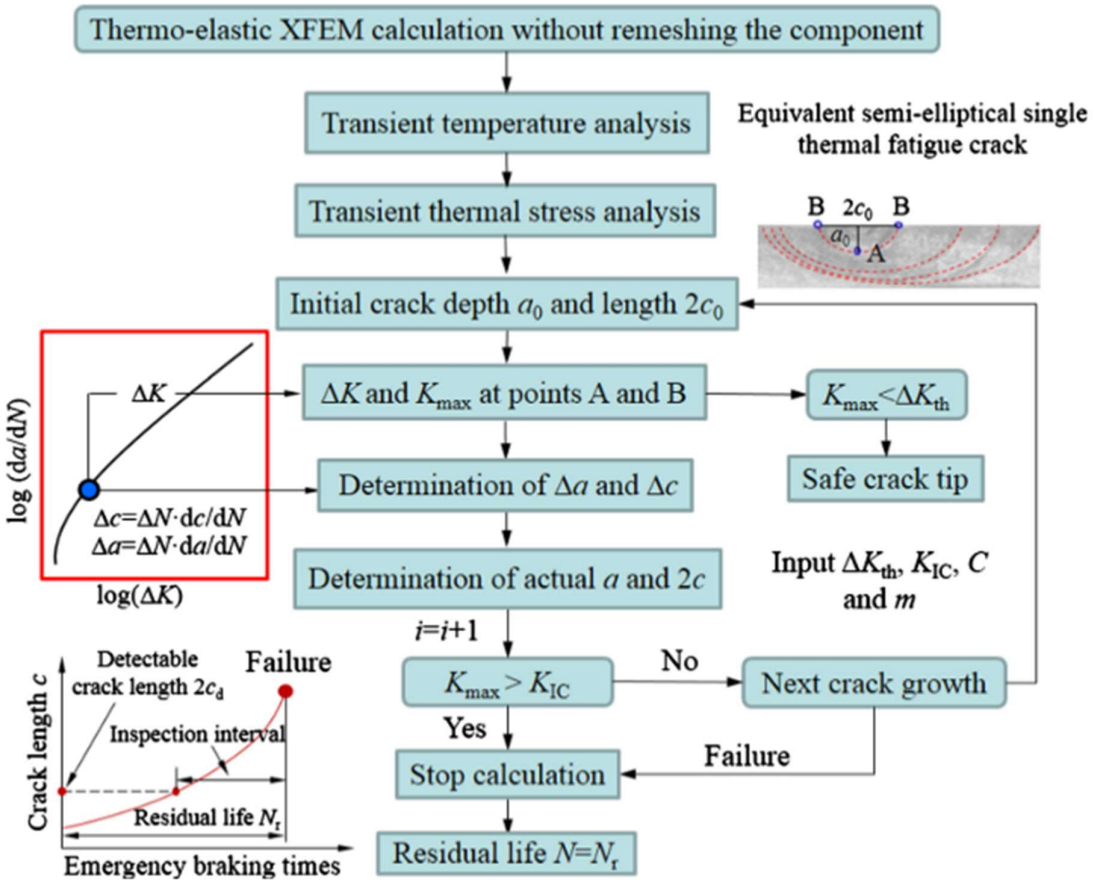

Figure 2.12 Axisymmetric model-based fatigue life propagation algorithm for high-speed railway brake disc [10].

Further application of a moving heat source was seen in investigating the effect of braking energy on fatigue crack propagation by Li et al. 2014 [76] for two emergency braking conditions. Heat input and dissipation were applied, bearing in mind their variation with the speed of the railway vehicle. Change in the location of the contact area between the disc and pad was determined by the relative position of the disc and pad at the different time steps. Fatigue test on specimen cut from friction surface revealed a 5mm crack depth, which was

close to the maximum depth of the overheated areas estimated by FEM. Depending on this analysis, it was inferred that the crack propagation was related to the braking energy (initial speed) for its initiation and propagation.

On the other hand, S. Zhang et al. 2019 [71] studied fatigue life initiation and propagation by coupled thermomechanical model for actual drag braking conditions. The simulation was performed by rotating a pressurized pad against a stationary disc. Axially two-dimensional disc geometry was taken which might seem to reduce convergence problems and simulation time. Combined Fe-safe (Miner's linear fatigue cumulative damage criterion Eq. 2.7) and nCode software (Paris law, Eq. 2.8) were implemented in determining fatigue life initiation and propagation, respectively. The crack initiation life was revealed after 12830 brakings and the crack propagation life was observed at 695000 number of braking.

$$D = \sum_{j=i}^{u} D_i = \sum_{j=i}^{u} \frac{n_i}{N_i} \quad i = 1, 2, 3... \tag{2.7}$$

$$\frac{da}{dN_f} = C(\Delta K)^m \tag{2.8}$$

$$\varepsilon_a = \frac{\varepsilon_e}{2} + \frac{\varepsilon_p}{2} = \frac{\sigma_f^{'}}{E}\left(2N_f\right)^b + \varepsilon_f^{'}\left(2N_f\right)^c \tag{2.9}$$

Where D is the fatigue damage; u is the total number of loads obtained by the rain flow counting method; N_i is the number of cycles required for the fatigue failure of the brake disc under i load; n_i is the number of cycles of the brake disc under i load, so D_i is the fatigue damage value of the brake disc under i load. Whereas m is a Paris' law exponent; a is the initial crack length; ΔK is the stress intensity factor range and C is a Paris' law coefficient. Finally, ε_a is the total strain amplitude; $\Delta\varepsilon_e$ is the elastic strain range; $\Delta\varepsilon_p$ is the plastic strain range; ε'_p is the fatigue ductility coefficient; σ'_f is the fatigue strength coefficient; $b^{'}$ is the fatigue strength exponent and $c^{'}$ is the fatigue-ductility exponent.

A coupled thermomechanical model was also highlighted in [94]. Such type of modeling fully considers rubbing surface spatial variation of temperature and stress, but its high computational cost hindered its application in considering full disc geometry. In estimating life, Coffin-Mansoon-Basquin (CMB) fatigue life prediction method was utilized (Eq. 2.9). Besides, Lu et al. 2021 [95] reported that the coupled thermomechanical model was better at revealing the multiaxial and out-of-phase character of fatigue failure, compared to the axisymmetric heat

input model. Yet, computational efficiency was reported feasible for the latter one, and the model was not extended further to predict disc service life.

Table 2.9 Summary fatigue life modeling in disc brake

Authors	FE Model	Presented results	Life prediction models	Disc Material	Spatial & temporal variation of HI[1]&BC[2]	
					Spatial (R^3, T^4)	Temporal
[67] [96]	Axisymmetric	Pressure temperature, stress, Life:	S-N curve	CI	x	✓
[73]	Axisymmetric	Temperature, stress, crack	--	Steel	x	✓
[9][76]	Moving Heat Source	Temperature, stress, crack	--	Steel	T	✓
[10]	Axisymmetric	Temperature, stress, life	Paris law	Steel	x	✓
`[71]	Coupled thermo-mechanical	Temperature, stress life	Miner and Paris law	Steel	R, T	x
[94]	Coupled thermo-mechanical	Temperature, stress life	CMB	CI	R, T	x
[95]	Coupled thermo-mechanical and Axisymmetric	Temperature, stress, strain	--	Steel	R, T	x
[19]	Axisymmetric	Temperature, stress, crack, life	Paris law	Steel	x	✓
[97][98]	Axisymmetric	Temperature, stress, life	SWT	CI	x	✓
[93]	Axisymmetric	Temperature, stress, life	SWT CM D_{TMF} Microcrack	CI	x	✓

Finally, uncoupled thermomechanical modeling was conducted on the friction surface by Cho et al., 2007 [67], from which pressure distribution, heat flux, and thermal stress were evaluated. Finally, fatigue life was evaluated from stress and S-N curve obtained by specimen collected from the disc. Likewise, D. J. Kim et al., 2010 [96] performed a similar model and reported contact pressure and thermal stress. And the life assessment of the brake disc was calculated from the linear relationship between stress and temperature. As a result, 769 trips were calculated, which was approximately 2 years and 1 month if this number is divided by 365 days. Although pressure distribution on the friction surface was revealed spatially varying,

[1] Heat input
[2] Boundary condition
[3] Radial variation
[4] Tangential variation

stress and life evaluation were conducted by uniform pressure (axisymmetric model) assumption.

As a summary FE modeling type, life prediction models, materials, and spatial and temporal variations of heat input and boundary conditions are presented in Table 2.9, in which "x" represent "not vary spatially" or "not vary tangentially".

2.5 Concluding Remark on Temperature, Stress, and Fatigue Life Modeling

The known priori models (both stationary and moving heat input methods) were shown as the most widely used method in heat flux calculations, comprising 53% of the studies, while pressure distribution-based uncoupled thermomechanical method and coupled elements-based thermomechanical were ranked second and third (Table 2.3). This might appear due to its simplicity in converting braking conditions (train axle load, speed, and deceleration) into heat flux [40], although the models were shown pitfall in predicting micro (wear) and macro (hot spots and hot bands) thermal effects [36]. Additionally, the models are feasible in computational time and computer memory usage. Two ways of conducting such calculations were highlighted in literature: mechanical to thermal energy conversion [33] and friction power methods [39]. Only averaged bulk surface temperature could be successfully predicted in this method [36], while macro and micro thermal effects not predicted.

In contrast, uncoupled thermomechanical was seen as capable of modeling micro and macro thermal effects [63][24][42], however, its decoupled analysis into three (contact pressure, thermal and mechanical analysis) made its simulation complex and time-consuming. This might be the reason why this method is currently not seen in published papers, after Tirovic & Sarwar, 2004 [35] and Gao et al. 2007 [7], respectively in railway and automotive disc brakes. The last heat input calculation FE model was coupled elements-based thermomechanical, in which the disc brake is allowed to rotate against two pads [8]. As a result, heat flux was generated due to friction, using coupled-field solid elements having two degrees of freedom: displacement (u_x,u_y,u_z) and temperature [99]. This type of heat input seems realistic modeling in considering the location variation of heat input. However, the convergence problem observed in massive CPU computational efforts and data storage [100] needs special care. To alleviate this challenge, wear consideration was seen omitted in ABAQUS [70], ANSYS [38] and LS-DYNA [72]. Still, the aforementioned problems were not completely avoided.

To alleviate long computational time and convergence problems, both coupled and uncoupled thermomechanical models developed so far were limited to short braking times (3.5 sec in [7]).

And for long braking times (62s [17][66], 80s [28], and 76s [24]), they were seen as limited to two-dimensional (axisymmetric) and a sector of three-dimensional disc geometries. And these types of assumptions violate the actual braking conditions.

Stationary/axisymmetric heat flux was seen as the well-known flux application, constituting 23 studies (Table 2.3), while uncoupled thermomechanical, coupled thermomechanical, and moving heat flux applications were ranked the second (10 studies), third (6 studies) and the fourth (5 studies), respectively. However popular it might be, the heat source is not stationary on the disc surface in actual braking conditions but changes continuously with time instead [70]. To some extent, coupled and uncoupled heat flux application solves this problem, as it varies on disc surface spatially and timely, except the convergence problems in its simulation.

Moving heat source model, in contrast, solved convergence problems in thermomechanical models, as well as spatially fixed heat source problem in axisymmetric model. In spite of its efforts, the methodology followed in simulating moving heat flux was seen far from the actual braking conditions in [33] [34], because, heat flux and convection were applied on the whole area of disc at different time increments. While, in [6][9], the method of revolving heat flux was not clearly defined. Moreover, the problems with spatial variation of heat input and boundary conditions, along the radial and circumferential direction of the disc have not been answered yet. The lack of friction surface partitioned into heat dissipative convection area and heated source area, and implementation of constant heat flux at the pad-disc interface are areas requiring further improvement in [30][31][9][91]. Moreover, it was seen as vulnerable to the problems in the axisymmetric model [33] [34] and not flexible in accordance to pads and disc geometry [86].

The amount of heat input generated at the disc pad contact interface is proportional to the pressure variation throughout the braking time, and also proportional to the radius of the disc. Beside, circumferential variation of heat input and boundary condition is undeniable, due to deceleration. Regardless of these facts, it is regrettable to observe the dominance of using constant heat flux spatially (both radially and circumferentially), accounting 43% of the studies (Table 2.6).

Relatively, spatial variation of heat flux was observed more along the radial direction than the circumferential direction of the disc (Table 2.6). This might be due to the capability of uncoupled thermomechanical and axisymmetric model in accommodating radially varying heat flux application [65]. In contrast, studies involving both spatially varying and constant heat

flux were also revealed [28][70], to investigate better results. Few studies revealed unspecified or no heat flux in the investigation of convective heat dissipation [87][44].

Consideration of all boundary conditions was shown only in 27% of the studies, while, conduction and convection cover a wide range of the study, constituting 47% (Table 2.5). Convection was considered for friction surface only, as enclosed areas of ventilation channels and pillars can be neglected due to obstacles [44]. This uncovered a high level of assumptions and simplifications in disc brake simulations. The exclusion of radiation from modeling might seem due to the high thermal conductivity of disc material [40], short braking time [29], or its low contribution at a low temperature, as stated in automotive disc brake studies [101][102][103]. Though the contribution of radiation in dissipating heat was seen as insignificant in many studies [56][104], appropriate provisions were seen as necessary in verifying FEM results with experimental [87].

In spite of researchers' recommendation to use all modes of heat transfer [61], studies were using only convection (4%), because, the studies' scope was focused on heat dissipation only [87][44]. In contrast, studies disregarding the modeling of convection were also highlighted (Table 2.5), assuming no practical influence of heat dissipation in short braking time [105], and even in long braking time [24]. And, other studies proposed the dominance of heat flux (conduction 22%) over other types of boundary conditions during braking, for their ignorance of convection and conduction [84]. Particularly, Olshevskiy et al., 2012 [5] investigated that heat flows by other boundary conditions did not exceed 3% of the frictional heat flow, while Wang et al., 2019 [79], and Jiguang and Fei, 2015 [37] estimated 8% and 5% for convection and radiation, respectively.

According to [66][17], the heat transfer by convection coefficient depends on the flow rate of the air, air velocity, air flow direction, and wall temperature. It also depends on the geometry of the disc design (full or air-cooled disc, geometry, and number of ribs, etc.). This heat transfer coefficient is then different at each point of the surface and varies as a function of time.

Various methods of convective heat dissipation predictions were highlighted, from which constant value taken from literature was displayed as the widely used method, accounting for 14 studies (Table 2.4). Despite its acceptance among researchers, its reliability remained under question, due to varying conditions of convection with disc rotational speed, geometry, and location [56]. An empirical equation was another method of estimating convection based on braking conditions of speed, air material properties and disc geometry [106]. Variation of

convection with speed and location (friction surface and vanes) has easily solved in this method. The variation of heat transfer coefficient at each point of the surface and time was seen simulated in CFD/FLUENT, representing the actual braking condition [64]. This doesn't mean that all CFD simulations accommodate spatial and time variations of convections (Table 2.6 & Table 2.7), as there were studies observed to export averaged and constant coefficients into thermal analysis [50].

The difference in heat input and boundary condition modeling is expected to result in variations in quantitatively reported results (temperature, stress, fatigue life), even for the same input parameters. The value of thermal results depends on disc type (size, material, geometry), braking conditions (deceleration, time, speed), train type (maximum speed, axle load and the number of discs per axle), and braking mode (service, emergency, single, repeated, stop or drag braking). Unfortunately, since none of the studies has the same input parameters in common, it is difficult to compare the presented models (heat input and boundary condition types in (Table 2.8)) and their corresponding results.

Nonetheless, few studies have shown clear comparison criteria. In the study of Dufrénoy and Weichert, 1995 [66], temperature calculation made by thermomechanical (694.8°C) was revealed twice as high as the stationary heat input method (329.5°C in Table 2.8). Besides, Kim et al. 2008 [68] identified higher temperature (159°C) and stress (100MPa) results for thermomechanical than stationary uniform pressure. This might be due to a variation of high contact pressure at the pad-disc contact interface, caused by wear. Nevertheless, this finding was not shown necessarily agree with studies in Table 2.8, due to various reasons. For instance, lower energy input discs' (<3MJ) temperature results shown for moving (197.6°C)[6], stationary (186°C)[85], and thermomechanical [68] (159°C) heat input methods were not proportional to energy input (2.5MJ, 2.7MJ and 2.62MJ, respectively). Because, there is a difference in disc and pad dimensions (respectively, 175mm and 320mm for inner and outer disc radius in [85], while, 165mm and 350mm for inner and outer disc radius, respectively in [6]).

Besides, taking different literature values of convective heat dissipations (100W/m^{2}K in [85], while 20-60 W/m^2°C in [6]), for the same cast iron material was expected to variate their results. Not only these, variations in convection calculation methods (CFD [64], empirical [81], or taking constant value from the literature [82]) and disc materials used (steel in [64], cast iron in [81][82]) were also revealed as other factors for result variations for the same input

energy of 14MJ (Table 2.8). Furthermore, the effect of considering or disregarding the convection coefficient during deceleration was seen in the study of Jiang et al. 2012 [39] for the same input energy (11MJ), resulting in 359°C with consideration, and 461°C without consideration. Based on this circumstance, studies disregarding convection coefficients [84][71] were expected to have higher temperature results, relative to studies regarding them. The remaining results and modeling in Table 2.8 were interpreted in similar ways.

In contrast, maximum results locations on the disc surface (outer, inner, mid-surface) and their corresponding braking times (early, mid, late and end braking) depend on types of heat input methods and braking mode (drag or downhill braking, and braking to standstill on a flat surface). For all stop braking displayed (Table 2.8), maximum results were seen at early or mid-braking time. Because, heat flux input is maximum at early braking, and reduced as time increases, as in [84][39]. In fact, the effect of convection on reducing temperature is observed at the ends of braking than early braking. These two factors limit the maximum result at mid-braking time. For drag braking, however, maximum results are observed at the end of braking time [82]. Because heat flux input is kept constant throughout braking. And, this dominates the effects of convection in reducing the temperature at the end of braking time.

Finally, the location of maximum results varied along the disc surface in thermomechanical (disc rotation) modeling. This was seen from extreme radii to mid-surface [8][70][69]. Because, hot bands or fire rings observed at early braking are converted to hot spots at the ends of braking. Furthermore, the outer surface of discs was reported to have the highest thermal results for stationary [64] and thermomechanical (disc rotation) [72]. This might be due to the absence of structures used for heat conduction on the outer radius of the disc, compared to the inner radius (hub and bolt structures). Mid-surface of the disc was also identified as the maximum temperature site [9]. It might appear due to the smaller and larger size of pad radii at outer and inner, respectively, compared to disc radius. Also, some studies revealed the surface as a position of high thermal results, without identifying a specific site [56][6].

According to the aforementioned studies (Table 2.3) and reviews conducted by the authors on a railway disc brake [26], four different FE thermal models were identified: uncoupled thermomechanical, coupled thermomechanical, moving heat source, and axisymmetric. It was reported that none of these models could account for the spatial (radial and circumferential) distribution of temperature, stress, and crack initiation sites, except coupled thermomechanical, where computation time is challenging. A similar problem was also reported for uncoupled

thermomechanical. And, axisymmetric (the largest volume of the utilized model), couldn't determine the particular location of the crack initiation site, as it assumes uniform temperature and thermal stress on the friction surface. Besides, the lack of kinematic non-linear material modeling is another shortcoming in the current literature, except [97][98] [93] (Table 2.9). If temperature distribution on a specific location is precisely determined, and a suitable kinematic model is applied, reliable stress and service is predicted

2.6. Applications of FE in Disc Brake Materials Modeling

Thermomechanical simulation of railway vehicle's disc brake is not only limited to modeling type but material type selections and materials' non-linearity expressed by stress-strain relationship and temperature-dependent thermo-physical and mechanical material properties also affect simulation accuracy. Based on this foundation, optimum material implemented, and its non-linearity is presented in this subsection.

2.6.1 Types: composites, steels, and cast irons

Mahmoudi et al. 2015 [33] investigated wheel-mounted brake disks materials made from a composite type known as functionally graded material (FGM) Al-A359/SiCp, Aluminum alloy (A359), and ductile cast iron (SGI) used in ER24PC locomotives. In FGM, the disk was checked for better optimization from the thermomechanical stress aspect, by varying the grading index axially from 1-5 (Figure 2.13). To have a better comparison, the safety factor was presented as the ratio of material yield stress to the maximum equivalent von Mises stress from ANSYS. It was reported that using FGM instead of ductile cast iron improved the safety factor by 59%, while the Al 359 material fall in between the two. This might seem due to the high thermal bearing and low thermal expansion coefficient of SiCp ceramic, accompanied by the higher heat conduction capability of aluminum in its higher volume fraction. Based on the study, the authors recommended proper design of the constituent of materials, for better strength and factor of safety of the disk.

In addition, Bayat et al. 2019 [38] studied FGM changes in material properties along radial direction by power law distribution. The effect of grading index and contact line ratio on displacement, strain, and stress under thermo-mechanical loading was investigated. The study was performed for pure metal and ceramic, respectively at the inner and outer radius of the disc brake. Elastic contact analysis was done with both temperature-dependent and independent material properties rotating with constant angular velocity. It was observed that higher grading index numbers resulted in higher nodal displacement, higher radial strain, and lower radial

stress. On the other hand, an increased contact line ratio led to a smaller value of displacement, lower radial strains, and lower radial stress.

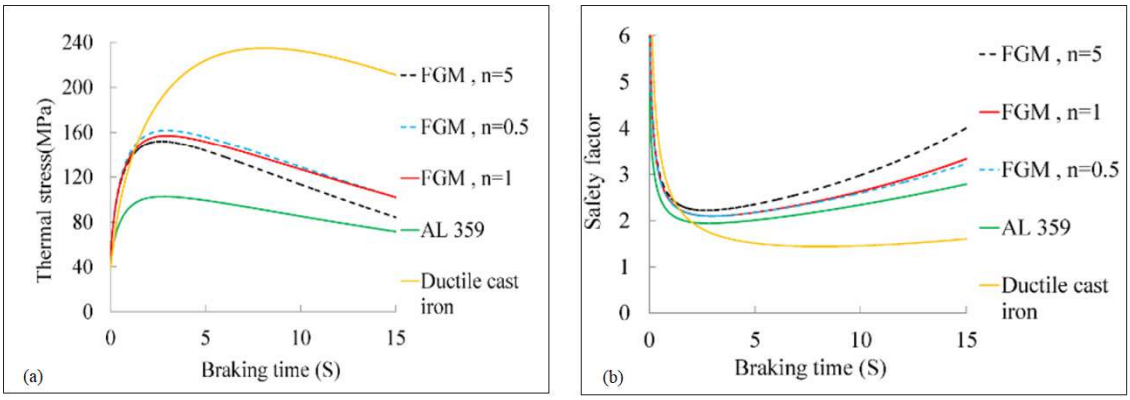

Figure 2.13 (a) Disc surface maximum thermal stresses (b) safety factors [33]

Jiang et al. 2012 [39] demonstrated SiC_n/6061 Al alloy composite material with the goal of finding the thermal and stress analyses with and without consideration of the airflow cooling, using CFD/Solidworks FEM. CFD/Solidworks FEM was used for calculated convection and radiation estimation and later used as a boundary condition in thermal analysis in the same software. It was concluded that SiC_n/6061 composite material accompanied by airflow cooling revealed effective to reduce maximum temperature and thermal stress.

Similarly, Nong et al. 2017 [40] investigated thermal and stress analysis of SiC_{3D}/Al alloy composite material, to identify its cooling effect, using finite element (FE) and computational fluid dynamics (CFD Solidwork) methods. Heat flux was calculated based on uniform wear assumption and convection coefficients were applied as input boundary conditions from Solidworks in thermal analysis. It was shown that considering air cooling reduced the maximum temperature by 14% than disregarding it. Owing to the absence of surface cracks and lower stress developed, it was concluded that the brake disc material was capable to meet the requirement of high-speed trains braking from 350 km/h in emergency cases.

Even though the presence of SiC improves disc wear, its hardness caused a high wear rate of the friction pads. Motivated by this conflicting interest, authors Jiang et al. 2019 [59] extended the study of Nong et al. 2017 [40] by reducing the hardness of SiC by adding Al_2O_3, to reduce the wear losses of the friction pads. The authors designed the new Aluminum alloy disc brake with variation in thickness of Al2O3-SiC (3D)/Al alloy composite wear-resisting surface layers and examined temperature and thermal stress distributions of the brake disc, by employing sequential coupling Solidwork in heat conduction and CFD heat transfer.

The impact of varying initial braking velocity and layer thickness of Al_2O_3-SiC(3D)/Al alloy composite on the temperature development of the disc was studied. It was found that temperature increase with initial braking velocity. In addition, the impact of the wear-resisting layer thickness on maximum temperature was not obviously seen, owing to its distribution uniformity resulting from the high conductivity and cooling ability of brake disc material under investigation.

Brake disks made up of SiC/7075Al composite were chosen by Yu et al. 2012 [84] due to their weight and cost-effectiveness, in determining thermal and stress distribution by COMSOL. Analysis simulation was done by paying no attention to convection and radiation and with consideration of two models of discs: disc without wear and worn out disc. The higher temperature and stress were displayed in the worn-out disc case, meanwhile, areas, where the wreath of the disk and the cooling ribs were not connected, were indicated to have higher temperatures. Based on the revealed results, it was concluded that induced thermal stress was released well for SiC/7075Al composite material, satisfying the requirements of axle mount discs for high-speed trains. Furthermore, thermal-stress fields and tribological property of C/C−SiC material was performed in the article [74] and displayed outstanding static and dynamic coefficient of friction.

Table 2.10 Summary of materials application in a disc brake, according to train speed

Range	Steel	Composite	Cast iron	Unspecified
V<200kph	[66] [17] [87] [8] [63] [69] [5] [90] [86]	[33] [78] [38] [30]	[96] [77] [85] [6] [81] [107] [60]	[68] [80] [75] [56] [67]
200 ≤ V≤300kph	[28] [42] [44] [89] [58] [9] [64] [76] [37] [70] [79] [71]	[39] [84] [59]	[82]	----
V>300kph	[36] [83] [11] [24] [35] [10] [72]	[74] [40]	----	[73]

To sum up, brake disc materials used in railway transportation are identified in Table 2.10 as cast iron, steel and Aluminum metal matrix composite. Cast iron application of these materials is the most common. The most important parameter that determines the material selection of the disc and pad is temperature [3].

2.6.2 Materials kinematic non-linearity modeling

In precise FE modeling, predictions of structures' life need inelastic material analysis, despite their requirement of large computation times, particularly under cyclic loading. Hence, El Abdi & Samrout, 1999 [83] proposed a model of an isothermal elastoviscoplastic constitutive

equation for steel 28CrMoV5-8 used in the brake discs of TGV train, to account for phenomena such as viscoplasticity, cyclic softening or hardening, relaxation, and strain memory effect. Stabilized stress-strain curve was revealed for the material, after five cycles of emergency stop braking from 320kph.

Besides, a non-linear kinematic hardening model was performed by El Abdi & Samrout, 2000 [108] to predict the effect of the 28CrMoV5-8 steel used in brake discs of TGV trains subjected to thermal and mechanical loading. The authors emphasized the use of two isotropic hardening variables and the inclusion of strain memory terms. Stabilized loop curve was obtained at 20°C and a strain amplitude of 1.4%, which was also verified by experimental results.

On the contrary, Dufrénoy, Bodovillé, & Degallaix, 2002 [47] introduced a non-linear kinematic and isotropic hardening jointly in Steel 28CrMoV5-08 material for two cases: assumption of uniform contact pressure and macroscopic hot spot. In the first case, multi-surface linear kinematic hardening displayed higher stress values at lower plastic strain values. Besides, it reached elastic shakedown quickly, which could be explained by the intrinsic properties of the kinematic material model disregarding the cyclic softening of the material. In Isotropic, elastic shakedown appeared late, as a result of the decrease in ratcheting strain, braking after braking. Besides, the occurrence of residual tensile stress was seen after cooling with low amplitude. In the second case, only a multi-surface model of linear kinematic hardening was applied, resulting stable stress-strain loop after 6 brakes, and was revealed as complex because of thermal expansion coefficient variations specifically at 715°C and 800°C. Irrespective of constitutive equations used, stress and strain were shown higher in the circumferential direction than in the radial direction, and their hysteresis loops were recommended to be applied in thermal fatigue for disc life prediction.

In the same way, the multi-surface linear kinematic model was applied by Dufrénoy & Weichert, 2003 [42] in their demonstration of thermomechanical modeling of brake disc fracture mechanisms. Additionally, it was introduced in performing a two/three-dimensional hybrid model of the thermomechanical behavior of disc brakes studied by Dufrénoy, 2004 [63], owing to its intrinsic properties leading to elastic or plastic shakedown quickly. But softening was not high, as the stabilized loop was obtained only after several cycles. Cyclic loading revealed the complicated shape of the stress-strain loop since the thermal expansion coefficient varies at a high temperature and material phase transformation. Because of the similarity in

braking conditions and constitutive law applied, equivalent results were reported, as in Dufrénoy, Bodovillé, & Degallaix, 2002 [47].

Unlike railway vehicles, automotive disc brakes were seen to use material nonlinearity in life evaluation, although limited in number. Axisymmetric model heat input was implemented by Le Gigan et al. 2017 [97], with GTN (Gurson-Tvergaard-Needleman) material model for grey cast iron. Uniform heat flux applied on the 10° sector of a brake disc was seen to investigate stress-strain responses of the material. The material model was seen to successfully mimicked the cyclic behavior of grey cast iron thermomechanical fatigue tests up to 650 °C. Next, Le Gigan 2017 [98] conducted disc design improvement on the ventilation arrangement of straight vanes and pillared layouts. He successfully reduced mass by 13% and increased the service life by 50%. Finally, Gigan et al. 2019 [93] extended this model to calibrate four fatigue life assessment models: Smith-Watson-Topper (SWT), Coffin-Manson (CM) model, and mechanism-based damage models. No matter how extensive the study performed, the questions of axisymmetric modeling in handling spatial variation of heat input and boundary conditions remained unanswered.

2.6.3 Temperature-dependent non-linearity modeling

In contrast, disc material variation with temperature is crucial for obtaining reliable results in FE analyses. Under these circumstances, Tirovic & Sarwar, 2004 [24] measured the two most important properties: tensile stress-strain relationships and thermal expansion, in part two of their study on design synthesis of non-symmetrically loaded disc brakes. The measurements were performed by certified test houses and equipment, using a sample taken from 15 CDV 06 materials. True stress–true strain measurement revealed that ultimate tensile strength and proof stress were reduced by 50% and 5% at 600 °C and 900°C, respectively. However, it was shown that the disc material's Young's modulus and strength reduced relatively little until 500°C. For thermal expansion coefficient, it was shown to increase with temperature from $4x10^{-6}K^{-1}$ at 100°C to $14x10^{-6}K^{-1}$ at 750°C. Nevertheless, the remaining disc material properties were adopted and used from different sources, such as literature and personal communications. It was also considered that specific heat increased, and thermal conductivity decreased with temperature rise. In contrast, density and Poisson's ratio were considered constant throughout the temperature range (20-1000 °C). Moreover, the consideration of plasticity and material properties change with temperature is summarized in Table 2.11.

Table 2.11 Application of materials non-linearity in reviewed studies

Plastic material modeling	Temperature-dependent material modeling
[83] [28] [42] [63] [76]	[66] [36] [83] [11] [28] [42] [63] [24] [35] [87] [44] [89] [76] [77] [10] [40] [38] [107] [59] [79] [71]

2.6.4 Concluding remark on materials selection and its non-linearity modeling

Disc brakes' required material properties are identified as lower density, lower price, lower thermal expansion coefficient, higher thermal conductivity, higher specific heat capacity, higher compressive strength, higher surface hardness, higher corrosion resistance, stable friction coefficient, and higher fracture toughness [109][110]. Based on these properties, selecting the optimum material is not an easy task, because no material exists that can fulfill all the required properties. Even, design requirements might be conflicting between thermal and mechanical properties. Cast irons were shown as better materials, having lower density, low price, low thermal expansion coefficient, and higher thermal conductivity, while steels on the other hand, were displayed as better materials having higher compressive strength, surface hardness, higher corrosion resistance and higher fracture toughness [109]. Besides, it was highlighted that steel was seen as advantageous over cast iron in having higher fracture toughness to density ratio (ten times) at a similar price, even though steel does not have the desired thermal properties of gray cast iron [109].

On the contrary, centrifugal force was seen contributed additional thermal load [74][82] in train operation. Since it was increased with the mass (density/volume) of the material, further lighter material was required. Because lower density gives an economic advantage (little fuel consumption) and ride comfort [110]. In Rak, 2000 [111] for example, all grey cast iron brake discs were seen to have a total weight of 460 kg, accounting for 20% of the entire bogie mass. As a result, new development in materials led to using the metal matrix composite for train disc brakes [84]. Their advantage was seen not only in weight reduction but their best thermal properties and corrosion resistance has been attracted researchers for high-speed trains also [39]. Unfortunately, their higher coefficient of thermal expansion coefficient [39][112] and low-temperature resistance [113] limited their application.

Furthermore, in the manufacturing stage, non-uniformity of ceramic particulate (SiC, Al_2O_3) and residual porosity were seen [114], which limits their application in disc brake. Further investigation on composites to solve such problems led to co-continuous composites, made up

of 3D continuous network structure of SiC ceramic reinforcement and discrete metal [39][40]. However, the high strength achieved by SiC exposed the pad to a high wear rate. To counteract such a problem, Jiang et al. 2019 [59] added Al_2O_3 to SiC.

Contrary to metal matrix composite (MMC), ceramic matrix composite (CMC) was seen better choice for brake discs owing to their superior tribological properties in comparison to grey cast iron, having higher tribological properties, lower density, lower thermal expansion coefficient and constant (stable) friction coefficients [115]. In spite of these opportunities, it was not seen used in railway disc brake thermal and stress simulation, except article by CHEN et al. 2019 [78]. Indeed, the researches on CMC were observed focusing on methods of preparation, thermophysical properties, and tribological properties yet [116]. Furthermore, its lower specific heat capacity might be the cause of its scarcity in rolling stock application [115].

Finally, FGM were seen as different in material construction, from all composites. Based on the required property, it was seen possible to vary ceramic concentration radially [38] or axially [33], which made FGM a more flexible and researchable area, from all composites. Yet, the research on composite material is still open-ended due to the lack of orthotropic modeling and fall of braking performance at a high temperature [14][117]. Besides, the methods of modeling material property variation in composites were seen as limited to power law [33][38], and not cross-checked with other methods, such as volume fraction [118]. Furthermore, materials involved in composite formation were seen as limited to aluminum alloy and silicon carbide, which promote a new line of research for other materials. To sum up, the application of composite materials in railway disc brake thermal simulation in decreasing order followed MMC, FGM and CMC, respectively.

To investigate the relations between materials type and their application in various speed ranges (Table 2.10&Figure 2.14.a), Knorr Bremse (brake discs and pads manufacturer Figure 2.14.b) specification is utilized in evaluating materials implemented by different researchers in this study [3]. Steels (the most widely used: 55%) and composites were displayed as applied in all speed ranges. Meanwhile, cast-iron materials were revealed to be dominant in low-speed trains. Although aluminum and ceramic materials were not observed, it was surprising to highlight that, the usage of the material in studies reviewed exactly agreed with the manufacturer's specification. In addition, the observed disc brake materials (steel, cast iron and MMC) are consistent with previously identified railway disc brake material in the study of Günay, Korkmaz, & Özmen, 2020 [3].

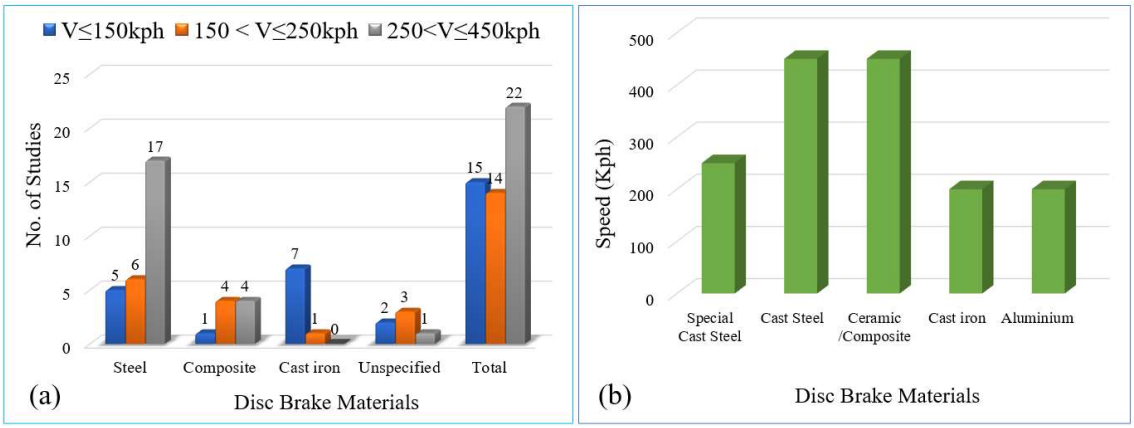

Figure 2.14 Materials type and their speed range: (a) In this study (b) Knorr Bremse [3]

From the steel types used, low carbon steel with low alloy contents were seen as the majority of steel types selected, while medium carbon steel accounted for the remaining. The use of cast iron in rolling stock disc brake material was seen as highly diversified, based on the shape of graphite: lamellar, grey or flake graphite cast iron (FGI) [107][77][88][82][60], nodular, ductile or spheroidal graphite cast iron (SGI) [33][119] and compact or vermicular graphite cast iron ((((a))][120][121].

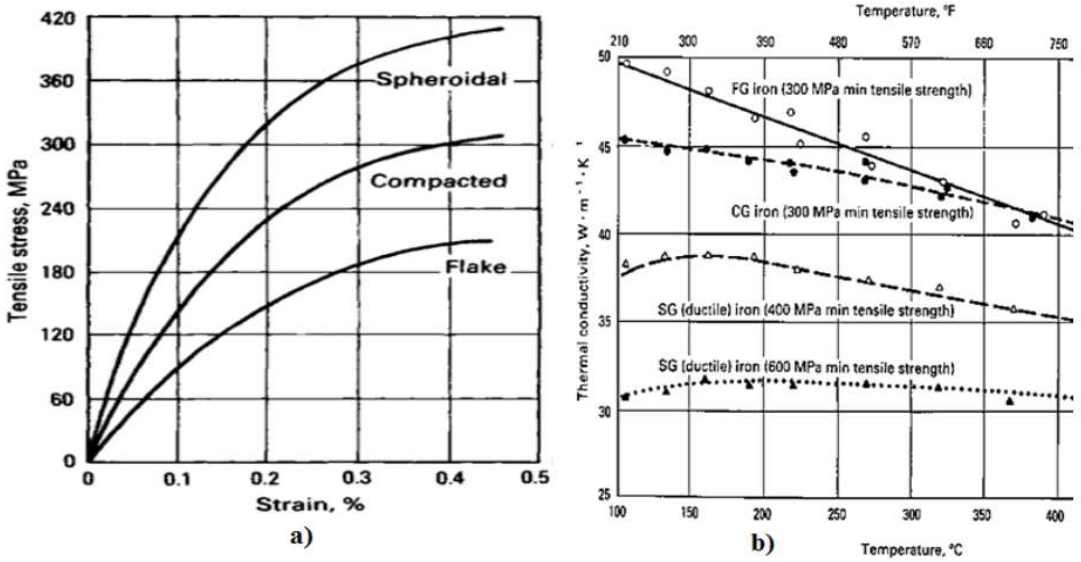

Figure 2.15 The influence of graphite morphology on (a) mechanical and (b) thermal properties of cast iron materials [122]

The popularity of FGI might be due to its high thermal conductivity owing to its graphite shape [122] (Figure 2.15.b). Next, compact or vermicular has better thermal performance than ductile cast iron [122]. Nonetheless, the reverse is seen as true in Figure 2.15.a in tensile stress,

displayed flake graphite cast iron as the lowest, spheroidal cast iron as the highest, and compact as intermediate [122]. That is why B. C. Goo & Lim, 2010 [123] uncovered higher thermal crack resistance of compact vermicular than flake cast iron. A similar conclusion was drawn in [3] also.

Modeling detailed material data have seen as challenging due to the friction process complexity observed in thermal, mechanical, wear, and friction processes. These include plasticity and temperature-dependent material properties, for exact modelling of thermo-elastic instability [24]. Material properties highly affected by temperature include Young's modulus, yield strength, coefficient of thermal expansion, specific heat capacity, conductivity, friction coefficient, and others also [78][123]. The relationships between strain and stress of metals are also vulnerable to changes in temperature, which needs the definition of constitutive equations, either in isotropic on kinematic [18].

Consequently, for better modeling of FE analysis, consideration of material properties and plasticity are highly significant. Unfortunately, only 41% and 10% of the studies considered material properties variation with temperature and plasticity, respectively (Table 2.11). These might appear due to assumptions and simplification taken to reduce computational costs.

Table 2.12 Ventilated wheel-mounted straight radial vane symmetries and disc connection

Authors	Axial	Circumferential	2/3D	Pad/disc	Disc connection
[24] [35]	Half	2D	2D	Both	HB[1]
[11] [83]	Half	2D	2D	Disc	HB
[60] [40]	Half	180°	3D	Disc	HB
[87]	Half	30°	3D	Disc	HB
[68] [67]	Half	360°	3D	Both	HB
[33] [75][52][10]	Half	360°	3D	Disc	FSB[2]
[9] [39] [76][79][84]	Half	360°	3D	Disc	HB
[36]	Half	7.5°	3D	Disc	HB

2.7 Symmetry Selection and Optimum Geometry Selection

The selection of geometry in disc and pad structural and thermal analysis is another parameter that could impact heat removal from the surface of the disc and pad. Besides, it could affect simulation accuracy. Hence, this area is reviewed in two directions: symmetry selection and optimum geometry selections, presented below.

[1] Hub-bolted connection between disc and axle
[2] Friction surface-bolted connection between disc and axle

2.7.1 Disc symmetry selection

Dufrénoy et al., 2002 [47] made two assumptions in their investigation of disc crack: axisymmetric and the presence of macroscopic hot spots. The assumption of uniform distributions of contact pressure was applied to two-dimensional geometry (axisymmetric), which resulted from uniform heat flux on the disc surface. For macroscopic hot spot, however, 3D and 30° of the disc model was used, due to hot spot regular distribution and anti-symmetric position. The authors suggested that it was not necessary to consider any contact variation, due to stationary position and uniform distribution of hot spot. Maximum temperature, circumferential stress, and strain were displayed on the surface of the disc. It was indicated that nearly twice the maximum temperature was revealed in the hot spot area than that of constant pressure distribution. Similar input parameters, geometry, and conclusions were also drawn in the work of Dufrénoy & Weichert, 2003 [42].

Table 2.13 Ventilated axle-mounted 3D disc geometries, symmetries, and disc connection

Author	Vane ventilation types	Axial symmetry	Circumferential symmetry	2/3D	Pad/ disc	Disc connection
[90]	Straight radial	Full	360°	3D	Both	FSB[1]
[74] [39]	Straight radial	Full	360°	3D	Both	HB[2]
[6] [81]	Straight radial	Half	180°	3D	Disc	HB
[28]	Straight radial	Half	30°	3D	Disc	HB
[59][30][86]	Straight radial	Half	360°	3D	Disc	HB
[96]	Straight radial	Half	360°	3D	Both	HB
[58]	Circular pillared	No	40°	3D	Disc	HB
[107]	Circular pillared	Half	45°	3D	Disc	HB
[77]	Circular pillared	No	30°	3D	Disc	HB
[64]	Circular pillared	Full	360°	3D	Disc	HB
[89]	Circular pillared	Full	360°	3D	Disc	HB
[37]	Circular pillared	Half	360°	3D	Disc	HB
[82]	Circular pillared	No	30°	3D	Disc	HB
[73]	Circular pillared	No	90°	3D	Disc	HB

In another study, Dufrénoy, 2004 [63] developed a hybrid two-/three-dimensional model to provide a negotiation between the limitations of a non-realistic two-dimensional (axisymmetric) model and the enormous computational time of a fully 3D approach, based on ANSYS. It was demonstrated that radial variation of contact pressure was responsible for circles of high temperatures called fire rings.

[1] Friction surface-bolted connection between disc and axle
[2] Hub-bolted connection between disc and axle

Table 2.14 Disc types with unspecified geometries ("x") and their geometries modeling[1]

Authors	Mount type	Disc Geometry	Ventilation type	Axial symmetry	Circum. symmetry	2D/3D	Pad/ Disc
[38]	x	x	x	Half	2D	2D	Both
[78][2]	model	model	model	Full	360°	3D	Disc
[44]	axle	solid and ventilated	pillared, radial, tangential	Full	360°	3D	Disc
[71]	x	x	x	Half	360°	2D	Both
[72]	x	ventilated	x	Half	360°	3D	Both
[85]	x	ventilated	straight radial vane	Half	360°	3D	Disc

Axial displacement on the disc external diameter was performed by Tirovic & Sarwar, 2004 [24] on a 2D axisymmetric and 3D model. It was inferred that similar disc axial deflection could be predicted by using a diversified model, including 3D disc segment, two-dimensional axisymmetric with the only disc, and two-dimensional axisymmetric with disc and pads. However, computational time and level of accuracy were not compared for all modeling.

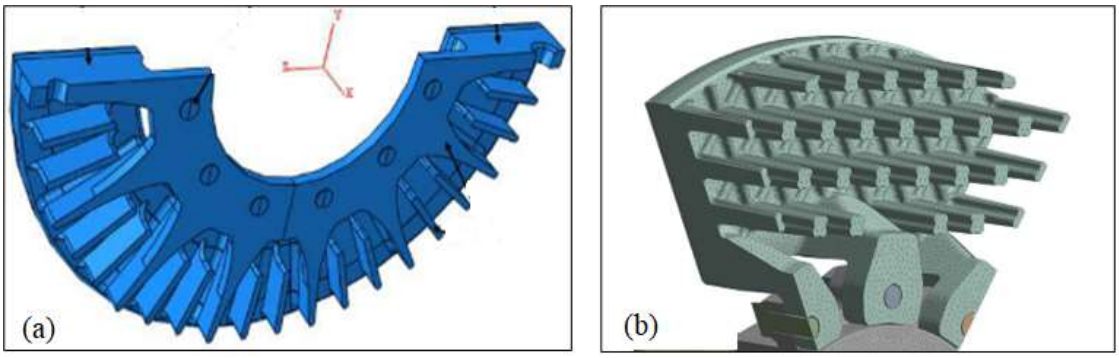

Figure 2.16 (a) Straight radial disc (half axial and 180° circumferential [6]) (b) Circular pillared disc (half axial and 45° circumferential [107])

As a summary, symmetry used, the inclusion and exclusion of pads in the simulation process are identified for straight radial vane wheel-mounted discs (Table 2.12), for both straight radial vanes and circular pillared vanes for axle mounted discs (Table 2.13). the geometry and symmetry used in straight radial vanes and circular pillared vanes are shown in Figure 2.16. Similarly, symmetry and pad-disc combination in the simulation process for unspecified disc

[1] All discs have hub-bolted connection
[2] Model is utilized

geometries and mount type (designated as “x”) and solid disc brakes is also displayed in Table 2.14 and Table 2.15, respectively.

Table 2.15 Axle-mounted solid disc brake symmetry and connection with bogie[1]

Author	Axial	Circumferential	2/3D	Pad/disc
[17] [66]	Half	2D	2D	Both
[42]	Half	30°	3D	Both
[8] [5]	Half	360°	3D	Both
[70]	Full	360°	3D	Disc
[63]	No	2D	2D	Both
[80]	No	90°	2D	Disc
[69]	Half	360°	2D	Both

2.7.2 comparative analysis of geometry selection

The design and geometry of the brake discs and pads are the main influencing factors in deciding the strength of friction heat applied on the brake disc, which varies from the center of the disc brake to the contact points and length of the contact line. Inspired by this perception, Benseddiq et al., 1996 [17] carried out design optimization of pads based on the thermomechanical algorithm proposed by Dufrénoy & Weichert, 1995 [66]. The effect of friction material compressibility, intermediate layer compressibility, pad backplate thickness, and number of grooves on the surface temperature distribution was examined by ANSYS and verified experimentally. The lower temperature was seen registered on the disc for the relatively higher number of pad grooves and lower modulus of elasticity (supple) of friction materials (Figure 2.17).

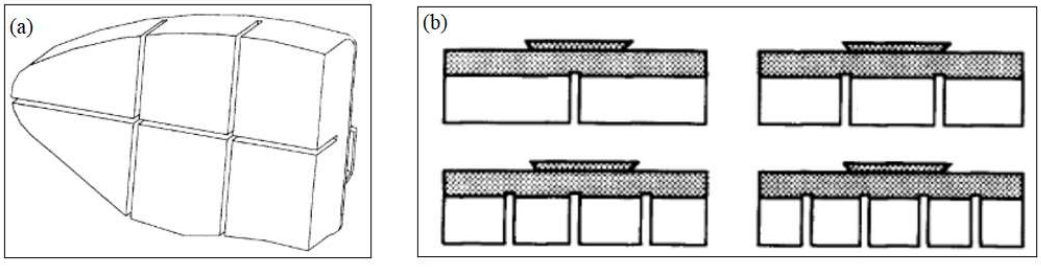

Figure 2.17 Shapes of composite pads (grooves) implemented in [17]

[1] All discs have hub-bolted connection

Likewise, Nong et al., 2011 [80] presented the concept of structure-function which described the friction contact between cylindrical friction pads and the brake disc with four different pad arrangements and geometries, using ABAQUS. It was found that changing patterns of the thermal stress and temperature on brake disc surfaces were matched with those of structure-function. Structure-function was observed as significant in designing pad geometry, due to its reflection of temperature and the thermal stress distribution. Additionally, Jiguang & Fei, 2015 [37] found the optimal design of pad geometry based on five prototypes including, circular, hexagonal, and triangular shapes varying in size and number. The disc was shown minimum and uniform temperature field and less thermal stress for the triangular pad with 10 numbers of blocks among the five candidate designs (Figure 2.18.e).

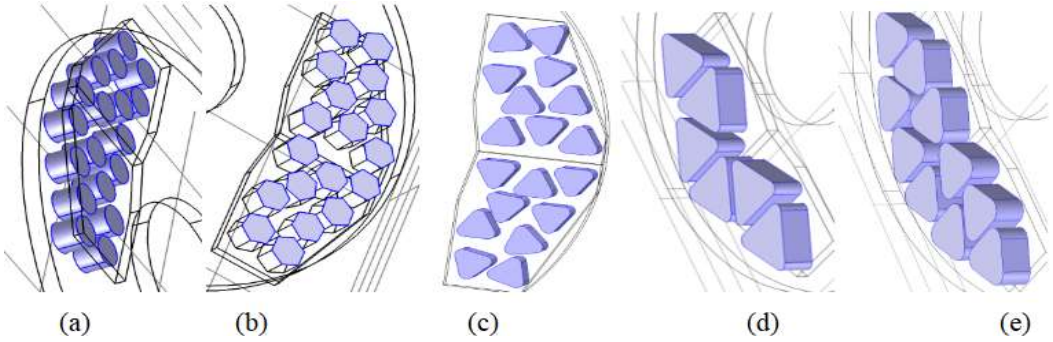

Figure 2.18 (a) circular, (b) hexagonal, and (c-e) triangular shapes varying in size and number [37]

On the other hand, Tirovic, 1998 [36] developed shape optimization for wheel mount discs of a high-speed train. Several design concepts were produced, from which the most promising designs were analyzed based on bulk thermal analyses (coning). The results showed good agreement with ABAQUS-FE predictions and proved design suitability for the required duty of 22MJ.

Similarly, to reduce high thermal coning, Tirovic & Ali, 2001 [11] developed two successful but fundamentally different hub designs for the Car Carrier disc and TGV Duplex power car disc. The optimization process proposed the flexible/ fingered hub for the car carrier, while a solid hub not contacting the wheel web was adopted for the TGV Duplex disc.

Disc was optimized in the work of Tirovic & Sarwar, 2004 [35], for preset criteria: low disc axial deformation (coning), acceptable hub stresses, low manufacturing costs, and efficiency of the optimization procedure. In addition, boxed dimensions were fixed, as a result of customer requirements, while dimensions around the wheel hub were varied to achieve the best disc

performance. As a result, eleven geometrical parameters varied with reasonable limits; consequently, thirty different designs (models) were used as input, including the existing (reference) disc design. According to the 'model data sheet' prepared for result comparison in terms of preset criteria, model 22 shown in [35] offered the best balance of hub stresses and disc deflection.

Optimization was also revealed in redesigning disc geometry, as in Šamec et al., 2011 [60]. According to the authors, unfavorable geometric design and excessive fastening moment of bolts resulted in exaggerated thermal stress (about 1.095GPa), which was seen as the main reason for crack initiation. And then, the authors redesigned the disk geometry around bolt mounting holes, so that the problem was alleviated when stress was reduced from 1.1 GPa to 0.170GPa.

Luo & Zuo, 2014 [64] resolved the thermal problem by optimizing wall thickness, resulting 30% improvement in heat transfer. In spite of the enhanced heat dissipation process, reducing disc wall thickness revealed a further rise in surface temperature, as a result of reduced heat capacity. Likewise, Grivc et al., 2019 [50] developed a new design of divided rail freight disc brake by altering the location and shape of the fins. About 280 different heights and shapes of hyperbolic radii and the junction of the fin-disc were simulated. Through systematic fin geometry optimization, ventilation losses were decreased by 37% with a 21% mass reduction. Consequently, a disc with better thermal performance with significant energy savings was designed. Besides, it was observed that the maximum ventilation losses derived from the cooling fins, disc hub and bolts, and frictional surface were about 75%, 20%, and 5% respectively. Similarly, further study on aerodynamic and convection coefficients on disc geometry was also investigated in [2][87].

2.7.3 Concluding remark on symmetry and optimum geometry selection

As highlighted in the introduction, FE analysis is not free from the challenge of computational cost, and to alleviate the problem, the use of symmetry was seen solution proposed in many papers. As a result, 84% of the publications were concerned with axial, circumferential, or both symmetry, although 16% of the studies still used full geometry (Table 2.12-Table 2.15 and Figure 2.19). Nevertheless, in order to reduce computation time in full geometry, many assumptions were seen made, which might affect the accuracy of the FE method. These include a lack of materials plasticity modeling [70][89] and temperature-dependent thermal and mechanical properties [39][74]. Moreover, implementing coarse mesh and excluding wear

(uniform pressure and wear) were another way of reducing computation times seen in full disc geometry [64].

Axial symmetry is used at the mid-plane of the disc and removes a half portion of the disc-pads system without affecting boundary conditions. Since it has the capability of reducing simulation costs in half, it was seen used in 71% of studies (Figure 2.19), either in 3D [10] or 2D [71]. The number of discs used and corresponding symmetry were seen based on mounting position. For the wheel mount, two discs were utilized: one from the left and the other from the right of the wheel [75]. In this type of disc, axial symmetry was observed implemented by removing one side of the disc, and the other side was preserved with a full wheel [79]. Nevertheless, heat from each side of the disc is expected to flow into the wheel, particularly for the long-drag braking type.

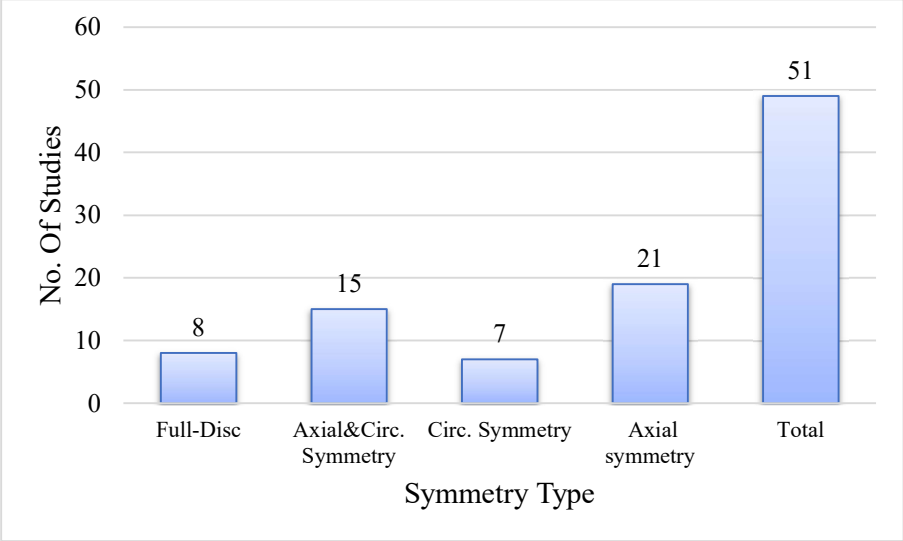

Figure 2.19 Distribution of symmetry types in reviewed studies

Consequently, the inclusion of a half wheel into the simulation is a fact, but none of the studies seen to perform accordingly. In contrast, axle mount discs were shown one disc set on the axle, either solid [42] or ventilated [88]. In straight radial ventilation [81] and solid disc types [69], axial symmetry was seen utilized at the mid-plane of the disc, and adiabatic heat transfer was displayed at a cutting plane position. Nonetheless, it was seen as difficult to do so in pillared ventilation types, due to its complex geometry, except in [107]. That is why in studies [73][82][77][58] seem difficult to use axial symmetry, and instead, they used circumferential geometry. Moreover, other authors were seen as vulnerable to high computational costs, in avoiding symmetry implementation [64][89].

Circumferential symmetry (axisymmetric) is based on the assumption of tangentially uniform thermal and stress distribution, although pad-disc contact covers only 70° of the disc [6]. It was observed to cover 43% of the study (Figure 2.19). Compared to axial, it was seen to lack consistency and more diversified in selected dimensions and size of the disc (Table 2.12-Table 2.15), among researchers. From this, 41% of the studies used circumferentially full (360°) and axially half geometry. This might appear in order to account for circumferential thermal gradient, while the remaining studies used 2D [24], 3D with 7.5°[36], 3D with 30°[28], 3D with 45°[107], 90° [73] and 180° [40], by considering axisymmetric. Despite this assumption, [33][124][125][25] reported the existence of circumferentially non-axisymmetric thermal load (existence of thermal gradient) caused by continuously changing pad-disc contact due to the rotational motion of the disc against fixed pads.

Although 41% of studies used axially half and circumferentially full geometry (360°), none of the studies considered thermal gradient in the tangential direction, except [8] and [70] both in 3D and [69] in 2D. Even, these three studies disregarded heat dissipation fins and pad cover angle thermal gradient to simplify the simulation.

Simplification in geometry modeling is not limited to the symmetry of the disc brake, but considering disc only or both disc and pads in thermal modeling, also affects the accuracy and computation time of FE analysis. Based on this foundation, evaluation of reviewed papers revealed 33.33% of the study considered pads and discs, while the remaining 66.67% considered only discs through heat partition coefficient between disc and pad (Table 2.12-Table 2.15). The calculated coefficient of heat partition revealed 90% of the heat generated to be absorbed by the disc and 10% by the pads, based on the material properties of pads and discs [126]. Besides, heat partition coefficients were observed constant in all studies with only disc analysis [70], while in reality, material properties vary with temperature throughout the braking process [59]. Others 4% accounts for those unspecified geometries. Even, from 33.33% of disc-pad consideration, in nine studies pads were included only for pressure distribution in uncoupled thermomechanical analysis, but not in temperature and stress simulation [63][24][35].

Ventilated disc brakes accounted for 74% of the study (Straight radial ventilated disc-57% and circular pillared ventilated disc-17%), as depicted in (Table 2.12-Table 2.14). This might appear due to the fact that ventilated design removes the heat from the disc surface approximately twice as large as the solid disc [106]. Moreover, the straight radial type

ventilation (57%) has the advantage of resisting crack propagation. Moreover, it was reported easily manufactured, and has uniform material distribution, compared to pillared type discs [127].

Disc brake optimum geometry selection included 22% of the studied review. For most of the study, optimum geometry was measured by temperature evolution [107][64], or stress and axial deflection [35] [60]. Nonetheless, the optimum geometry in temperature doesn't mean optimum in every aspect. As the maximum temperature and stress developed appeared at different braking times and locations [89], any design must be checked for both parameters before being accepted as optimum. Since the maximum stress might be observed at lower temperatures [89], geometric design with lower temperatures doesn't mean an acceptable design in structural analysis (stress). Therefore, optimum geometry selection made on only temperature value in any design is not guaranteed in thermal stress and might cause fatigue crack initiation.

Optimum geometry selection was seen and evaluated through modeling pad structures [17][80][37]. Besides, it was seen conducted by geometries around the disc hub [11], hub-disc junction geometry [35], the holes around the bolt area [60], disc wall thickness [64], and the location and shape of the pillared fins [50]. Although 57% of studies were done on straight radial ventilated discs, none of the studies highlighted its optimum selection in terms of fin numbers and orientations.

Based on the disc connection with other parts of bogies, disc brake geometries are further classified into two: friction surface-bolted and hub-bolted, displayed in Figure 2.3 and Figure 2.4, respectively. The latter accounts for about 90% of the studies reviewed (Table 2.12-Table 2.15). The remaining 10% includes friction surface-bolted, from which four studies are wheel-mounted discs and one study is from axle-mounted disc brakes. Three main difference is revealed in selecting optimum geometry from them. Firstly, the pad-disc contact area is low in friction surface-bolted discs. And this could greatly affect the distribution of temperature, stress, and fatigue life in a significant manner. Secondly, the presence or absence of bolt holes on the friction surface could significantly influence the development of temperature and stress, either positively or negatively. And finally, the variation in mass could affect the specific heat capacity of the disc. So, to evaluate better disc geometry from both, further investigation is mandatory.

On the other hand, CFD-based geometry selection through heat dissipation by convection coefficient was observed and is also a current research area. It was seen as possible to design fin geometry that highly dissipates heat to the environment [107]. Despite that, disc brake cooling characteristic by itself is not sufficient in evaluating its performance; instead, energy lost in pumping characteristics (aerodynamic resistance) is also another parameter to be determined by brake designers [44].

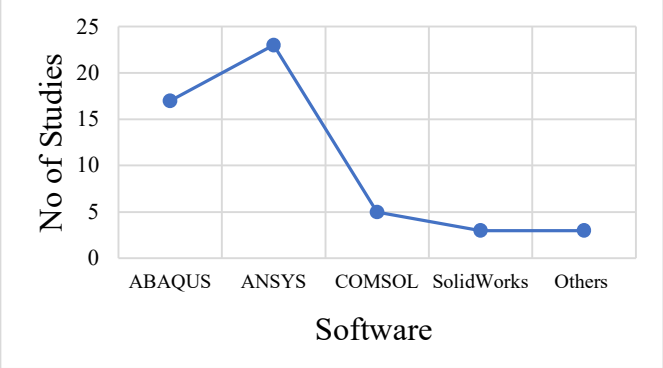

Figure 2.20 Frequency of software used in disc thermomechanical simulation

Various types of commercial computing codes of FE were used including ANSYS, ABAQUS, COMSOL, and Solidwork, sorted from maximum to minimum. Additionally, three software used with a frequency of one were LS-DYNA, DSMFEM, and CASTEM 2000. ANSYS has seen as the most widely used software in railway disc brake modeling and analysis (Figure 2.20). This might be due to the fact that coupled fluid thermal analysis was seen simulated more in ANSYS than any other software, although Solidwork has the capability to do so [39][40][59]. This result agrees with the review done by Afzal and Abdul Mujeebu 2019 [61] on automobile disc brakes thermo-mechanical and structural performances, in which ANSYS was displayed as the widely used FE code.

2.8 Future Directions and Gap Identification

Regardless of substantial advances observed in modeling heat input, boundary conditions, and material modeling, the following areas require further progress in leading to complete and realistic braking conditions, and reliable results.

- Further development of the FE simulation model that considers time and spatial (radial and circumferential) variation of heat input (flux) and boundary conditions. This type of modeling is expected to mimic realistic braking conditions and lead to accurate prediction of temperature, stress, and fatigue life

- Application of reliable FE model in selecting optimum geometry and material in disc brake system design development and maintenance management.
- Consideration of significant boundary conditions, their proper calculation method, and the selection of their application areas.
- Consideration of material non-linearity in FE modeling, in terms of plasticity and temperature-dependent properties in thermomechanical analysis. These are important in extreme braking conditions where thermal stress reaches beyond the material's yield strength, and temperature affects material properties.
- Consideration of orthotropic material modeling for composite materials, where structure and composition of materials vary in disc geometry. Because this variation leads to material property variations.
- Use of appropriate symmetry that includes variation of heat input and boundary conditions radially and tangentially, in all types of disc. Application of symmetry that represents actual braking condition is mandatory for precise failure determination
- Proper selection of disc material according to the maximum operating speed of the train, braking type (emergency, repeated, service), thermal material properties, and structural material properties. Because no material exists that can fulfill all the required properties
- Application of both thermal and mechanical analysis in comparative analysis of geometry and material selection, instead of relying solely on temperature or stress results of the simulation. Because disc geometry is more sensitive to thermal stress, compared to temperature

Nevertheless, considering all the abovementioned areas might overshoot computation time. That is why the researchers simplify the modeling, as seen in this review. But, instead of simplifying the modeling by the assumptions, as seen in this review, new methodologies have emerged enabling us to accommodate the cost of simulation without compromising accuracy. Just to highlight a few of them: use of APDL code in ANSYS [77] [77], use of Python in ABAQUS [128], and use of UDF (user-defined function) in fluent [64]. These programming languages use FORTRAN, C++, and Python scripts that make the simulation process more flexible in importing-exporting results from physics to physics.

CHAPTER 3: STUDY METHODOLOGY

3.1 Introduction

A methodology followed in this dissertation implements both primary and secondary data. Firstly, a systematic literature review is conducted in collecting, filtrating (including and excluding) and accepting recently published articles related to the problem. Eventually, FE modeling types are identified with their advantages and shortcomings. And then, primary data (disc geometry and braking conditions) are collected from AALRT. This chapter also reveals the implemented software, methods of data analysis, interpretation, and validation of the developed model.

3.2 Literature Review

Different sources are critically and systematically reviewed, from which four FE models are extracted. Every one of these models is evaluated, based on actual braking conditions and recent literature. The problems related to these models are identified, in terms of spatial and temporal heat input and boundary condition calculation and application. Besides, the role of these models in geometry design and material selection is also identified.

The main focus of this chapter is to explore the modeling of railway axle mount and wheel mount disc brakes, as they differ significantly from automotive or aircraft braking systems. However, in order to provide a comprehensive overview of the current state-of-the-art, studies that address frictional heating in automotive brakes, which are related to the topic at hand are also discussed in comparison to the railway disc brakes.

The review is accomplished by preferred reporting items for systematic reviews and meta-analyses (PRISMA) statements [129] (Figure 3.1). At the end of the review, the paper aims to answer the question: “What FE modeling has been used in railway disc brake temperature, stress, and fatigue simulation?” How these models have been implemented in studying optimum geometry and material? Studied papers are identified by searching electronic databases from March 03/2020- April 24/2022, mainly science direct and Scopus, in addition to hand searching and scanning reference lists of articles.

Keywords used for searching databases are accompanied by logic “or”, “and”, an asterisk (*) to protect missing any article. Keywords are constructed as “railway disc brake temperature”, “railway disc brake stress”, “railway disc brake material” and “railway disc brake geometry”.

Although the same in concept, different organization of keywords is used repeatedly for all databases, because the way they accept keywords is different. Synonyms of words, like “railway”, “train”, and “rolling stock”, as well as “structural” “thermomechanical”, and "thermo-mechanical” are easily managed by “OR” logic.

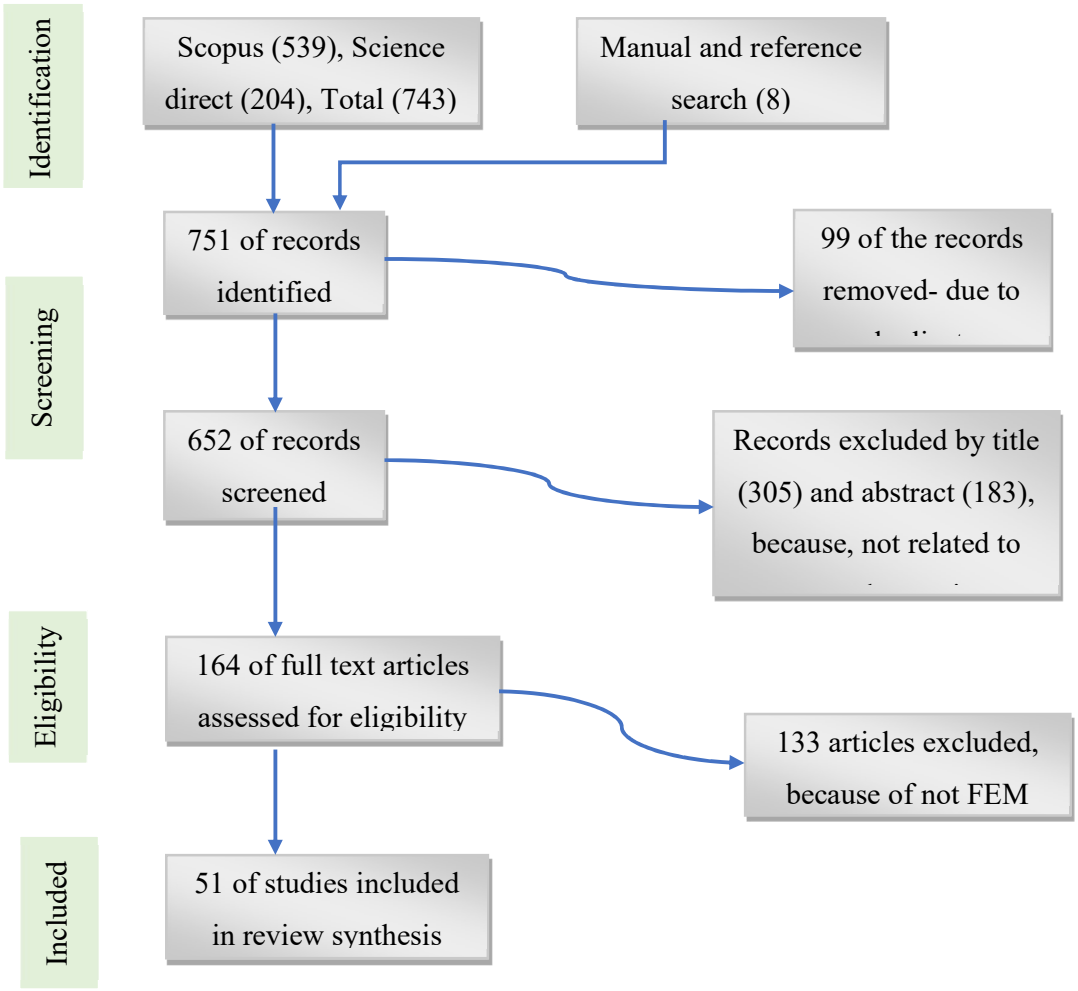

Figure 3.1 Flow of information through different phases of a systematic review

Built on this foundation, search strings “disc AND brake* AND ("Finite element") AND (thermal OR temperature OR structural OR thermomechanical OR "thermo-mechanical" OR stress OR geometry) AND (railway OR train OR "rolling stock")” is used in Scopus, while different organizations of keywords are applied for science direct. All subject areas are selected, but only articles, conference papers, and reviews are selected from the document type. In addition, the source type of conference proceedings and journals written in the English language since 1995 are selected, because no significant article was found earlier than 1995.

In total, 743 studies from all sources are exported to Mendeley desktop and Excel software, for further filtration. To collect all relevant studies from this amount, inclusion and exclusion protocols are set: Only disc brakes in the railway industry are selected, with a focus on FE modeling related to temperature, thermal stress, and thermal fatigue. Other forms of brakes in rolling stock, like tread/block or shoe, electromagnetic are excluded. Disc brakes in other industries including automotive, mine hoist, crane brakes, wind turbine, belt conveyors, and aircraft are also excluded, except for explanations and comparisons of results and discussion in this investigation. Models associated with a squeal, noise, vibration, judder, dynamic, and disc thickness variations are excluded. Additionally, methodologies similar to experimental and analytical analysis are excluded. Finally, 51 studies are accepted based on inclusion criteria. Data are extracted and coded in an Excel spreadsheet. All information is synthesized and reported through narrative synthesis.

3.3 Data Collection

AALRT is manufactured by CNR-CRC (Chinese railway corporation). It has a maximum load-carrying capacity of 66220kg, with a maximum running speed of 65kph. Besides, it has a combined length of 31.6 km and 39 braking stations. From which, East to West route has 21 stations (braking point) and fifteen trips per day. As a result, the disc brake is vulnerable to temperature variations as high as 630 times per day. Consequently, both disc and pads are vulnerable to failure (due to temperature, stress and crack), resulting high maintenance cost and accident. The worn out brake pads and disc surfaces witness this information (Figure 1.2 a-b).

Therefore, AALRT is purposefully chosen for data collection, because of the many repeated braking observed per day. But what the reader should understand here is that the model developed here is neither train-specific nor disc-type-specific. Variation of input data couldn't alter the validity of the model to be developed. Data input is collected from two sources: Firstly, the primary data source is precisely gathered, including disc geometry dimensions, disc material type, and train braking conditions. The actual measurement of disc geometry is conducted carefully by a stainless steel digital vernier caliper, having a measuring range of 0-150mm, within the accuracy of +/- 0.02 mm. GVC-15KD M-type standard slide caliper is also employed in parallel (Figure 3.2). Besides, the operation and maintenance manual of AALRT [32] is crosschecked with measured geometry parameters for the accuracy of measured dimensions.

In addition, braking condition parameters are obtained from the operation and maintenance manual [32]. These include deceleration (both for service and emergency braking), acceleration, train mass, number of bogies per train, number of discs per axle, and maximum design speed. From these parameters, braking time and braking distance are traditionally determined by empirical kinematic equations [3]. Moreover, a mobile phone stopwatch is utilized at three randomly selected stations to measure train stop time at stations, when passengers get in or get out: Ayat 1, Stadium, and Lideta stations. From which the average time is selected for service brake. For emergency braking, however, half stopping time in service braking is implemented, by discussing with train operators.

Besides, secondary data sources (literature data) are collected, whenever the limitations in data related to thermal and mechanical material properties are limited. Particularly, in the areas of comparative analysis of materials, candidate materials' thermomechanical properties are extracted from the literature. This kind of method is also utilized in other investigations [85][130]. Since there is no single literature having all thermal and mechanical properties at the same time, literature data are carefully collected and utilized for material kinematic modeling parameters, to consider non-linearity due to stress-strain behavior. Materials of the same grades having similar microstructures are cautiously used in thermomechanical simulation.

Figure 3.2 Disc and pad dimensional data extractions at AALRT

Once all the braking parameters and conditions are extracted, the empirical equations are employed in converting mechanical energy to thermal energy in the form of heat flux [84]. Next, empirical equations are also implemented for calculating boundary conditions expressed by convection on friction surfaces and vanes [31][33][54]. Finally, the way in which these

calculations are performed and the way these heat and boundary conditions are applied is the modeling part of the NAMHS algorithm.

Once the effectiveness of the NAMHS modeling is proven, the model's applicability for other research areas is tested in two ways: applicability in comparative analysis of material and geometry. Candidate materials are FGI, CGI, and SGI. Their selection is based on the research gap identified for low-speed train types. In addition, various geometries of pads and discs are utilized.

The connection between the disc and axle might be friction surface-bolted type (Figure 3.3. b) or hub-bolted type (Figure 3.3.a,c). The surface-bolted type is taken from AALRT. Due to the unavailability of the hub-bolted disc on AALRT, the author is required to make adjustments to the surface-bolted type on AALRT (friction surface-bolted) by preserving the key dimensions such as the internal radius, external radius, and thickness. Hence, hub-bolted type design is employed by modifying the actual or original friction surface-bolted type of AALRT trailer or motor bogie, by removing the bolt holes from the friction surface and reinforcing structures around holes from the fins side. Then the spatial study of these two types of geometry is presented. Determining the optimum disc geometry cannot be determined without conducting thermomechanical analysis, mainly due to two reasons. Firstly, the decrease in mass on the friction surface-bolted disc may be balanced by the removal of supportive structures around the fins in a hub-bolted disc. Secondly, the presence or absence of bolt holes on the friction surface can have a positive or negative impact on temperature and stress development. Hence, it is required to investigate the disc design geometry effect on spatial failure analysis

Figure 3.3 Axle mount disc brake designs: (a) solid hub-bolted [131] and (b) friction surface-bolted [AALRT] (c) ventilated hub-bolted [20]

A mechanism-based fatigue life prediction is selected to estimate the cycles to failure, as the growth and coalescence of the originally smaller cracks (cast iron microstructure) as the lifetime limiting factor

3.4 Computational FEM

The high safety and comfort expectations under varying braking conditions have required the development of brake systems in railway vehicles. In addition, the increase in maximum running speed and load-carrying capacity on modern trains have pushed the braking design and failure analysis more and more to their limits [66]. Consequently, three different methods have been observed in disc brake development: experimental, analytical, and FEM. The issue of the analytical model has been controversial and much disputed in handling material non-linearity and complexity in disc geometry [124][85]. Furthermore, although the experimental method is a reliable way of developing brakes, it is expensive and timely ineffective [79]. The finite difference technique uses only orthogonal mesh to create finite elements, which is very difficult to model complex geometries. Contrarily, the mesh in the finite element method is generated by non-orthogonal elements, including linear, triangular, or quadrilateral [132].

Hence, numerical methods based on FEM modeling are free from drawbacks seen in analytical methods, particularly in the application of non-linear problems and when disc geometry is complex [124][85]. Consequently, FEM modeling has proven to be a very crucial tool to aid in the design process of the railway brake disc [51][133]; except that they allow only approximate solutions [85], not free from assumption, and have high computational cost [134]. Besides, the discovery of the FE model has triggered a huge amount of innovative scientific investigation in disc failure analysis (temperature, stress, life,) and optimum material and geometry selection.

The finite element technique is a numerical method for resolving physics issues defined by an energy theorem in the form of a differential equation. It differs from other numerical processes due to two features [135]. Firstly, the technique creates a system of algebraic equations using an integral formulation. Secondly, the method approximates the unknown quantities by using interpolation. The methods followed in FEM consist of four approaches:

- Geometry discretization- Assigning co-ordinates to each node
- Formulation of an approximate equation- interpolation function for every element
- System equation development, and
- Calculation of interested quantity- temperature, stress, strain, etc.

3.4.1 ANSY APDL

According to the review conducted in this study, 47% of FE thermomechanical analysis models are performed by ANSYS [26]. ANSYS-based finite element modeling of disc brake involves three distinct cornerstone procedures: preprocess, solution, and post-process [136][137] [138].

The detailed functions conducted in these procedures are presented in Figure 3.4. Therefore, ANSYS Parametric Design Language (APDL) is utilized here for the simulation of temperature and stress. It is a scripting language used to automate common tasks or even build complex algorithm models in terms of parameters (variables) and arrays.

These APDL commands are the foundation for sophisticated features and encompass a wide range of other features such as repeating a command, macros, if-then-else branching, do-loops, APDL math, scalar, vector, and matrix operations [139]. Parameters are APDL variables, more similar to FORTRAN variables, and mechanical APDL uses two types of parameters: scalars and arrays. Time and space-varying heat input and heat dissipation coefficient calculations are easily conducted by APDL math, as it can accept empirical equations used for calculating heat input and heat dissipation coefficients. APDL computer program algorithm in ANSYS software is developed to do so. It is utilized to code commands and operators in defining spatial and timely varying heat input and boundary conditions. Users are required only to choose and fill in parameter values, and the system will automatically call the calculation program of ANSYS to conduct meshing, loading, and solving analysis [77].

3.5 Conceptual/Theoretical Model Configuration

The FE modeling starts by revising the current state of the art in disc brake thermomechanical FE modeling. The pros and cons of these models are examined in terms of spatial variation of temperature, thermal stress, and fatigue. The factors contributing to spatial variation of these parameters are also identified, before the development of the new NAMHS model algorithm that could solve the problems in traditional models seen in literature.

Once the newly developed model is completed, its effectiveness in spatial temperature assessment is evaluated by comparing it with two traditional models (used as a reference): axisymmetric and non-axisymmetric moving heat source of Pan and Cai, 2018 [31]. The reason behind the selection of this study([31]) is that it clearly displayed the physical movement of the heat source, compared to other studies [34][33][91]. Besides, according to the review conducted by the authors [26], axisymmetric modeling is covered the majority of modeling (popular). The exclusion of the remaining two is due to the difficulty to preserve accuracy while completing the calculations within reasonable CPU times.

However, it should be noted that only the modeling methods (physical rotation or movement of heat source along friction surface in [31], and circumferentially the same heat application in axisymmetric) are taken as modeling, but not the geometries, materials, or other input

parameters. The same geometry, material, and braking power calculations are used for all models.

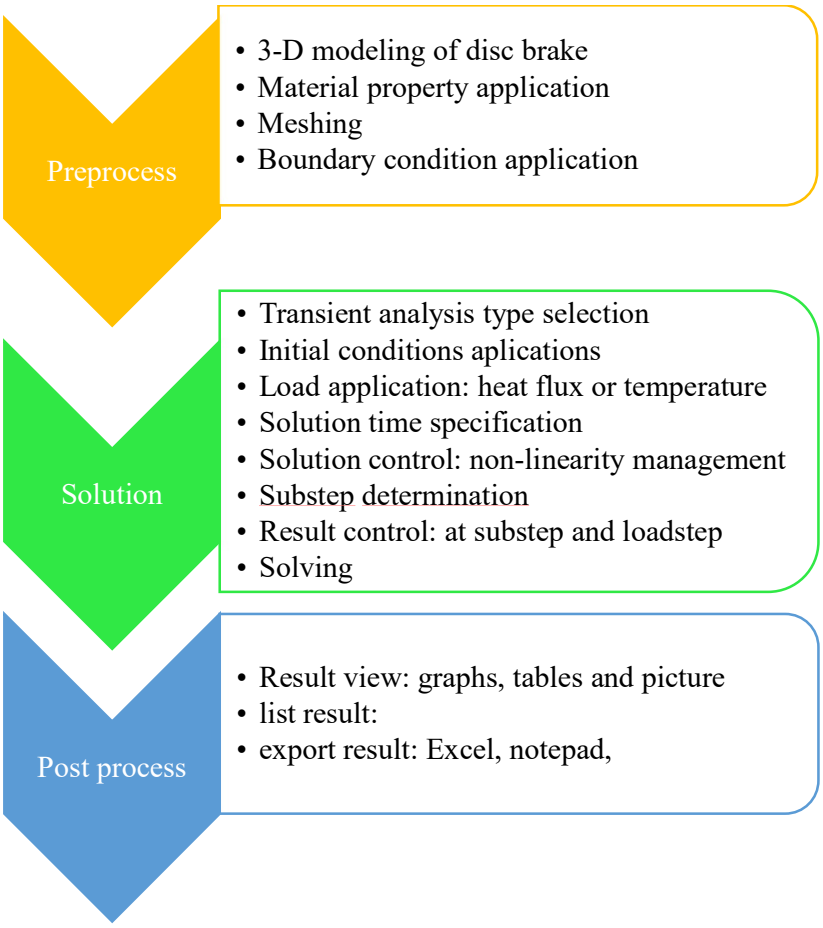

Figure 3.4 ANSYS simulation process [136][137]

Once the NAMHS is tested and accepted in managing space and time parameters, it is extended to structural analysis (calculating thermal stress and life). Thermal results for each node is exported to structural analysis for stress and strain calculation. To evaluate the implementation of the NAMHS model in braking energy variation, service braking of trailer bogie and emergency braking of motor bogie are implemented. Spatial variation of stress-strain hysteresis loop is assessed for both conditions. Besides, to evaluate the model implementation in comparative analysis of disc geometries, the friction surface-bolted and hub-bolted geometries are utilized. Finally, the thermal stress result is implemented in estimating fatigue life, based on fracture mechanics. But the life analysis is conducted for emergency braking of motor bogie, as failure is predicted on its surface, compared to trailer bogie.

The NAMHS thermal and structural model development by itself is not enough, unless their implementation is tested for comparative analysis geometries and materials. To do so, NAMHS thermal model and NAMHS structural model are applied in comparative analysis of pad geometries and disc brake materials, respectively, to select the best one. The detail study plan is presented in flow diagram of Figure 3.5.

3.6 Data Analysis and Interpretation

Based on the model developed, the data analysis, discussion, and interpretation have been made. The analysis of the research has been largely quantitative, which has been used to highlight patterns and make the analysis more robust, exploratory, or descriptive, summarizing data in the form of charts, tables, percentages, and averages. Besides, Origin 2018, MATLAB R19, and Excel 2016 are utilized in plotting diagrams of temperature, stress, and fatigue life. Finally, by combining the findings of the research with the related literature, ways forward have been proposed.

3.7 Validation and Verification

To verify the accuracy of the results of the developed FE model, experimental data on temperature and stress are collected from published papers in peer-reviewed journals. All experimental parameters and conditions are extracted and implemented on the newly developed FE model. And then, a comparison of the results is performed by applying the developed NAMHS model algorithm to the experimentally conducted temperature and stress analysis, to verify the accuracy of the computational model. Besides, field observation is condacted to compare the real world braking components, and those identified by the NAMHS model.

3.8 Methodology Flow Diagram

Finally, Figure 3.5 depicts the overview of the methodology chapter.

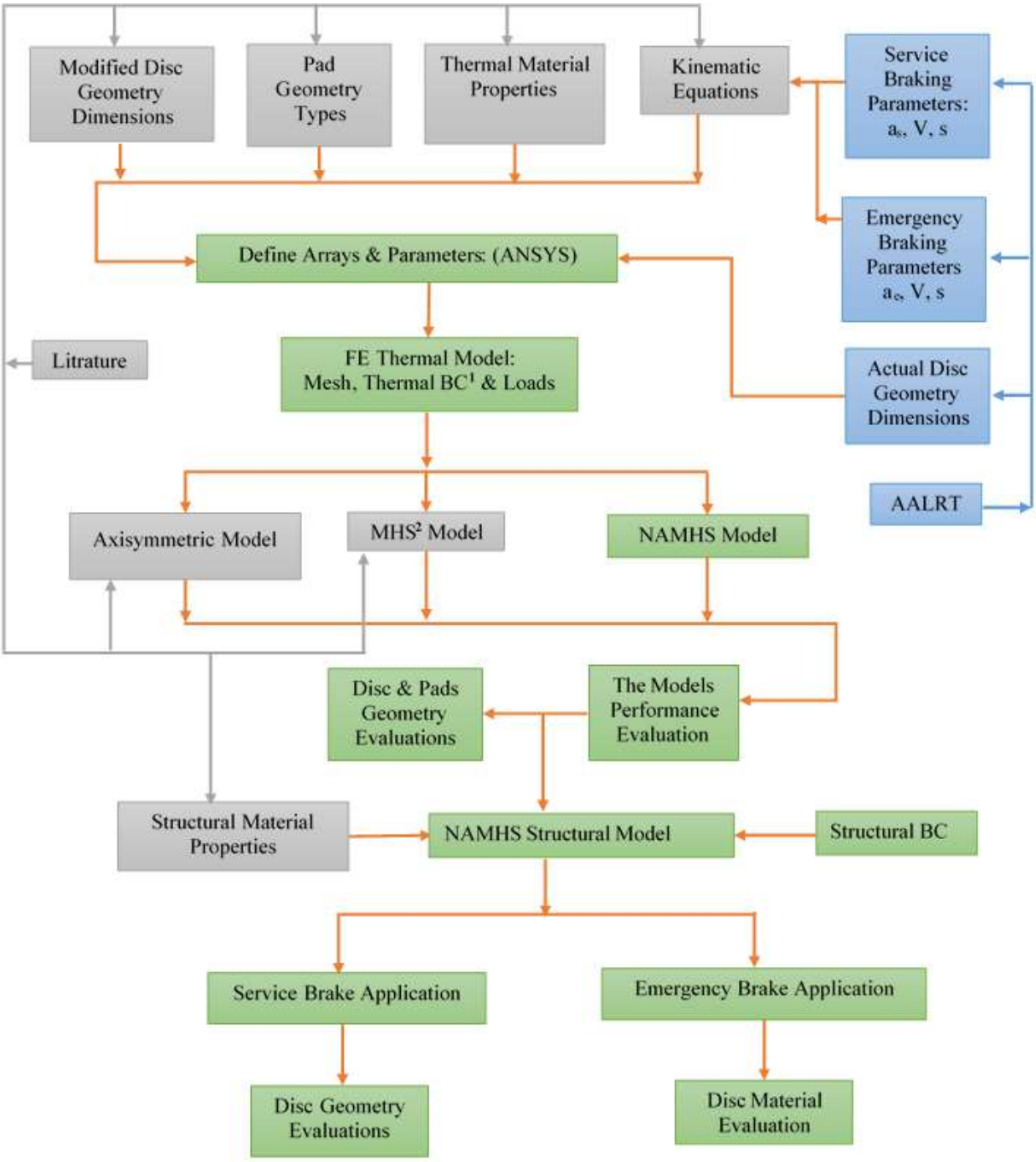

Figure 3.5 Methodology flow diagrams [1] [2]

[1] Boundary condition
[2] Moving heat source of Pan and Cai 2018 [31]

CHAPTER 4: FE THERMAL MODELING OF NON-AXISYMMETRIC MOVING HEAT SOURCE IN RAILWAY VEHICLES DISC BRAKE

4.1 Introduction

When the magnitude of the heat equivalent to the pad cover angle heats the friction surface through rotation with speed corresponding to the disc, it is known as non-axisymmetric. The nature of the thermal load on the disc brake is not symmetric with the disc axis and is asymmetrical instead. Since the current works of literature have not answered the problems in the spatial and temporal variation of heat and boundary conditions, NAMHS is presented in this chapter to answer the problems in radial, circumferential, and temporal management of heat and boundary conditions variation. In addition, its effectiveness in spatial temperature assessment is evaluated by comparing it with two traditional models (used as a reference): axisymmetric and non-axisymmetric moving heat sources of Pan and Cai,2018 [31].

The model development and its assessment, as well as its application in comparative analysis of geometry, is conducted on the service braking type of trailer bogie. In parallel to developing and evaluating the NAMHS model algorithm effectiveness, comparative analysis of disc geometry selection is performed between the hub-bolted (modified) and friction surface-bolted (original) design, based on temperature evolution.

4.2 General FE Equation Formulation in Transient Thermal Analysis

FE formulation for computation of transient heat conduction T(r,θ,z,t) is presented in the parabolic heat conduction equation, along the circumferential-θ and axial-z direction of the disc (Eq. 4.1). This is the general cylindrical coordinate with global cartesian Z as the axis of disc rotation, global cartesian X is used as radial and global cartesian Y is used as circumferential-θ for disc orientation observed in Figure 4.1. This default axis is customized according to the orientation of the disc geometry. At the same time, δ_d and k represent disc thickness (m) and thermal diffusivity ($m^2\ s^{-1}$), respectively [124].

$$\frac{\partial^2 T}{\partial r^2}+\frac{1}{r}\frac{\partial T}{\partial r}+\frac{1}{r^2}\frac{\partial^2 T}{\partial \theta^2}+\frac{\partial^2 T}{\partial z^2}=\frac{1}{k}\frac{\partial T}{\partial t} \qquad 4.1$$

This heat conduction equation is solved subject to a boundary condition and an initial condition (Eq. 4.2-4.4) on all portions of the disc surface. Analytical equations followed in predicting convection and heat input as a boundary condition are the same in many studies, as displayed in Figure 4.1 [6][85]. But their specific location and their spatial distribution were seen to vary in literature.

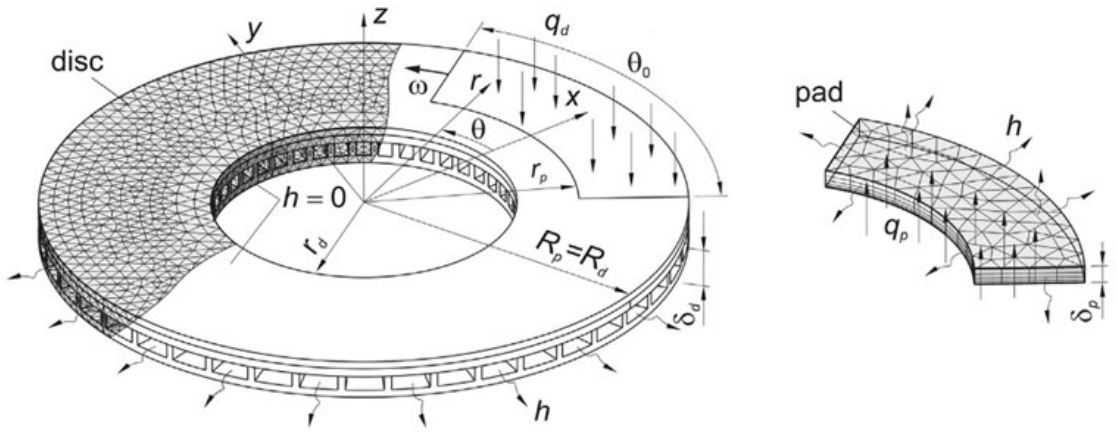

Figure 4.1 Heat input and boundary conditions specification on disc geometry [6]

Nonetheless, considerations and specific locations of radiation and insulated boundary conditions are not uniform among investigators in railway disc brakes. This is due to the fact that heat transfer due to radiation has an impact only at higher temperatures, as seen in other automotive disc brake studies [101][103][104][140].

$$K_d \frac{\partial T}{\partial z} = q_d\left(r,\theta,z,t\right) \tag{4.2}$$

$$K_d \frac{\partial T}{\partial r} = h\left(T_a - T\left(R_d,\theta,z,t\right)\right) \tag{4.3}$$

$$T\left(r,\theta,z,0\right) = T_o\left(r,\theta,z,0\right) \tag{4.4}$$

Where, θ_o is pad cover angle (°), h is heat transfer convection (W/m^{2}K) and T_a is the ambient temperature (°C).

Galerkin's criteria with the methods of the weighted residual are implemented to drive element equations. For thermal problems in disc brakes, a special case of a general element equation is presented in Eq. 4.5 [135]. Because, heat conduction is a non-linear transient problem, in which surface heat input (R_q) and surface heat dissipation (R_h) are temperature (T) and time (t) dependent. Element matrics are assembled to form system equations from this individual element, with iteratively solved non-linear equations.

$$\left[C(T)\right]\left\{\frac{\partial T}{\partial t}\right\}+\left[\left[K_c(T)\right]+\left[K_h(T,t)\right]\right]\left\{T(t)\right\}=\left\{R_q(T,t)\right\}+\left\{R_h(T,t)\right\} \tag{4.5}$$

Where,

$$[C] = \int_{\Omega} \rho c \{N\}[N] d\Omega$$

$$[K_c] = \int_{\Omega} [B]^T [k][B] d\Omega$$

$$[K_h] = \int_{S} h \{N\}[N] d\Gamma$$

$$\{R_q\} = \int_{S_2} q_s \{N\} d\Gamma$$

$$\{R_h\} = \int_{S_3} hT_a \{N\} d\Gamma$$

[C] is element capacitance matrix. Besides, [K_c] and [K_h] are element conductance matrices, and relate to conduction and convection, respectively. And finally, {R_q}and {R_h} are heat load vectors arising from specified surface heating, and surface convection, respectively.

[k] is the thermal conductivity matrix,

[N] is the temperature interpolation matrix

[B] is the temperature gradient interpolation matrix

4.3 FE Input Parameters Identification from AALRT

AALRT is manufactured by CNR-CRC (Chinese railway corporation). It is a 70% low-floor vehicle with grey cast iron disc material having a maximum running speed of 65kph. The two roots of AALRT are displayed in Figure 4.2. Both lines have a combined length of 31.6 km and 39 braking stations. From Ayat village to Torhailoch, the East-West line of the two train lines travels 17.4km, passing through Megenagna, Meskel Square, Legehar, and Mexico Square. Menelik II Square, Merkato, Lideta, Legehar, Meskel Square, Gotera, and Kaliti are all on the 16.9 km long north-south route. Nonetheless, the two lines have a common track of about 2.7 km, which runs from St. Lideta to Meskel Square, with 5 stations.

Besides, the East to West route has an inter-station distance ranging from 0.554km (between Road Authority to Mexico Square) to 1.149km (between Coca-Cola to Tor Hailoch) (Table 4.1). East to West route has 21 stations (braking point) and fifteen trips per day. As a result, the disc brake is vulnerable to thermal variations as high as 630 times per day. Hence, to develop FE thermal model, the average distance between these stations is taken, which is 0.852km.

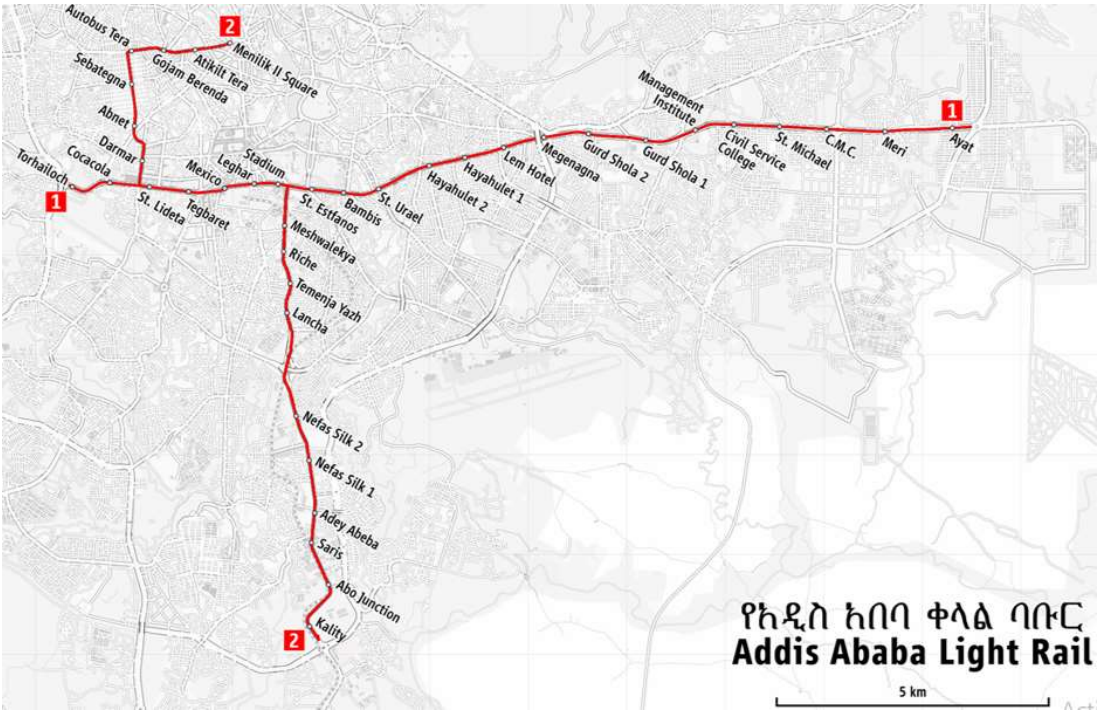

Source: Ethiopian Railway Corporation

Figure 4.2 AALRT main routes: East-West and North-South stations

AALRT single train consists of three cars on three bogies, with MTM power arrangements, or configurations, where M is the motor bogie, and T is the trailer bogie Figure 4.4. It has a maximum load-carrying capacity of 66220kg, with a maximum running speed of 65kph. The number of disc brakes per bogie is identified as 2 and 4, in trailer and motor bogies, respectively (Table 4.2). Besides, it has a Bo-Bo (two axles per bogie) arrangement of axle distribution within bogies.

The original disc geometry investigated here is a split type. It is is the assembly of two disc plates (at the right and left) and axile plate at the middle, assebled by many fastenes: hex-head blolts, body fit bolts, washers, lock nuts, stud bolts, and connecting rings. Besides, it is friction surface-bolted type having six bolt holes 60° far from one another at a radial distance of 141mm. The detail positions of these components are displayed in Figure 4.3 and APPENDIX B. Each disc is attached to one side of the central axile plate, with four hex-head bolts and two body-fit bots (Figure 3.3.b, Figure 4.5.a). On its bottom side, 48 cooling fins or vanes are used to dissipate heat. Due to axial symmetry, only one disc is selected for simulation. Two reinforcement structures with 5mm thickness are added around each hole vanes, and collectively 12 for six holes.

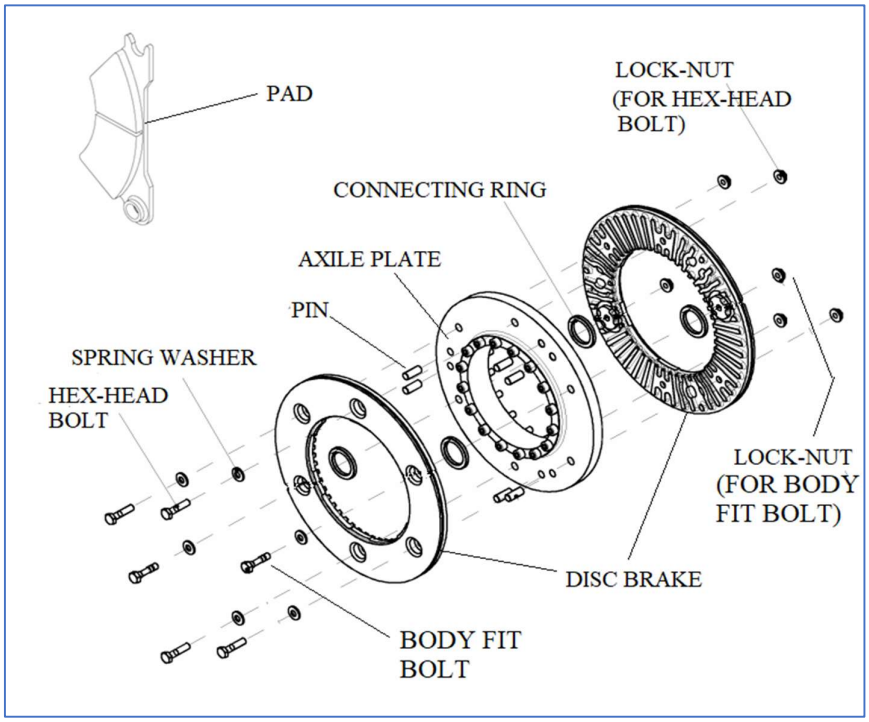

Figure 4.3 Exploded view of the friction surface-bolted disc brake assembly [32].

AALRT braking system has two types of pad geometries, based on the number of grooves: one radial groove (Figure 1.2.b) and two radial grooves (Figure 1.2.a). To model and analyze the thermomechanical analysis of disc brake, the former is selected randomly. For both types of disc analysis, the former pad is made up of one groove width of 5mm wide running radially, and a contact area of 0.01200m^2 with a 50° cover angle (Figure 4.3). Input parameters for geometric modeling and thermal calculations are taken from the trailer bogie of AALRT. All disc and pad geometries are measured by caliper, and used for modeling in ANSYS APDL (Table 4.2).

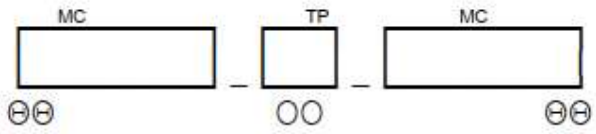

Figure 4.4 Configuration of AALRT [32]

In contrast to the friction surface-bolted disc, various studies have explored a different geometry design known as the hub-bolted type disc. This type of disc is characterized by its connection with the axle and has been depicted in Figure 2.4.a-b [58][59] and Figure 3.3.c [20]. One notable feature of the hub-bolted type disc is the increased pad-disc contact area, which can have a significant impact on the spatial distribution of temperature, stress, and fatigue life.

Table 4.1 AALRT East to West route station distances

S/N	Starting Station Name	End Station Name	Distance (km)
1	Ayat 2	Ayat 1	1.300
2	Ayat 1	Meri/CMC 2	1.034
3	Meri/CMC 2	CMC 1	0.896
4	CMC 1	St.Michael Church	0.865
5	St. Michael Church	Civil Service College	0.785
6	Civil Service College	Sahlite Mhiret Church	0.906
7	Sahlite Mhiret Church	Gurd Sholla	0.922
8	Gurd Sholla	Adwa square	1.004
9	Adwa square	Lem Hotel	1.035
10	Lem Hotel	Traffic Police HQ.	0.838
11	Traffic Police HQ.	Chemical Corporation	0.694
12	Chemical Corporation	Urael church	0.875
13	Urael church	Yordanose Hotel	0.570
14	Yordanose Hotel	Estifanose	0.569
15	Estifanose	Stadium	0.700
16	Stadium	La Gare	0.865
17	La Gare	Road Authority	0.555
18	Road Authority	Mexico Square	0.554
19	Mexico Square	Lideta	0.936
20	Lideta	Coca Cola	0.848
21	Coca Cola	Tor Hailoch	1.149
Averaged distance			0.852

Source: Ethiopian Railway Corporation, technical specification of the vehicle

Since the hub-bolted disc is not available on AALRT, the author is obligated to modify the original disc (friction surface-bolted), by keeping or maintaining the major dimensions of the

discs: internal radius, external radius, and thickness. The modification is limited to friction surfaces and geometries around the fins. The hub-bolted type design is obtained by modifying the original friction surface-bolted type design of AALRT trailers or motor bogies, by removing bolt holes from the friction surface and eliminating reinforcement structures beneath the friction surface, and finally depicted in Figure 4.5.b.

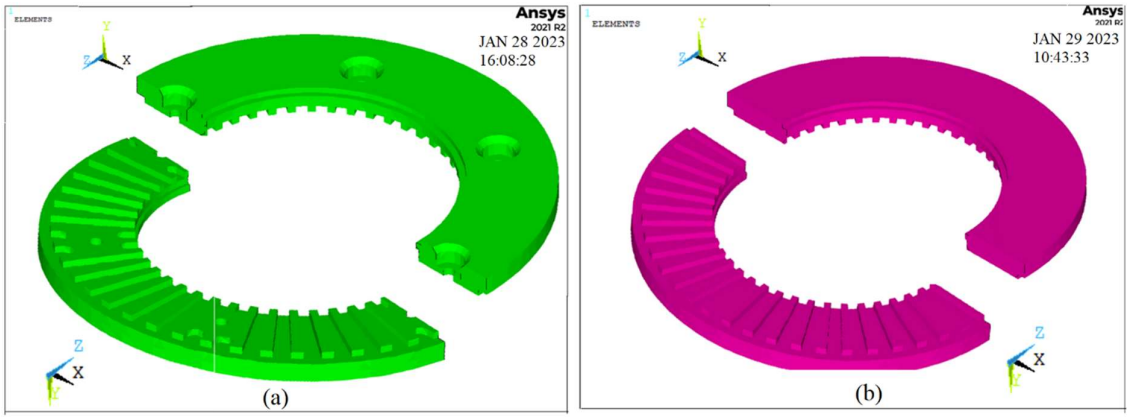

Figure 4.5 Disc geometry: (a) Original and (b) modified

Conducting thermomechanical analysis is essential in determining the optimum disc geometry. This is primarily due to two key factors. Firstly, in the case of a friction surface-bolted disc, the reduced mass from the friction surface may be counterbalanced by the elimination of supportive structures around the fins in a hub-bolted disc. Secondly, the presence or absence of bolt holes on the friction surface can significantly influence the development of temperature and stress, either positively or negatively.

The influence of contact area and mass variations on temperature, stress, and thermal fatigue, should not be underestimated. In fact, it has been observed that these effects may not be insignificant and could even dominate over other factors [141]. Understanding and quantifying these variations is crucial for assessing the performance and reliability of both the friction surface-bolted and hub-bolted disc geometries. By removing the bolt holes from the friction surface, the disc contact area with the pad is increased, which can have a significant impact on the spatial distribution of temperature, stress, and fatigue life. This modification aims to optimize the design and performance of the hub-bolted type by reducing stress concentrations and improving the overall structural integrity of the disc. Furthermore, the removal of reinforcement structures beneath the friction surface helps to simplify the design and potentially reduce weight. This modification is based on the understanding that since no more

bolt holes on the friction surface, the reinforcement structures may not be necessary in this specific design.

To investigate these effects, the NAMHS model algorithm is employed in this study. By utilizing this approach, it is possible to analyze and compare the thermal behavior, stress distribution, and fatigue life of both the friction surface-bolted and hub-bolted disc geometries. This analysis will provide valuable insights into the performance and potential advantages or disadvantages of each design, in addition to evaluating the application of the NAMHS in disc geometry selections.

Table 4.2 Braking conditions and disc geometry parameters [32]

Train and disc brake parameters	**Symbols**	**Values**
Mass of vehicle(kg)	M	66220
Number of discs per trailer bogie	--	4
Number of discs per motor bogie	--	2
Number of bogies per train	--	3
Number of motor bogies per train	--	2
Initial speed(kph)	V_o	65
Deceleration(m/s^2)	a	1.1
Time of braking(s)	t_b	16.4s
Disc internal radius(m)	r_d	0.113
Disc external radius(m)	R_d	0.18
Number of fins	--	48
Disc thickness(m)	δ_d	0.0145
Fin thickness(m)	δ_f	0.005
The effective radius of the disc(m)	r_m	0.1465
Number of pad grooves	--	1
Pad internal radius(m)	r_p	0.1225
Pad external radius(m)	R_p	0.170
Wheel radius (m)	R_w	0.31
Disc contact area (m^2)	A_d	0.0436
Pad contact area (m^2)	A_p	0.012

Additionally, in the modeling process, bolt holes around the hub (for connection with the axle) are not considered since failure is expected to occur primarily at the friction surface rather than in the region far from the friction surface (Figure 4.5.b). A similar assumption is also implemented in other studies [6].

4.4 Material and FE Modeling

AALRT disc brake is made from flake or grey-type cast iron [32]. Due to the registration of a high temperature during braking, the variation of thermo-physical material properties is an undeniable fact. Hence, thermo-physical material properties for grey cast iron disc considers non-linearity due to temperature for thermal conductivity and specific heat capacity, by Eq. 4.6 and Eq. 4.7, respectively, where T is the temperature (°C)[54]. In contrast, the asbestos friction material on the rubber-resin binder is used as pad material, whose physical properties are highlighted in Table 4.3 [6].

Table 4.3 Disc and pad material input parameters at room temperature [6][54]

Disc and pad thermal properties	Pad	Disc
Density (kg/m^3)	2700	7144
Specific heat capacity (J/Kg °C)	921.82	516
Thermal conductivity (W/m °C)	0.92	49.55

$$k = 50 - 0.0178T \ W/m°C \tag{4.6}$$

$$c = 506.5 + 0.377T \ \text{J/kg°C} \tag{4.7}$$

SOLID90 is used for meshing and creating finite elements (Figure 4.6.a). It has a temperature degree of freedom and is applied in two shapes: hexahedron shape of 20 nodes (fins and enforcing structures) and tetrahedral shape of 10 nodes (disc without fins and enforcing structures) [142]. Although a disc and fins are meshed differently, they have common nodes at their interface. It is well suited to model curved boundaries.

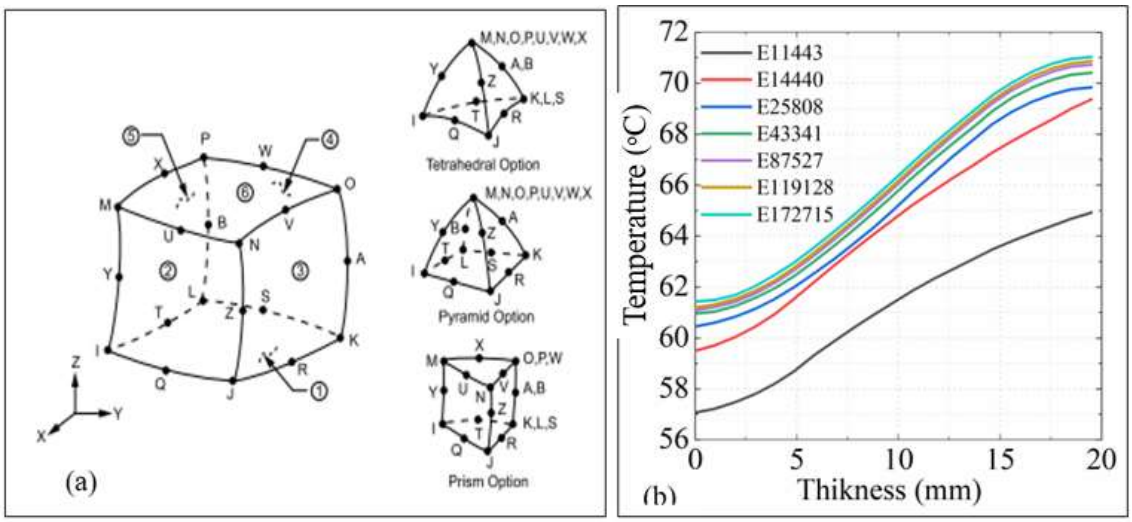

Figure 4.6 (a) Solid90 geometry (b) Mesh convergence test

Accuracy and computation feasibility are conducted by mesh convergence test by varying the number of elements from 11443 to 172715. Mesh convergence test is performed based on temperature variation along a disc thickness for a sample braking time of 2.5s (Figure 4.6.b). Elements on the surface were more refined than those far away from it, for each test. As a result, computation time is seen to vary from 6 to 24 hours on Intel (R) Xeon (R) silver 2.1GHz, 32GB RAM computer. Further increasing time beyond 2.5s has no impact on this test, except for the delay in computation time. Finally, 87527 elements with 143628 nodes were selected to proceed to the next simulation. Because the variation of temperature between the finest (172715 elements) and the selected mesh (87527 elements) was seen as less than 0.6%.

4.5 Heat Input and Boundary Condition Calculations

In the actual braking process, all modes of heat transfer (conduction, convection, and radiation) are involved. However, radiation has shown insignificant contribution in many studies [37][33]. Therefore, only conduction and convection are focused in this modeling. By description, the retardation power equals the negative of the work per unit time done by the friction forces in pad-disc interfaces for the whole brakes. By considering constant deceleration, the amount of kinetic energy predicted for one disc brake is comparable to the energy balance written below (Eq. 4.8) [84]:

$$c\frac{1}{2}Mv_o^2 = \int_0^{t_s} P(t)\,dt = 2F_{disc}\int_0^{t_s} v_{disc}(t)\,dt \qquad 4.8$$

Where,

c is the percentage of weight distribution on a single disc, and it is c_m for the motor bogie, and c_t for the trailer bogie, as presented in Eq. 4.9-4.10.

$$c_t = \frac{mass \text{ on single disc}}{\text{total mass of vehicle}} x100 = \frac{(M/3)/4}{M} = 8.33\% \quad 4.9$$

$$c_m = \frac{mass \text{ on single disc}}{\text{total mass of vehicle}} x100 = \frac{(M/3)/2}{M} = 16.67\% \quad 4.10$$

The braking (friction) force and corresponding instantaneous heat flux radial and temporal variation on the single pad-disc interface are expressed in Eq. 4.11 and Eq. 4.12.a- Eq. 4.13, respectively [84]. It is noted that the pad-disc interface area *(A_p)* is used for the non-axisymmetric moving heat input of Pan and Cai 2018 [31] and NAMHS models (Eq. 4.12.a-4.12.b), where pad area is expressed in Eq. 4.16.b. And, their difference is that radially constant heat input is implemented in Pan and Cai 2018 [31] as shown in Eq. 4.12.b. A similar empirical formula is used for axisymmetric disc thermal modeling (Eq. 4.13), except that disc contact surface area *(A_d)* and mean effective radius *(r_m)* are used instead, as shown in Eq. 4.16.a and Eq. 4.15, respectively. Heat source spatial variation in Pan and Cai 2018 [31], was presented constant at the pad-disc interface. Hence, Eq. 4.12.b with $r = r_m$ is utilized in calculating its heat input. Moreover, the dependence of heat input on the radial variation of the disc surface is seen for the NAMHS model algorithm (Eq. 4.12.a). However, the tangential variation of heat input in the NAMHS model requires new modeling (see section 4.6.3), because, the empirical formula couldn't evaluate it.

$$F_{disc} = \frac{c\frac{1}{2}Mv_o^2}{2\frac{R_d}{R_w}\left(v_o t_s - 0.5at_s^2\right)} \quad 4.11$$

$$q_s(r,t) = \frac{\gamma F_{disc} v_{disc}(r,t)}{A_p} = \frac{\gamma F_{disc}\omega(t) r}{A_p} \quad 4.12.a$$

$$q_s(r,t) = \frac{\gamma F_{disc} v_{disc}(r,t)}{A_p} = \frac{\gamma F_{disc}\omega(t) r_m}{A_p} \quad 4.12.b$$

$$q_s(t) = \frac{\gamma F_{disc}\omega(t) r_m}{A_d} \quad 4.13$$

Where, heat partition coefficient [37], mean effective radius [6], and full disc friction surface area [64] are expressed according to equations Eq. 4.14, Eq. 4.15, and Eq. 4.16.a, respectively.

$$\gamma = \frac{1}{1+\left(\frac{\rho_d c_d k_d}{\rho_p c_p k_p}\right)^{1/2}} \tag{4.14}$$

$$r_m = \frac{2}{3}\frac{\left(R_p^3 - r_p^3\right)}{\left(R_p^2 - r_p^2\right)} \tag{4.15}$$

$$A_d = \pi\left(R_p^2 - r_p^2\right) \tag{4.16.a}$$

$$A_p = \frac{\theta_o}{360°}\left(R_p^2 - r_p^2\right) \tag{4.16.b}$$

Besides, the disc brake is also exposed to convection boundary conditions at the rubbing surface *(h_s)* and vanes or fins *(h_f)*. The time-dependent coefficient of heat transfer convection is approximated for laminar ($Re < 2.4 \times 10^5$) and turbulent ($Re > 2.4 \times 10^5$) flow on the friction surface, based on Eq. 4.17 and Eq. 4.18, respectively [31]. However, it should be noted that rubbing surface convection is applied only in NAMHS, as it was not seen applied in traditional models.

$$h_s = 0.7\left(\frac{k_a}{D_d}\right)\mathrm{Re}^{0.5} \tag{4.17}$$

$$h_s = 0.04\left(\frac{k_a}{D_d}\right)\mathrm{Re}^{0.8} \tag{4.18}$$

$$\mathrm{Re} = \frac{v(t)_{disc} R_d}{v} \tag{4.19}$$

However, for the ventilation side of the disc brake, a timely varying convection coefficient is estimated for turbulent($Re>10^4$) and laminar ($Re<10^4$) flow, according to Eq. 4.20 and Eq. 4.21, respectively [33][54]. Since vanes' cross-section varies throughout their length, averaged hydraulic diameter (d_h) and cross-sectional area (A_c) are determined at the mid-length of vanes. Air kinematic viscosity and thermal conductivity are taken at 1atm and 25C°. Moreover, it must be noted that for all convection calculations made, the Prandtl number effect is nearly constant (0.7) for most cases [143][106].

$$h_f = 0.023\left(1+\left(\frac{d_h}{l}\right)^{0.67}\right)\mathrm{Re}_{dh}^{0.8}\,\mathrm{Pr}^{0.33}\,\frac{k_a}{d_h} \tag{4.20}$$

$$h_f = 1.86\left(\mathrm{Re}_{dh}\,\mathrm{Pr}\right)^{1/3}\left(\frac{d_h}{l}\right)^{0.33}\frac{k_a}{d_h} \tag{4.21}$$

Where,

$$\mathrm{Re}_{dh} = \frac{d_h}{v} V_{average} \tag{4.22}$$

$$d_h = \frac{4A_c}{2\left(\delta_f + w\right)} \tag{4.23}$$

$$v_{avg} = \frac{v_{input} + v_{output}}{2} \tag{4.24}$$

$$v_{in} = 0.0158N\left(D_d^2 - d_d^2\right)^{1/2} \tag{4.25}$$

$$v_{out} = v_{in}\frac{A_{in}}{A_{out}} \tag{4.26}$$

As a summary, calculated convective heat dissipation, heat input, and train speed are displayed as a function time for service brake conditions (Figure 4.7). The convective coefficient is shown the same for all modeling, except their application area at the friction surface. Furthermore, heat input is shown five times higher in non-axisymmetric, because, pad-disc interface area and full disc surface area are used for heat flux calculations, respectively in non-axisymmetric [31] and axisymmetric modeling. In addition, heat flux is seen steadily raised to 4 sec, as hydraulic pressure is fully operated after 4 sec [85].

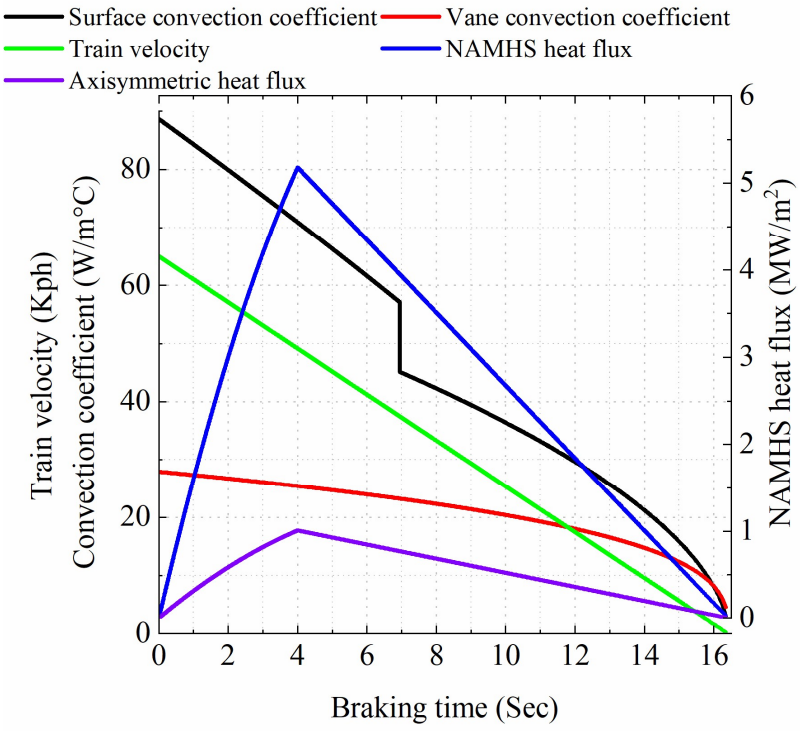

Figure 4.7 Input heat flux and convection heat dissipation,

4.6 Identification of Heat Source Spatial Variation and its Modelling

In this section, terms used in defining the spatial variation of heat are introduced first. And then, the cause of these variations is identified, based on previously defined terms. Once the NAMHS modeling is completed, disc brake boundary value problems are defined lastly.

4.6.1 Moving heat source leading and trailing edge

The disc is the rotating component, while the pads are stationary. For this type of simulation, the leading edge of a brake pad is the one that first touches the rotor as it rotates, while the trailing edge touches the same point at the last [144]. For the decelerating type of braking, the heat absorbed by a specific point on the disc from the leading edge of the pad is expected to be higher than the heat absorbed by the same point of the disc from the trailing edge. Because, the angular speed of the disc is higher when it enters the leading edge of the pad and is lower when it leaves the trailing edge of the pad. As a result, the leading edge of the pad could be exposed to higher temperatures, if we assume higher speed leads to higher temperatures. This argument is also seen as consistent with other researchers who found higher temperatures at the leading edge of the pads [145]. This observation could guide us to hypothesize the presence of heat input spatial variation at the pad-disc interface.

In contrast, the pads and the disc are assumed respectively, rotating and stationary components of the braking system in moving heat source modeling [6]. For the clockwise rotation of the disc brake (assumed in this study) heat source rotates counterclockwise. The rotating heat source geometric size is assumed equivalent to the pad cover angle [31]. In addition, heat source angular speed is assumed equivalent to disc rotational speed. For the single load step, it is assumed that the heat source starts to heat at a specific angular displacement on the disc and continues to heat the remaining friction surface until the pad cover angle is completed (one load step). This assumption is based on the aforementioned disc angular velocity variation between the leading and trailing edges, for the stationary pad and rotating disc. For example, for a pad cover angle distance (50° in this case), if it starts heating at 0°, it will continue to heat until it reaches the other side of the pad (50°). Thus, friction surface that received heat earlier (0°) is the leading edge, and the one that heated late will be trailing edge. As a result, aforementioned terminologies in rotating disc and stationary pads are interchanged.

4.6.2 Identifying the cause of spatial variation of heat input on the friction surface

Firstly, while the heat source is rotating, its speed variation due to deceleration reduces the amount of heat input from leading to the trailing edge. Thus, the particular node on the disc

surface does not receive the same amount of heat from all contacting nodes on the pad circumference. This point of view is consistent with the other investigations that reported contact pressure drop from the leading to trailing edge, for rotating disc and stationary pads [146][147]. Thus, it is hypothesized that heat flux could vary in the same way across the pad-disc interface, as it could be calculated from contact pressure.

Secondly, braking power and corresponding heat flux are directly proportional to disc radius (Eq. 4.12.a, Eq. 4.27), in spite of its constant assumption in traditional models. Thirdly, pads are accompanied by grooves of different layouts for composite type: radial [147], tangential [85], or both [17]. Besides, it might have a different geometry and the arrangement for sintered type [80]. This diversified design is reported to be the main factor that could affect spatial temperature distribution [17]. The last, but not the least factor that can affect heat flux spatial variation is hydraulic pressure in early braking time. Its increase in a short period of time requires further spatial and temporal investigations on heat flux and temperature. Surprisingly, the simultaneous effects of these factors on spatial and temporal temperature distribution have not been comprehensively examined in moving heat source.

4.6.3 Non-axisymmetric modeling of moving heat input

To consider space and time variation of heat input and boundary condition, the APDL programming model is displayed (Figure 4.8). The first part (the upper one) is applied for calculating and storing them as an array and scalar parameters for later use. Once the calculation is completed, the second part (the lower one) is applied for calling and applying them to the required location at the required time. The model is executed through APDL parameters (scalars and arrays) similar to FORTRAN written commands (Listed in Appendix A).

Prior to calculation, train kinematic inputs (V_o, a, t_b), disc geometric dimensions (Table 4.2), and material properties (Table 4.3) are defined as scalars in the ANSYS database, from which heat source total rotation angle (θ_{tot} in °) could be calculated. Then circumferential heat variation is evaluated and updated based on small heat distance increment $\Delta\theta$ and is also saved in the database as arrays. Thus, the circumferential variation of the heat source is assumed to occur every $\Delta\theta$, and the heat source is assumed to start rotational displacement from θ_o=0°. Hence, nodes within the same $\Delta\theta$ are assumed to have the same angular speed (rpm), but differ in tangential speed (m/s), due to their radius. Consequently, they will have the same and

varying heat flux, respectively along the circumferential and radial direction (Eq. 4.27). Then, θ_{tot} could be converted to the total number of heat source circumferential variation *(n)*.

Nonetheless, the exact selection of $\Delta\theta$ seems challenging as it can dramatically affect the circumferential heat variation (0°-360°). In previous moving heat source modeling, it was assumed to be 360° in axisymmetric for each load step [34][33][91]. In contrary, this assumption is a little bit modified in [31], since the authors reduced circumferential thermal variation to the pad cover angle (1.152 rad, corresponding to 66°). Despite that, still, heat variation is still expected within the pad-disc interface, as it is aforementioned. To select the appropriate heat distance increment, an increment-independent test is carried out for 25° and 10°. This is by assuming respectively, two heat source variations and five heat source variation areas, within the pad-disc interface. Besides, this test is also conducted further for 5° and 2.5° in the same way. Consequently, circumferential heat variation areas are raised further to 10 and 20, respectively.

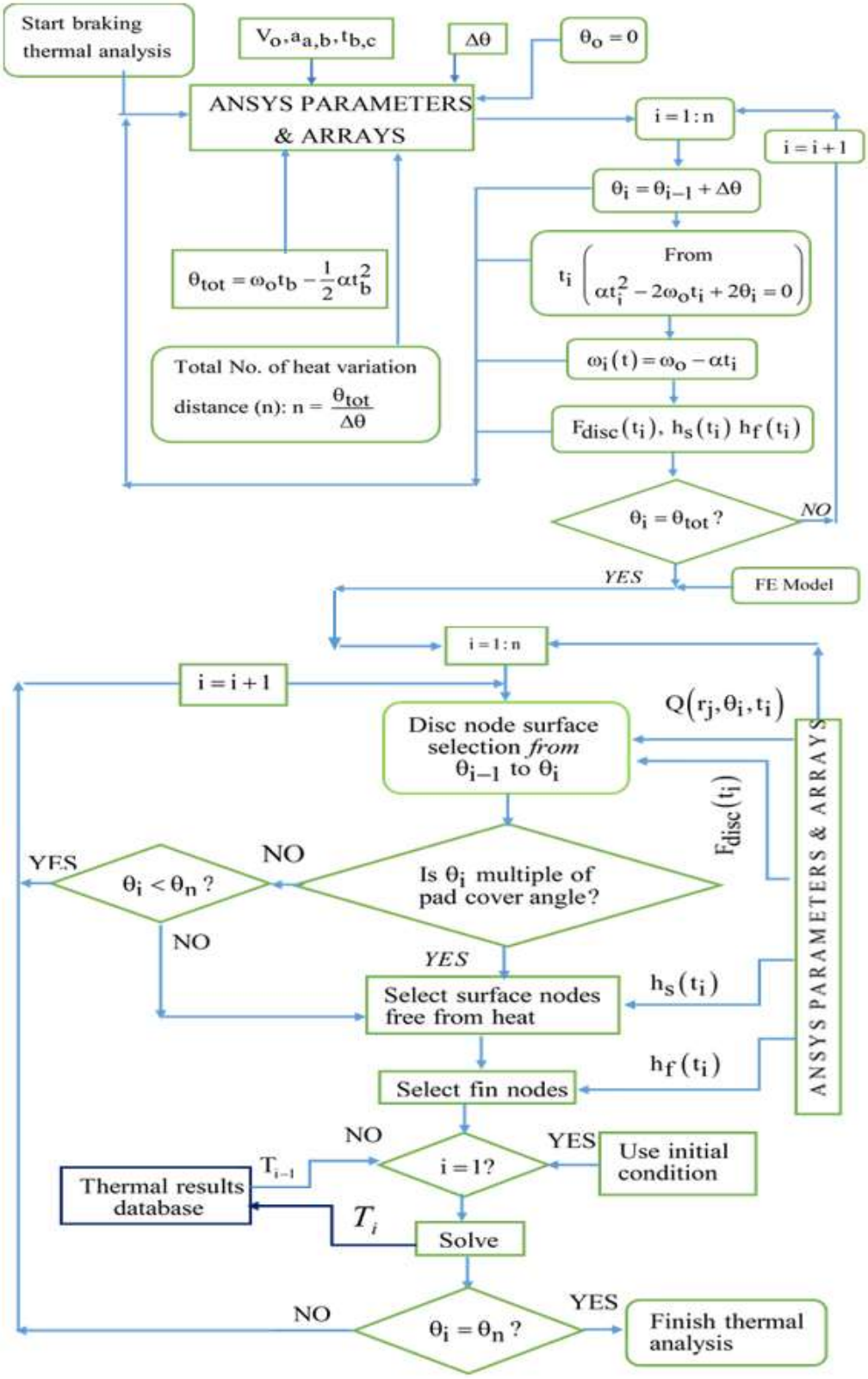

Figure 4.8 NAMHS algorithm flow diagram of heat flux and convection calculations (left), applications, and solving (right)

The corresponding circumferential temperature variation is plotted on mid-braking time at the mean radius (Figure 4.9). It is inferred that no more increase in the number of varying heat areas is required beyond 2.5°, as a similar result is displayed for 5° also. As a result, the pad cover angle (50°) is partitioned into 20 different heat source areas, decreasing or increasing in heat and temperature from leading to trailing edge, based on braking time.

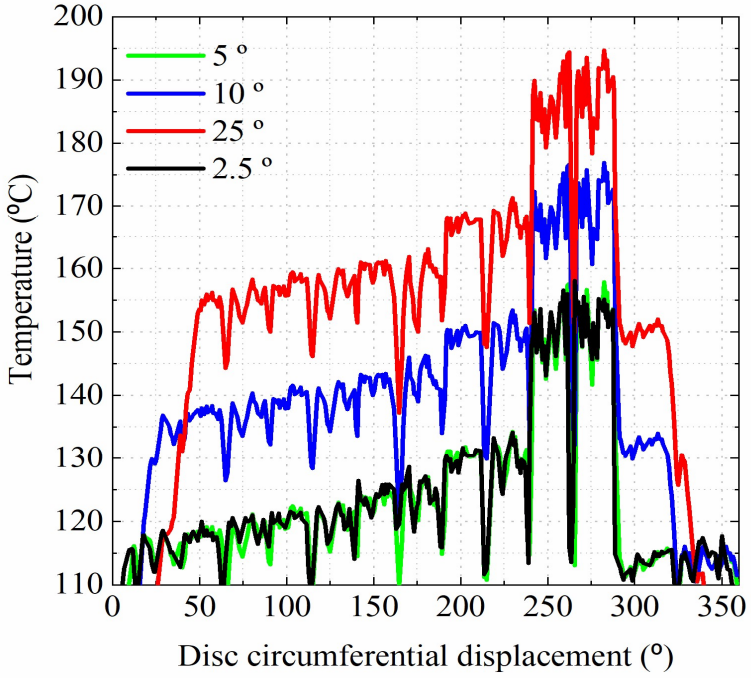

Figure 4.9 Increment independent test (Δθ) on mid-braking time, at the mean radius for hub-bolted disc

However, radial variation of heat is performed differently during heat source application. For every angular increment θ_i, time increment (t_i), friction force (F_{disc}), and angular velocity $\omega(t_i)$ could be calculated and stored as array parameters, by the formulae expressed in the flow diagram (Figure 4.8). And then, at every t_i, friction force (Eq. 4.11) and convection coefficients (Eq. 4.17-4.21) are also calculated and saved in the ANSYS database for later calling. While the calculation is conducted, every angle θ_i is checked if it is equal or not equal to θ_{tot}. If θ_i is not equal to θ_{tot}, the process will continue for another θ_i. Or else, the calculation is completed for $\theta_i=\theta_{tot}$. As a result, heat input is expected to drop on every θ_i (i varied from 0 to n) until $\theta_{i=n}= \theta_{tot}$, due to deceleration.

Once the $\theta_i=\theta_{tot}$ is satisfied for calculations, the second part of the modeling is initiated for heat source calculation and application, and boundary condition application. This is performed

according to the t_i and its corresponding convection coefficient. One load step is assumed to have locally varying heat source application on the pad cover angle domain [31], in addition to the convection coefficient on the remaining surface nodes *(h_s)* and fin nodes *(h_f)*. Surface nodes are selected based on heat variation distance (from θ_{i-1} *to* θ_i, where $\theta_i - \theta_{i-1}=2.5°$) extracted from the database. Nodes at a location of the radial pad groove (insulated) are excluded from these selections, and there are FORTRAN commands written to do so in APDL [148]. And, at bolt holes also no nodes are selected (for the original disc), even when it is ordered by the commands. For the specific locations of θ_{i-1} *to* θ_i, the heat source is calculated from arrays extracted within the database *(F_{disc}, $\omega(t_i)$, A_p)*, and from the inner radial location of selected nodes, according to Eq. 4.27.

Finally, the linearly varying heat source with radial location is calculated and applied from the heat gradient slope [149], for every θ_i. This loop will continue until the pad cover angle distance is completed (θ_i=multiple of 50°, or i=multiple of 20) for $\theta_i < \theta_n$. Once θ_i assumes pad cover angle multiple (at i multiple of 20), the surface convection *(h_s)* and fin convections *(h_f)* are called from the database and applied to their respective locations free from heat flux. For the first load step (i=1-20, or θ_i=0-50°) initial condition (25°C) is used, while for the remaining load steps, the nodal temperature at the previous load step ($t_i - t_{i-20}$) is used as initial condition. Moreover, the solution time for one load step *(t_{ls})* is taken as the time required for the heat source rotation to cover a pad cover angle rotation distance. It is unique for each load step and increases from early to late braking times. Because, a higher time is required to complete one pad cover angle in late than early braking time.

Following the solution of each load step, every multiple of pad cover angle θ_i is checked if it is equal or not equal to θ_n. If θ_i is not equal to θ_n, the process will continue for another load step. Otherwise, the solution is completed for $\theta_i = \theta_n$. However, this condition is a very rare case to occur and is expected if and only if θ_n will be multiple of pad cover angle, or n will be multiple of 20.

If θ_n is not the multiple of the pad cover angle, the same procedure is followed up to the highest multiple of pad cover angle θ_m (where m is the highest multiple number of 20), which will be close to θ_n by $\theta_n - \theta_m$<pad cover angle. In another way, the highest multiple numbers of 20 ($i=m$) will be close to n by $n-m$<20. After θ_m, the heat will be applied in the same trends for $\theta_i=\theta_m$ to θ_n. But since θ_n is not multiple of pad cover angle, the solution for the final load step will be

executed in different loops (θ_i=θ_n satisfied), with heat source application area less than a pad cover angle distance.

For this particular braking conditions (service braking type) and disc dimensions, θ_{tot}=θ_n=27387.5°, n=10956, m=10940, θ_m=27350°, and the total load step is 548. For the first 547 load steps, heat is applied on full pad cover angle, and for the last load step, it is applied on 37.5°. The position occupied by heat flux at a given time is displaced by convection at the next time, and vice versa. As a result, the friction surface is heated and cooled on small angular increments periodically, with heat flux and convective heat dissipation, respectively (Eq. 4.27 and Figure 4.10. a-c).

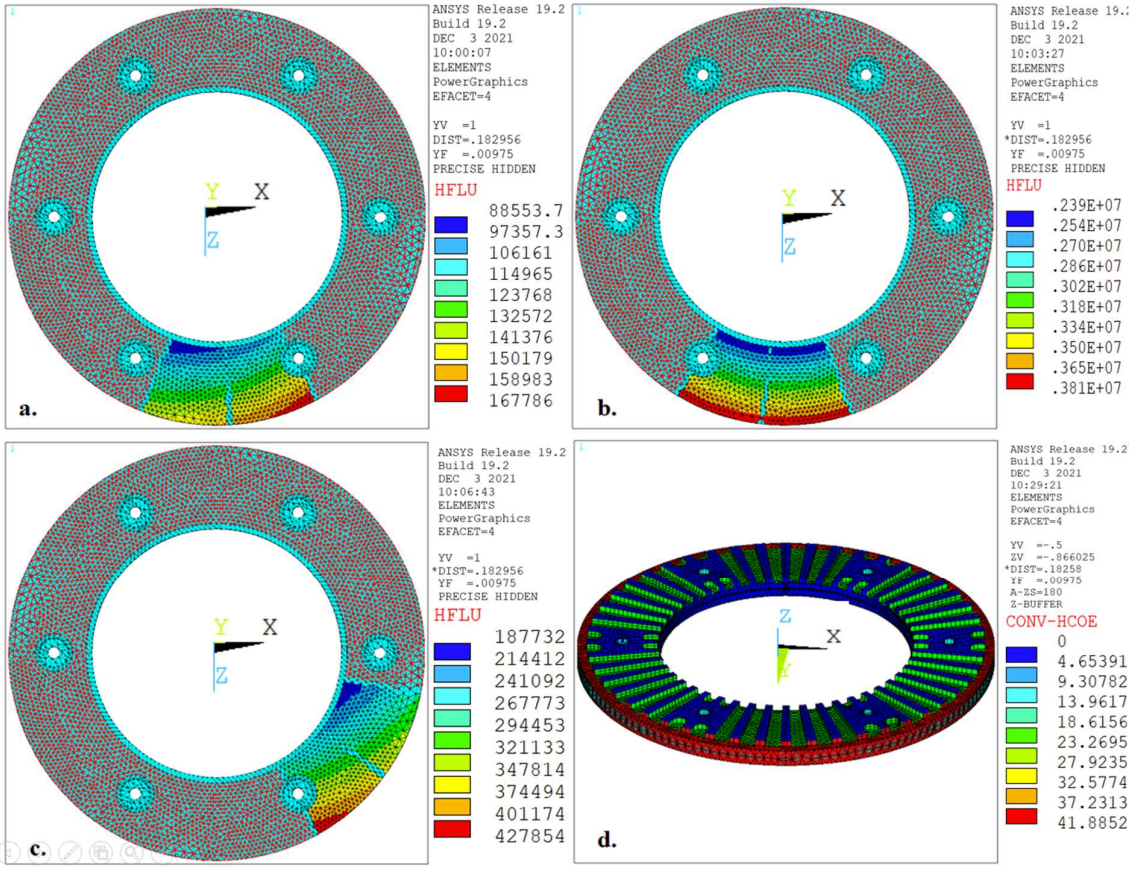

Figure 4.10 NAMHS heat flux and convection applications, at different braking times: (a) early, (b) middle, (c) late, (d) middle for bottom disc convection

To observe the impact of the NAMHS model algorithm on spatial heat flux variation, three braking times are randomly taken: early (0.089s), middle (8.151s), and late (15.783s) braking times (Figure 4.10). The influence of radius on heat flux variation is observed at all braking times. Nonetheless, the impact of circumferential heat flux variation is prevalent with the

increase in braking time (Figure 4.10. c). Because, heat source displacement comparable to pad cover angle distance is covered within a very short period of time during early and mid than late braking time (due to deceleration). This means circumferential speed variation among pad incremental distance will have insignificant variation in early braking, and significant during late braking. As a result, the magnitude of the heat source within the pad cover angle decreased from leading to the trailing edge, but not seen abruptly in mid-braking time (Figure 4.10. b), as in late time.

Even though the pad leading edge is expected to have relatively higher heat flux, it is surprising to observe higher heat at the pad trailing edge, contrary to expectations (Figure 4.10 .a). This rather contradictory result might be due to a significant increase in hydraulic pressure with time, resulting increase in heat flux from the pad leading to the trailing edge (Figure 4.7). This dominates the reduction of heat flux from leading to the trailing edge of the pad due to deceleration (reduction of speed with time). For the late braking, however, heat flux decreases from leading to the trailing edge as expected, as no hydraulic pressure interferes with the heat flux (Figure 4.10.c). In this modeling, consideration of wear heat generation is neglected as its effect is low compared to friction heat generation [7]. Besides, the NAMHS model algorithm is conducted on the composite pad with one radial pad groove, though its application on sintered and other composite pads (one tangential and two radial grooves) is tested, and seen as successful (Figure 4.11).

$$Q(r_j, \theta_i, t_i) = \frac{\gamma F_{disc} \omega(\theta_i, t_i) r_j}{A_p} \qquad 4.27$$

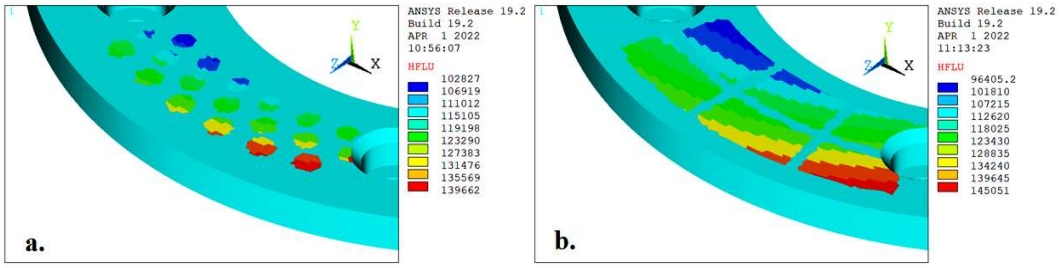

Figure 4.11 Flexibility of NAMHS to accommodate various pad designs: (a) sintered, (b) composite

The heat input model is also displayed for traditional models: axisymmetric (Figure 4.12. a) and Pan and Cai 2018 [31] (Figure 4.12. b). Heat flux is spatially constant on all friction surfaces, in the former one. Meanwhile, heat flux is independent of space at the pad-disc

interface in the latter. Heat flux is calculated at the mean effective radius and varied timely in both traditional models (Eq. 4.12.b and Eq. 4.13). Besides, for Pan and Cai 2018 [31], the friction surface area is shared for heat flux only, and the remaining surface area is insulated.

4.6.4 Friction heating boundary value problem (Axial Z-Y, radial X-Y)

Non-axisymmetric boundary value problem of the parabolic heat conduction equation is presented in Eq. 4.1 for a single load step in transient analysis. However, it should be a little bit modified here according to the orientation of the disc in this analysis (Figure 4.11).

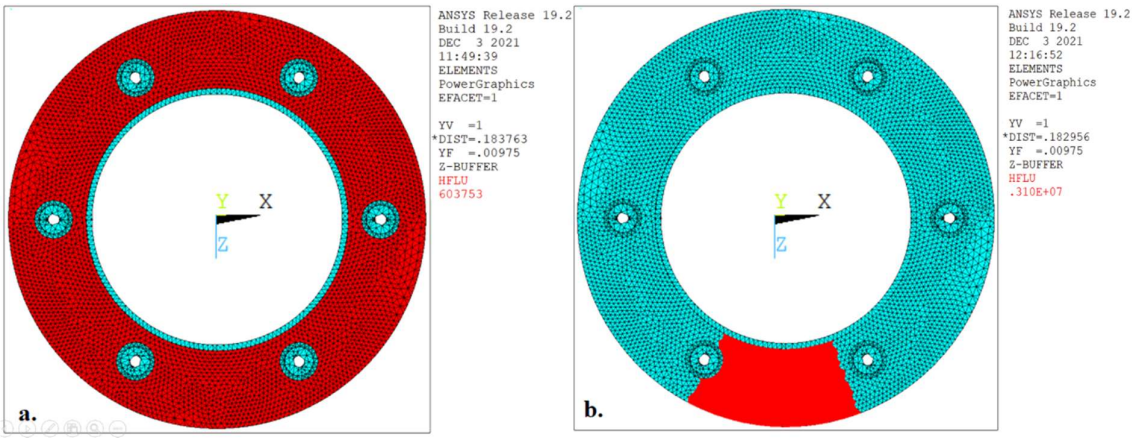

Figure 4.12 Heat flux applications at mid-braking (a) axis-symmetric, (b) Pan and Cai, 2018 [31]

In this study, the global cartesian Y (instead of Z in Eq 4.1 and Figure 4.1) is the axis of rotation of the disc brake. Hence, the global cartesian Y is axial-z, the global cartesian X is circumferential-θ, and the global cartesian Z is used as radial-r in cylindrical coordinates for disc orientation observed in (Figure 4.11). As a result, the general cylindrical parabolic heat equation (Eq 4.1) is represented in Eq 4.28 with a different interpretation: r, θ, z, t represent radial (r), circumferential (θ), axial (z), and time (t) variables, respectively [6]. Besides, cylindrical coordinates r, θ, and z are equivalent to cartesian coordinates Z, X and Y, respectively. Hence, the transient temperature hyperbolic equation expressed in cylindrical coordinate T(r,θ,z,t) is equivalent to T(Z, X,Y,t) in the cartesian coordinate system. According to the diagram of the pad (the heating area) and the disc shown in Figure 4.11.b, the cylindrical coordinates on the friction surface (Y=0) with Y as the axis of rotation comprised the spatial regions of the pad (Γ_p) and disc (Γ_d) defined in Eq. 4.29 and Eq. 4.30, respectively.

$$\frac{\partial^2 T}{\partial r^2}+\frac{1}{r}\frac{\partial T}{\partial r}+\frac{1}{r^2}\frac{\partial^2 T}{\partial \theta^2}+\frac{\partial^2 T}{\partial z^2}=\frac{1}{k_d}\frac{\partial T}{\partial t} \text{ for } \begin{Bmatrix} \mathrm{r}_d < r < R_d \\ |\theta| \le \pi \\ -(\delta_d+\delta_f) < z < 0 \\ t_i < t \le t_{i+20} \end{Bmatrix} \quad 4.28$$

$$\Gamma_p = \begin{Bmatrix} r_p \le r \le R_p \\ |\theta| \le \theta_o \\ 0 \le z \le \delta_p \end{Bmatrix} \quad 4.29$$

$$\Gamma_d = \begin{Bmatrix} r_d \le r \le R_d \\ |\theta| \le \pi \\ -\left(\delta_f+\delta_d\right) \le z \le 0 \end{Bmatrix} \quad 4.30$$

$$k_d \left.\frac{\partial T}{\partial z}\right|_{z=0} = \begin{Bmatrix} Q(r_j,\theta_i,t) \text{ for } \left\{ \mathrm{r}_p \le r \le R_p \;\; |\theta_i| \le \theta_o,\; t_i \le t \le t_{i+20} \right\} \\ h_s\left(T_a - T(R_d,\theta_i,0,t_i)\right) \text{ for } \begin{pmatrix} \left\{ r_d < r < r_p, |\theta_i| \le \pi \right\} \cup \left\{ r_p \le r \le R_p, |\theta_i| \ge \theta_o \right\} \\ \cup \left\{ R_p < r < R_d, |\theta_i| \le \pi, t_i \le t \le t_{i+20} \right\} \end{pmatrix} \end{Bmatrix} \quad 4.31$$

$$k_d \left.\frac{\partial T}{\partial r}\right|_{r=R_d} = h_s(T_a - T(R_d,\theta_i,0,t_i)),\ \text{for } |\theta_i| \le \pi,\ \text{-}\delta_d < z < 0,\ \mathrm{t}_i \le t \le \mathrm{t}_{i+20} \quad 4.32$$

$$k_d \left.\frac{\partial T}{\partial r}\right|_{-(\delta_f+\delta_d)<z\le\delta_f} = h_f(T_a - T(R_d,\theta_i,z,t_i)),\ \text{for } |\theta_i| \le \pi,\ \mathrm{t}_i \le t \le \mathrm{t}_{i+20} \quad 4.33$$

$$\left.\frac{\partial T}{\partial r}\right|_{r=r_d} = 0 \text{ for } \text{-}(\delta_f+\delta_d) < \mathrm{z} < 0,\ |\theta_i| \le \pi,\ \mathrm{t}_i \le t \le \mathrm{t}_{i+20} \quad 4.34$$

$$\left.\frac{\partial T}{\partial z}\right|_{z=-(\delta_f+\delta_d)} = 0 \text{ for } r_d < \mathrm{r} < R_d,\ |\theta_i| \le \pi,\ \mathrm{t}_i \le t \le \mathrm{t}_{i+20} \quad 4.35$$

And, Eq. 4.27 is rewritten with surface convection in Eq. 4.31 to account for spatial variation of heat and convection, where i and j are circumferential and radial variation of heat respectively. In addition, other boundary conditions include outer radius convection (Eq. 4.32), fin convection (Eq. 4.33), and insulated convections at the disc internal radius (Eq. 4.34) and disc bottom surface (Eq. 4.35).

For hub-bolted type discs, bolt holes at the internal radius of the disc, which is used as the connection between the disc and axle are removed or omitted. This simplification does not impact the results but enables us to decrease the total number of finite elements, resulting in a substantial reduction in computational time [30] [86]. It should be noted that the disc surface is taken as reference (0) from where other disc thicknesses are measured negatively along the

axial direction. And these equations are written for one load step time $(t_{ls}=t_{i+20}-t_i)$, and repeated for the remaining load steps (Figure 4.8).

4.7 Results and Discussions

The response of varying heat input load spatially and temporally is investigated along radial, circumferentially, and axially (along disc thickness) directions of the disc. Moreover, its temporal effect is examined at three different braking times: early, middle, and late braking.

4.7.1 Radial transient temperature evaluation

For better result analysis, it would be sensible to take six radially varying points (but circumferentially 90°) on the friction surface: disc inner radius (R_1=113mm), pad inner radius (R_2=122.5mm), mean or effective radius (R_3 or R_m=146.5mm), transitional radius (R_t = R_4=154mm), outer pad radius (R_5=170mm) and outer disc radius (R_6=180mm). The results of these points are illustrated for actual disc geometry on the left side of Figure 4.13, while the right side of the figure displays the variation between the NAMHS and traditional models (axisymmetric and [31]). R_3 or R_m is taken from Eq. 4.15, the position at which heat flux or breaking power is calculated for both traditional models (Eq. 4.12.b and Eq. 4.13). Besides, it is presented as the best position to compare thermal results, because, all models will have the same radial heat flux (Eq. 4.12.a- Eq. 4.13) here.

On the contrary, R_t is the NAMHS model algorithm finding from this investigation, as the NAMHS model temperature starts to surpass Pan and Cai, 2018 [31] model (Figure 4.13. d). Despite registration of lower temperature displayed by the NAMHS from R_1 to R_3, this trend is not shown beyond R_t. At this point, both moving heat source models display equivalent results, except at early (0-4s) and late braking times. This might be associated with NAMHS's hydraulic pressure increase and prevalence of surface convective coefficient on former and later braking times, respectively. Beyond R_t, the NAMHS model is shown to surpass Pan and Cai 2018 model [31], due to the higher radius used in heat source calculation.

The temperature variation results at the mean effective radius (R_3) demonstrated that, both traditional models exaggerated surface temperature distribution as high as 0%-60% and 0-5%, respectively for axisymmetric and moving heat sources of Pan and Cai, 2018 [31] (Figure 4.13 .c). It should be noted that the temperature variation calculated here is in absolute value for all radii. This much variation in axisymmetric modeling is likely attributed to a huge difference in the surface area shared for heat flux application. In axisymmetric, 360° surface area is exposed to heat flux, meanwhile only pad cover angle in moving heat sources.

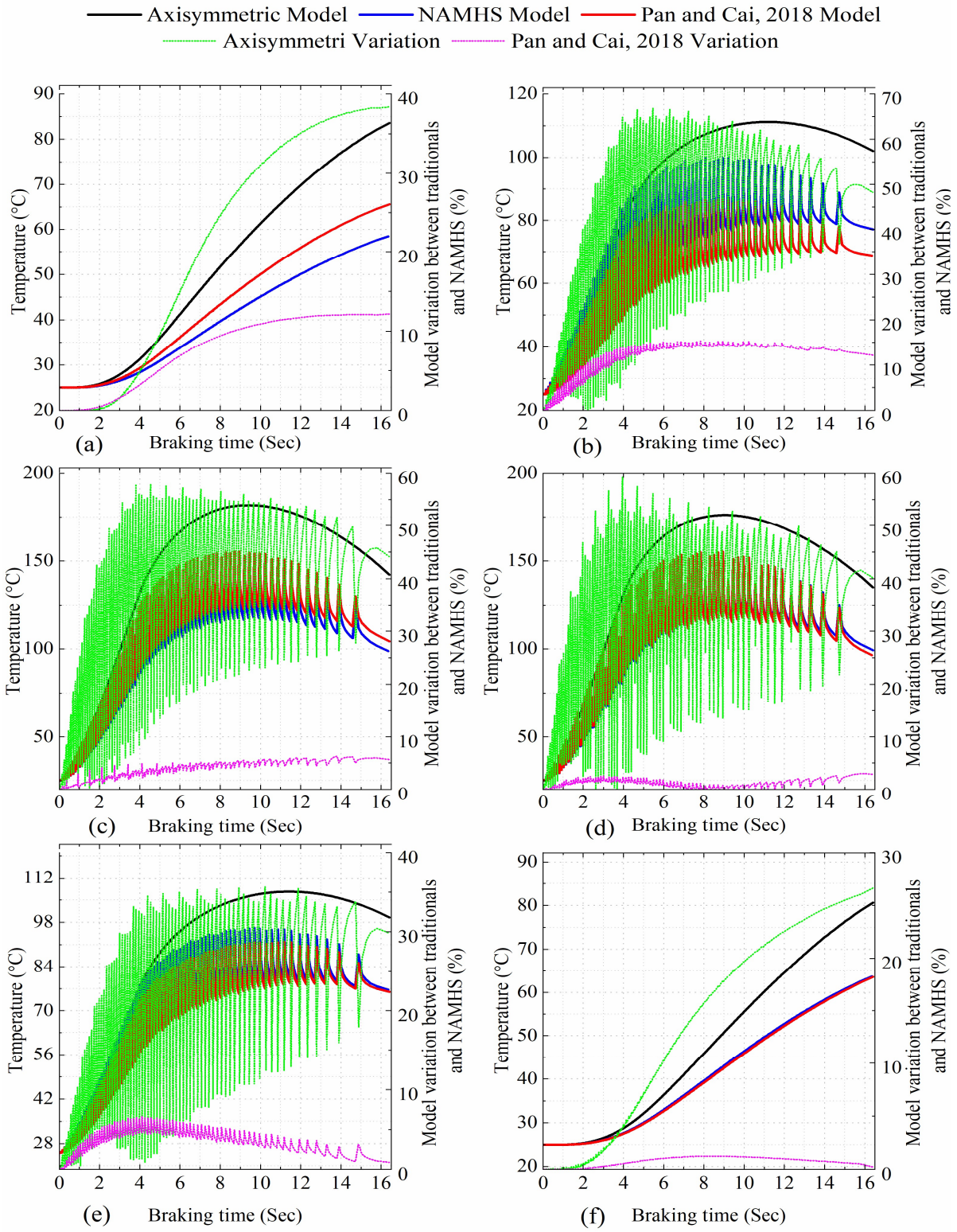

Figure 4.13 Transient temperature at different radii: (a) disc inner-R1, (b) pad inner-R2, (c) mean-R3 or Rm, (d) Transitional-R4 or Rt, (e) pad outer-R5, (f) disc outer-R6

Overestimation of the results by axisymmetric is a rather surprising result, as a higher heat flux value is displayed for moving heat sources (Figure 4.7). The prediction of conservative fatigue life in the works of Gigan et al. 2019 [93] might seem due to this axisymmetric modeling. Therefore, the findings reported here suggest that the size of the area on which heat is applied would have a remarkable impact on temperature, thermal results, and thermal fatigue prediction, compared to any other factors affecting heat flux calculation and application.

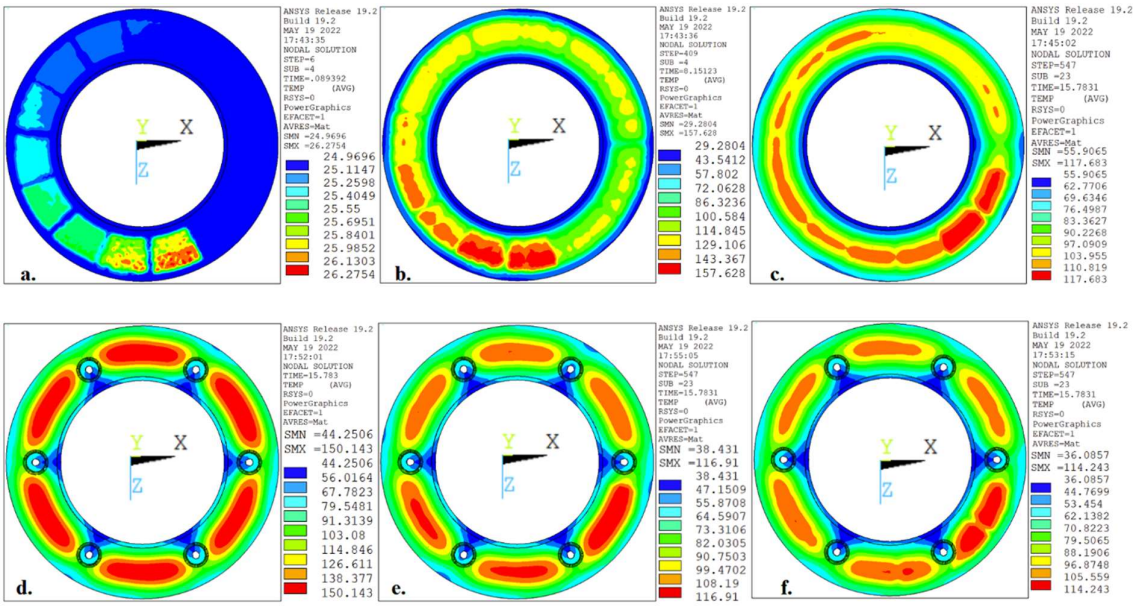

Figure 4.14 Temperature plot for modified disc (NAMHS: (a) early, (b) mid, (c) late-braking times) and original disc ((d) axisymmetric-late, (e) [31]-late and (f) NAMHS-late braking times)

Though the moving heat sources are observed to have similar results, still the presented value is significant (5%) in late braking time (Figure 4.13. c). This could be further enlightened by the insulated pad groove and circumferential variation of heat flux (due to hydraulic pressure and train deceleration). Furthermore, exposure of friction surface outside the pad-disc interface to convection in the NAMHS model could be associated with this variation. Particularly, the rising impact of circumferential heat flux and surface convection coefficient on the late time appears responsible for the gradual rise of their difference. Unfortunately, this finding is somewhat disappointing, as their share or their individual contribution to result variation is not revealed. Furthermore, this outcome is contrary to that of Pan and Cai, 2018 [31]who found almost the same temperature results, for axisymmetric and moving heat sources. The insulated surface area outside the pad-disc interface could explain this discrepancy, as it could raise the temperature in moving heat source up to axisymmetric model temperature.

The other most striking result to emerge from the NAMHS model is the contribution of radius in affecting temperature. This is apparently seen where pad extreme radii are used in the NAMHS model (Figure 4.13. b&e). It is displayed that the variation of the NAMHS model from [31] model is dropped from 10% to 0, as the radius rises from R_2 to R_t. The rise of heat flux with radius in the NAMHS model explains this observation (Eq. 4.12.a). In contrast, from R_t to pad external radius, its variation is also shown to rise with radius, due to the same reasoning. However, its variation is not seen as substantial as in the inner radius (Figure 4.13. e). This unexpected result might be associated with a higher contribution of circumferential heat variation in reducing the temperature, at the outer radius than the inner radius (Figure 4.10.a,c & Figure 4.16). Consequently, the effect of radius in rising temperature is shown minimized. These results suggest the NAMHS model's capability to reveal the combined effect of radial and tangential variation of heat input on spatial variation of temperature.

Particularly, the effect of radius consideration on temperature is obviously seen when an equal radius is used for all models in heat flux calculation (Figure 4.13. c). The variation is seen massively reduced with gradually increased (0-5%). Hence, it could be inferred that the NAMHS model is the best in revealing radial variation of temperature. Furthermore, this could highlight convincing evidence for the argument that radius took a significant share, if not the only one, for temperature variation. In contrast, a possible explanation for the 5% variation might give a clue or tentative evidence for the presence of additional factors to be considered. These include circumferential heat flux variation, insulated pad groove, and friction surface convection in the NAMHS model. Hence, this finding has drawn our attention to the significance of considering the spatial variation of heat source in a modeling disc brake, which couldn't have been supported in traditional models. So, the findings reported here suggest the radial distance is the second major factor to be considered, in causing spatial temperature variation.

However, the most surprising result observed on the NAMHS model is the registration of the lowest temperature for R-value ranging from R_m up to R_t, in spite of the higher R-value used in calculating heat flux (Eq. 4.12.a). This result also offered additional evidence on the contribution of circumferential heat input variation (deceleration), friction surface convection, and consideration of pad groove in thermal modeling. Collectively these factors are seen to overcome heat rise by a 7.5mm increase in radius from R_m to R_t. Hence, these findings suggested the third factors to be considered in spatial temperature variation, as deceleration, pad groove, and friction surface convection.

Regardless of this investigation, some recently reviewed studies by the authors reported almost half of the disc brake thermal studies (49%) regrettably disregarded heat flux radial variation [26]. Yet, few studies reported its consideration, but their heat input calculation methods were different from the current investigation: uncoupled thermomechanical [28][67] and coupled thermomechanical [8][30]. It is, obvious to consider spatial effect in such models, though convergence problems in these methods forced us to consider different modeling.

For all presented models, the temperature is displayed higher at the middle radii (Figure 4.13. c&d) than pad extreme radius. Besides, disc extreme radii are observed to have the lowest temperature. This is not surprising, as these points are 'far' from the heat source area. In accordance with the presented results, other studies also confirmed the maximum temperature location at the mid-surface of the disc [79][85]. On the other hand, this finding is contrary to previous studies that reported maximum temperature at the outer radius of the disc [64], meanwhile, others reported extreme radius (inner and outer) as the location of the maximum temperature [37][90]. These variations in conclusion seem to emerge from using different pad types (cover angle, size, groove number, and layout), disc types, and designs.

4.7.2 Circumferential surface temperature variations

To include the effect of disc geometry on circumferential temperature fluctuation, the result is displayed for both modified (hub-bolted- Figure 4.15.a-c) and original (12 reinforcing structures around 6 holes- Figure 4.15.d-f) disc geometries. These results are reported for three braking times at the mean radius (R_m) for all models.

Six sinusoidally fluctuated temperatures are displayed for the original disc geometry in a way that steadily raised and then dropped, for all models (Figure 4.15.d-f, Figure 4.14.d-f). In contrast, circumferentially smooth development of temperature is observed for modified (hub-bolted) disc geometry in all models (Figure 4.15.a-c, Figure 4.14.a-c). These results in the original disc are directly related to two reinforcement structures added around each bolt hole between two consecutive fins, resulting increase in disc thickness, every 60° (Figure 4.10.d). This increase will lead to a drop in temperature. Consequently, surface temperature variation is presented 30°C and 42°C by the axisymmetric model on late and mid-braking times, respectively (Figure 4.15.e-f). Similar surface temperature variations are also seen in the remaining models. In spite of this difference, the maximum temperature registered is the same in both disc types. At mid-braking time on both disc geometry, 155°C, 165°C, and 180°C

temperature is observed for NAMHS, Pan and Cai 2018 [31], and the axisymmetric model, respectively (Figure 4.15. b&e).

One interesting finding here is the irrelevance of maximum temperature in conducting comparative analysis disc geometry. And, another important finding observed is the high-temperature gradient along the original disc surface. The surface temperature gradient is not recommended, as it promotes crack initiation due to thermal stress. Hence, further comparison of disc design requires structural analysis, in which thermal stress and fatigue life are calculated (Chapter 5).

Further analysis of all braking time in moving heat sources models reveals a slight rise of each peak or interface (Figure 4.15), as we move further from the lower to the higher angle. A possible explanation for this might be the disappearance of high-temperature positions as time passed, owing to heat dissipation by either conduction ([31]) or both conduction and convection. As a result, interfaces close to the pad cover angle are highlighted higher in temperature, compared to those far away from it.

Since this impact of disc geometry is shown dominant in spatial temperature variation, the modified geometry seems preferred to investigate the individual effect of the NAMHS model at mean radius, just to investigate circumferential temperature fluctuation (Figure 4.15). Hence, two specific positions are selected on mid (28°&263°) and late (28°&302°) braking times. The highest surface temperature difference is revealed by the NAMHS as 49°C, and14°C at mid and late braking times, respectively. Likewise, [31] displays 42°C and 10°C at mid and late braking times, respectively. Nonetheless, 0°C and 2°C surface temperature variations are revealed by the axisymmetric model at mid and late braking time (Figure 4.15.b-c). This late braking time variation in the axisymmetric model might seem due to the increasing effect of fins' conduction and heat dissipative convection with time. Fins', circumferential distribution might appear to vary in temperature, although its value is shown insignificant, compared to moving heat source models. Besides, the capability of all models in accommodating spatial temperature variation is also obviously revealed in Figure 4.14. d-f. Spatial variation is seen better displayed in NAMHS than in both traditional models, and, the [31] model is illustrated better than the axisymmetric.

During early braking time, surface temperature differences (gradient) are seen clearly for both moving heat sources only, although their magnitude is not seen as significant (1°C) (Figure 4.15. a&d, Figure 4.14.a). This might be due to less temperature development in early braking

time. Moreover, the maximum angular velocity attained here could lead to inconsequential surface temperature variation. In spite of these, both moving heat sources display a gradual increase of temperature in the first half (0-180°), followed by a 'dramatic' increase as it approaches the pad-disc interface area (250°-300°). Beyond this interface, they have shown a 'massive' drop in temperature.

Despite the similarity in the trends of moving heat sources, their careful observation identifies their differences (Figure 4.15. a&d). In Pan and Cai 2018 [31] model, a stepwise rise in temperature is seen between consecutive interfaces, but not varied with time within interfaces. However, in the NAMHS model, a continuous rise in temperature (including, at the pad-disc interface) is shown instead. One reason that could explain this observation is the circumferential increase of heat flux due to hydraulic pressure in the NAMHS model Figure 4.10.a & Figure 4.14.a). Meanwhile, the constant temperature depicted at the interfaces in the traditional models is related to the heat flux constant assumption, spatially (Figure 4.12.a&b). One of the issues that emerged from these findings is the consideration of hydraulic pressure as the fourth factor that could affect temperature evolution.

Another remarkable effect of heat flux circumferential variation in the NAMHS model is prevailed in terms of circumferential temperature drop, due to deceleration. At a contact interface of 300°-350°, temperature variation is reported 7°C (Figure 4.14. c,f -Figure 4.15. c,f), meanwhile, the traditional models are seen not to predict it at all. Nonetheless, such trends of temperature are not seen to exist at mid-braking times (Figure 4.15. b,e). It is attributed to a relatively higher rotational speed of the heat source, resulting in insignificant variation.

Thus, the result presented in the NAMHS model revealed an encouraging outcome, as it imitated the linear rise of hydraulic power and showed the best surface temperature difference, compared to traditional models. And these results uncovered two remarkable findings. Firstly, the NAMHS model successfully reported spatial temperature variation. Secondly, disc geometry accounted for a significant amount of surface temperature difference in all models (Figure 4.14.d-f).

Two specific positions appear as a clear gap (free from heat) between two heat source areas in Figure 4.14 and Figure 4.15. Particularly, on the early braking time of both figures, they are seen obviously. Two possible explanations are put forward. Firstly, insulation on the pad groove might reduce temperature. Secondly, the migration of surface heat from the pad's extreme border to neighboring nodes, either by convection and conduction (in NAMHS) or

conduction only (in [31]). This seems the jumps in heat source rotation between consecutive pad cover angles, but not in actual loading conditions. Furthermore, the spatial surface temperature presented here (Figure 4.14) is not observed as similar to hot spots and hot bands in other studies [27], which might be due to negligence of thermoelastic contact wear between the pad-disc interface. However, compared to traditionally known models, it is believed that the NAMHS model has successfully uncovered surface temperature spatial variations at any braking time.

NAMHS findings seem to be consistent with other research which found a 50°C temperature difference at rubbing zones [29]. In contrast, another result reported a 5% error between axisymmetric and non-axisymmetric thermal analysis [27]. This might appear due to the higher initial velocity used (twice compared to this study). Because, the time required by a heat source to complete one revolution is relatively small, resulting in close results between axisymmetric and non-axisymmetric modeling. Thus, the NAMHS model might seem recommended for low-speed trains, having frequent stops, like light rail transit. But this didn't mean not applicable to high speed, rather, a similar result would be expected with axisymmetric modeling.

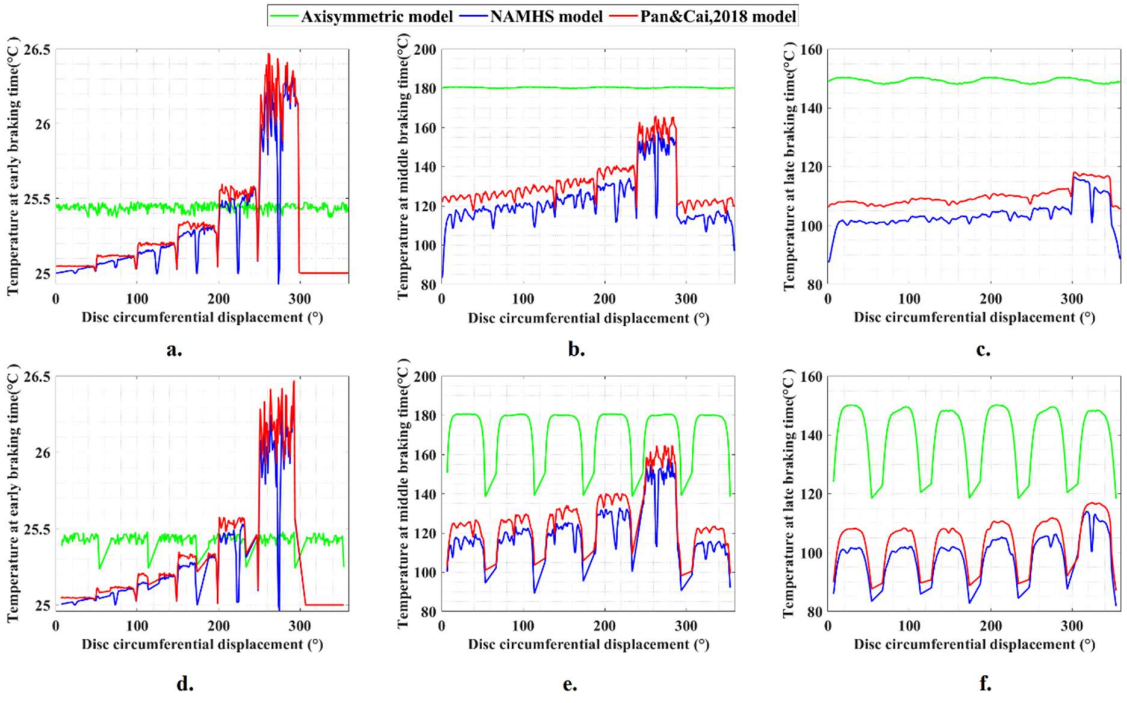

Figure 4.15 Circumferential temperature distribution for modified (a-c) and original (d-f) disc at the mean radius and different braking time: early (a,d), middle, (b,e) late, (c,f)

Furthermore, the circumferential temperature at the interface 300°-350° is expected to decrease from the leading to the trailing edge (Figure 4.15.c&f). But this factor is seen apparently at the outer radius rather than the inner radius. And, this meant no circumferential heat flux variation at the inner radius. Rather, it could be explained by the impact of circumferential heat variation prevalence at the outer radius rather than the inner, as aforementioned in section 4.6.3 (Figure 4.10). On the contrary, interface temperature variation for the original disc is depicted differently (Figure 4.15. d-f). This could be enlightened by two issues. Firstly, the proximity of the leading edge or first half of the pad cover angle (301°-325°) to the bolt hole area at 300°, where low temperature is registered. Consequently, the leading and trailing edges appeared to have similar temperatures (Figure 4.15.f & Figure 4.14.f). Secondly, the inner radius is closer to the bolt center hole (by 28mm) than the outer radius, which is 39mm far. Due to these issues, surprisingly the results seem to contradict the previous argument, resulting in lower or similar temperatures at the leading edge (Figure 4.15.f). Therefore, these results need to be interpreted with caution for the original disc, as geometry could interfere with temperature distribution. For either of the disc, however, this observation of the higher temperature at the leading edge in NAMHS is consistent with previous investigations of temperature [145] and contact pressure [146][147] (which could be utilized to calculate temperature) of the pad-disc interface.

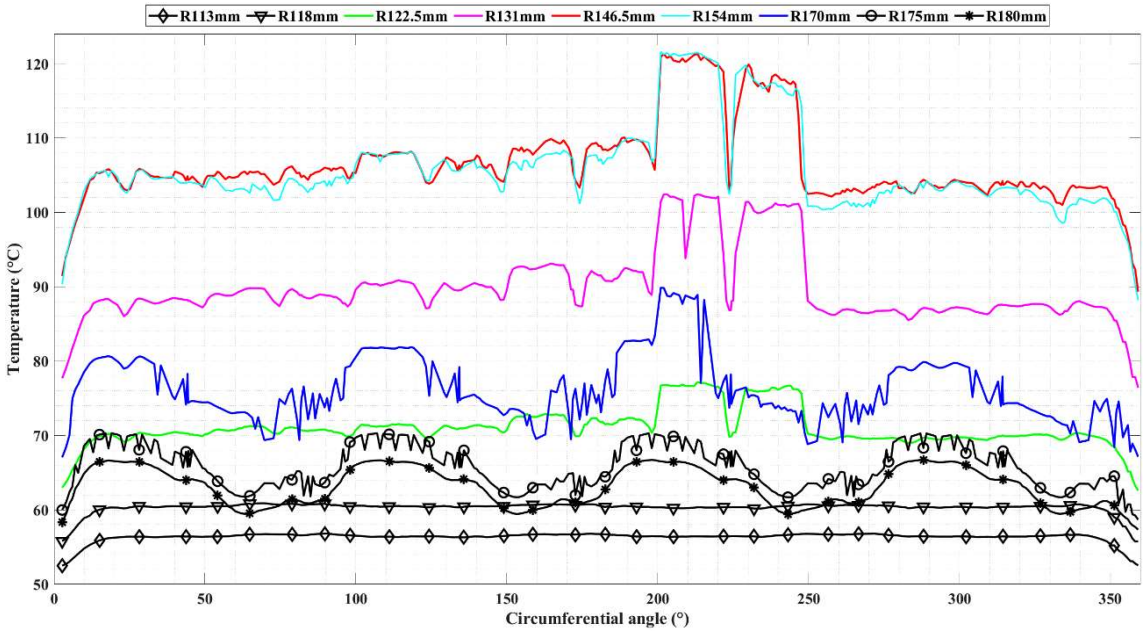

Figure 4.16 Hub-bolted disc circumferential temperature distribution at various radii on late braking time

4.7.3 The effect of pad groove in circumferential surface temperature variations

As we approached the interface, increasing trends of sharp drop and rise of temperature are observed throughout the braking time, due to the pad groove (Figure 4.15-Figure 4.16). Since temperature is not developed yet in early braking, its difference at the pad groove compared to its neighborhood nodes is seen as insignificant (1°C). In addition, at mid-braking time for mid-radius, relatively the influence of the pad groove is also observed (Figure 4.15.b). Likewise, in late braking time, the pad groove effect is illustrated as influential as it approaches the last peak (Figure 4.15.c,f & Figure 4.16). The maximum temperature variation between the groove location and its neighboring nodes within the same pad cover angle is uncovered 44°C and 15°C at the mid and late braking, respectively (Figure 4.15.b&c). Temperature variation due to the groove is seen rising, as it approaches the peak interface. This is associated with the migration of high heat area to lower temperature area by conduction (to pad groove) and convection (to surrounding). Finally, temperature variation at the peak pad cover angle has shown a negative slope (change in temperature within pad-disc interface to pad cover angle) of -0.122°C/° (Figure 4.15. c). Meanwhile, a positive slope is demonstrated for early braking. Nevertheless, such results are not noticed in mid-braking times, as tangential heat variation is perceived during early and late braking times (Figure 4.10. b).

This effect of pad grooves in spatial temperature reduction is in line with the findings of other studies [85]. Thus, further reduction of temperature is hypothesized as pad grooves raised in number, and this is seen to agree with other investigations, which found lower distortions and Mises stress for pads with grooves [150]. Hence, this result provides another support for the hypothesis that pad groove consideration could influence result variation, spatially. Consequently, the NAMHS model algorithm might help us to select the optimum pad design based on its numbers, shapes, and location of grooves as in [80][17][37].

4.7.4 Temperature investigation through disc thickness

Further analysis by the NAMHS model showed the zigzagged behavior of temperature to have only 6.5mm depth from the surface (Figure 4.17). This ceases of zigzagged behavior is likely related to the delay of heat conduction along the circumferential direction, as the disc thickness increased from the surface. This is seen in agreement with other studies that reported 5mm depth [86]. Hence, the NAMHS model algorithm provides a better chance to reveal the spatial and temporal variations of temperature.

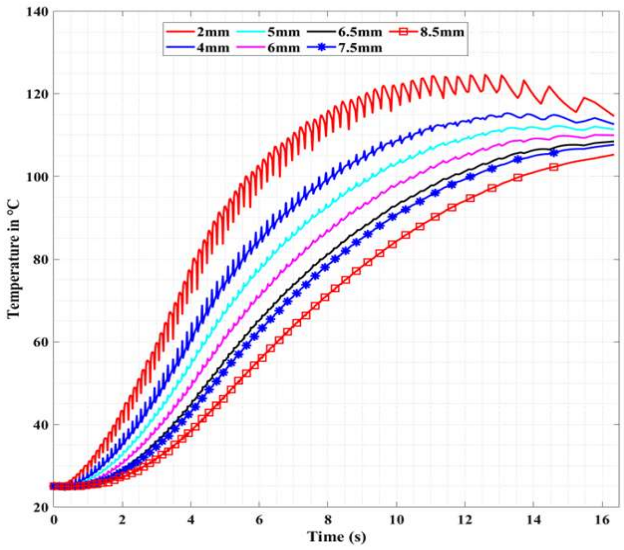

Figure 4.17 Temperature distribution along disc thickness by the NAMHS

4.7.5 Validation of the NAMHS temperature model

In addition to FE simulation, the disc brake has been investigated by analytical/mathematical model and dynamometer experimental test. The well-known analytical or mathematical method implemented in disc brake temperature and stress analysis has been Duhamel's principle [65][106][151][152] [65].

Besides, dynamometer experimental determination of disc brake failure analysis is believed to be reliable, although financially expensive and time-consuming. Two well-known setups have been utilized in temperature investigation: thermocouples and thermocameras. The former is applied to retrieve temperature at a specific location. According to UIC Code 541-3 standard, six thermocouples should be implemented at equidistant positions. The depth in which a thermocouple is embedded or buried beneath the friction surface of the disc or pads varies from 1 mm [86] to 2mm [43].

Meanwhile, the thermocamera is implemented to scan and report the friction surface temperature. It is installed near to friction surface where it can capture temperature local variations. It has been widely implemented in many investigations, including automotive disc brakes [43] [98] and railway tread braking [153] [154].

Experimentally (thermocouple) and analytically (Duhamel's principle) studied solid disc brakes by Fermér 1992 [152] is selected to validate the NAMHS model developed in this study (Figure 4.18.a). Three main reasons influenced the author, to select this study for validation. Firstly, the investigation was conducted by both analytical method and experimental

dynamometer test in parallel, both reported consistent. Secondly, both temperature and stress are determined in the study. Thirdly, all input parameters (geometry, material properties, braking conditions) are clearly documented, so that the method is easily repeated by other methods. Finally, the NAMHS model algorithm is applied to study solid disc brakes by Fermér 1992 [152].

All input experimental conditions or parameters (geometry, thermophysical material properties, braking times, braking powers) are extracted to APDL simulation from the investigation, and then the NAMHS model is implemented. The 35.431s analysis time is completed within 1249 load steps. The nodal temperature at a radial distance of 232mm, 2mm from the friction surface, and at a random circumferential location is displayed in Figure 4.18.b.

The transient temperature displayed in Figure 4.18.b is extracted at a radial distance of 232mm and 2mm deep from the friction surface. Experimentally (thermocouple) a maximum temperature of 215°C registered in Figure 4.18.b at 17.5s. At the same instant, the NAMHS model temperature prediction displays agreement with Fermér's experiment within a 5% variation (225°C). Though deviation from experiment and analytical is seen during early and late braking, the modeling showed an acceptable correlation. This deviation might seem due to the limited number of thermocouples (only three) used in experimental investigation, while six thermocouples are required according to UIC 541-3 [85].

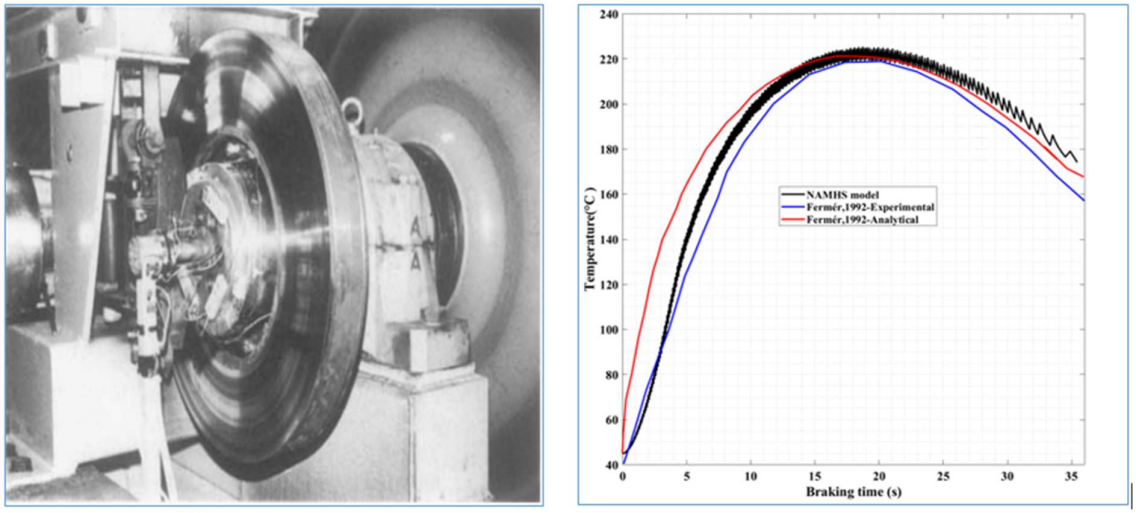

(a) (b)

Figure 4.18 (a) Model set up, (b) Model validation for axle load of 22.5 tonnes and braking from 130kph [152]

Similarly, the temperature at this particular point is obviously seen in Figure 4.19.b (2mm from surface and 232mm radial location). The scale of temperature is displayed around the entry to yellow color (221.498 °C), or the border depicted between the green and yellow colors. However, the maximum surface temperature is revealed 310°C at the outer surface of the disc. This is attributed to the radial increase of heat flux (Eq. 4.12.a). Temperature at this point couldn't identified by thermocouple, and requires thermocamera.

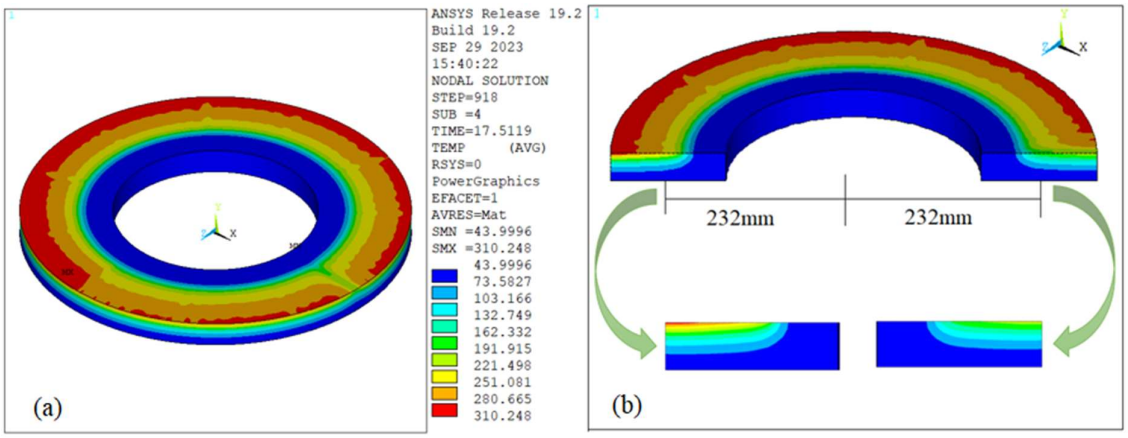

Figure 4.19 Maximum temperature at mid-braking time: (a) full disc, (b) along disc cross-section

When we come to thermocamer-based validation, it is advantageous, compared to thermocouples as it can scan and report friction surface temperature, where the crack could be initiated. The temperature at friction surface couldn't be reported by the thermocouples, since it has no setup location. Hence, it is required to validate the NAMHS model surface temperature, where maximum temperature is identified. To do so, an experimental study of temperatures and cracks conducted on automotive disc brakes by Le Gigan et al. 2015 [43] is selected. The reason behind the selection of this study is the same as the selection criteria aforementioned for Fermér 1992 [152].

The APDL simulation incorporates all the experimental conditions and parameters, including geometry, thermophysical material properties, braking times, and braking powers, extracted from the temperature and crack investigation. Subsequently, the NAMHS model is applied. The analysis for drag braking, which lasts for 45 seconds, is successfully accomplished within 1434 load steps. The maximum friction surface temperature predicted by the NAMHS model confirms thermocamera conducted Le Gigan et al. 2015 [43] temperature by 3% variation (Figure 4.20).

Although the maximum temperature registered by both methods seems to agree, the lower temperature predicted between the two is inconsistent (250°C and 25°C). This might be attributed to the disc geometry far from the friction surface, and where lower temperature was found (e.g. 25°C around the disc hub) was not incorporated in thermocouple results. However, At the junction of the friction surface and disc hub, 356.563°C is identified, which is very close to the thermocouple minimum temperature reported (350°C). Besides, the spatial temperature distribution predicted on the friction surface by thermocamera revealed six hotspots, meanwhile, the NAMHS model did not. This might be due to the lack of wear consideration in the NAMHS model.

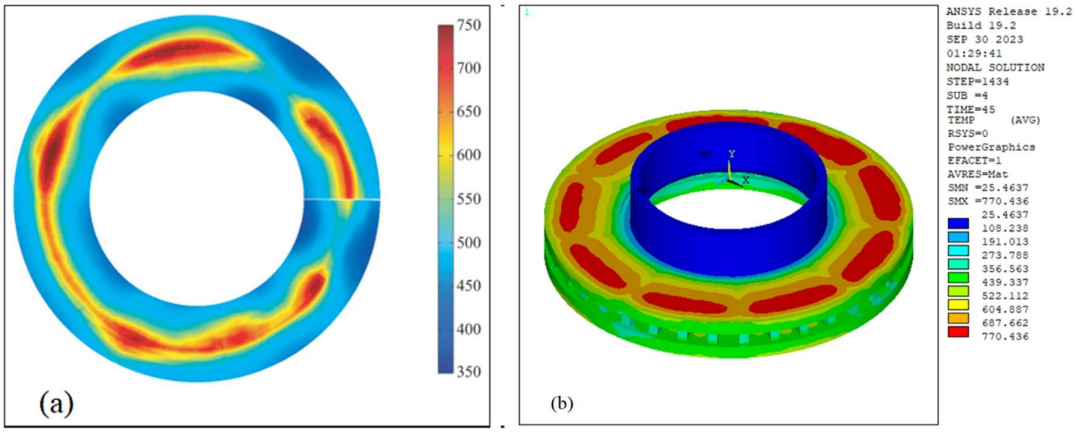

Figure 4.20 (a) Thermocamera result [43], (b) NAMHS result

Notwithstanding these limitations, the application of the NAMHS model in Fermér 1992 [152] and Le Gigan et al. 2015 [43] investigation of temperature revealed acceptable similarities with respective studies. Hence, it could conceivably be hypothesized that the extension of the NAMHS model in thermal stress and fatigue life determination could lead to a better failure prediction model.

4.8 Conclusions and Recommendations

Non-axisymmetrical moving heat source (NAMHS) is developed for disc brake temperature analysis, and its success is evaluated with traditional models, within feasible computational time. NAMHS model algorithm is successfully implemented the major factors affecting spatial temperature distributions, including friction surface exposed to convection and heat source, radial and circumferential heat flux variation, early braking hydraulic pressure, and pad groove effects. The main findings of the model are summarized below:

- The size and shape of the area in which heat flux applied is shown a remarkable effect on surface temperature variation
- Consideration of radial distance showed surface temperature variation as high as 10% and 60% in [31] and axisymmetric, respectively.
- Heat flux variation within pad cover angle, and partition of friction surface area to the heat source and convection in NAMHS resulted in maximum circumferential surface temperature variation as high as 49°C at mean radius on mid-braking time
- The consideration of the pad groove at the interface led to a 44°C difference in temperature within the pad cover angle.
- Temperature variation within the pad cover angle is shown as the maximum negative slope (-0.122°C/°), positive slope, and unnoticed slope at late, early, and mid-braking times, respectively.
- Reinforcement geometry around bolt holes contributed significant surface temperature variation
- The maximum temperature is shown the same for hub-bolted and friction surface-bolted disc brakes, except for its spatial distribution
- The effect of circumferential heat variation is more prevalent at the outer radius than at the inner radius
- Hydraulic pressure in early braking time dominates the effect of deceleration on the temperature within the pad cover angle.
- The model might predict close temperature with the axisymmetric model for high-speed trains

In the light of these remarkable findings, it would seem to provide convincing evidence for the capability of the NAMHS model algorithm in forecasting specific areas of high temperature, within acceptable computation time. Furthermore, its results shed new light on extending how to implement different pad groove sizes, layouts, and shapes. Consequently, our work has led us to conclude that the model could be applied quite reliably in estimating pad optimization, thermal stress, and fatigue life of disc brakes. But, the generalizability of this model is subject to certain limitations, including lack of wear, CFD convection, and experimental validation. Nevertheless, this study is the first step towards enhancing the observance of spatial and temporal thermal results on the friction surface of disc brake, with acceptable validation. Using the developed modeling, further research into disc brake fatigue life estimation is in progress by the authors. Although it is recommended for trains with low speeds with frequent stops (like

light rail transit), it could be implemented for any braking types (emergency or service), disc types (solid or ventilated), and pad types (sintered or composite). Hence, we hope that our findings could influence disc brake manufacturers, researchers, and maintenance personnel in disc brake damage investigations.

CHAPTER 5: FE STRUCTURAL MODELING OF NAMHS IN RAILWAY VEHICLES DISC BRAKE

5.1 INTRODUCTION

During thermal cycling, the thermal expansion and contraction are constrained by the nonuniform temperature distribution and its interaction with nearby components, leading to local stresses and inelastic strains. The effects of thermal stress on brakes might be of two different kinds [25]: i) bulk thermal effects (such as deformation known as coning) and ii) local effects (e.g. thermal cracks). Localized overheating and thermal stress in a brake disc can result in material structure changes, cracks, and other degradation that reduces its service life. Therefore, an accurate temperature, stress, and fatigue life estimation model is crucial in responding timely.

Numerous expensive and time-consuming dynamometer test techniques are necessary to guarantee the safe operation of brake discs throughout their fatigue lifetimes [9][76]. The issue is that this validation takes a long time and is quite expensive. Consequently, in recent years, there has been a demand for robust Finite element (FE) modeling that enables the determination of the disc brake stress and its lifetime. Although the FE approach is very practical, it requires comprehensive and realistic loading and material input (thermal, mechanical, and fatigue) [92]. Particularly, the quality of the FE modeling strongly depends on the reliability of heat input and boundary condition applications, and material constitutive models followed. According to Thomas et al. 2004 [41], an error of 10% in temperature leads usually to a factor of 2 on the fatigue life. Consequently, reliable temperature forecast modeling is mandatory for precise stress and fatigue life prediction.

In the previous chapter, the NAMHS model algorithm is shown effective in managing spatial variation of heat input and boundary condition application. And, in this chapter, it is required to extend the NAMHS model algorithm in investigating the stress and fatigue life of disc brake. The simulation is conducted for service braking of trailer bogie and emergency braking of the motor bogie, just to evaluate the effect of braking load/energy on stress evolution and service life. In parallel to this, the model is also implemented in comparative analysis of disc geometry selection, between original (friction surface-bolted) and modified (hub-bolted) disc designs.

The cylindrical coordinates system and the corresponding stress components definitions are displayed for circumferential stress (σ_θ), radial stress (σ_r) and axial stress (σ_z) in Figure 5.1. For the disc orientation observed in this dissertation (Cartesian Y axis is the axis of rotation, see

section 4.6.4), the corresponding stress components in result extractions are designated by S_X, S_Z, S_Y for circumferential stress (σ_θ), radial stress (σ_r) and axial stress (σ_z), respectively (section 5.7).

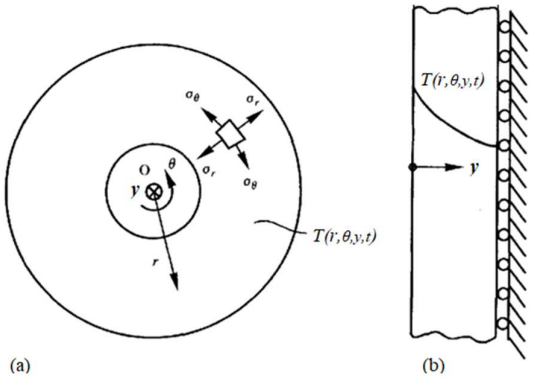

Figure 5.1 Stress components definition of disc brake (a) front, (b) side views [152]

5.2 FE Thermal-Mechanical Coupling Equation Formulation

When the temperature of one or more elements in the disc brakes is changed, then it tends to expand. However, this expansion is partially and fully constrained by the surrounding members along radial and circumferential directions, respectively. Eventually, thermal stresses develop. These constraining members are bolt holes (constrained in all directions) and tangentially closed disc geometry (constrained circumferentially). Relatively disc brakes are free to expand axially. The constraining members will also experience a force as a reaction to this constraint, which in turn, produces thermal stresses in the members. When the temperature is different from the reference temperature T_o, the linear relation between stresses and strains is determined from the thermoelastic stress-strain relations implemented in one dimension (Eq. 5.1). According to Eq. 5.1, the mechanical strain, which is the difference between the total strain ε_{tot} and the thermal strain ε_{th}, causes the stress and is proportional to it [155].

$$\sigma = E\left(\varepsilon_{tot} - \varepsilon_{th}\right) \ where$$
$$\varepsilon_{tot} = \frac{\Delta L}{L} \qquad 5.1$$
$$\varepsilon_{th} = \alpha_T \Delta T$$

In 3-D, the thermal stress components (σ_{ij}, i, j = r, θ, z) in the disk brake volume are evaluated from the solution to Navier's uncoupled thermoelasticity equations given in the cylindrical coordinate system in Eq. 5.2 [156].

$$\left(\lambda+2\mu^{'}\right)\frac{\partial e}{\partial r}-2\mu^{'}\left(\frac{1}{r}\frac{\partial \omega_z}{\partial \theta}-\frac{\partial \omega_\theta}{\partial z}\right)=\alpha_T\frac{\partial T}{\partial r}$$
$$\left(\lambda+2\mu^{'}\right)\frac{\partial e}{\partial \theta}-2\mu^{'}\left(\frac{\partial \omega_r}{\partial z}-\frac{\partial \omega_z}{\partial r}\right)=\alpha_T\frac{1}{r}\frac{\partial T}{\partial \theta} \qquad 5.2$$
$$\left(\lambda+2\mu^{'}\right)\frac{\partial e}{\partial z}-\frac{2\mu^{'}}{r}\left(\frac{\partial\left(r\omega_\theta\right)}{\partial r}-\frac{\partial \omega_r}{\partial \theta}\right)=\alpha_T\frac{\partial T}{\partial z}$$

Where,

$$e=\varepsilon_{rr}+\varepsilon_{\theta\theta}+\varepsilon_{zz}=\frac{\partial u_r}{\partial r}+\frac{u_r}{r}+\frac{1}{r}\frac{\partial u_\theta}{\partial \theta}+\frac{\partial u_z}{\partial r}$$
$$\omega_r=\frac{1}{2}\left(\frac{1}{r}\frac{\partial u_z}{\partial \theta}-\frac{\partial u_\theta}{\partial z}\right)$$
$$\omega_\theta=\frac{1}{2}\left(\frac{\partial u_r}{\partial z}-\frac{\partial u_z}{\partial r}\right)$$
$$\omega_z=\frac{1}{2}\left(\frac{\partial\left(ru_\theta\right)}{\partial r}-\frac{\partial u_r}{\partial \theta}\right) \qquad 5.3$$
$$\lambda=\frac{\nu E}{\left(1+\nu\right)\left(1-2\nu\right)}$$
$$\mu^{'}=\frac{E}{2\left(1+\nu\right)}$$
$$\alpha_T=\frac{\alpha E}{1-2\nu}$$

A solution to a system of partial differential equations of quasi-static thermoelasticity above (Eq. 5.2 and Eq. 5.3) has been solved for the structural homogeneous boundary conditions using the finite element method, presented in Eq. 5.4:

$$\boldsymbol{\sigma}=\mathbf{DBu}-\mathbf{D}\boldsymbol{\varepsilon}_{\mathbf{th}} \qquad 5.4$$

Where

$$\mathbf{D}=\frac{\lambda}{a}\begin{bmatrix}1 & a & a & 0 & 0 & 0\\ a & 1 & a & 0 & 0 & 0\\ a & a & 1 & 0 & 0 & 0\\ 0 & 0 & 0 & b & 0 & 0\\ 0 & 0 & 0 & 0 & b & 0\\ 0 & 0 & 0 & 0 & 0 & b\end{bmatrix}\quad \mathbf{B}=\begin{bmatrix}\frac{\partial}{\partial r} & 0 & 0\\ 0 & \frac{\partial}{\partial z} & 0\\ \frac{1}{r} & 0 & \frac{1}{r}\frac{\partial}{\partial \theta}\\ \frac{\partial}{\partial z} & \frac{\partial}{\partial r} & 0\\ \frac{1}{r}\frac{\partial}{\partial \theta} & 0 & \frac{\partial}{\partial z}\\ \frac{1}{r}\frac{\partial}{\partial \theta} & 0 & \frac{\partial}{\partial r}-\frac{1}{r}\end{bmatrix} \qquad 5.5$$

$$\boldsymbol{\sigma}=\left[\sigma_r\ \sigma_\theta\ \sigma_z\ \sigma_{r\theta}\ \sigma_{rz}\ \sigma_{\theta z}\right]^{\mathbf{T}}\quad \mathbf{u}=\left[u_r\ u_\theta\ u_z\right]^{\mathbf{T}}\quad \boldsymbol{\varepsilon}_{\mathbf{T}}=\alpha_T T\left[1\ 1\ 1\ 0\ 0\ 0\right]^T$$

and

$$a=\frac{\nu}{1-\nu}\qquad b=\frac{1-2\nu}{2(1-\nu)}$$

5.3 Braking Conditions and Disc Specification

AALRT has two crossing routes: North to the South and East to the West (Figure 4.2). East to West route has a 17.9km distance and 21 stations ranging from 0.554km (between Road Authority to Mexico Square) to 1.149km (between Coca-Cola to Tor Hailoch). Hence, to take similar braking condition parameters, the average distance between stations is taken, which is 0.852km (Table 4.1). To create a heating and cooling period for thermal stress, this distance is further classified into three driving conditions: braking distance from previous constant speed driving, accelerating distance after stopping at the station, and constant speed driving distance up to second braking time. Their corresponding time is also displayed in Table 5.1-Table 5.2. This classification of time and distance traveled is conducted based on train kinematic parameters: service brake deceleration of 1.1m/s^2, emergency brake deceleration of 2.2m/s^2 and acceleration of 0.75m/s^2 for both braking conditions (extracted from AALRT technical manual [32]). Then the equivalent braking time and braking distance are calculated from kinematic empirical equations described in Eq. 5.6-5.7 for deceleration and acceleration parts. A constant speed driving distance is obtained by subtracting the summation of decelerating and accelerating distances from the averaged total distance (0.852 km). For constant speed driving (a=0), Equation 5.7 is modified, to calculate constant speed distance and time. Besides, train stopping time varies from station to station, based on the number of passengers getting on or out. Hence, the average value is taken as 4min and 2min for service and emergency braking, respectively.

$$t_b = \frac{v_o - u_o}{a} \quad 5.6$$

$$S = v_o t_b - \frac{1}{2} a t_b^2 \quad 5.7$$

Table 5.1 Braking conditions for fatigue life analysis [source: AALRT technical manual [32]]

Braking Type	Deceleration (m/s2)	Acceleration (m/s2)	Max. speed (kph)	Braking time (s)	Braking distance (m)	stopping time (s)
Service	1.1	0.75	65	16.41	148.18	240.00
Emergency	2.2	0.75	65	8.21	74.09	120.00

Other input parameters are extracted from the previous thermal investigation on non-axisymmetric modeling of moving heat sources for the spatial and temporal investigation of temperature in railway vehicles' disc brakes (Chapter 4). These include train specifications (axle load, number of bogie and disc on each bogie), disc geometric parameters (dimensions (Table 4.2)), materials (Table 4.3), heat input calculations (Eq. 4.11-4.12.a), convective heat dissipation empirical calculations (Eq. 4.17-Eq. 4.21), braking conditions (initial speed, deceleration, and braking time (Table 4.2)), and finite element formulation (mesh and element type (Figure 4.6)).

Table 5.2 Calculated braking conditions by kinematic empirical equations source: [source: AALRT technical manual [32]]

Braking Type	Accelerating time (s)	Accelerating distance (m)	Constant speed distance (m)	Constant speed time (s)	Total distance (m)	Total time (s)
Service	24.07	217.34	486.48	26.94	852.00	307.43
Emergency	24.07	217.34	560.57	31.05	852.00	183.33

AALRT train is made up of three cars per train with an M-T-M configuration (Figure 4.4). Each car is supported by one bogie, receiving 33.33% of the total mass of 66220kg [32]. Each motor bogie has two discs (one per axle), and a trailer bogie has four discs (two discs per axle). Since the motor bogie is occupied by traction equipment (motor and its transmission) there is no more space for the additional number of disc brakes. Hence, when emergency braking is applied in the absence of dynamic braking, substantial braking energy is absorbed by the motor bogie disc, compared to the trailer bogie disc. Therefore, to investigate the effect of braking energy on disc brake life, a mass of 11037kg and a deceleration rate of 2.2m/s^2 are implemented for the motor bogie (Eq. 4.10). For service braking, however, no input parameter is changed

for thermal analysis (the same input parameters as Chapter 4), except for the addition of cooling period boundary conditions presented in Table 5.1-2.

Besides, structural analysis (thermal stress and fatigue life determination) is the better method for disc geometry comparison, between hub-bolted and friction surface-bolted design. Because, thermal analysis conducted in Chapter 4 revealed similar maximum temperatures. Eventually, in addition to developing the NAMHS structural model, its application in selecting comparative analysis of geometry is also examined for identical input parameters and braking conditions.

5.4 Finite Element Modeling

For both types of braking conditions and disc geometries, material kinematic modeling, mechanical properties, and structural boundary conditions are the newly added modeling in NAMHS structural modeling, in which stress and fatigue analysis is conducted.

5.4.1 Linear and non-linear material modeling

Table 5.3 Lammelar cast iron EN-GJL-250 kinematic parameters [157][98][93][158]

Porosity parameters						Gurson coefficients		
f_F	f_c	f_o	σ_N(Mpa)	S_N(Mpa)	f_N	q_1	q_2	q_3
1	1	0.125	-30	50	0.25	1.5	1	2.25

The accuracy of fatigue life prediction does not solely depend on FE model type, but material non-linearity (kinematic) is also another factor. The kinematic type selection is material-specific. Gurson-Tvergaard-Needleman (GTN) material model has been shown to handle the behavior of cast iron materials (asymmetric stress-strain hysteresis) in many cast iron material structural studies and is selected in this investigation [157][98][93][158].

Table 5.4 Tensile and compressive properties of EN-GJL-250 material [92]

Temp (°C)	Young's modulus, E (Gpa)		Yield strength, σ_y (Mpa)		Ultimate stress, σ_u (Mpa)	
	Tensile	Compressive	Tensile	Compressive	Tensile	Compressive
RT	104	109	244	411	284	>578
500	84	88	182	305	228	>441
600	77	86	133	206	158	>287

Although it is the first to be applied in a railway disc brake, to the best of the author's knowledge, it was seen as fruitful in automotive disc brakes [97][98][93] and engine cylinder blocks [159][160]. The full presentation of the model is defined by six plasticity parameters

[157], and three Gurson coefficients [158]. About nine parameters are reported in Table 5.3 for the flake type of cast iron materials used for disc brakes. Besides, temperature-dependent linear mechanical material properties are extracted from the work of Pevec et al. 2014 [92], and displayed in Table 5.4 for the flake-type cast iron (EN-GJL-250).

5.4.2 Thermomechanical boundary conditions

Thermal boundary condition calculations and applications are retrieved from Figure 4.10 of previous Chapter 4 for both braking types. Beyond braking time, additional cooling time and corresponding boundary condition (convection) are computed from speed variations due to accelerating time on startup and constant speed driving time up to the next braking. The position of boundary conditions however remains the same, except that heat flux is completely removed from the friction surface and substituted by heat-dissipating convection. For accelerating and constant speed driving, the same empirical equation in Eq.4.23- Eq.4.27 is used to calculate convective coefficients at friction surface and fin areas. For stopping time, however, constant convection coefficients of 10 $W/m^{2o}C$ and 9 $W/m^{2o}C$ are taken from late braking time, and applied on friction surface and vane areas, respectively [161].

Bolted areas and internal radius area displacements along x,y, and z directions are constrained degrees of freedom, or taken as zero $\left(u_x, u_y, u_z = 0\right)$ for original disc geometry (Figure 5.2. a). And, its backside (fin areas) are constrained only along the y direction $\left(u_y = 0\right)$. For modified geometry (hub-bolted), in contrast, the back side of the heat-dissipating fins and its internal areas are constrained in all directions $\left(u_x, u_y, u_z = 0\right)$, due to axial symmetry and its firm attachment to the axle by bolts, respectively (Figure 5.2. b). The interior radius of the disc mates with the axle through bolts [Figure 3.3.c]. But for the separate analysis of the disc, the bolt holes and axle are excluded, because the temperature and its consequences (thermal stress) are insignificant as we move far from the friction surface [6][30][86]. Hence, for both types of disc geometry, zero displacements are applied in all directions $\left(u_x, u_y, u_z = 0\right)$ at the interior radius of the disc.

5.5 Mechanism-Based Fatigue Life Prediction (D_{TMF}) for Cast Iron Materials

For both maintenance and safety, it is essential to anticipate the fatigue life of mechanical components that experience cyclic thermal loads. A wide range of damage models are offered in the scientific literature, with various levels of complexity and life prediction capability. Unfortunately, a well-accepted framework for the prediction of fatigue life has been elusive

[162]. Whatever model it might be, a damage model must meet three essential criteria, which are crucial from an industrial perspective: simple formulation (which permits an easy implementation), fewer number of estimated parameters, and good prediction capabilities [163].

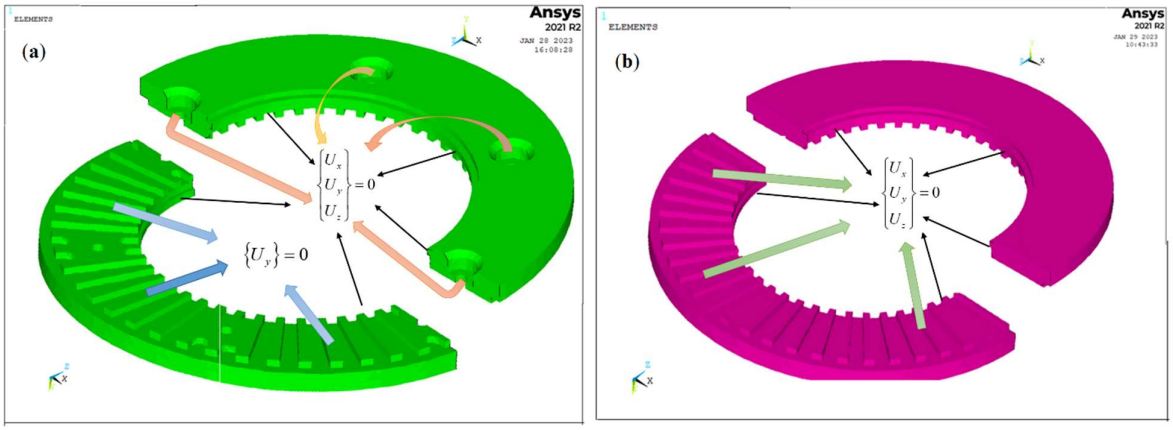

Figure 5.2 Structural boundary condition

In their investigation of methods for metal fatigue life prediction, Santecchia et al. 2016 [164] reported the key drawbacks of the Miner and Palmgren method as lack of sequential effects, residual stress effects, and threshold effects. Moreover, the application of the strain energy density method in extreme environments of disc brake has not been observed, to the best of the author's knowledge. And, no clear method was developed in the calculation of strain energy from the FE stress-strain hysteresis loop. Besides, Paris' law type of life prediction was mostly implemented into finite element life prediction of engine cylinder by ABAQUS [159] [165], and once in disc brake [93]. Nonetheless, Paris' law does not account for mean-stress effects on crack growth as stated in its original form.

In contrast, Seifert and Riedel 2010 [166] as well as Metzger, Knappe, and Seifert 2011 [159], criticized the strain-based fatigue life predictions of CMB (Coffin Manson Basquin) and SWT (Smith-Watson-Topper) approach. First, the model contains a relatively large number of material parameters whose determination is a non-trivial task and purely phenomenological. Furthermore, the higher strain amplitudes raised due to the constrained thermal strains in the applications of the disc brake and combustion engines result in early life nucleation of the cracks. Therefore, the authors argued that the lifetime limiting mechanism should be the growth of these cracks instead of their initiation. Based on these shortcomings, they preferred a mechanism-based fatigue life prediction. In addition, according to [167] [160] [159], because of cast iron microstructure (graphite precipitations in steel matrix), cast iron materials have

several cracks from the beginning (virgin material). Therefore, it is appropriate to interpret the estimated cycles to failure as the growth and coalescence of these originally smaller cracks as the lifetime limiting factor. As a result, these limited our selection of fatigue life prediction method to Mechanism-based D_{TMF}.

A Mechanism-Based Model for LCF model assumes that crack growth is the lifetime limiting mechanism and that the crack advance in a loading cycle da/dN correlates with the cyclic crack-tip opening displacement ΔCTOD [93]. The crack growth law for this model, here denoted the 'D_{TMF} model', is expressed as in life prediction (Eq. 5.8-5.11)of disc brake made from flake cast iron material [93]. But mostly this type of prediction was implemented into finite element life prediction of engine cylinders in ABAQUS [159] [165]. It is presented in Eq. 5.8, where A and B are parameters to be adjusted to experiments. A and B parameters for several types of cast iron materials were reported 2.71 and 1 in [166] at room temperature, respectively. Similar results were also identified for flake cast iron at 300°C and 600°C for the isothermal material test [93].

$$N_f = \frac{A}{\left(D_{TMF}\right)^B} \tag{5.8}$$

$$D_{TMF} = \frac{Z_D}{\sigma_Y} F(t, \sigma, T) \tag{5.9}$$

$$Z_D = 1.45 \frac{\Delta\sigma_{eff}^2}{E} + \frac{2.5 \Delta\sigma \Delta\varepsilon^p}{\sqrt{1+3N_r}} \tag{5.10}$$

$$\Delta\sigma_{eff} = 3.72 \frac{\Delta\sigma}{\left(3-R\right)^{1.74}} \tag{5.11}$$

Where, $R_r = \frac{\sigma_{\min}}{\sigma_{\max}}$ and $\Delta\sigma = \sigma_{\max} - \sigma_{\min}$

σ_Y is the cyclic yield stress defined as the 0.2%-offset stress with respect to the point of load reversal. Z_D is related to the cyclic J integral, and can be calculated from characteristic quantities of the stress-strain hysteresis loop. E is Young's modulus. $\Delta\sigma, \Delta\varepsilon$ are the range of the stress and the viscoplastic strain of saturated stress-strain hysteresis loops. N_r is the Ramberg-Osgood hardening exponent. R_r is the ratio of minimal stress in a loading. $F(t, \sigma, T) = 1$ for cast iron material [93], where, t is time history, σ is stress and T is temperature

5.6 Applications of the NAMHS Model Algorithm in Stress Analysis

The full modeling of thermal analysis (braking and cooling) and structural analysis consists of five blocks of information flows: pre-analysis (in which parameters and arrays are defined), braking time thermal analysis, cooling time thermal analysis (stopping, accelerating, and constant speed drive), structural analysis and fatigue life prediction. The first two of these models were discussed in previous chapter (Figure 4.8), in which heat flux was varied spatially from θ_i to θ_{i+1} (i=1-n) and temporally from t_i to t_{i+1} (i=1-n). The remaining three blocks and the result database of the braking time thermal analysis are presented in Figure 5.3. In the current NAMHS modeling, cooling time thermal analysis is conducted. Besides, the model is further developed to carry out structural analysis for the whole time (braking and cooling times). As the total braking time was subdivided into 548 for service braking of the trailer bogie (section 4.6.3), the total braking time of 8.21sec is split into 274 load steps for emergency braking of the motor bogie.

In the cooling thermal analysis case, however, heat flux is completely removed from the friction surface. And, a timely varying convective heat dissipation coefficients $h_s(t_c)$ and $h_f(t_c)$ are applied on friction surface and in fin areas, respectively from ANSYS parameters and arrays, where c varies from 1 to the total number of substeps *(r)* within cooling time thermal analysis. Thermal results from the last load step of braking time analysis (T_n), are imported as the initial condition of cooling time thermal analysis, for all nodes (right side red line in the model). Finally, cooling thermal analysis is solved within one load step having 291sec and 183 sec for service and emergency braking, respectively. This total cooling time of the simulation consists of stopping, accelerating, and constant speed driving time (Table 5.1-2). This load step is further subdivided into r=145 and 91 substeps at which results are saved in the thermal results database (black line in the model) for service and emergency braking, respectively. Once the thermal analysis is completed, we will have a nodal temperature, for each node and at each braking time increment *(t_i* and *t_c),* resulting total time of thermal analysis t_v ($t_v = t_n + t_r$). These results are stored in the ANSYS thermal results database for later structural analysis. Now thermal result database is occupied by the whole simulation times t_v.

Finally, structural analysis is started by reusing the thermal FE model (meshed geometry with material property) and removing all thermal boundary conditions. And then the element type is automatically changed to a structurally fit element type (SOLID186). This is the first preparation for structural analysis and is executed by FORTRAN commands. Finally, structural boundary conditions and material properties are implemented. These conditions should be

completed before the start of importing temperature in thermal analysis into structural analysis at each t_k. SOLID186 is a higher-order 20-node 3-D solid element that displays behavior with quadratic displacement. The element consists of 20 nodes, each of which has three degrees of freedom: translations in the nodal x, y, and z directions. Plasticity, hyperelasticity, creep, stress stiffening, large deflection, and big strain capabilities are supported by the element.

Next, another APDL FORTRAN program is developed, which successfully exports nodal temperature T_k (where k varies from 1 *to v, v* is the summation of n and r) in thermal analysis into the structural simulation at each time increment of t_k. The imported results serve as an initial condition for each node at each time step t_k (vertical red line in the model on Figure 5.3). Finally, the reference temperature (24°C) is added for every solution. Once, all these conditions and requirements are fulfilled, the modeling is ready for the first solution time (k=1, the first load step in structural analysis). Subsequently, nodal stress (σ_k) and strain (ε_k^p) are calculated and stored for each node at each time increment t_k, in a separate structural database. And this cycle is repeated for each time increment until the simulation time is completed (t_k=t_v). The model is executed using APDL parameters, including scalars and arrays, which are similar to FORTRAN written commands (listed in Appendix A).

After completion of the structural analysis for the whole braking time, it is imaginable to estimate fatigue life for any node located in any direction. Because every node's stress and strain reside in the structural results database, from which the appropriate prediction method is selected and applied (D_{TMF}). A simple flow chart of brake disc fatigue life is provided, next to structural analysis (Figure 5.3). Life prediction analysis starts by identifying stress amplitude ($\Delta\sigma$) and stress ratio (R). Then the sequence of operation continues from equation 5.11, and ends in equation 5.8.

In total, three temperature and stress loading cycles are computed to reach a stabilized stress-strain hysteresis, whereas the third is used for the lifetime prediction, in both braking types. This is a reasonable assumption, as it was also assumed in life computation in other disc brakes [98] and cast iron material engine cylinder heads [165][160][159]. Each thermal cycle consists of the heating period and cooling period: stopping time at the station, acceleration period, and constant speed period.

The main advantage of the NAMHS model is its flexibility to different variations, because, the model is developed by APDL ANSYS commands. It is flexible to variations in disc dimensions (radius, thickness), disc geometry types (hub-bolted, friction surface-bolted, solid, ventilated),

pad geometry types (sintered, composite, groove numbers), material property types (steel, cast iron) and braking conditions (service, emergency, drag brakings).

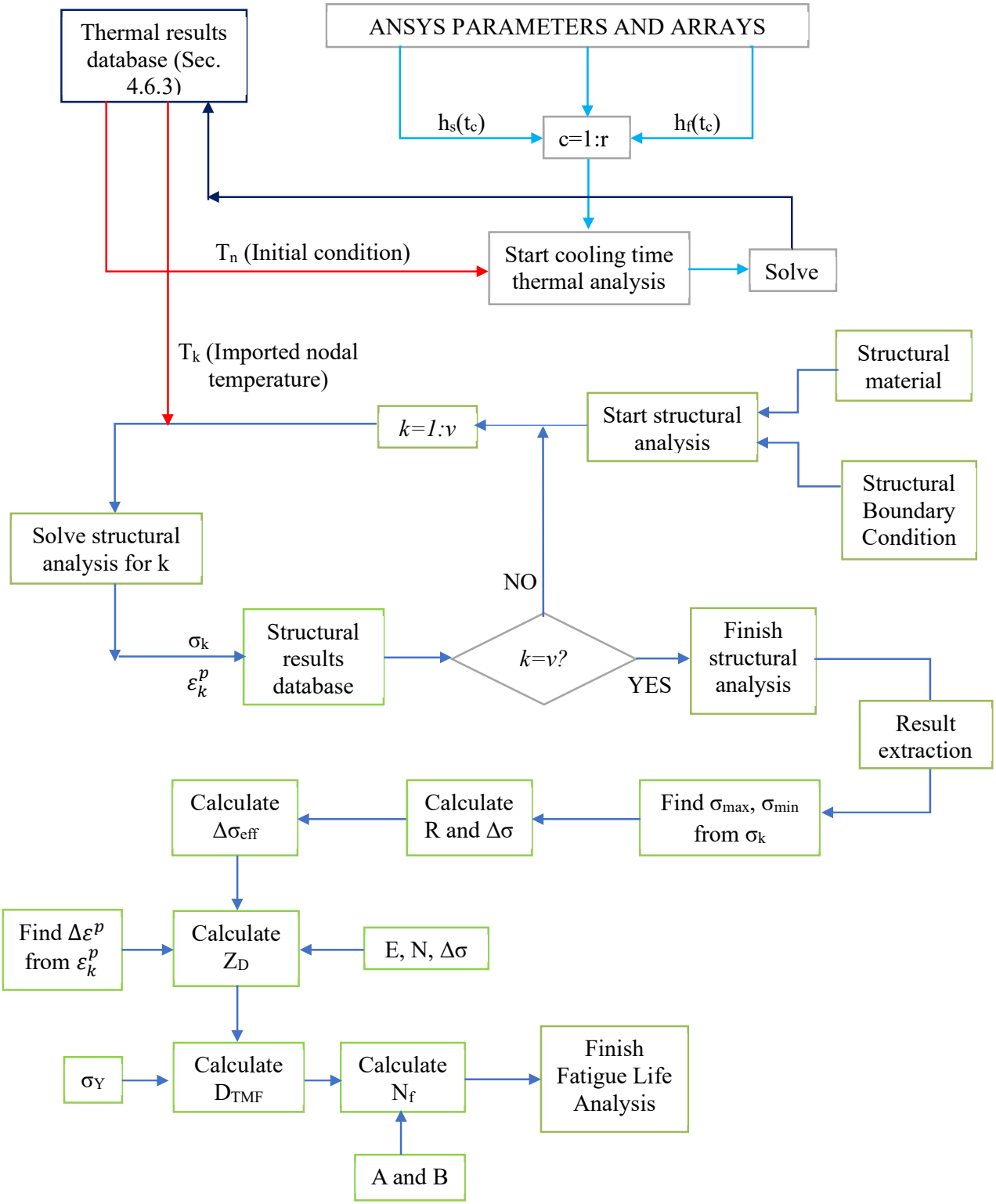

Figure 5.3 NAMHS model algorithm flow chart for thermomechanical analysis

This is possible through redefining commands of arrays and parameters written in Microsoft Word, Notepad, or any other software. Then, copying the commands (from Microsoft Word) and pasting them in ANSYS, or reading the command files (from Notepad) in ANSYS completes the simulations. Any user who is not familiar with the ANSYS software can easily utilize the model developed here, once the parameters and arrays are defined. These arguments are witnessed by disc geometries simulated in this study: hub and friction surface-bolted, solid disc brake in validation (Figure 5.10) and drag braking in validation (Figure 4.20.b)

5.7 Result and Discussion

One of the main goals of this investigation is to attempt the NAMHS model algorithm stress and fatigue evaluation. Besides, the effect of braking energy is studied by varying braking types (service brake of trailer bogie and emergency brake of motor bogie). Moreover, comparative analysis of disc geometry investigation is performed between friction surface-bolted (original) and modified designs. And fatigue life is presented for emergency braking on friction surface-bolted disc only.

5.7.1 Transient temperature, stress, strain, and hysteresis loop analysis

For the stress result presentation, the global coordinate axis is defined based on disc geometry: y is axial, x is circumferential, and z is the radial direction of the geometry. For different orientations, if z is axial, x and y could be radial and circumferential directions, respectively [7]. Whatever the orientation the disc might have, it is immaterial in the results reported. In this subsection, transient temperature, stress, strain trends and stress-strain hysteresis loops are presented.

Temperature and stress simulation is performed for three consecutive stations. The pattern of temperature and stress at any station is displayed in three paths (Figure 5.4.a,c). First, a sharp increase and fall in temperature and stress amplitude are observed in the initial and final stages of braking time, respectively. This is due to the drop and rise of heat flux and the convection-conduction effects with time, respectively. And secondly, both temperature and stress are seen steadily declined, owing to the train's stationary position. Finally, both are shown a steep drop at the end of the cooling time. This is linked to the higher convective convection at the train's acceleration and constant speed motion, compared to its stationary position. Von Mise stress also displayed the same trends as temperature (Figure 5.4.c). As the number of stations increases, the rise in temperature and stress is undeniable, since a random station's temperature

is taken as the initial condition for the next station. For the service braking, temperature fluctuation is shown to vary between 58°C and 170°C.

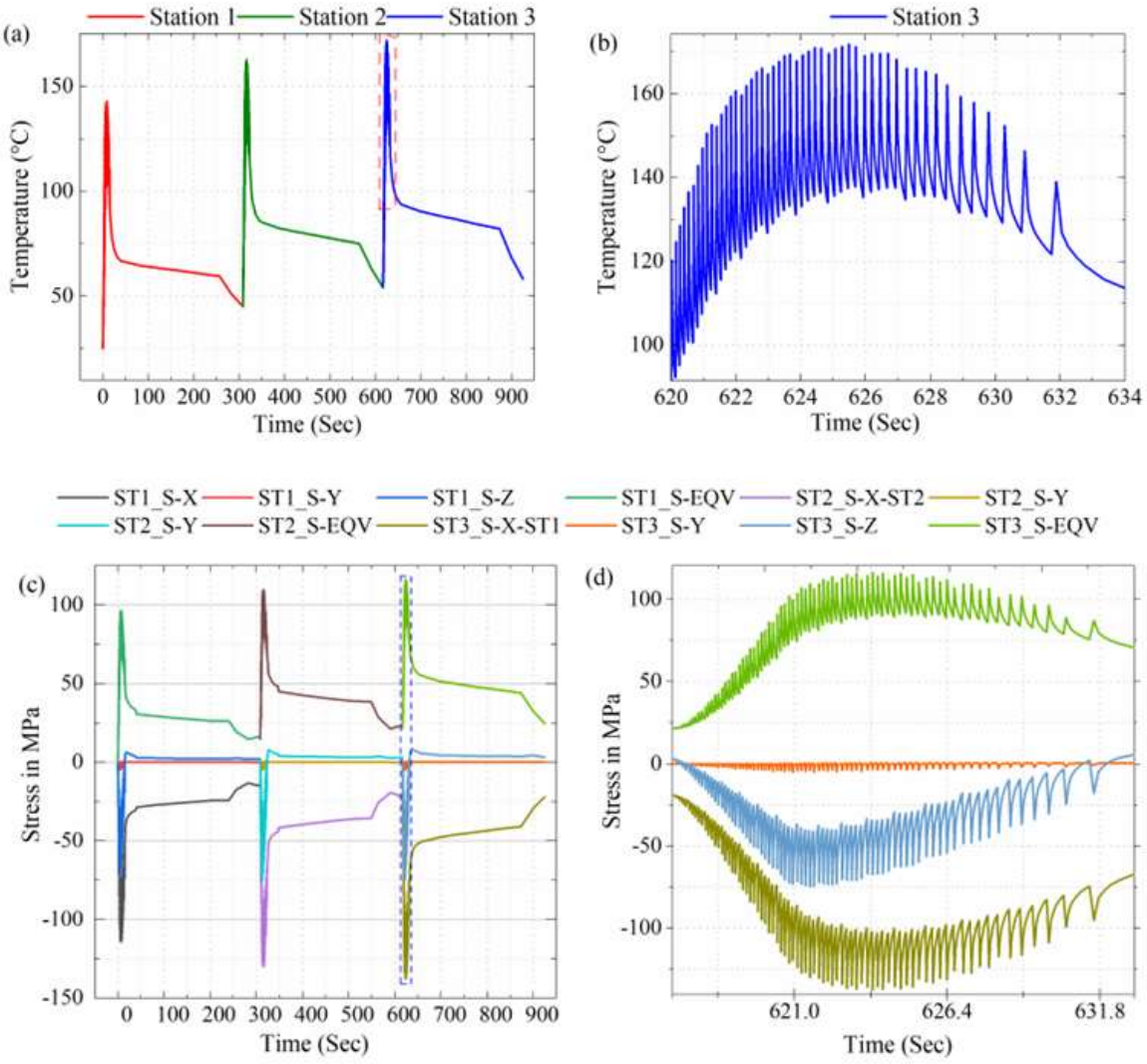

Figure 5.4 Station 1-3 original disc's friction surface (Rm,90°) transient (a) temperature and (c) stress and their enlarged plot for station 3 (b,d) service braking

One remarkable result that emerges from the NAMHS heat application is the oscillation or zigzagged behavior (peak and valley) of the stress profile (Figure 5.4.d). It is the consequence of high heat flux during pad-disc contact time (peak point) and exposure of the same point to the conduction and convective heat dissipation for the remaining time (valley), when the pad is displaced to the next position [168]. The cumulative number of peaks or valleys is equivalent to the total number of disc revolutions, as it fluctuates once within one rotation (360°). This is the evidence suggesting the NAMHS model's convenience in resolving spatial tangential

variation of stress components, compared to axisymmetric modeling. Besides, the fluctuation of stress with time supports the postulate that NAMHS model stress calculation avoids overprediction seen in axisymmetric stress prediction. The conservative fatigue life prediction reported by the axisymmetric model in the study of Gigan et al. 2019 [93], confirmed this speculation. Eventually, The NAMHS model algorithm outlined here promises insight into a more reliable estimate of fatigue life estimates contrary to axisymmetric modeling.

In addition, the periodic frequency of zigzag repetition (saw-toothed) is portrayed as condensed at early braking and significantly relaxed at late braking (Figure 5.4.b,d). And, the time between the two oscillations seen rises near the end of the braking. This is obviously displayed by the compacted (dense) distance between two consecutive peaks or valleys at early braking, and relatively 'far' away at the ends of braking. It is due to the fact that, more time is consumed by heat sources to complete one revolution at late braking time than early braking, because of train deceleration.

Periodic saw-toothed stress outlines reported by uncoupled thermomechanical [7] and coupled thermomechanical models [71] provide support for this investigation. Contrarily, this outcome contradicts that of Lu et al., 2021 [95] who found negligible differences between axisymmetric and rotating thermal loading and coupled thermomechanical model of temperature, strain, and stress. Their corresponding stress variations from rotating heat sources were reported −1.8%1 and -5.1% for the axisymmetric and coupled thermomechanical models, respectively. This might seem due to inappropriate thermal boundary condition application since saw-toothed stress outlines were seen as missing. Nonetheless, uncoupled thermomechanical modeling has very limited application in examining stress spatial variation, according to the review of the literature in [26]. This might seem due to computational limitations linked to convergence, simulation time, and computer capacity in examining temperature, pressure, and stress. Moreover, although somewhat published works of literature were seen in coupled thermomechanical stress simulations, the problems seen in uncoupled modeling remained as it is [31].

Similarly, Pan and Cai 2018 [31] conducted stress calculation comparisons between other traditional models including axisymmetric, coupled thermomechanical, and moving heat sources. The authors highlighted almost similar results, except for the convergence problem and simulation time explosions in coupled thermomechanical modeling. Besides, they concluded axisymmetric model cannot precisely simulate the actual rotation of the heat source.

This unexpected finding might be enlightened by the absence of convective heat dissipation on the friction surface free from heat flux. Besides, the contribution of convection on other surfaces appeared insignificant, due to low braking time. Furthermore, the moving heat source's trends of transient thermal stress (saw-toothed) lack uniformity and regularity as in NAMHS. Motivated by this problem, this investigation attempted to propose a better model that can provide a more reliable estimate.

According to this demonstration, we can infer that the state of stress development follows the footsteps of temperature evolution, which is better modeled by NAMHS compared with other traditional models [168]. And, this inference is consistent with that of Kim et al. 2010 [96] who found a linear relationship between temperature and stress. Although stress is not simulated by other traditional models in this study, the model described here enables a more comprehensive estimate of stress temporal variation, which could not be seen in the axisymmetric or other traditional models. Furthermore, though this finding is limited to deceleration-type braking, it could be easily implemented in drag-type braking, in which uniform stress frequency is expected.

Turning now to the stress components at mean radius, Figure 5.4.d the maximum friction surface compressive stress of 138MPa, 75Mpa, and 0 are illustrated, along circumferential (S-X), radial (S-Z), and axial directions (S-Y), respectively for the third station. The minimum axial stress might seem due to the free expansion of the friction surface in the axial direction, meanwhile, high circumferential compressive stress is attributed to the tangentially closed shape of the disc. A sharp increase of compressive radial and circumferential stress is presented, with the rise of braking time. At the late braking time and cooling period, a steady recovery of stress is displayed in reversing the compression trend.

The observation of higher circumferential stress is consistent with the experimental demonstration of other studies on fatigue crack initiation and propagation [9][76]. Due to its superiority in the tangential direction, the crack was reported to propagate in the radial direction, which could be confirmed plastic strain in an emergency type of braking (Figure 5.5.a). Hence, it is intriguing to speculate that circumferential stress could play a remarkable role in crack initiation and propagation. And this implication is analogous to the works of [96][19][97][42], where only the circumferential stress component was involved in fatigue life estimation.

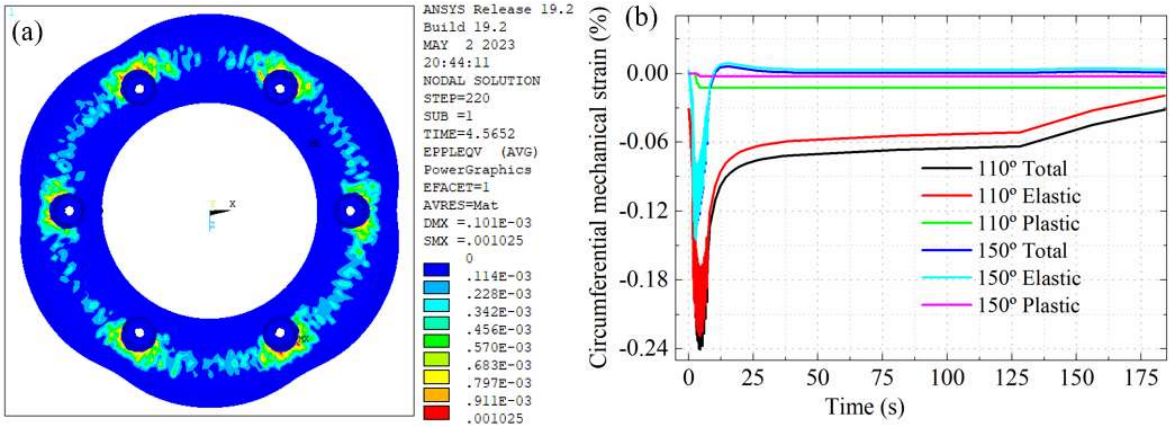

Figure 5.5 Emergency braking of motor bogie (original disc geometry): (a) plastic von Mise strain and (b) circumferential strain for selected positions on mean radius

The other most obvious finding to emerge from this result is that the residual tensile stress is never achieved at the end of the cooling time (Figure 5.4). This unexpected finding could be attributed to the selected braking parameters: convection coefficient and low cooling time. Due to these reasons, the temperature of the disk is not seen to cool down to the level required for a transition to tensile stress. This report is in accordance with the previous investigation that examined stress and thermal fatigue fracture by thermomechanical coupling [7]. Besides, [9] presented that the value of the circumferential stress curves is always negative during routine or service braking action from beginning to end. Meanwhile, tensile stress was reported in emergency braking. Nonetheless, these results need to be interpreted with caution. Because, if convection and cooling time is raised further, the occurrence of tensile stress is undeniable. This explanation seems true when it is interpreted by the study of Li et al. 2014 [76] who reported residual tensile stress within the cooling time from 500 sec to 5000 sec. Besides, Dufrénoy, Bodovillé, and Degallaix 2002 [28] reported residual tensile stress as high as 790MPa after a cooling time of 1200 sec. This observation may support the hypothesis that the nature of stress behavior is influenced by breaking input parameters.

Moreover, von Mise stress is revealed 116Mpa, which is below half the yield limit of the material, resulting in no permanent deformation of the material (Figure 5.4.c-d). This is undeniable since the selected input braking parameters are design parameters (for safe braking operation). Hence, this deduces the absence of plastic strain development, throughout the braking time for the trailer bogie of the service brake.

In contrast, permanent deformation presented in plastic von Mises strain and circumferential mechanical strain is displayed for emergency braking of motor bogie (Figure 5.5). Besides,

elastic and plastic strain at mean radius for station 3 is compared for two tangential points: 110^{o} and 150^{o} in (Figure 5.5. b). What is interesting about the comparisons in this figure is that plastic strain remains constant, despite variations in elastic and total strains, followed by braking conditions. This discrepancy could be attributed to two reasons. Firstly, once the plastic strain is registered at the specific node, it can't regain its initial position (deformed permanently). Secondly, plastic strain occurs only up to two-thirds of braking time. Beyond this time no additional thermal load could rise plastic strain further, due to convective heat dissipation. Eventually, maximum plastic strain is revealed 0.0123% and 0.0026% at 110^{o} and 150^{o}, respectively. Unlike stress in the hub-bolted disc (Figure 5.8.b-d), the trace of the pad is not noticed for the plastic strain on the heating area. Maximum plastic strain is illustrated on the outer side of bolt holes, which is explained by constrained structural boundary conditions. The von Mise strain reported above suggests that the NAMHS model algorithm could provide convincing evidence of where a crack could be initiated and the direction in which it could propagate.

The effect of braking energy is observed by plastic strain development (permanent deformation), mainly associated with two parameters. Firstly, the braked mass per disc in the motor bogie is twice in the trailer bogie (Eq. 4.9 & Eq. 4.10). Secondly, braking time in emergency case is half the service brake, resulting in reduced conduction and convection time for emergency case. These contribute to the rise in temperature and stress, finally leading to permanent deformation. An implication of this result suggests the possibility of damage in motor bogie discs, compared to trailer bogie-mounted discs. Particularly, whenever dynamic brakes fail or the emergency brake is applied, discs on the motor bogie are vulnerable to failure. This finding will help us to develop a bogie that has enough space for accommodating enough discs per axle.

For the study of a cyclic loading analysis, the stresses and the total mechanical strains (elastic and plastic) are taken in the circumferential direction on the friction surface of the trailer bogie. Compressive stress cycling is seen without plastic flow during each cycle (plastic strain is zero in mechanical strain). And, the stabilization of the stress-strain hysteresis loops is assumed to be achieved after the third consecutive stop brake application [98]. The hysteresis loops for three braking processes are shown for three repeated braking in Figure 5.6.a, and Figure 5.6. b gives the stabilized loop for the third one.

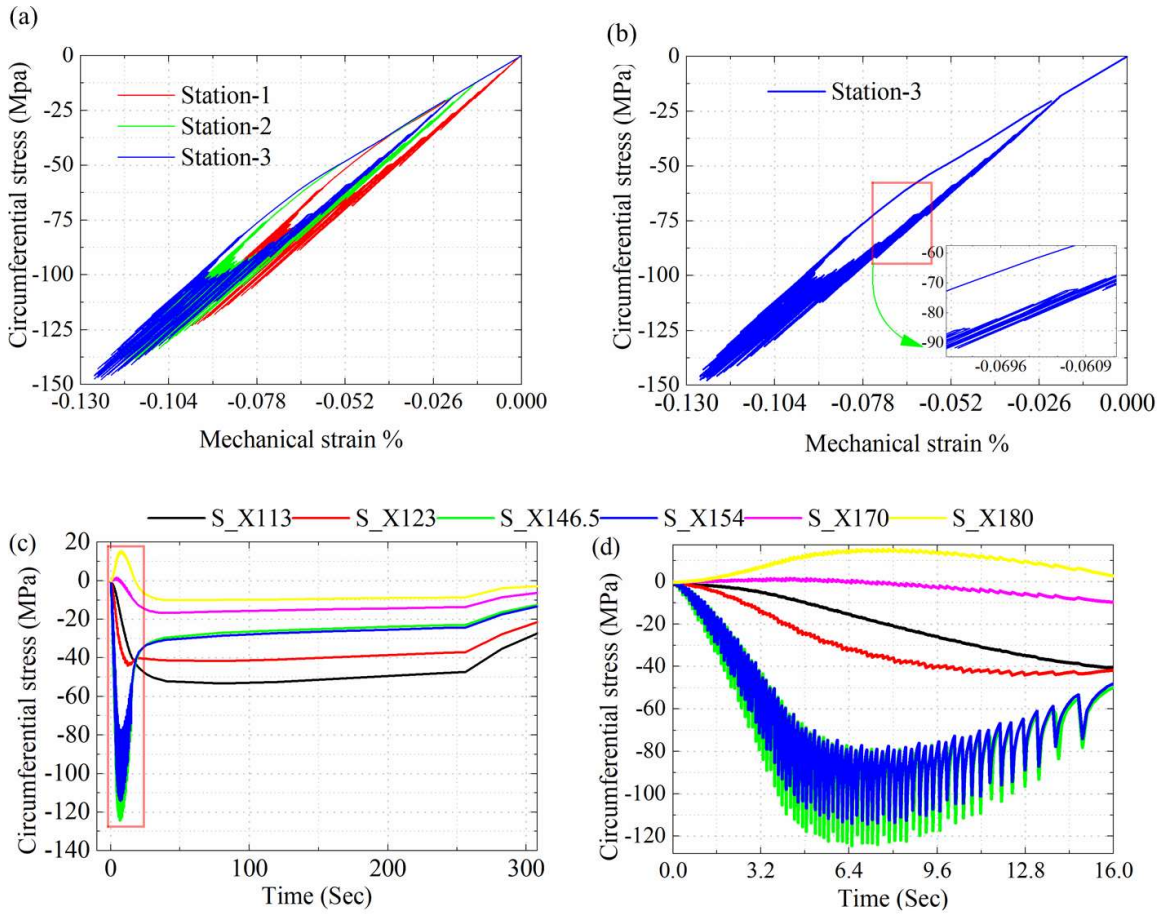

Figure 5.6 Original disc's friction surface (R_m,90°) stress-strain hysteresis loop for service brake ((a) station 1-3 and (b) its enlarged plot for the third station) and their stress radial variation ((c) for station 1, (d) its enlarged plot)

The enlarged plot of the loop (Figure 5.6. b) revealed the complex forward and backward movement of hysteresis loops during the heating period. This interesting result is attributed to the rise and fall of temperature at the selected node (peak and valley). A specific node has only one chance of getting heat (being within the pad-disc interface or pad cover angle) within one revolution (360˚) of the heat source. When the selected node is heated, its temperature rises sharply (Figure 5.4.b), and so does the compressive stress (move downward). But the stress is seen not continue in this trend, since the heat source is migrated toward the neighboring nodes, resulting in a drop of circumferential stress (backward movement). The same phenomena are shown repeated for the second and the next revolution of the heat source. To the best of the authors' knowledge, this study provides a first step toward forward and backward movement trends of the stress-strain hysteresis loop, compared to uniform trends reported in [42][97][98].

Hence, this NAMHS finding will help us to predict thermal fatigue life in a better way, compared to any traditional modeling.

5.7.2 Spatial investigation of stress

In this section, stress along the radial direction of the disc, Stress along the circumferential direction and the stress along the axial direction are presented sequentially.

What stands out in the NAMHS model algorithm stress report is its continual growth with disc radius until a mean radius of 146.5mm (Figure 5.6.d), though applied heat flux was seen to rise with radius due to the modified equation used in heat flux calculation and its way of application in NAMHS (Eq. 4.27). The relationship between stress and radius is shown the same as that of temperature in Figure 4.13, with a little bit of variation. It has been revealed a marked rise with radius, only until the mean radius, unlike temperature which was seen to increase up to R_t (154mm). Besides, close observation of circumferential stress revealed higher results for the transitional radius at the heating area (250˚-300˚) and lower results for cooling areas ($\theta<250^{\circ}\&\theta>300^{\circ}$) (Figure 5.7.b). Beyond the mean radius ($146.5<r\leq170$mm), surprisingly stress has been seen to drop despite the rise in heat flux within the radius from $123<r\leq170$mm. In contrast, the temperature was displayed to rise to R_t in Figure 4.13. This discrepancy could arise from two factors. Firstly, due to the proximity of the surface ranges from R_m to R_t toward the non-contacting region of the disc (radius $170\leq r\leq180$mm). Eventually, the flow of temperature through conduction and convection is expected from the high potential to the lower potential surface. Secondly, due to the absence of cooling fins (constrained boundary conditions), the outer radius has more opportunity to expand (Figure 5.2), leading to 15MPa tensile stress. The Fall of stress outside the pad cover angle from the inside (radius from $113\leq r\leq123$mm) is also ascribed to the same reasoning. However, relatively higher stress displayed at the inner radius (113mm) compared to the pad outer radius (170mm) and disc outer radius (180mm) might require a different explanation. The constrained boundary conditions at the inner radius and cooling fins might appear responsible for relatively higher stress, as it hinders freedom of expansion. An inspection of the stress plot in Figure 5.8 witnesses this radial variation of stress.

Circumferential (0-360°) variation of stress is where the new contribution of the NAMHS model is obviously seen in managing the spatial and temporal distribution of stresses (Figure 5.7. c). Furthermore, the comparative analysis of disc design is obviously revealed based on the presented stress result. Since the original disc geometry has an additional 12 structures

around 6 holes for reinforcement (Figure 5.2) it has been seen to overshadow the effect of NAMHS spatial variation of stress. Therefore, it appears preferable to explore the separate effect of the NAMHS model at different radii using modified geometry (Figure 5.7. b,c,d), in addition to the actual geometry (Figure 5.7. a).

For either actual or modified geometry, the maximum temperature at the friction surface was revealed similar, except for spatial variations (Figure 4.15). In contrast, what is extraordinary about actual disc stress results is unexpectedly more than twice the stress found in modified disc geometry: 226Mpa and 100Mpa in the former and later, respectively (Figure 5.7. a&b). This result is related to constrained boundary conditions on six holes, which may appear responsible for exaggerated results in actual disc geometry (Figure 5.7.a). Because, expanding in any direction is difficult due to restrictive boundary constraints ($u_x = u_{y,} = u_z = 0$), which increases stress. Displacement constraint due to bolt holes on every 60° of the disc circumference resulted double in stress value, compared to when there is no bolt hole on the friction surface (hub-bolted disc). It is intriguing to speculate that as there is a rise in the number of bolt holes in friction surfaces, the probability of surface damage is high. Hence, there is evidence to indicate that, the friction surface-bolted type design of the disc brake is more vulnerable to crack initiation and propagation, compared to hub-bolted discs.

What is striking in Figure 5.7.a & Figure 5.8.a is the dramatic rise of stress every 60˚, where displacement is restricted due to boundary conditions, resulting in higher stress concentration at sharp edges of holes. Consequently, von Mise stress is displayed as high as 490MPa (Figure 5.8.a). This position of high stress is seen as consistent with those of X Xie et al., 2021 [19] and Han et al. 2018 [94].

This finding reveals some tentative suggestions on the similarity in stress trends between the NAMHS model, and if an axisymmetric model is applied on a modified disc geometry with 60˚ sector. Because in both cases middle nodes ($0^\circ<\theta<60^\circ$) would have equal opportunity for tension and compression, resulting in somewhat related results. But if the sector in disc geometry increases (for example, $0^\circ<\theta<90^\circ$, or four bolt holes on friction surface), relatively lower stress may be expected, as the impact of boundary conditions on middle nodes could reduce. Hence, another outstanding implication drawn from this result is the effect of the disc symmetry or sector selections in previous investigations in axisymmetric modeling: 2D [17], 30°[77][28], 45°[107], 90°[73], 180°[81]. The most obvious finding to emerge from this result is that stress appeared higher in lower sector assumption studies, compared to higher degree

sector assumptions. This finding suggests that axisymmetric model results are biased according to geometry selection, and are not a true representation of the thermomechanical modeling of disc brake. Hence, this study provides a first step towards a realistic representation of FE modeling, which could be implemented in fatigue life prediction.

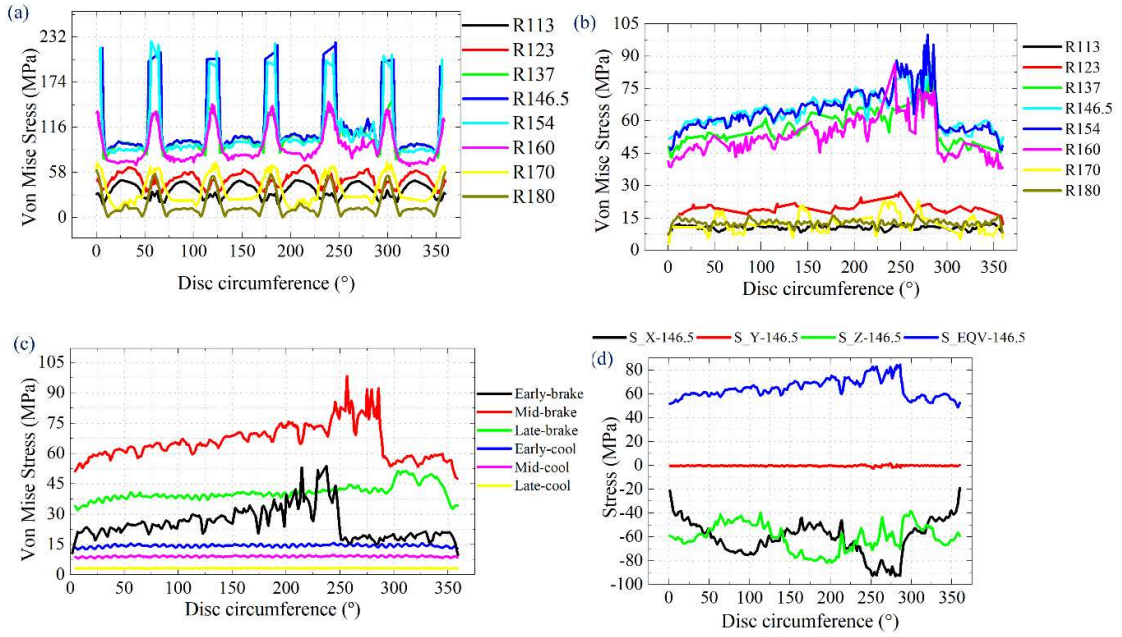

Figure 5.7 Station 2 friction surface stress spatial variation for service brake: (a) original disc, (b) modified disc, (c) modified disc at R_t and at different times, (d) modified disc stress components at R_m on mid-braking time

As we travel tangentially from the lower to the higher angle, a significant rise of stress is shown by the investigation of the NAMHS models in each interface at the middle braking time (Figure 5.7.b, c and Figure 5.8.b). Surfaces close to the pad cover angle are shown under more stress than those farther away. This could be enlightened by the removal of high-temperature positions over time due to heat dissipation by conduction and convection. To examine tangential stress variation, two specific positions are selected on the modified geometry on mid-braking time on the transitional radius (Figure 5.7.b): at minimum stress point (320°) and maximum stress point (278°). Close inspection of the selected points illustrates a 46Mpa variation in von Mise stress on a specific point in time (8.1512 sec). But this change is noticed for only selected middle radii:137≤r≤160mm. This does not imply constant circumferential stress at the surface close to the inner or outer pad radius |r|<137-160mm. Instead, it might be explained by the insignificant impact of circumferential flux and temperature change on the pad's extreme radius, due to heat dissipation.

There are similarities in the disc surface stress variation between this study and those described by Rashid & Strömberg, 2013 [169], in which three repeated braking were studied by sequential simulation of thermal and stress. Although moving heat source stress simulations were seen as limited in literature, it is encouraging also to compare this result with that found by Baron Saiz et al., 2015 [91] who applied circumferential stress variations for conducting comparative analysis disc geometry, and with that of Mahmoudi et al., 2015 [33] who implemented in optimum disc material selection. In contrast to earlier findings, the findings reported here suggest a comprehensive spatial description of stress on the friction surface.

Another novelty in the NAMHS model algorithm is its accommodation of hydraulic pressure variation during early braking time (0-4 sec). This factor is seen in varying spatial temperature distributions (Figure 4.15.a,d). Its effect on von Mises stress is apparent in Figure 5.7.c & Figure 5.8. c on the early braking of station 2 (3.0555 sec) at the transitional radius. According to the data, stress is shown to rise steadily (positive slope) up to the heating area (200°-250°). One reason that could explain this observation is the circumferential increase in heat flux due to hydraulic pressure in the NAMHS model (Figure 4.7). In contrast, the surface far from the heating point is illustrated to have a lower stress area, due to convection and conductions on the friction surface. One of the issues that emerged from these reports is the flexibility of the NAMHS model in uncovering the hydraulic pressure variations throughout the braking time.

Another important finding of the NAMHS model prevailed in terms of circumferential stress drop at the heating area of the pad cover angle, due to deceleration. Although this effect is present throughout braking time, its influence is prominent only at the heating area of late braking time (300°-350°) and mid-braking time ranging from 250°-300° (Figure 5.7.c). The narrower trace of the stress plot on the trailing compared to the leading edge is also evident in Figure 5.8.d. Stress variations here are displayed as having a negative slope trend. Stress variation on the heating area of the pad cover angle (between the leading and trailing edge of the pad) is illustrated 3MPa and 6MPa on late and mid-braking times, respectively. This is related to the heat source's speed drop owing to deceleration, which could lower the quantity of heat input from the leading to the trailing edge while it is rotating. As a result, not all of the sliding nodes on the pad circumference supply the same amount of heat to the specific node on the disc surface.

Contrary to this expectation, the result presented on early braking time disproves the deceleration effects seen in mid and late braking time (Figure 5.7. c & Figure 5.8. c).

Interestingly, the narrower trace of the stress is visible on the leading edge compared to the trailing (Figure 5.8.c). These conflicting results could be associated with the dominance of the hydraulic pressure over the deceleration effect. Although stress circumferential variation reports have been seen as rare in previous studies, Belhocine and Bouchetara [146] reported the highest contact pressure at the pad's edges, where it was shown to decrease from the leading edge to the trailing edge of the pads.

Further analysis of the heating area at early, mid, and late braking time uncovers one important finding related to the insulated pad groove on the middle surface of the pad (Figure 5.7- Figure 5.8). What stands out in this figure is the variation between steep fall and rise of the stress within a heating area with 26.5MPa, 30MPa, and 7.5MPa, at early, mid, and late braking times, respectively (Figure 5.7.c). To find these amounts of stress variation within a 50° sector of the disc is really interesting. This finding is most plausibly explained by the vulnerability of the pad cover angle to substantial heat at the right and left side of the groove area, meanwhile totally insulated surface in the middle. Moreover, it is not only the groove area that appeared to decline in stress, at the pad's extreme borders also stress is illustrated to fall (Figure 5.7-Figure 5.8). It results from the transfer of surface heat from the pad's extreme border to nearby surface nodes by convection.

In accordance with the present results, Belhocine et al., 2016 [147] also demonstrated a sharp drop in the contact pressure and stress around the radial groove pad and a slight rise at the leading edge. This work demonstrates a striking difference between the NAMHS model algorithm and other traditional models in facilitating spatial and temporal variation of stress. It is conceivable that the proposed technique could be easily implemented and suitable in the area of any sliding frictions, linearly or tangentially (as in disc brake). These might include, but not limited to thermal and stress analysis of tread brakes, drum brakes, engine piston-cylinder, and camshafts are just to cite a few of its application areas.

This study also sets out to assess the stress components (S_X, S_Y, S_Z) relationships with one another along with the disc circumference, illustrated in Figure 5.7 .d. Circumferential and radial stress components are displayed to have sine and cosine relations along the disc circumference. The cause of this stress tendency is related to their geometric location on the disc surface (90° apart). Eventually, if the maximum stress of S_X is found at a specific location, the minimum value of S_Z is expected at the same point. Besides, circumferential stress shows significant sensitivity toward the heating area (250°-300°), compared to radial

stress. Furthermore, axial stress is portrayed as indifferent to the disc tangential dimension, which might be linked to its opportunity to swell axially on the disc surface, resulting minimum stress component.

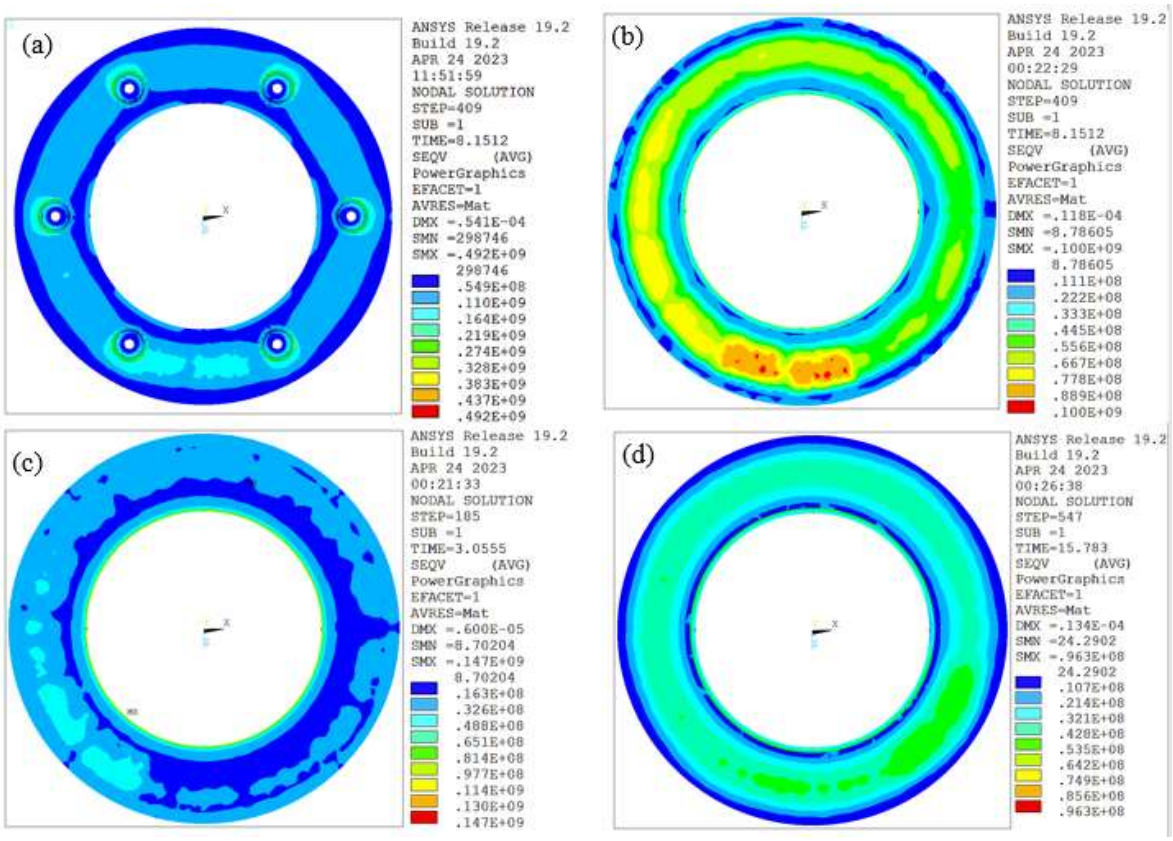

Figure 5.8 Disc surface stress plot on various braking times: mid ((a) original, (b) modified), (c) early, (d) late

The NAMHS model's further investigation of spatial stress through disc thickness revealed saw-teethed behavior to have a maximum depth of 8.5mm from the surface (Figure 5.9.a). Spatial variation of surface stress due to moving heat source is not seen noticed beyond half of the disc thickness. Based on this foundation, it is possible to hypothesize that these fluctuations of stress in depth close to the friction surface could lead to crack initiation and propagation in the axial direction. And, this inference reflects those of Li et al. 2014 [76] who revealed the maximum depth of radial cracks as 10mm. Eventually, the approach presented in the NAMHS model algorithm is suitable for problems where spatial and temporal thermomechanical information is incomplete.

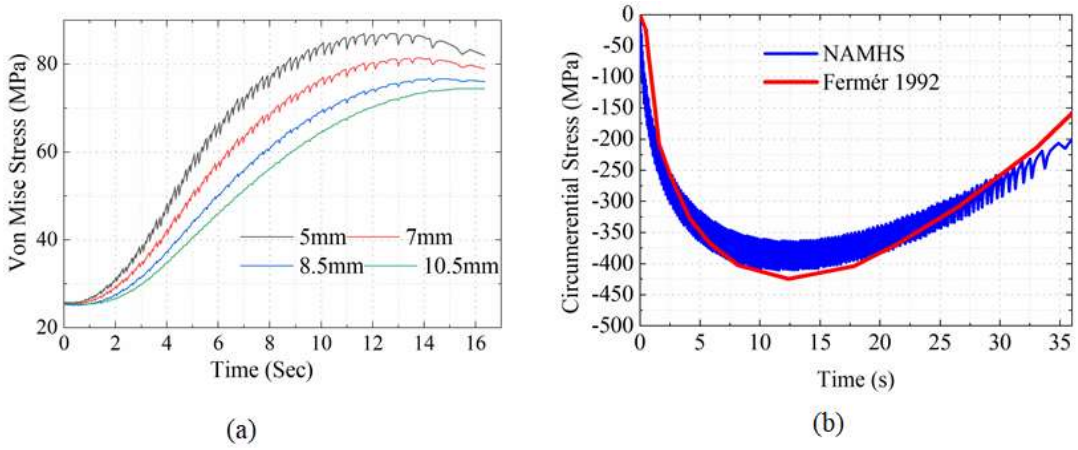

Figure 5.9 (a) Stress variation along original disc thickness, (b) Validation

5.7.3 The model validation

To the best of the author's knowledge, experimental investigation of disc brake thermal stress has been rare, and those few performed by strain gage lack detailed geometry, input loads, and braking conditions [42]. So that it is difficult to conduct the NAMHS model in the scarcity of these parameters. Most of the thermal stress determination has been conducted by analytical and thermocouple methods [106][151][152][170]. Eventually, the analytical thermal stress performed by Fermér 1992 [152] is selected here to validate thermal stress, because the method's temperature result was validated by an experiment. As far as reliable temperature result is determined, analytical thermal stress is believed to be reliable, since the temperature is input for thermal stress calculations.

Loading case A with an axle load of 20 tonnes and initial speed V_o = 130 km/h is selected for thermal stress simulation. The analytical and simulations are performed for 36s of braking time and an additional 26s of cooling time. However, circumferential stress is selected for braking time only, since cooling time is not related to moving heat source (Figure 5.9.b). Since radial and circumferential stress displays sinusoidal behavior (Figure 5.7.d), circumferential stress is selected for the node at 232mm and 180° on the friction surface, which is revealed 428MPa (Figure 5.10.a). This value agrees with the maximum circumferential stress depicted in Figure 5.9.b. Comparison of the NAMHS model stress findings with that of Fermér 1992 study confirms similarity in stress trends, within 4% variation at 12.5s of braking time. Besides, von Mise stress is displayed to highlight spatial temperature distribution at the middle gracing time (Figure 5.10.b).

In spite of this similarity, a little bit of variation between the two models is highlighted at early and late braking time, which might be associated with assumptions made in Duhamel's analytical model derivations. Notwithstanding this limitation, this finding provides some tentative initial evidence of the reliability of the fatigue life and failure prediction performed by the NAMHS model.

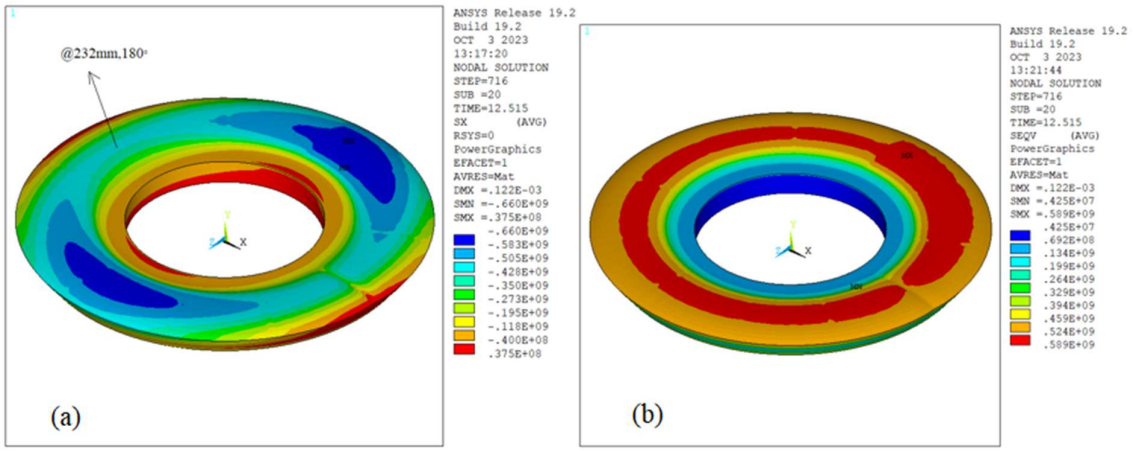

Figure 5.10 Stress (a) Circumferential and (b) Von Mise at 12.5 sec

5.7.4 Hysteresis loops spatial variation and fatigue life prediction

Further investigation of stress effects on fatigue life spatial variation leads us to focus on the stress-strain hysteresis loop for nodes found in three different positions. Firstly, mean radius nodes at a 30˚circumferential distance from the holes are selected: 30˚, 90˚, 150˚, 210˚, 270˚, 330˚ (Figure 5.11.a,c). This is to investigate circumferential variations of fatigue life. At these points, it is believed that bolt-hole effects are eliminated. Secondly, mean radius nodes 10˚ close to the holes: 110˚ and 290˚. This is to analyze the effect of holes (disc geometry) on surrounding points. Finally, radial variation of fatigue life is presented at 90˚ for six points: 113mm, 123mm, 146.5mm, 154mm, 170mm, and 180mm (Figure 5.11.b,d). The effect of braking energy variation is also presented in the hysteresis loops, for both service and emergency braking.

Moreover, as the service brake is designed for infinite fatigue life, life is estimated here only for emergency braking in a motor bogie (Figure 5.11. c-d), based on the fracture mechanics approach (Eq. 5.8). The service brake is utilized only for investigating the spatial behavior of hysteresis loops (Figure 5.11. a-b). The rise in braking energy through emergency braking on motor bogie uncovered a doubled rise in stress and strain range. This is attributed to the reduced braking time and due to the rise in mass per disc in the motor bogie. Consequently, the

additional plastic strain registered raised stress and strain ranges (Figure 5.5). These findings suggest that emergency braking damages the motor bogie twice that of the trailer bogie. And the maintenance personnel are recommended to conduct regular inspections to prevent surface failure, whenever emergency braking is applied.

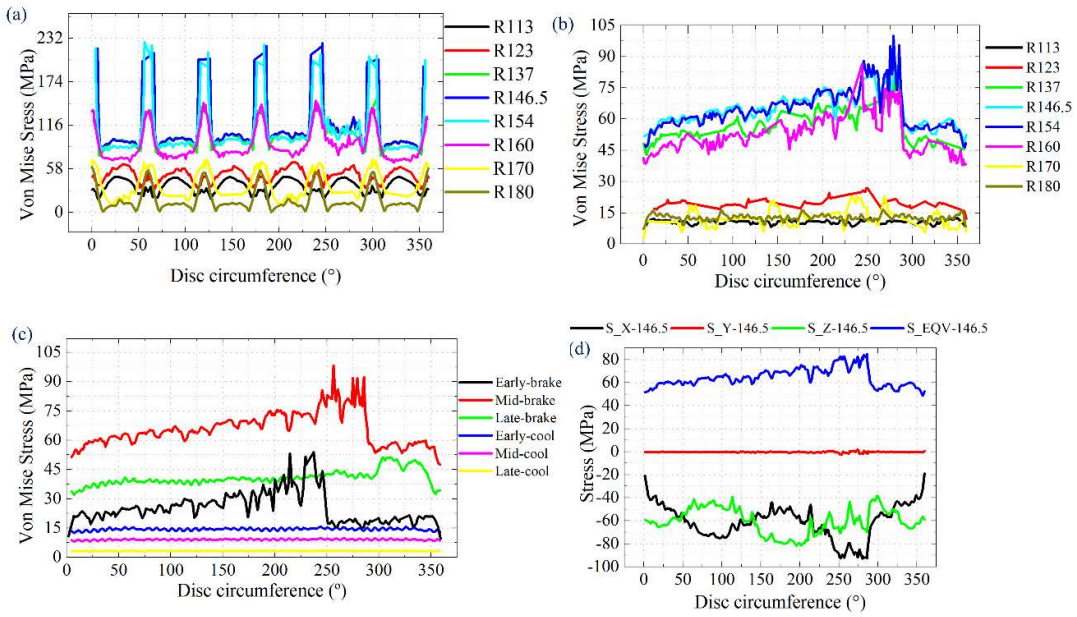

Figure 5.11 Original disc design friction surface circumferential stress-strain at R_m for service brake (a-b) and emergency brake (c-d) at selected circumferential (a,c) and radial (b,d) points

Circumferential variation of the stress-strain plot in Figure 5.11 demonstrates two sets of hysteresis loops, irrespective of braking types: lower (30^o,150^o,210^o,330^o) and higher (90^o,110^o,270^o,290^o) strain ranges. Lower strain ranges and higher strain ranges are presented ($\Delta\varepsilon$=0.0614%) and ($\Delta\varepsilon$=0.1079%), respectively for the service brake of the trailer bogie (Figure 5.11. a-b), and doubled for the motor bogie (Figure 5.11. c-d). A higher strain range observed for 110^o and 290^o stems from their proximity to the holes (10^o close). This confirms the results presented in Figure 5.7 which displays higher stress at 120^o and 300^o, due to disc geometry. The sudden fall of fatigue life in (Figure 5.12. a) for emergency braking is associated with this effect. Perhaps the most unexpected finding is the rise in strain ranges for nodes at 90^o and 270^o, though they appear 30^o far from bolt holes. It is significantly associated with the sinusoidal behavior of circumferential stress. A marked increase in S_X stress at 90^o and 270^o (Figure 5.7.d) supports this assertion. Consequently, an almost equivalent fatigue life is presented for both nodes (Figure 5.12. a).

A lower strain ranges are observed for nodes: 30˚, 150˚, 210˚, and 330˚. At these nodes, strain ranges are caused by thermal stress only, and disc geometric effects are not involved. Interestingly, considerable variation of strain range is noticed for the node at 330°. A possible explanation for this result may be its proximity to 360°, where circumferential stress has a minimum value due to its sinusoidal property. The resulting fatigue life is raised substantially by 1000 emergency braking, compared to nodes at 30˚, 150˚, and 210˚. This observation may support two hypotheses that could disturb circumferential stress spatial variation. Firstly, disc geometry. And secondly, the sinusoidal behavior of stress components, particularly circumferential and radial stress. Although circumferential stress is found the dominant and crack-raising stress component in many investigations [96][19], its intervention in the spatial investigation of stress, due to its sinusoidal behavior remains disappointing.

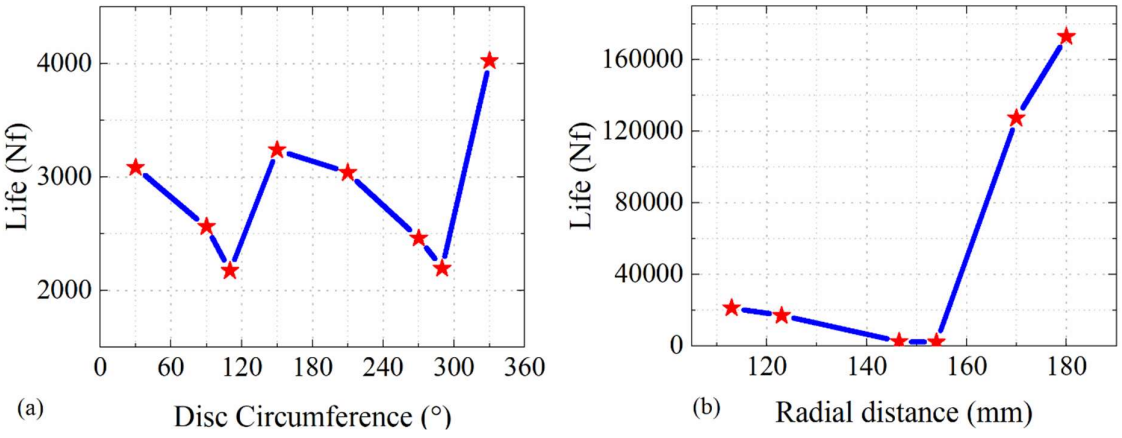

Figure 5.12 Friction surface (R_m,90°) fatigue life estimation for emergency braking of original disc: (a) along disc circumference at R_m, (b) along disc radius at 90°

Finally, for the middle radius nodes (146.5mm and 154mm), Figure 5.11.b highlighted a massive rise in strain range, respectively 1.06×10^{-03}% and 9.95×10^{-04}%, compared to outer (170-180) and inner radial nodes (113-123mm). This could be stemming from its remote position from convection areas. Figure 5.8 and low fatigue life in Figure 5.12.b provide a support for this explanation. Another obvious finding to emerge from the analysis is that the outer disc is the only vulnerable point to both tensile and compressive strain range, due to its chance of expansion associated with lack of extruding fins underneath the surface (Figure 5.2). And, to some extent, the inner radius nodes revealed a noticeable increase in strain range, attributed to constrained structural boundary conditions at the inner radius. Consequently, fatigue life is uncovered to increase radially, starting from the middle to the inner and from the middle to the outer (Figure 5.12. b).

The effect of braking energy variation between motor and trailer bogies' discs and the corresponding pads is assessed by the NAMHS model. Nonetheless, to confirm this assessment, observation of the real-world braking components (pad and disc) in braking condition seems mandatory. Eventually, the field observation is conducted on out-of-service pads (worn out) and on service discs, for both motor and trailer bogies. Their surface damage is compared to prove the conclusions drawn by the NAMHS model. However, since the number of emergency braking performed and the initial velocity from which braking is carried out is not documented by AALRT, it is impossible to make a direct comparison with the NAMHS model. But, it is possible to relate the severity of the surface damage between the two methods.

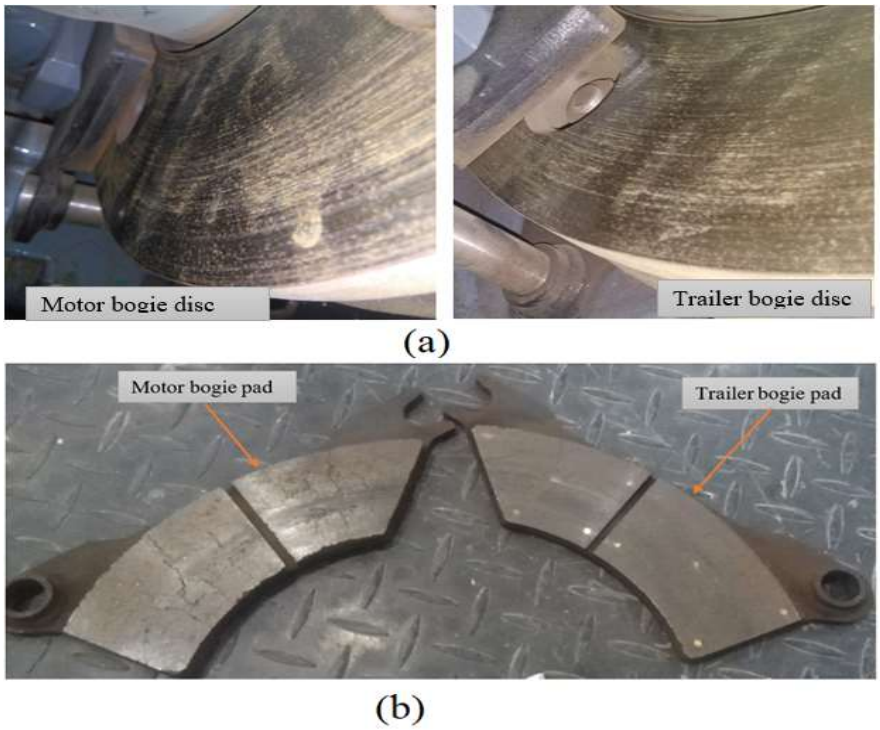

Figure 5.13 Field observation of AALRT discs and pads for motor and trailer bogies: (a) discs and (b) pads

The motor bogies' braking components (disc and pad) are displayed as vulnerable to damage compared to trailer bogies' pad and disc (Figure 5.13), due to heavier mass supported by the former. However, this implication is more clear for pads, compared to discs, because discs are designed for longer life. This work demonstrates that the NAMHS predictions can provide a more reliable estimate of failure observed in the actual braking conditions.

5.8 Conclusions and Recommendations

This study set out to evaluate the effectiveness of the NAMHS model algorithm in examining the spatial and temporal variation of stress and fatigue life prediction. The spatial trends of stress and strain are investigated for service brakes on actual and modified disc geometry, while fatigue life is determined for emergency braking on actual disc geometry. The main findings of the model are summarized below:

- NAMHS model algorithm stress and strain assessment with time illustrates saw-toothed oscillation varying in frequency and amplitude. Eventually, the stress-strain hysteresis loop displayed complex forward and backward movement during the heating period. It is inferred that the state of stress development follows the footsteps of temperature evolution. The model revealed saw-toothed behavior to have a maximum depth of 8.5mm from the surface.
- The circumferential stress component is shown to play a remarkable role in crack initiation and propagation and hence involved in fatigue life estimation. Circumferential and radial stress components are displayed to have sine and cosine relations, respectively along the disc circumference. This effect is seen in maximum fatigue life prediction for the node on the mid radius of 330^{o}. Furthermore, axial stress is portrayed as indifferent to the disc tangential dimension, and the minimum stress component.
- The effect of braking energy is studied by emergency braking and rising mass per disc on the motor bogie. It is uncovered a doubled rise in stress and strain ranges. Consequently, plastic strain and permanent deformation are registered only for motor bogie
- Stress spatial variation due to disc geometry overshadows its circumferential variation. This is prevailed by more than twice the stress and strain value seen in actual disc geometry, compared to modified geometry. And, the sudden fall of fatigue life reported for nodes close to the bolt holes for emergency braking, also proved this effect.
- Stress has revealed a marked rise with the radius until the mean radius, and the impact of conduction and convection is shown to reduce it, beyond the mean radius. And, relatively higher stress is displayed at the inner radius compared to the pad's outer radius. The friction surface is exposed to radial stress variations from tensile stress of 20MPa to compressive stress of -125MPa. Consequently, fatigue life is uncovered to

increase radially, starting from the middle to the inner, and from the middle to the outer radius

- Two extreme points on the middle radius of the friction surface illustrate a 46Mpa von Mise stress variation on a specific point of time, for modified disc geometry. Stress variation between the leading and trailing edge of the pad trace due to deceleration is illustrated 3MPa and 6MPa on late and mid-braking times, respectively.
- The effect of hydraulic pressure and deceleration on disc circumference stress variation prevails in the heating area (pad cover angle). The former is prevailed by a positive slope on early braking and the latter is revealed by a negative slope on mid and late braking time. The effect of hydraulic pressure is shown to dominate the deceleration effect, on early braking time.
- The effect of pad groove on stress variation is displayed by steep variation of stress as high as 30MPa within a heating area on middle braking time.

The findings of this study suggest that the NAMHS model could predict the depth of axial crack propagation, based on the depth of stress fluctuations. The rise and fall of stress with time support the idea that the NAMHS model stress calculation avoids results exaggeration seen in other traditional models of stress prediction. Besides, this finding suggests that axisymmetric model stress results are biased according to geometry selection, and are not a true representation of the thermomechanical modeling of disc brake. It is intriguing to speculate that as there is a rise in the number of bolt holes in friction surfaces, the probability of surface damage is high. Hence, there is evidence to indicate that, the friction surface bolted type design of the disc brake is more vulnerable to crack initiation and propagation, compared to hub-bolted discs. Moreover, these findings highlight the potential usefulness of NAMHS model flexibility in managing spatial variation of stress due to hydraulic pressure, pad groove, and deceleration. Hence, it could represent convincing evidence of where a crack could be initiated and the direction in which it could propagate. Therefore, this study provides a first step towards a realistic representation of FE modeling, which could be implemented in fatigue life prediction.

Finally, this work demonstrates a striking difference between NAMHS and other traditional models in facilitating spatial and temporal variation of stress. It is conceivable that the proposed technique could be easily implemented and suitable in the area of any sliding frictions, linearly or tangentially (as in disc brake). These might include, but not limited to thermal and stress analysis of tread brakes, drum brakes, engine piston-cylinder, and camshafts are just to cite a few of its application areas. Using the developed modeling, further research into disc

comparative analysis in material selection and pad-disc geometry optimizations are in progress by the authors.

Some limitations need to be noted regarding the present study for further investigations. Firstly, the model presented here couldn't solve the sinusoidal effect of circumferential stress in intervening fatigue life prediction. Secondly, the assumption of a stabilized stress-strain hysteresis loop after the third braking time needs more repeated simulation. Thus, further modeling work will have to be conducted in order to use Von Mise stress-strain and more braking time for better results. To apply the model in more repeated braking where wear is influential, it is required to develop the model further to include the effect of material removal rate. This could be performed by implementing parameters involved in Archard wear analysis: applied load, sliding distance, and material properties. Because these could be easily managed in ANSYS APDL by definitions of arrays and parameters. These APDL commands are easily adopted to Archard wear analysis due to their sophisticated features that can encompass a wide range of data flow such as repeating a command, macros, if-then-else branching, do-loops, APDL math, scalar, vector, and matrix operations [77][139].

CHAPTER 6: APPLICATION OF NON-AXISYMMETRIC MOVING HEAT SOURCE IN COMPARATIVE ANALYSIS OF MATERIAL AND GEOMETRY SELECTION

6.1 Introduction

Since the early development of railway and automotive transportation, braking performance has been improved in two areas of investigation: brake geometries and their materials. With a compact size geometry, that could dissipate heat easily to the neighboring areas, has been developed to minimize failure and increase service life. And still, it is an ongoing research area in transportation industries. However, the success of this study requires the development of a better FE model.

Simulation is conducted for emergency braking on the trailer bogie of AALRT and modified disc geometry. Braking conditions are identified in Table 5.1 and Table 5.2. Nonetheless, the best geometry identification is performed for 5,516 kg mass per disc (Eq. 4.9) in one braking time, without the cooling time. Because, the braking duration of 8.23s is the period in which the maximum temperature could be revealed. Besides, disc geometry is the same as in Figure 5.2. b (modified disc geometry). And, FE modeling in terms of meshing and boundary conditions are extracted from Figure 4.6 and Figure 4.10, respectively. But heat input load follows the shape of candidate pad geometries. Moreover, only thermal analysis seems enough to predict optimal pad geometry. Because, stress follows temperature footstep, according to stress and fatigue evaluations conducted in chapter five, and other studies also confirm this assumption [80].

On the other hand, disc brakes' required material properties are identified as lower density, lower thermal expansion coefficient, higher thermal conductivity, higher specific heat capacity, higher compressive strength, higher surface hardness, higher corrosion resistance, stable friction coefficient, and higher fracture toughness [109][110]. Based on these properties, conducting the comparative analysis in material is not an easy task, because no material exists that can fulfill all the required properties. Even material property requirements might conflict with one another between thermomechanical analysis. and, the appropriate material selection also requires a computationally effective FE model.

Like pad geometry simulation, stress simulation for comparative analysis of material is conducted for emergency braking on the trailer bogie of AALRT having a mass of 5,516 kg/disc. In contrast, the original disc geometry (Figure 5.2. a) is implemented for material

investigation. And, FE meshing and boundary conditions are extracted from Figure 4.6 and Figure 4.10, respectively. But both braking (8.21 sec) and cooling time (175.12 sec) are implemented (Table 5.1 and Table 5.2). Because, the rate at which materials cool could differ, owing to their thermal conductivity variation. Eventually, a cooling time simulation is added here.

Based on this foundation, this chapter tries to evaluate the effectiveness of the NAMHS FE model in selecting the comparative analysis of pad groove geometry, and comparative analysis of material in the service life of cast iron material families.

6.2 Pad Geometry Variation

The pad and disc contact area varies depending on pad geometries. And, the variations in contact geometry due to pad type substantially affect the spatial distribution of temperature. Although various types of pad geometries were seen in the literature (Figure 2.17-Figure 2.18), they are mainly classified into two groups: composite and sintered pads. Composite pads are further classified based on their grooves' number and position. The positions of grooves are seen as radial [86], tangential [147], or both [17]. Besides, composite pads may have no groove [68], one radial groove [147], two radial grooves [171], and a maximum of four grooves [81]. On the other hand, sintered pads are the same in number (18), but vary based on their pin geometries, such as circular, hexagonal, and triangular [37].

Table 6.1Composite pad geometry variations

Tangential groove variations	**Radial groove variations**	
	R1	**R2**
T0	T0R1(AALRT pad)	T0R2 (AALRT pad)
T1	T1R1	T1R2
T2	T2R1	T2R2

Hence, in this section, it is required to assess the effectiveness of the NAMHS model algorithm in handling the comparative analysis of geometry of the pad. To do so, only composite pad design is selected, as it is representative of all pad geometry designs. For all selected pad geometries, the applied braking power is the same. But, heat flux varies, due to contact area variations. As the number of grooves rises in number (tangentially or radially), applied heat flux increases, due to the reduction of contact area (Eqn. 4.16.a). In addition to varying heat application spatially, heat is removed from groove locations. The selection of pad geometry

candidates is based on the types of pad geometry found in AALRT: one radial groove without a tangential groove (Figure 1.2. b) and two radial grooves without a groove (Figure 1.2. a, Figure 4.5. c. For each of these basic geometries, tangental grooves are varied from 0 (no tangential groove) to two. As a result, a total of six pad groove geometries are presented as candidates from which the optimum is selected (Table 6.1). Since the main objective here is to evaluate the NAMHS model in conducting comparative analysis of geometry, increasing additional numbers of grooves (tangentially or radially) might appear not to alter the conclusion drawn based on selected geometries. Further diversification of the pad geometry is beyond the scope of the study, and cannot disprove the conclusion arrived on selected geometry.

6.3 Disc Brake Comparative Analysis in Material Selection

According to the review conducted in this dissertation, composite materials are the newly emerging technology for high-speed trains. Steels were displayed as the most widely used material (55%), applied in all speed ranges. Besides, cast irons are utilized in low-speed trains [3]. This includes AALRT and other freight trains. Cast irons have shown better materials for low-speed rail and automotive vehicles, having lower density, low price, low thermal expansion coefficient, and higher thermal conductivity [109]. Nonetheless, the use or selection of cast iron material in rolling stock disc brakes has been shown highly diversified, based on the shape of graphite:

- Flake (grey or lamellar)[107][77][96][107][82][60],
- Compact or vermicular cast iron [20] [120][121] and
- Nodular (spheroidal or ductile)[33][119] [172].

According to the ASM handbook material standard [122], typical unalloyed cast iron families aforementioned have the following composition (Table 6.2). Mechanical and thermal properties are also available within the specified range of compositions.

Table 6.2 Range of composition for selected cast iron families [122]

		Composition %				
Type	Designation	C	Si	Mn	P	S
Flake	FGI	2.5-4	1-3	0.2-1	0.002-1	0.02-0.25
Compacted	CGI	2.5-4	1-3	0.2-1	0.01-0.1	0.01-0.03
Spheroidal	SGI	3.-4	1.8-2.8	0.1-1	0.01-0.1	0.01-0.03

The preceding literature revealed inconsistent findings about the thermal fatigue resistance of cast iron families: FGI, CGI, and SGI. Lee J et al. 1995 [173] showed that CGI provides better thermal fatigue resistance compared to FGI due to its higher strength-to-thermal stress ratio. Likewise, based on their experimental analysis Ruff G F, 1976 [174] and Lee S 1991 [175] inferred a similar conclusion. On the contrary, Fredriksson, Sunnerkrantz, and Ljubinković 1988 [176] uncovered that FGI has better resistance to thermal fatigue owing to its lower modulus of elasticity and higher heat diffusivity. Zieher F. and Langmayr F. [177] and Nechtelberger, 1975 [178] confirmed the results obtained by Fredriksson. The contradictory conclusion of the above studies can be explained by the complex thermal fatigue behavior and inhomogeneous structure of cast iron. Many studies have revealed that thermal fatigue life is influenced by material properties, such as thermal conductivity, tensile strength, thermal expansion coefficient, and Young's modulus. Wang et al., 2022 [179], for example, found a contradictory relationship between tensile strength and thermal conductivity of cast irons, which is also reported due to their difference in microstructure (Figure 6.1).

Grey cast iron has the best thermal performance due to its high thermal conductivity owing to its graphite shape [122]. Graphite flakes are linked and arranged in plates, providing a simple pathway for rapid heat dissipation. Next, compact cast iron has better thermal performance than nodular cast iron [122]. And finally, nodular/ductile cast iron has the poorest thermal performance. Because, the microstructure of graphite is in the form of a sphere results in low heat dissipation through the pearlite matrix [180]. Hence, thermal results comparison alone couldn’t give a life warranty for disc brakes.

In contrary, the reverse was shown true in tensile strength and ductility. Flake cast iron has the lowest tensile strength, meanwhile nodular cast iron has the highest [122]. And, compact or vermicular has intermediate tensile strength. This is due to the fact that the size and shape of graphite microstructure affect strength and conductivity in the pearlite matrix [122]. Therefore, to investigate the effect of both thermal conductivity and tensile strength on disc performance, stress and fatigue life prediction seems the right comparison, among cast iron families. Hence, the question behind the best fatigue life material among cast iron families remained unanswered in literature. And, this chapter struggle to answer this type of question.

Table 6.3 Chemical composition of FGI [92], CGI [20] and SGI [18]

Weight (%)	Elements									
	C	Si	Mn	P	S	Cr	Ni	Cu	Mo	Mg
FGI	3.32	2.11	0.56	0.055	0.09	0.098	--	--	--	--
SGI	3.80	2.70	0.60	0.050	0.020	0.25	0.15	0.5	--	--
CGI	3.75	2.41	0.401	0.04	0.013	0.403	1.05	0.353	0.433	0.015

Motivated by the lower tensile strength of flake cast iron Lim and Goo 2011 [20] developed compacted graphite cast iron used for rail vehicle disc brakes. The results revealed better Mechanical and thermal material properties than the conventional flake cast iron, resulting in longer life before crack initiation. Even though the life comparison of cast iron was performed, the experimental conditions were seen very far from the actual braking conditions. Firstly, the thermal cycle between heating and cooling, temperature range, and the cooling mechanism (water) did not represent the actual braking in railway vehicles. Secondly, the crack initiation mechanism by rotating bending fatigue tester (tools used in measuring fatigue strength) is not the same as in disc brake. Finally, heat dissipation in specimen geometry is not according to the disc brake fins. Hence it is required to identify better material from cast iron families (flake, spheroidal and compacted), using NAMHS-based fatigue life prediction.

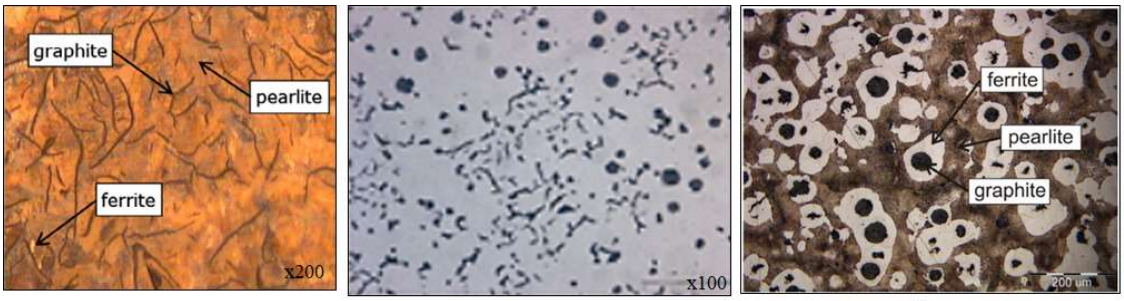

Figure 6.1 Microstructure of graphite: flake [92], compacted [20] and spheroidal [18]

6.4 Structural and Thermal Material Property Selections for Cast Iron Families

First mechanical properties are extracted for disc brake materials implemented in railways. These include Young's modulus, tensile, yield stress, thermal expansion coefficient, and Poisson's ratio. These properties are utilized in determining stress evolution in disc brakes. Besides, thermal properties utilized in thermal analysis including thermal conductivity, specific heat capacity, and density are determined for the same materials used in structural analysis.

Table 6.4 Microstructure of the candidate materials [92][20][18]

Cast iron	C wt%	Si wt%	N	Ferrite/pearlite	$F_{cementite}$	Reference
FGI	3.32	2.11	-100	1/99	0.2	[92]
CGI	3.77	2.33	19	25/75	0.2	[20]
SGI	3.52	2.6	95	33.7/59.57	0.2	[18]

6.4.1 Mechanical properties

For flake graphite cast iron, all mechanical properties are extracted from grey cast iron investigated by Pevec et al. 2014 [92] for disc brakes. The studied materials' chemical composition is shown (Table 6.3). Likewise, their microstructures are presented in Table 6.4 and Figure 6.1. a.

A metallographic analysis of the investigated material microstructure displayed a pearlite matrix with graphite flakes (dark areas), and traces of ferrite (white areas located next to the graphite flakes) as shown in Figure 6.1. a. Young's modulus, yield strength, and thermal expansion coefficient are presented temperature dependent, and highlighted to fall as temperature rises for the first two properties (Figure 6.2).

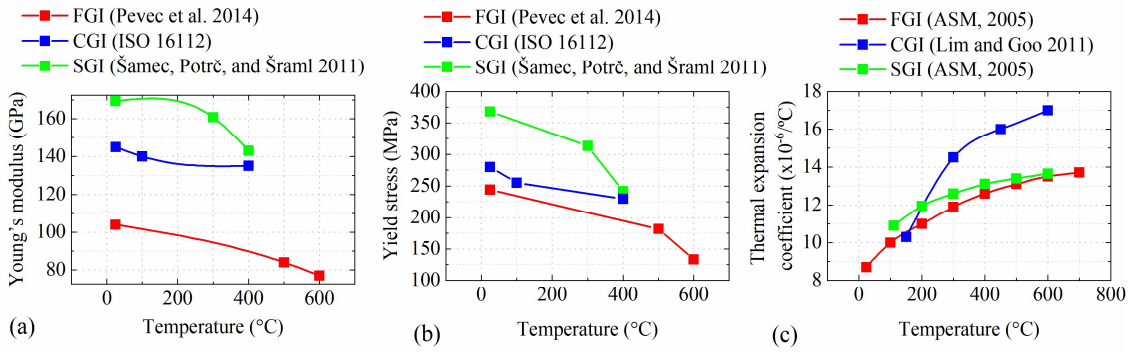

Figure 6.2 Mechanical properties [92][20][18][122][181]: (a) Young's modulus, (b) yield stress, (c) thermal expansion coefficient

Similarly, chemical compositions of nodular cast iron used for railway brake discs are taken from tensile strength and low-cycle fatigue (LCF) behavior evaluations conducted by Šamec, Blaž, Iztok Potrč, and Matjaž Šraml, 2011 [18]. Material property variations were made at RT, 300, and 400°C for Young's modulus and yield stress (Figure 6.2). A metallographic analysis carried out revealed a ferrite-pearlite matrix with graphite nodules (Table 6.4), and the microstructure of the material remains stable at 400 °C (Figure 6.1.c). The average area percent of ferrite and pearlite was reported 33.77% and 59.57% respectively, the rest was graphite. From the selected cast iron families in this study, coefficients of thermal expansion for disc

brake material were reported only for compacted cast iron. Eventually, the ASM standard properties [122] are implemented for flake and spheroidal cast irons, according to their microstructure matrix (Figure 6.2.c).

Finally, compacted cast iron is taken from its development as a railway vehicle disc brake by Lim and Goo 2011 [20]. From three compacted and conventional flake cast iron, material C was seen as the best in fatigue life. Therefore, its chemical compositions (Table 6.3) and microstructure (Figure 6.1. b) are shown. Its thermal expansion coefficient is directly implemented in this study (Figure 6.2.c). However, since the other mechanical properties were not presented in detail, reviewing further literature is mandatory. The investigated compacted iron material by Lim and Goo 2011 [20] has a tensile strength of 445.4Mpa, more similar to the international standard grade of GJV 450, from five grades of ISO 16112 international standard [181]. The chemical composition of the studied material also resides within the ranges specified by ISO 16112 for GJV 450 compacted cast iron. So we could have, Young's modulus and yield stress presented in Figure 6.2.a-b

Moreover, Poisson's ratio is taken 0.3, and kept constant despite variations in microstructure and temperature, found in the investigation of Seifert and Riedel 2010 [166][182] on cast iron families' material development. Besides, the density of cast iron materials did not seen vary with temperature, and has been observed to have similar values of 7200kg/m^3 [49][141][183], 7125kg/m^3 [184][185], and 7100kg/m^3 [184][82] for flake, compacted and spheroidal, respectively.

6.4.2 Thermal properties

For specified chemical compositions listed in Table 6.3, thermal conductivity and specific heat capacity are required. Unfortunately, the presence of these properties for specified composition is rare, in scientific literature. Hence, the thermal conductivities of various grades of pearlitic cast iron family are taken from regressional modeling investigated by Holmgren and Selin 2010 [186] for three graphite morphologies: Flake, compacted, and spheroidal.

The model developed by Holmgren and Selin 2010 [186] took the carbon content in wt%, C, the silicon content in wt% Si, the nodularity N, as well as the fraction of cementite $f_{cementite}$ into consideration (Eq. 6.1). The coefficients in Eq. 6.1 were reported to show how thermal conductivity is affected by temperature (Table 6.5). Besides, the microstructure expressed by nodularity and fraction of cementite is also extracted from respective cast iron families (Table 6.3). A flake graphite iron was represented by a nodularity of -100% in the model investigation

[186]. In addition, the developed model was applicable for temperature variations between 0-500°C.

$$K(T) = a(T) + C \times b(T) + Si \times c(T) + N \times d(T) + f_{cementite} \times e(T) \quad (6.1)$$

Finally, the calculated thermal conductivity of the respective material are presented in Figure 6.3.a. And the validity of the predicted property is checked by the ASM international handbook material standard [122]. The developed model is revealed to fit the ASM standard within a maximum of 9%, 5%, and 7% variation at 100˚C for flake, compacted, and spheroidal cast iron, respectively.

Table 6.5 coefficients a(T), b(T),c(T),d(T), and e(T) versus temperature [186]

T (°C)	Coefficients W/m°C				
	a(T)	b(T)	c(T)	d(T)	e(T)
24	-35.3561	15.70136	8.800905	-0.24354	-0.2053506
100	-10.0163	11.17647	4.841629	-0.17546	-0.2640221
200	10.04525	7.782805	0.995475	-0.1179	-0.298893
300	18.9819	5.859729	-0.58824	-0.08524	-0.2861624
400	21.92308	4.841629	-1.15385	-0.06753	-0.24631
500	25.54299	4.38914	-2.17195	-0.05092	-0.2103321

For the specific heat capacity, however, there is no validated unified empirical equation developed, to the best of the author's knowledge. Hence literature value is taken from the ASM standard, according to the reported microstructures (ferrite/pearlite %) in Table 6.4, except compacted graphite iron. And, for the compacted graphite iron, Lim and Goo, 2011 presented specific heat capacity properties in disc brake material up to 300˚C [20], and interpolation is conducted for the remaining temperature.

To sum up, both mechanical/strength properties and thermal properties of candidate materials revealed conflicting interests in improving stress and fatigue life. Because thermal performance is observed to increase from spheroidal to flake graphite iron (Figure 6.3). In contrast, strength or mechanical performance is displayed to decrease from spheroidal to flake graphite iron (Figure 6.2). Compacted graphite iron is shown intermediate performance in either case. On the other hand, it has the poorest thermal expansion coefficient (Figure 6.2.c). Therefore, thermal stress analysis with the NAMHAS model reveals the best material for railway vehicles' disc brakes with lower velocity.

6.4.3 Comparison methods

Emergency braking is implemented on the trailer bogie of AALRT. Braking parameters, braking conditions, and non-linear material modeling (GTN) are similar to the analysis conducted on motor bogie in the previous chapters. However, braking energy is reduced due to the fact that mass per disc is limited to 5,516 kg. Thermal and mechanical analyses are conducted, sequentially. Instead of calculating thermal fatigue life, stress ratio is used in this study. Material with a lower stress ratio (<1) is assumed to have higher fatigue life, and vice versa. Temperature is extracted, in the first analysis, meanwhile, stress and stress ratio are taken from the structural analysis, as a comparison parameter. To generate a comparison ratio, Von Mise equivalent yield criteria is divided for materials' yield stress (Eq. 6.2).

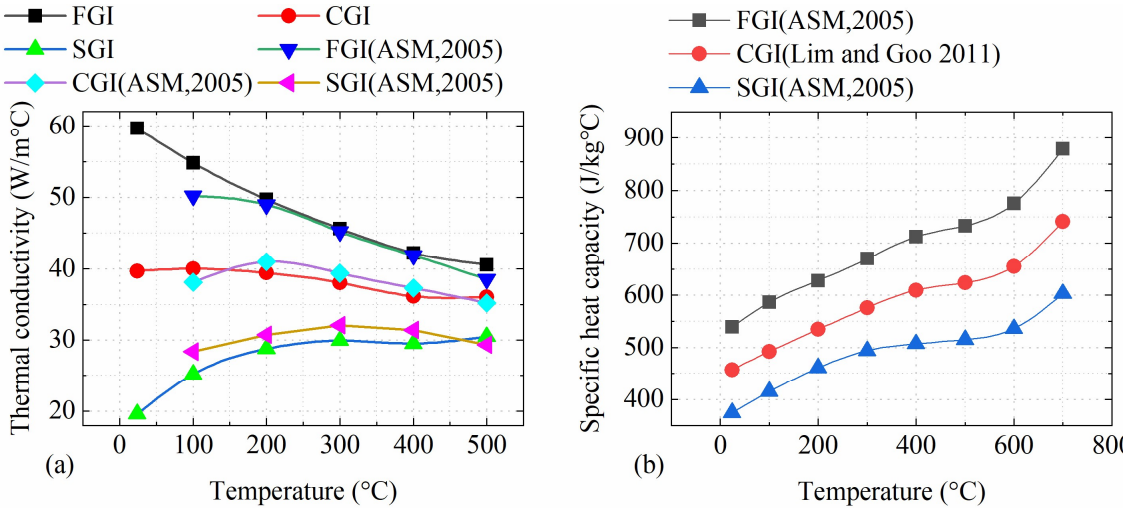

Figure 6.3 (a) Thermal conductivity [186] and specific heat capacity [20][122] (b) of the candidate materials

$$Stress\ ratio = \frac{von\ Mise\ equivalent\ stress}{Yield\ stress} \tag{6.2}$$

According to von Mise failure criteria, yield would occur when von Mise stress σ_e equals or exceeds yield stress σ_y, where σ_X, σ_Y, σ_Z are component stress: circumferential, axial, and radial stresses (Eq. 6.3) [187]. When the yield stress is exceeded by the von Mises stress elastic-plastic damage is calculated from plastic deformation. Elastic damage is calculated only if the von Mises stress is smaller than the yield stress [188]. This type of failure criteria (Von Mise equivalent) has been widely utilized in disc brake failure analysis [189][39][35], and in the thermo-mechanical fatigue behavior of the cast iron families [167][190].

$$\sigma_e = \left(\frac{(\sigma_X - \sigma_Y)^2 + (\sigma_Y - \sigma_Z)^2 + (\sigma_Z - \sigma_X)^2}{2} \right)^{1/2} \geq \sigma_y \tag{6.3}$$

6.5 Results and Discussion

Two-dimensional graphs of friction surface temperature are presented for temperature and von Mise stress. In addition, contour plots from ANSYS are also reported as additional evidence for spatial variation of temperature and stress. Only thermal analysis and corresponding temperature are observed for pad geometries. Meanwhile, both thermal and mechanical analyses are conducted for material selection.

6.5.1 Pad geometry investigations

The next set of questions aimed to investigate the applicability of the NAMHS model algorithm in handling spatial variation of heat and boundary conditions due to pad geometry. The analysis is performed for emergency braking of AALRT trailer bogie, with modified geometry. And, the spatial and contour results are extracted at the time when the maximum temperature is recorded, which is 3.5 sec.

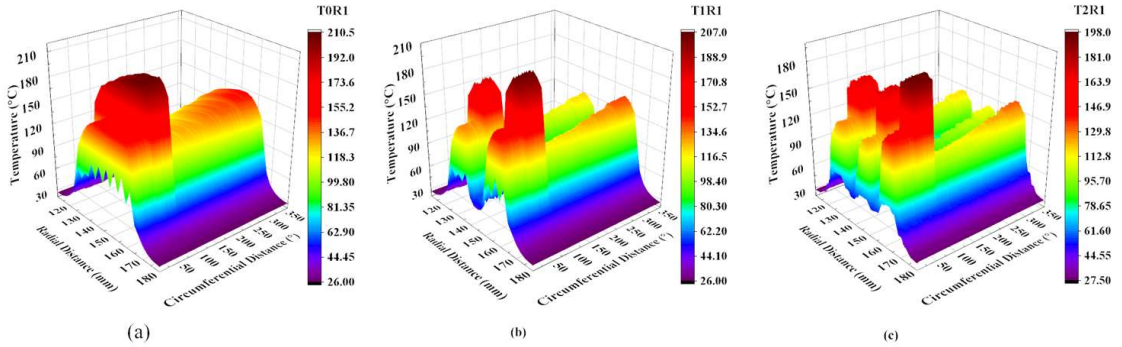

Figure 6.4 Maximum temperature distribution for tangential groove variation with one radial groove: (a) T0R1, (b) T1R1, (c) T2R1

As is apparent from Figure 6.4. a&c, the rise in the tangential groove from 0 (T0R1) to 2 (T2R1) demonstrates the reduction in temperature by 12.5˚C, for constant one radial groove. Besides, for the constant radial groove of two, the rise in the tangential groove from 0 (T0R2) to 2 (T2R2) uncovers the fall of temperature by 17˚C, as illustrated in Figure 6.5. a&c, respectively. The contour plot is displayed in Figure 6.6. a-f witnesses these findings. Based on these findings, it is reasonable to assume that the number of tangential grooves has more influence at a higher number of radial grooves.

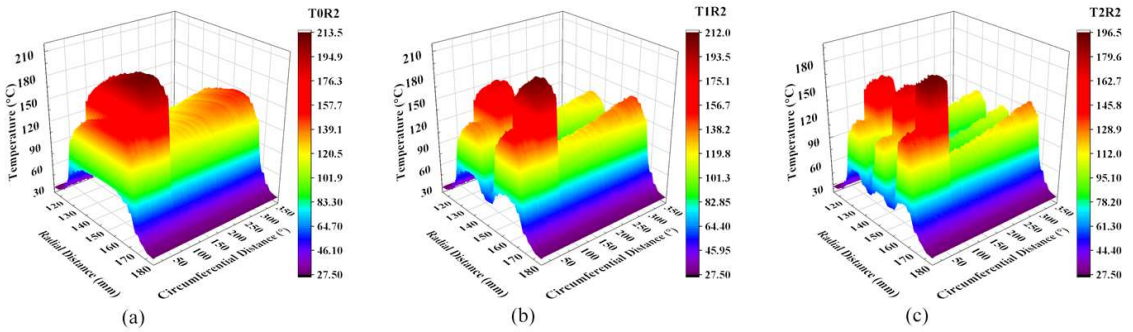

Figure 6.5 Maximum temperature distribution for tangential groove variation with two radial grooves: (a) T0R2,(b) T1R2,(c) T2R2

Another interesting aspect of this graph is the effect of the rising radial groove when the tangential groove is kept constant. It is observed that the temperature slightly rises (3˚C) with the increase of radial groove from 1-2 when there is no tangential groove. This is evident by comparing the results displayed in Figure 6.4. a and Figure 6.5. a. Likewise, the maximum temperature is raised by 5 ˚C when one tangential groove is utilized with radial groove variation from 1-2 (Figure 6.4. b and Figure 6.5. b). Contrary to these expectations, the maximum temperature is seen to drop by 1.5 ˚C when the radial groove is raised from 1 to 2, for 2 tangential grooves (2T2R) Figure 6.4. c & Figure 6.5. c. But this is not surprising, as the tangential groove's impact in reducing temperature is significant at its higher number. This implies the temperature-rising capability of the radial groove is counterbalanced by the temperature temperature-reducing effect of the tangential groove. These findings suggested that the presence of a higher number of radial grooves in pad design geometry is not encouraged, as it increases friction surface temperature.

The lack of radial grooves in many pad geometries supports this finding [68]. Even if available, the limitation of its maximum number to one [86] or two in AALRT (Figure 1.2.a) agrees with this study. Moreover, Benseddiq et al. 1996 [17] reported a reduction in temperature from 1136 to 600°C by varying tangential grooves from 1 to 4.

The finding reported in this study could eventually lead to recommendations for the implementation of the NAMHS model as a broadly applicable approach that can be used in conducting comparative analysis of pad geometry selection, that could reduce friction surface temperature. The approach presented in the NAMHS model algorithm is seen as suitable for handling spatial heat variation due to pad geometries.

6.5.2 Temperature results of the candidate materials

To demonstrate the comparative analysis of material from contradicting thermal and mechanical properties of the candidate materials, three critical analysis times are selected: maximum braking time (3.8574 sec), end of braking time (8.2071 sec), and end of the cooling time (184.2 sec). As can be seen from the Table 6.6, temperature, von Mise stress, and stress ratio are presented for all candidate materials at these critical times. Yield stress at the corresponding time and temperature is calculated from Figure 6.2.b by interpolation. Besides, these results are compatible with spatial and contour plots displayed on figures Figure 6.8. c-d and Figure 6.9. c-d.

From the data in Table 6.6 and Figure 6.7, it is apparent that the temperature is presented higher in SGI, CGI, and FGI, in reducing order, at maximum and end braking time. But this is not surprising, as it can be predicted easily from thermal properties. FGI has shown the best thermal performance, eventually displaying lower temperatures. The same argument is put forward for the remaining materials. Nonetheless, what stands out in this thermal analysis is the rate at which temperature is removed is interestingly higher in SGI, followed by CGI and FGI. This means the temperature is found to drop by 299.15 ^{o}C, 228.7^{o}C, and 183.8^{o}C in SGI, CGI, and FGI, respectively between cooling time and maximum temperature time (within 180.3426 sec).

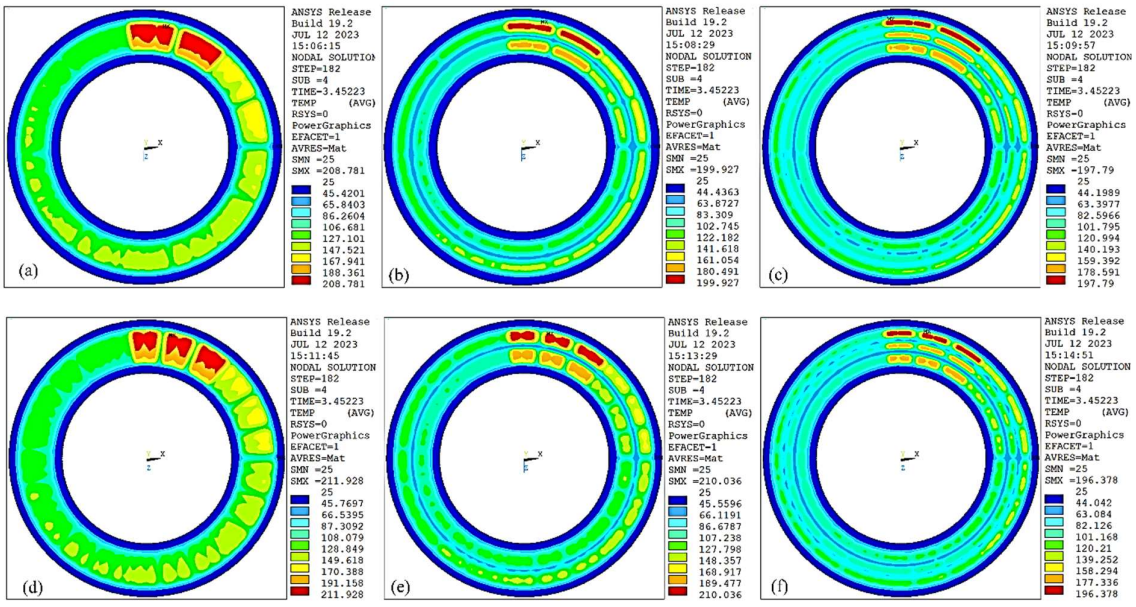

Figure 6.6 Friction surface temperature: (a) T0R1, (b) T1R1, (c) T2R1, (d) T0R2, (e) T1R2, (f) T2R2

One possible explanation for this result might be thermal diffusivity α (m^2/s), another significant thermal property (Eq. 6.3). It is the capability of a material to conduct thermal energy compared to its capability to store thermal energy [187]. Materials of higher α will reply quickly to variation in temperature through conduction, while materials of lower α will respond more sluggishly (taking a longer time to reach a new equilibrium condition, Figure 6.7. b).

Eventually, for SGI (material with lowest α), the temperature is concentrated on the friction surface and no further rise in temperature is expected in disc thickness, for the whole braking time. This is due to its poor thermal diffusivity α. As braking time is completed, convective heat dissipation is applied as a boundary condition on the friction surface (where a higher temperature is found). Consequently, SGI has a higher opportunity to dissipate heat, compared to other candidate materials (FGI, CGI), in which temperature is distributed in disc thickness, where no further chance to dissipate heat to the atmosphere.

Table 6.6 Temperature, Von Mise Stress, and Stress ratio of candidate materials at different times

Candidate materials	Comparison Parameters	Braking and cooling times (seconds)		
		3.8574 sec	8.2071 sec	184.2 sec
FGI	Temperature (°C)	246.5	158	62.7
	Von Mise Stress (Mpa)	424	482	216
	Yield stress (Mpa)	211.95	223.11	235.12
	Stress ratio	2	2.16	0.92
CGI	Temperature (°C)	287	176.5	58.3
	Von Mise Stress (Mpa)	620	710	280
	Yield stress (Mpa)	241.3	252.35	271.12
	Stress ratio	2.57	2.81	1.03
SGI	Temperature (°C)	358.7	217.5	59.55
	Von Mise Stress (Mpa)	872	1050	337
	Yield stress (Mpa)	268.91	327.93	362.27
	Stress ratio	3.24	3.20	0.93

$$\alpha = \frac{k_d}{\rho_d c_d} \qquad 6.1$$

Furthermore, a higher reduction in temperature is also observed between maximum braking time and end braking time (within time variation of 4.3497 sec) for SGI and CGI with a magnitude of 141.2 °C and 110.5°C, respectively, compared to FGI (88.5°C). Likewise, the same possible explanation could be proposed for this result is the removal of friction surface concentrated temperature by convection during braking at the location where heat flux is removed (Figure 6.8 a-d). This result suggests that SGI responds more quickly to friction surface heat spatial variation, followed by CGI and FGI. Hence, it could conceivably be hypothesized that the NAMHS model algorithm spatial variation of heat and boundary condition is more suitable for SGI, followed by CGI and FGI. Application of other traditional methods, like the axisymmetric model couldn't provide these results, because of incapability in varying heat and boundary conditions spatially on the friction surface.

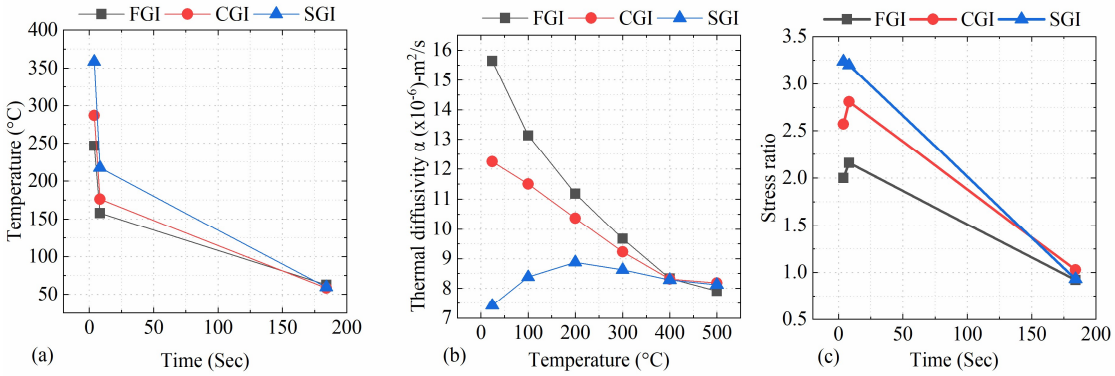

Figure 6.7 Candidate materials (a) temperature variation, (b) thermal diffusivity (c) stress ratio

Friction surface temperature spatial variation is presented for CGI and SGI at maximum temperature (3.8574 sec), radially, and circumferentially (Figure 6.8 a-b). Besides, the contour plot is depicted for the original disc geometry for both materials (Figure 6.8 c-d), and presented in Table 6.6 for FGI. For these presented results, the heat source is rotating counterclockwise and found within 78° to 128°.

This observation may support the hypothesis that SGI should be utilized in repeated braking where enough cooling time is available between consecutive braking. Whereas FGI seems

better in braking conditions with lower cooling time observed, including long braking time and drag or continuous braking. CGI is highlighted intermediate between these two extreme results.

6.5.3 Stress and stress ratio results of the candidate materials

The next section of the study is concerned with stress and its ratio, where the exact comparison of the materials is revealed. Because the contribution of both opposing thermal and mechanical properties in stress evaluation is clearly seen. To do so, stress spatial variation is illustrated in Figure 6.9 for CGI and SGI at the end braking time. For the remaining braking and cooling times, and for the FGI material, still Table 6.6 is utilized.

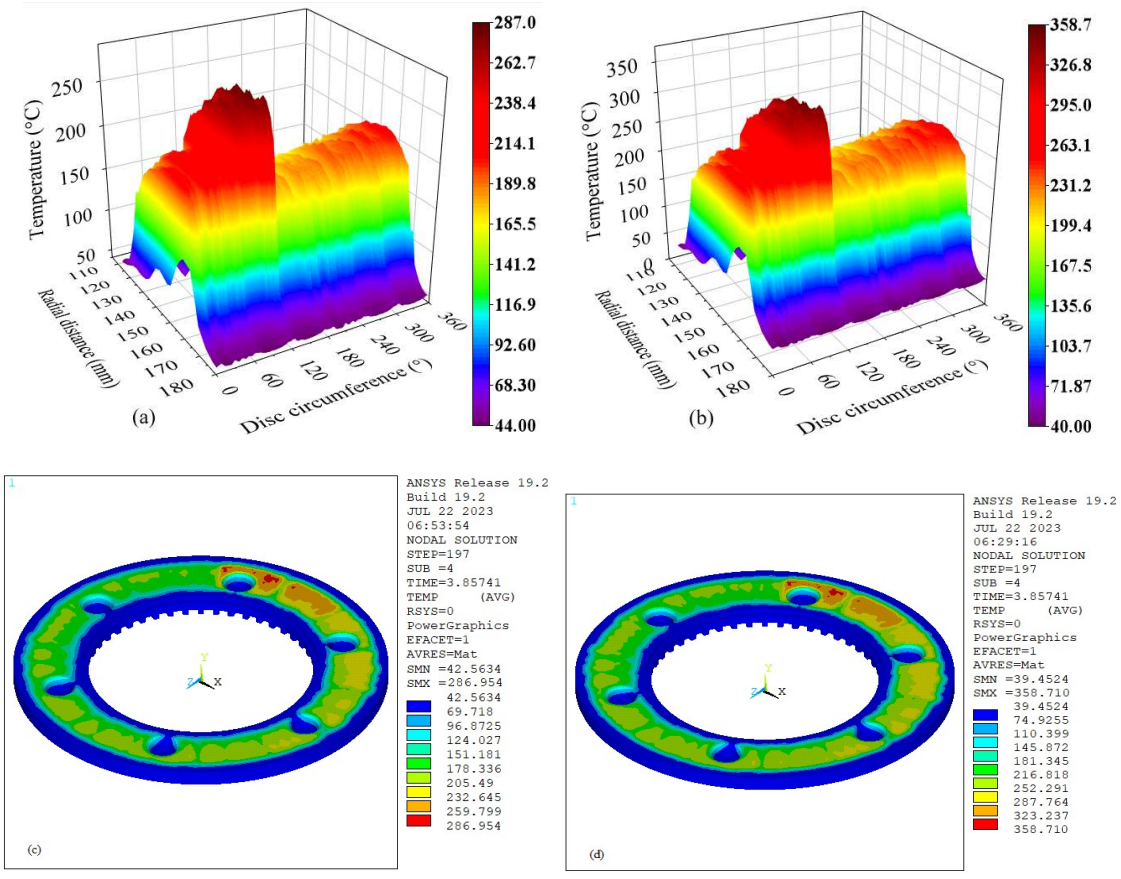

Figure 6.8 Spatial maximum temperature (3.8574 sec) distribution: Compacted (a,c) and spheroidal (b,d)

It can be seen from the data in Table 6.6 and Figure 6.9 that stress is higher in SGI, at any braking and cooling time, followed by CGI and FGI. These relationships may fully be

explained by their corresponding thermal performance. Spatial variation of stress result in friction surface-bolted disc is fully dominated by disc geometry, compared to the other factors contributing to spatial variations. This is manifested on nodes around bolt holes, due to their proximity to constrained boundary conditions *(u_x=x_y=u_z=0)* and stress concentrations at sharp edges. These nodes are displayed in Figure 6.9 every 60°, starting from 0° to 360°. Eventually, stress at these nodes is illustrated as high as 710MPa and 1050Mpa in CGI and SGI, respectively (Figure 6.9 a-b). Despite that, the contour plot displayed in Figure 6.9 c-d, unfortunately, reported higher results, 926MPa and 1320MPa for CGI and SGI, respectively. This inconsistency is due to the inclusion of nodes residing in the holes (and far from the friction surface), where extensive stress is reported due to constrained boundary conditions.

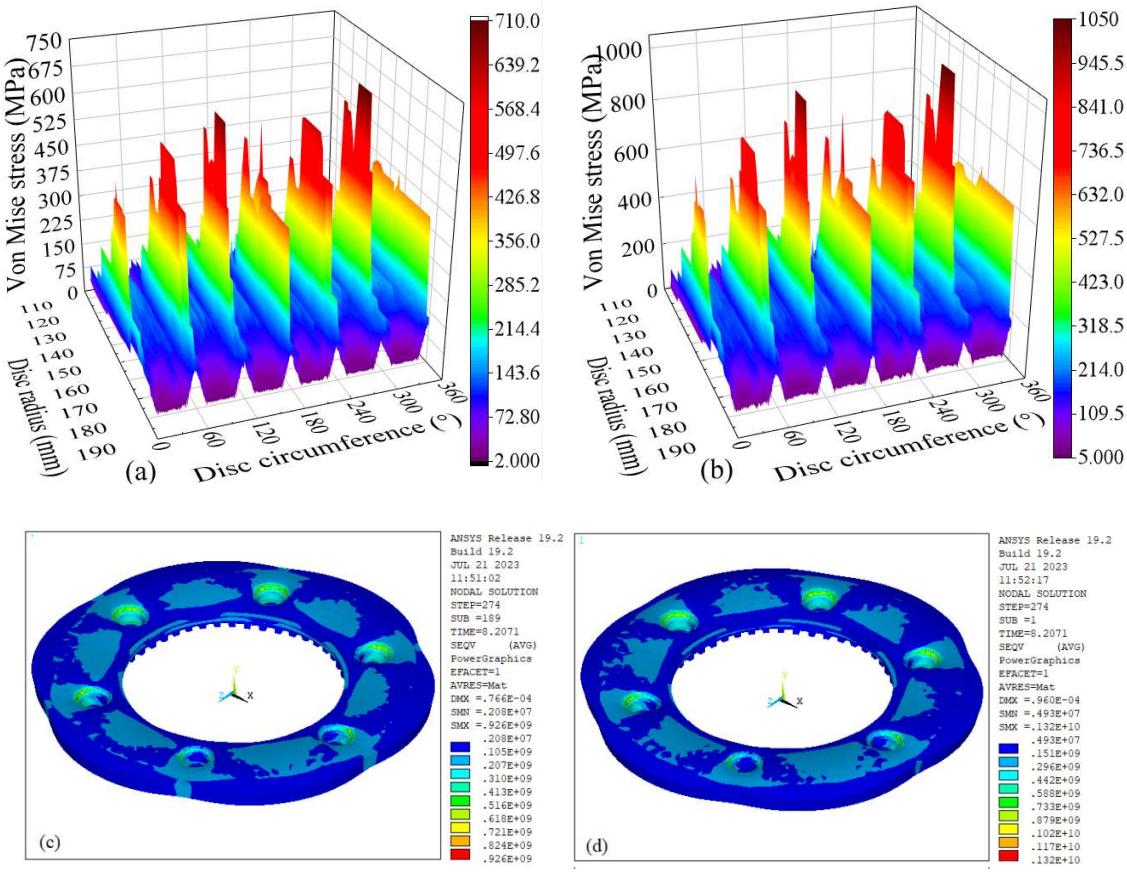

Figure 6.9 End braking von Mise stress CGI (a,c), SGI (b,d) station 3

But, to decide in which material the crack is early initiated is based on comparison with their respective yield stress, through stress ratio presented in Figure 6.10. Firstly, the yield stress is extracted from mechanical properties presented in Figure 6.2.b by interpolation at reported

temperature values in Table 6.6. And then stress ratio is calculated and presented for friction surface nodes of FGI, CGI and SGI at the end of braking and cooling times (Figure 6.10). And finally, the stress ratio is summarized and presented in Figure 6.7. c for all materials. According to this Figure, we can infer that FGI material is seen as the best material throughout braking time. This might seem due to the contribution of its lower Young's modulus and its higher thermal diffusivity [176]. Nonetheless, this trend is seen overtaken by SGI before 150 sec (within the cooling period). And if cooling time is continued beyond 184 sec, SGI might overtake FGI. This observation may support the hypothesis that the rate of concentrated heat removal is high from the SGI friction surface. And this concentrated heat is appeared due to its poor thermal diffusivity. Eventually, during and when braking is completed, friction surface with high heat is exposed to convective boundary conditions, leading to a steep reduction in stress ratio (Figure 6.7.c). It can thus be suggested that SGI is the best material whenever excess cooling time is allowed, and followed by CGI.

On the other hand, CGI is not shown to overpass FGI, at the end of cooling time. This result may be explained by the fact that it has a higher thermal expansion coefficient, which could reduce thermal stress and fatigue [176]. Therefore, this finding adds to a growing body of evidence that suggests FGI material for drag and long braking time. This type of braking is implemented to maintain constant braking on downhill driving. Besides, these results suggest SGI and CGI for short braking time with long cooling time. This type of braking is observed in emergency braking and frequent or repeated braking stations of light rail transit, including AALRT.

Fredriksson et al., 1988 [176] conducted friction surface temperature and stress comparison for FGI and SGI. The study was performed on the drum brake of a lorry with a load of 20000 kg driving with a speed of 110kph, to identify the best material. They reported that FGI has better thermal fatigue compared to CGI as well as SGI, in spite of its lower rupture stress. Besides, it was reported that its lower elasticity modulus and its higher heat diffusivity contributed to its success in thermal fatigue. Although their study is in good agreement with this investigation during braking time, they disregarded the effect of convective heat dissipation during cooling time, in which SGI might seem the best. Furthermore, the disc brake optimum material section was also investigated by Sakamoto & Hirakawa, 2006 [191] among different types of steel and cast iron materials. In application outside braking, other authors investigated better thermal fatigue material in engine cylinders, between different cast iron families [167][192].

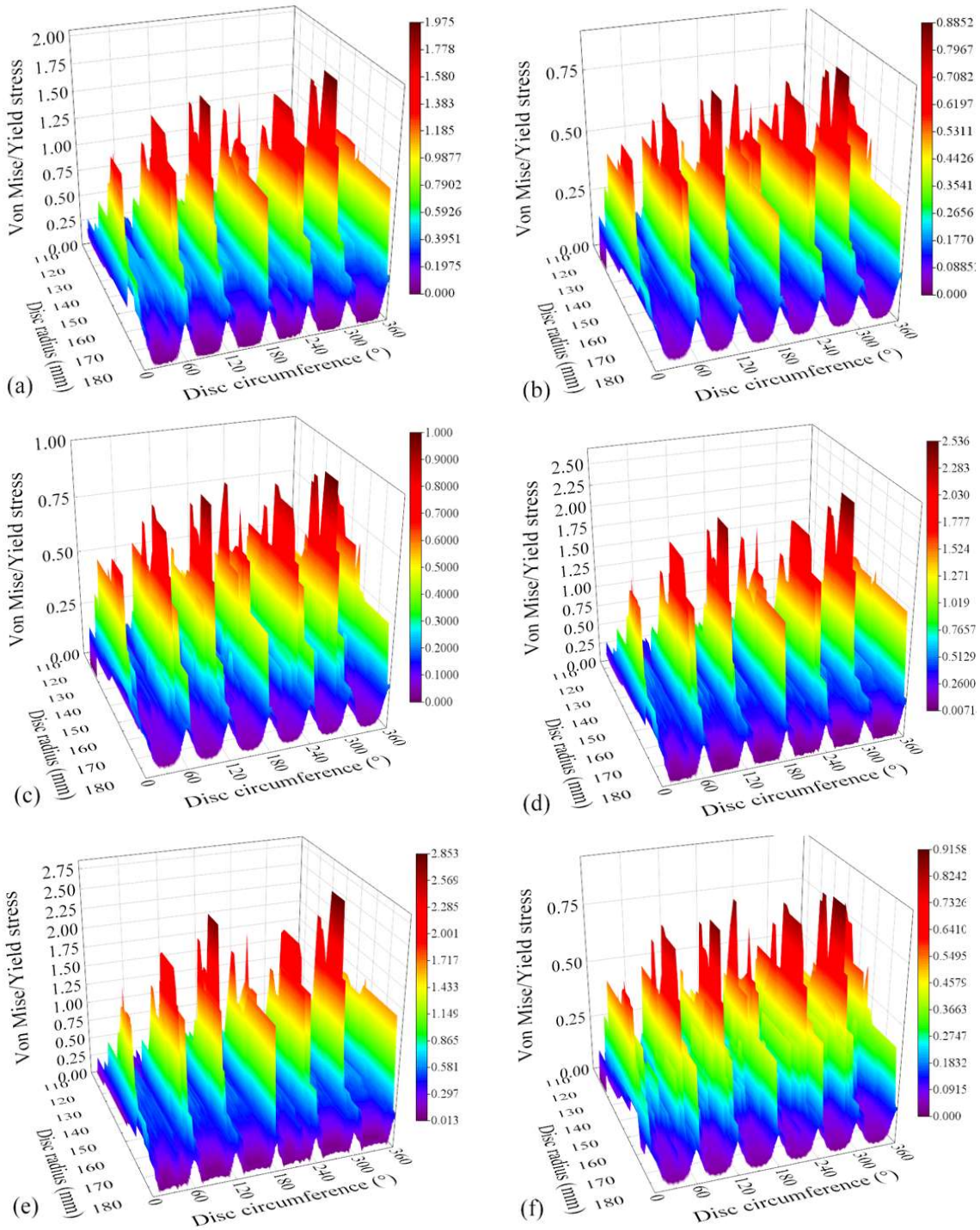

Figure 6.10 Spatial stress ratios at the end of braking (a,c,e) and cooling (b,d,f) for Flake (a-b), Compacted (c-d), and Spheroidal (e-f)

6.6 Conclusion and Recommendations

Comparative analysis of pad geometry selection is performed by the NAMHS model, based on the number and orientation of grooves on the pad friction surface. Thermal analysis is

conducted for emergency braking of trailer bogie on AALRT, and the key findings are summarized as follows:

- The NAMHS model algorithm has proven to be a successful method for accurately and efficiently identifying the optimal pad geometry through thermal analysis.
- Increasing the number of tangential grooves has a greater impact on reducing temperature compared to increasing the number of radial grooves.
- Encouraging a higher number of radial grooves in pad design geometry is not advisable, as it leads to an increase in friction surface temperature.

Comparative analysis of material selection is also conducted for three cast iron material families having an application in a disc brake. Thermal and mechanical analysis are performed sequentially, resulting in temperature, stress, and stress ratio as comparison parameters. Thermal fatigue is evaluated indirectly by the stress ratio presented as the ratio of von Mise equivalent stress and materials' yield stress. The main findings are highlighted as follows:

- The NAMHS model algorithm is observed successful model in identifying the best disc material, from structural analysis within acceptable accuracy and computational cost.
- The best material is selected based on the magnitude of cooling and braking time ranges
- In lower braking and cooling time, the best material is presented in reducing order as follows: FGI, CGI, SGI. Whenever sufficient cooling time is provided between braking frequencies, the selection of the best material in decreasing order is presented in reversed order as SGI, CGI, and FGI.
- The concentration of maximum temperature on the friction surface, due to poor thermal diffusivity revealed a greater chance to dissipate heat by convection in SGI, followed by CGI and FGI.
- NAMHS's capability in providing convective coefficient and heat flux simultaneously on friction surface served the SGI more, and other materials according to their maximum surface temperature
- Thermal conductivity, thermal expansion coefficients, Young's modulus, and yield stress are identified to affect stress and fatigue life

This study is focused on thermal and mechanical properties variation, in determining the temperature, stress, and stress ratio of the materials. But, many of the properties important for thermal fatigue are influenced by chemical composition, type of matrix, shape, morphology, and fraction of the graphite in cast iron families. Hence, recommendations for future studies

should include these parameters accompanied by the NAMHS model, for better selection of the best materials for rail vehicles disc brake.

References

[1] M. Jones, *Lancashire Railways: The History of Steam*. Countryside Books, 2012.

[2] M. Tirović, "Energy thrift and improved performance achieved through novel railway brake discs," *Appl. Energy*, vol. 86, no. 3, pp. 317–324, 2009, doi: 10.1016/j.apenergy.2008.04.017.

[3] M. Günay, M. E. Korkmaz, and R. Özmen, "An investigation on braking systems used in railway vehicles," *Eng. Sci. Technol. an Int. J.*, vol. 23, no. 2, pp. 421–431, 2020, doi: 10.1016/j.jestch.2020.01.009.

[4] A. Yevtushenko, M. Kuciej, and P. Wasilewski, "Experimental study on the temperature evolution in the railway brake disc," *Theor. Appl. Mech. Lett.*, vol. 9, no. 5, pp. 308–311, 2019, doi: https://doi.org/10.1016/j.taml.2019.06.008.

[5] A. Olshevskiy, A. Olshevskiy, O. Berdnikov, and C.-W. Kim, "Finite element analysis of railway disc brake considering structural, thermal, and wear phenomena," *Proc. Inst. Mech. Eng. Part C J. Mech. Eng. Sci.*, vol. 226, no. 7, pp. 1845–1860, 2012, doi: 10.1177/0954406211428705.

[6] A. A. Yevtushenko, M. Kuciej, P. Grzes, and P. Wasilewski, "Temperature in the railway disc brake at a repetitive short-term mode of braking," *Int. Commun. Heat Mass Transf.*, vol. 84, pp. 102–109, 2017, doi: 10.1016/j.icheatmasstransfer.2017.04.007.

[7] C. H. Gao, J. M. Huang, X. Z. Lin, and X. S. Tang, "Stress analysis of thermal fatigue fracture of brake disks based on thermomechanical coupling," *J. Tribol.*, vol. 129, no. 3, pp. 536–543, 2007, doi: 10.1115/1.2736437.

[8] G. S. Wang, R. Fu, and L. Zhao, "Numerical modeling and simulation analysis of temperature field of disc brake on trains," *Adv. Mater. Res.*, vol. 199–200, pp. 1492–1495, 2011, doi: 10.4028/www.scientific.net/AMR.199-200.1492.

[9] Z. Yang, J. Han, W. Li, Z. Li, L. Pan, and X. Shi, "Analyzing the mechanisms of fatigue crack initiation and propagation in CRH EMU brake discs," *Eng. Fail. Anal.*, vol. 34, pp. 121–128, 2013, doi: 10.1016/j.engfailanal.2013.07.004.

[10] S. C. Wu, S. Q. Zhang, and Z. W. Xu, "Thermal crack growth-based fatigue life prediction due to braking for a high-speed railway brake disc," *Int. J. Fatigue*, vol. 87, no. March, pp. 359–369, 2016, doi: 10.1016/j.ijfatigue.2016.02.024.

[11] M. Tirovic and G. Ali, “Design synthesis of non-symmetrically loaded high-performance disc brakes Part 1,” *Proc. Inst. Mech. Eng. Part F J. Rail Rapid Transit*, vol. 215, no. 2, pp. 101–109, 2001, doi: 10.1243/0954409011531431.

[12] Z. Li, J. Han, Z. Yang, and L. Pan, “The effect of braking energy on the fatigue crack propagation in railway brake discs,” *Eng. Fail. Anal.*, vol. 44, pp. 272–284, 2014, doi: 10.1016/j.engfailanal.2014.05.022.

[13] P. Zhang *et al.*, “Fade behaviour of copper-based brake pad during cyclic emergency braking at high speed and overload condition,” *Wear*, vol. 428–429, pp. 10–23, 2019, doi: https://doi.org/10.1016/j.wear.2019.01.126.

[14] A. Kumella Eticha, “Analysis of the Performance of Disc Brake System of Addis Ababa Light Rail Transit Using Temperature and Coefficient of Friction as a Parameter,” Addis Ababa University, 2016.

[15] Z. Wang, J. Han, J. P. Domblesky, Z. Li, X. Fan, and X. Liu, “Crack propagation and microstructural transformation on the friction surface of a high-speed railway brake disc,” *Wear*, vol. 428–429, pp. 45–54, 2019, doi: 10.1016/j.wear.2019.01.124.

[16] K. Handa, K. Ikeuchi, and F. Morimoto, “Temperature-dependent wear of tread-braked railway wheels,” *Wear*, vol. 452–453, p. 203265, 2020, doi: https://doi.org/10.1016/j.wear.2020.203265.

[17] N. Benseddiq, D. Weichert, J. Seidermann, and M. Minet, “Optimization of design of railway disc brake pads,” *Proc. Inst. Mech. Eng. Part F J. Rail Rapid Transit*, vol. 210, no. 1, pp. 51–61, 1996, doi: 10.1243/PIME_PROC_1996_210_326_02.

[18] B. Šamec, I. Potrč, and M. Šraml, “Low cycle fatigue of nodular cast iron used for railway brake discs,” *Eng. Fail. Anal.*, vol. 18, no. 6, pp. 1424–1434, 2011, doi: 10.1016/j.engfailanal.2011.04.002.

[19] X. Xie *et al.*, “Analysis of deep crack formation and propagation in railway brake discs,” *Eng. Fail. Anal.*, vol. 128, p. 105600, Oct. 2021, doi: 10.1016/j.engfailanal.2021.105600.

[20] C.-H. Lim and B.-C. Goo, “Development of compacted vermicular graphite cast iron for railway brake discs,” *Met. Mater. Int.*, vol. 17, no. 2, pp. 199–205, 2011, doi: 10.1007/s12540-011-0403-x.

[21] O. Chiello *et al.*, “Squeal noise generated by railway disc brakes: Experiments and stability computations on large industrial models,” in *Proceedings of Meetings on Acoustics*, 2013, vol. 19, doi: 10.1121/1.4799696.

[22] A. Heckmann, “A brake model with thermoelastic disc for the analysis of vehicle judder vibrations,” *Veh. Syst. Dyn.*, vol. 44, no. SUPPL. 1, pp. 360–367, 2006, doi: 10.1080/00423110600871574.

[23] D. J. Meng, L. J. Zhang, and Z. P. Yu, “Modeling and simulation of brake judder considering the effects of thermo-mechanical coupling,” *J. Vibroengineering*, vol. 16, no. 7, pp. 3637–3654, 2014.

[24] M. Tirovic and G. A. Sarwar, “Design synthesis of non-symmetrically loaded high-performance disc brakes part 2: Finite element modelling,” *Proc. Inst. Mech. Eng. Part F J. Rail Rapid Transit*, vol. 218, no. 2, pp. 89–104, 2004, doi: 10.1243/0954409041319678.

[25] A. A. Yevtushenko, M. Kuciej, P. Grzes, and P. Wasilewski, “Temperature in the railway disc brake at a repetitive short-term mode of braking,” *Int. Commun. Heat Mass Transf.*, vol. 84, pp. 102–109, 2017, doi: 10.1016/j.icheatmasstransfer.2017.04.007.

[26] K. T. Deressa and D. A. Ambie, “Thermal Load Simulations in Railway Disc Brake: A Systematic Review of Modelling Temperature, Stress and Fatigue,” *Arch. Comput. Methods Eng.*, vol. 29, no. 4, pp. 2271–2283, 2021, doi: 10.1007/s11831-021-09662-y.

[27] J. Tang, D. Bryant, H. Qi, B. Whiteside, and M. Babenko, “Simplified three-dimensional finite element hot-spotting modelling of a pin-mounted vented brake disc: an investigation of hot-spotting determinants,” *Proc. Inst. Mech. Eng. Part D J. Automob. Eng.*, vol. 232, no. 7, pp. 877–895, 2018, doi: 10.1177/0954407017713080.

[28] P. Dufrénoy, G. Bodovillé, and G. Degallaix, “Damage mechanisms and thermomechanical loading of brake discs,” *Eur. Struct. Integr. Soc.*, vol. 29, no. C, pp. 167–176, Jan. 2002, doi: 10.1016/S1566-1369(02)80073-5.

[29] C. H. Gao and X. Z. Lin, “Transient temperature field analysis of a brake in a non-axisymmetric three-dimensional model,” *J. Mater. Process. Technol.*, vol. 129, no. 1–3, pp. 513–517, 2002, doi: 10.1016/S0924-0136(02)00622-2.

[30] Z. Yuan, C. Tian, M. Wu, and G. Wang, “A modified uniformly distributed heat source

method for predicting braking temperature of railway brake disc," *Int. J. Rail Transp.*, vol. 10, no. 2, pp. 216–229, Feb. 2022, doi: 10.1080/23248378.2021.1882890.

[31] G. Pan and R. Cai, "Thermal Stress Coupling Analysis of Ventilated Disc Brake Based on Moving Heat Source," *Adv. Mater. Sci. Eng.*, vol. 2018, 2018, doi: 10.1155/2018/8162028.

[32] AALRT, *Operation and Maintenance Manual for 70% Low Floor Light Rail Vehicle Project in Addis Ababa, Ethiopia*. 2013.

[33] T. Mahmoudi, A. Parvizi, E. Poursaeidi, and A. Rahi, "Thermo-mechanical analysis of functionally graded wheel-mounted brake disk," *J. Mech. Sci. Technol.*, vol. 29, no. 10, pp. 4197–4204, 2015, doi: 10.1007/s12206-015-0914-3.

[34] A. Adamowicz and P. Grzes, "Influence of convective cooling on a disc brake temperature distribution during repetitive braking," *Appl. Therm. Eng.*, vol. 31, no. 14–15, pp. 2177–2185, Oct. 2011, doi: 10.1016/j.applthermaleng.2011.05.016.

[35] M. Tirovic and G. A. Sarwar, "Design synthesis of non-symmetrically loaded high-performance disc brakes part 3: Verification and optimization," *Proc. Inst. Mech. Eng. Part F J. Rail Rapid Transit*, vol. 218, no. 2, pp. 105–115, 2004, doi: 10.1243/0954409041319641.

[36] M. Tirovic, "Development of a wheel mounted disc brake for a high-speed train," *Proc. Inst. Mech. Eng. Part F J. Rail Rapid Transit*, vol. 212, no. 2, pp. 113–121, 1998, doi: 10.1243/0954409981530724.

[37] C. Jiguang and G. Fei, "Temperature field and thermal stress analyses of high-speed train brake disc under pad variations," *Open Mech. Eng. J.*, vol. 9, no. 1, pp. 371–378, 2015, doi: 10.2174/1874155X01509010371.

[38] M. Bayat, I. M. Alarifi, A. A. Khalili, T. M. A. A. El-Bagory, H. M. Nguyen, and A. Asadi, "Thermo-mechanical contact problems and elastic behaviour of single and double sides functionally graded brake disks with temperature-dependent material properties," *Sci. Rep.*, vol. 9, no. 1, 2019, doi: 10.1038/s41598-019-51450-z.

[39] L. Jiang, Y. L. Jiang, L. Yu, N. Su, and Y. D. Ding, "Thermal analysis for brake disks of SiC/6061 Al alloy co-continuous composite for CRH3 during emergency braking considering airflow cooling," *Trans. Nonferrous Met. Soc. China (English Ed.*, vol. 22,

no. 11, pp. 2783–2791, 2012, doi: 10.1016/S1003-6326(11)61533-1.

[40] X. D. Nong, Y. L. Jiang, M. Fang, L. Yu, and C. Y. Liu, “Numerical analysis of novel SiC3D/Al alloy co-continuous composites ventilated brake disc,” *Int. J. Heat Mass Transf.*, vol. 108, pp. 1374–1382, 2017, doi: 10.1016/j.ijheatmasstransfer.2016.11.108.

[41] J. J. Thomas, L. Verger, A. Bignonnet, and E. Charkaluk, “Thermomechanical design in the automotive industry,” *Fatigue Fract. Eng. Mater. Struct.*, vol. 27, no. 10, pp. 887–895, Oct. 2004, doi: 10.1111/j.1460-2695.2004.00746.x.

[42] P. Dufrénoy and D. Weichert, “A thermomechanical model for the analysis of disc brake fracture mechanisms,” *J. Therm. Stress.*, vol. 26, no. 8, pp. 815–828, 2003, doi: 10.1080/01495730390207622.

[43] G. Le Gigan, T. Vernersson, R. Lundén, and P. Skoglund, “Disc brakes for heavy vehicles: An experimental study of temperatures and cracks,” *Proc. Inst. Mech. Eng. Part D J. Automob. Eng.*, vol. 229, no. 6, pp. 684–707, 2015, doi: 10.1177/0954407014550843.

[44] M. Tirović, “Energy thrift and improved performance achieved through novel railway brake discs,” *Appl. Energy*, vol. 86, no. 3, pp. 317–324, 2009, doi: 10.1016/j.apenergy.2008.04.017.

[45] O. Maluf *et al.*, “Thermomechanical and Isothermal Fatigue Behavior of Gray Cast Iron for Automotive Brake Discs,” *New Trends Dev. Automot. Syst. Eng.*, 2011, doi: 10.5772/13970.

[46] X. Wirth, “Isobar enhances disc brake performance,” *Railw. Gaz. Int.*, vol. 153, no. 7, pp. 477,479-480, 1997.

[47] P. Dufrénoy, G. Bodovillé, and G. Degallaix, *Damage mechanisms and thermomechanical loading of brake discs*, vol. 29, no. C. 2002.

[48] S. Fujii, M. Saito, and D. Ph, “Transient Heat Transfer Analysis of High Speed Train Disc Brake Systems,” pp. 1–12, 2011.

[49] M. S. Milošević, D. S. Stamenković, A. P. Milojević, and M. M. Tomić, “Modeling thermal effects in braking systems of railway vehicles,” *Therm. Sci.*, vol. 16, no. SUPPL.2, 2013, doi: 10.2298/TSCI120503188M.

[50] U. Grivc, D. Deržič, and S. Muhič, "Numerical optimisation and experimental validation of divided rail freight brake disc crown," *J. Mod. Transp.*, vol. 27, no. 1, 2019, doi: 10.1007/s40534-018-0174-x.

[51] P. Wasilewski, "Frictional Heating in Railway Brakes: A Review of Numerical Models," *Arch. Comput. Methods Eng.*, vol. 27, no. 1, pp. 45–58, 2020, doi: 10.1007/s11831-018-9302-3.

[52] B. Ghadimi, F. Kowsary, and M. Khorami, "Thermal analysis of locomotive wheel-mounted brake disc," *Appl. Therm. Eng.*, vol. 51, no. 1–2, pp. 948–952, 2013, doi: 10.1016/j.applthermaleng.2012.10.051.

[53] M. Tirovic and C. H. Galindo-Lopez, "Convective heat dissipation from a wheel-hub-mounted railway brake disc," *Proc. Inst. Mech. Eng. Part F J. Rail Rapid Transit*, vol. 222, no. 4, pp. 355–365, 2008, doi: 10.1243/09544097JRRT135.

[54] S. Missori and A. Sili, "Optimizing Proportions of Railway Brake Discs by Temperature Transients Evaluation," *Proc. Inst. Mech. Eng. Part D Transp. Eng.*, vol. 202, no. 2, pp. 91–99, 1988, doi: 10.1243/pime_proc_1988_202_161_02.

[55] Y. C. Yang and W. L. Chen, "A nonlinear inverse problem in estimating the heat flux of the disc in a disc brake system," *Appl. Therm. Eng.*, vol. 31, no. 14–15, pp. 2439–2448, 2011, doi: 10.1016/j.applthermaleng.2011.04.008.

[56] B. Ghadimi, F. Kowsary, and M. Khorami, "Thermal analysis of locomotive wheel-mounted brake disc," *Appl. Therm. Eng.*, vol. 51, no. 1–2, pp. 948–952, 2013, doi: 10.1016/j.applthermaleng.2012.10.051.

[57] B. Ghadimi, R. Sajedi, and F. Kowsary, "3D investigation of thermal stresses in a locomotive ventilated brake disc based on a conjugate thermo-fluid coupling boundary conditions," *Int. Commun. Heat Mass Transf.*, vol. 49, pp. 104–109, 2013, doi: 10.1016/j.icheatmasstransfer.2013.10.009.

[58] X. Wu, J. Zuo, and M. Wu, "Heat simulation of high-speed train's brake disc considering the wind speed of disc surface influence on convection coefficient," in *Proceedings of the 2nd International Conference on Electronic and Mechanical Engineering and Information Technology, EMEIT 2012*, 2012, vol. 7, no. 7, pp. 145–149, doi: 10.2991/emeit.2012.28.

[59] L. Jiang, Y. Jiang, L. Yu, H. Yang, Z. Li, and Y. Ding, “Thermo-mechanical coupling analyses for al alloy brake discs with Al2O3-SiC(3D)/al alloy composite wear-resisting surface layer for high-speed trains,” *Materials (Basel).*, vol. 12, no. 19, 2019, doi: 10.3390/ma12193155.

[60] B. Šamec, G. Oder, T. Lerher, and I. Potrč, “Numerical analysis of railway brake disc,” *J. Shanghai Jiaotong Univ.*, vol. 16, no. 2, pp. 149–151, 2011, doi: 10.1007/s12204-011-1111-x.

[61] A. Afzal and M. Abdul Mujeebu, “Thermo-Mechanical and Structural Performances of Automobile Disc Brakes: A Review of Numerical and Experimental Studies,” *Arch. Comput. Methods Eng.*, vol. 26, no. 5, pp. 1489–1513, 2019, doi: 10.1007/s11831-018-9279-y.

[62] A. A. Yevtushenko and M. Kuciej, “One-dimensional thermal problem of friction during braking: The history of development and actual state,” *Int. J. Heat Mass Transf.*, vol. 55, no. 15–16, pp. 4148–4153, 2012, doi: 10.1016/j.ijheatmasstransfer.2012.03.056.

[63] P. Dufrénoy, “Two-/three-dimensional hybrid model of the thermomechanical behaviour of disc brakes,” *Proc. Inst. Mech. Eng. Part F J. Rail Rapid Transit*, vol. 218, no. 1, pp. 17–30, 2004, doi: 10.1243/095440904322804402.

[64] Z. Luo and J. Zuo, “Conjugate heat transfer study on a ventilated disc of high-speed trains during braking,” *J. Mech. Sci. Technol.*, vol. 28, no. 5, pp. 1887–1897, 2014, doi: 10.1007/s12206-014-0336-7.

[65] A. Modanloo and M. R. Talaee, “Analytical thermal analysis of advanced disk brake in high speed vehicles,” *Mech. Adv. Mater. Struct.*, vol. 27, no. 3, pp. 209–217, 2020, doi: 10.1080/15376494.2018.1472340.

[66] P. Dufrénoy and D. Weichert, “Prediction of railway disc brake temperatures taking the bearing surface variations into account,” *Proc. Inst. Mech. Eng. Part F J. Rail Rapid Transit*, vol. 209, no. 2, pp. 67–76, 1995, doi: 10.1243/PIME_PROC_1995_209_258_02.

[67] S. K. Cho, J. H. Choi, Y. M. Lee, and C. S. Seok, “Life Evaluation of a Disk Brake of Railway Vehicles Considering Pressure Distributions at a Frictional Surface,” *Key Eng. Mater.*, vol. 353–358, no. PART 1, pp. 303–306, 2007, doi:

10.4028/www.scientific.net/kem.353-358.303.

[68] D. J. Kim, Y. M. Lee, J. S. Park, and C. S. Seok, “Thermal stress analysis for a disk brake of railway vehicles with consideration of the pressure distribution on a frictional surface,” *Mater. Sci. Eng. A*, vol. 483–484, no. 1-2 C, pp. 456–459, 2008, doi: 10.1016/j.msea.2007.01.170.

[69] L. Tang and G. Wang, “Simulation analysis of train disc brake temperature field,” in *Proceedings of the 2012 International Conference on Computer Application and System Modeling, ICCASM 2012*, 2012, pp. 0718–0721, doi: 10.2991/iccasm.2012.182.

[70] H. Hong *et al.*, “A study on an analysis model for the thermo-mechanical behavior of a solid disc brake for rapid transit railway vehicles,” *J. Mech. Sci. Technol.*, vol. 32, no. 7, pp. 3223–3231, 2018, doi: 10.1007/s12206-018-0322-6.

[71] S. Zhang *et al.*, “Fatigue life calculation of high-power disc brake under thermal-mechanical coupling,” in *IOP Conference Series: Materials Science and Engineering*, 2019, vol. 692, no. 1, doi: 10.1088/1757-899X/692/1/012022.

[72] J. Chen and F. Gao, “Thermo-mechanical simulation of brake disc frictional character by moment of inertia,” *Res. J. Appl. Sci. Eng. Technol.*, vol. 7, no. 2, pp. 227–232, 2014, doi: 10.19026/rjaset.7.245.

[73] L. Zhang, Q. Yang, D. Weichert, and N. Tan, “Simulation and Analysis of Thermal Fatigue Based on Imperfection Model of Brake Discs,” *Pamm*, vol. 9, no. 1, pp. 533–534, 2009, doi: 10.1002/pamm.200910239.

[74] L. Yu, Y. L. Jiang, S. Lu, K. Luo, and H. Q. Ru, “Numerical simulation of brake discs of CRH3 high-speed trains based on Ansys,” in *Proceedings of the 1st World Congress on Integrated Computational Materials Engineering, ICME*, 2011, pp. 183–188, doi: 10.1002/9781118147726.ch25.

[75] B. Ghadimi, R. Sajedi, and F. Kowsary, “3D investigation of thermal stresses in a locomotive ventilated brake disc based on a conjugate thermo-fluid coupling boundary conditions,” *Int. Commun. Heat Mass Transf.*, vol. 49, pp. 104–109, 2013, doi: 10.1016/j.icheatmasstransfer.2013.10.009.

[76] Z. Li, J. Han, Z. Yang, and L. Pan, “The effect of braking energy on the fatigue crack propagation in railway brake discs,” *Eng. Fail. Anal.*, vol. 44, pp. 272–284, 2014, doi:

10.1016/j.engfailanal.2014.05.022.

[77] M. L. Wu, X. Y. Zhu, and J. Y. Zuo, *Secondary developments of ANSYS for temperature and stress field simulation of brake disc based on VB*, vol. 597. 2014.

[78] G. yi CHEN *et al.*, "Tribological properties and thermal-stress analysis of C/C-SiC composites during braking," *Trans. Nonferrous Met. Soc. China (English Ed.*, vol. 29, no. 1, pp. 123–131, 2019, doi: 10.1016/S1003-6326(18)64921-0.

[79] Z. Wang, J. Han, X. Liu, Z. Li, Z. Yang, and E. Chen, "Temperature evolution of the train brake disc during high-speed braking," *Adv. Mech. Eng.*, vol. 11, no. 1, 2019, doi: 10.1177/1687814018819563.

[80] W. Nong, F. Gao, R. Fu, and Q. Yu, "On structure function and the temperature and the thermal stress of brake discs," *Appl. Mech. Mater.*, vol. 80–81, pp. 521–526, 2011, doi: 10.4028/www.scientific.net/AMM.80-81.521.

[81] B. C. Goo, "A study on the contact pressure and thermo-elastic behavior of a brake disc-pad by infrared images and finite element analysis," *Appl. Sci.*, vol. 8, no. 9, 2018, doi: 10.3390/app8091639.

[82] G. Oder, M. Reibenschuh, F. Čuš, and I. Potrč, "Modelling and analysis of thermal and stress loads in train disc brakes - Braking from 250 km/h to standstill," *Stroj. Vestnik/Journal Mech. Eng.*, vol. 55, no. 7–8, pp. 494–502, 2009.

[83] R. El Abdi and H. Samrout, "Anisothermal modelling applied to brake discs," *Int. J. Non. Linear. Mech.*, vol. 34, no. 5, pp. 795–805, 1999, doi: 10.1016/s0020-7462(98)00042-0.

[84] L. Yu, Y. Jiang, S. Lu, H. Ru, and M. Fang, "FEM for brake discs of SiC 3D continuous ceramic reinforced 7075 Aluminum alloy for CRH3 trains applying Emergency Braking," *Appl. Mech. Mater.*, vol. 120, pp. 51–55, 2012, doi: 10.4028/www.scientific.net/AMM.120.51.

[85] P. Grzes, W. Oliferuk, A. Adamowicz, K. Kochanowski, P. Wasilewski, and A. A. Yevtushenko, "The numerical-experimental scheme for the analysis of temperature field in a pad-disc braking system of a railway vehicle at single braking," *Int. Commun. Heat Mass Transf.*, vol. 75, pp. 1–6, 2016, doi: 10.1016/j.icheatmasstransfer.2016.03.017.

[86] A. Yevtushenko, M. Kuciej, P. Grzes, and P. Wasilewski, "Comparative analysis of

temperature fields in railway solid and ventilated brake discs," *Materials (Basel).*, vol. 14, no. 24, p. 7804, Dec. 2021, doi: 10.3390/ma14247804.

[87] M. Tirovic and C. H. Galindo-Lopez, "Convective heat dissipation from a wheel-hub-mounted railway brake disc," *Proc. Inst. Mech. Eng. Part F J. Rail Rapid Transit*, vol. 222, no. 4, pp. 355–365, 2008, doi: 10.1243/09544097JRRT135.

[88] D. J. Kim, C. S. Seok, J. M. Koo, W. T. We, B. C. Goo, and J. I. Won, "Fatigue life assessment for brake disc of railway vehicle," *Fatigue Fract. Eng. Mater. Struct.*, vol. 33, no. 1, pp. 37–42, 2010, doi: 10.1111/j.1460-2695.2009.01412.x.

[89] G. Oder, B. Šamec, T. Lerher, and I. Potrě, "Numerical analysis of braking discs for a taurus class locomotive," *J. Shanghai Jiaotong Univ.*, vol. 16, no. 3, pp. 320–323, 2011, doi: 10.1007/s12204-011-1152-1.

[90] W. Nong, F. Gao, R. Fu, and X. Han, "Investigation of friction temperature in railway disc brake," *Adv. Mater. Res.*, vol. 479–481, pp. 202–206, 2012, doi: 10.4028/www.scientific.net/AMR.479-481.202.

[91] C. Baron Saiz, T. Ingrassia, V. Nigrelli, and V. Ricotta, "Thermal stress analysis of different full and ventilated disc brakes," *Frat. ed Integrita Strutt.*, vol. 9, no. 34, pp. 608–621, 2015, doi: 10.3221/IGF-ESIS.34.67.

[92] M. Pevec, G. Oder, I. Potrč, and M. Šraml, "Elevated temperature low cycle fatigue of grey cast iron used for automotive brake discs," *Eng. Fail. Anal.*, vol. 42, no. 1, pp. 221–230, Oct. 2014, doi: 10.1016/j.engfailanal.2014.03.021.

[93] G. Gigan, V. Norman, J. Ahlström, and T. Vernersson, "Thermomechanical fatigue of grey cast iron brake discs for heavy vehicles," *Proc. Inst. Mech. Eng. Part D J. Automob. Eng.*, vol. 233, no. 2, pp. 453–467, 2019, doi: 10.1177/0954407017739723.

[94] M. J. Han, C. H. Lee, T. W. Park, and S. P. Lee, "Low and high cycle fatigue of automotive brake discs using coupled thermo-mechanical finite element analysis under thermal loading," *J. Mech. Sci. Technol.*, vol. 32, no. 12, pp. 5777–5784, 2018, doi: 10.1007/s12206-018-1125-5.

[95] C. Lu, J. Mo, R. Sun, Y. Wu, and Z. Fan, "Investigation into Multiaxial Character of Thermomechanical Fatigue Damage on High-Speed Railway Brake Disc," *Vehicles*, vol. 3, no. 2, pp. 287–299, Jun. 2021, doi: 10.3390/vehicles3020018.

[96] D. J. Kim, C. S. Seok, J. M. Koo, W. T. We, B. C. Goo, and J. I. Won, “Fatigue life assessment for brake disc of railway vehicle,” *Fatigue Fract. Eng. Mater. Struct.*, vol. 33, no. 1, pp. 37–42, Dec. 2010, doi: 10.1111/j.1460-2695.2009.01412.x.

[97] G. Le Gigan, M. Ekh, T. Vernersson, and R. Lundén, “Modelling of grey cast iron for application to brake discs for heavy vehicles,” *Proc. Inst. Mech. Eng. Part D J. Automob. Eng.*, vol. 231, no. 1, pp. 35–49, 2017, doi: 10.1177/0954407016632090.

[98] G. Le Gigan, “Improvement in the brake disc design for heavy vehicles by parametric evaluation,” *Proc. Inst. Mech. Eng. Part D J. Automob. Eng.*, vol. 231, no. 14, pp. 1989–2004, 2017, doi: 10.1177/0954407016688421.

[99] I. ANSYS, *Coupled-Field Analysis Guide*, no. August. 2018.

[100] T. K. Kao, J. W. Richmond, and A. Douarre, “Brake disc hot spotting and thermal judder: an experimental and finite element study,” *Int. J. Veh. Des.*, vol. 23, no. 3, pp. 276–296, 2000, doi: 10.1504/ijvd.2000.001896.

[101] F. Talati and S. Jalalifar, “Investigation of heat transfer phenomena in a ventilated disk brake rotor with straight radial rounded vanes,” *J. Appl. Sci.*, vol. 8, no. 20, pp. 3583–3592, Dec. 2008, doi: 10.3923/jas.2008.3583.3592.

[102] R. A. García-León and E. Flórez-Solano, “Análisis dinámico de tres frenos de disco autoventilados,” *Ing. e Investig.*, vol. 37, no. 3, pp. 102–114, 2017, doi: 10.15446/ing.investig.v37n3.63381.

[103] R. A. G. León and E. P. Rojas, “Análisis de la cantidad del flujo de calor entre canales de refrigeración en tres discos de frenos ventilados,” *Ing. y Univ.*, vol. 21, no. 1, 2017, doi: 10.11144/Javeriana.iyu21-1.aahf.

[104] A. Belhocine and M. Bouchetara, “Thermomechanical analysis of vehicle braking,” *UPB Sci. Bull. Ser. D Mech. Eng.*, vol. 76, no. 1, pp. 71–84, 2014.

[105] R. Limpert, *Brake Design and Safety*, Second., vol. Volume 154, no. Issue 2. Society of Amomotive Engineers, 1999.

[106] R. Limpert, *Brake Design and Safety, Third Edition*, 3rd ed. Warrendale, Pa. (400 Commonwealth Dr., Wallendale PA USA) : Society of Automotive Engineers, 2011.

[107] U. Grivc, D. Deržič, and S. Muhič, “Numerical optimisation and experimental validation

of divided rail freight brake disc crown," *J. Mod. Transp.*, vol. 27, no. 1, pp. 1–10, 2019, doi: 10.1007/s40534-018-0174-x.

[108] R. El Abdi and H. Samrout, "A non-linear kinematic hardening model for a steel under complex loadings," *Comput. Struct.*, vol. 76, no. 5, pp. 675–681, 2000, doi: 10.1016/S0045-7949(99)00130-3.

[109] M. Kanapickas, "Report on Brake Disc. Coventry University, School of Mechanical, Aerospace and Automotive Engineering," 2015.

[110] M. A. Maleque, S. Dyuti, and M. M. Rahman, "Material selection method in design of automotive brake disc," *WCE 2010 - World Congr. Eng. 2010*, vol. 3, pp. 2322–2326, Jun. 2010.

[111] Z. S. Rak, "CMC material for train brake systems," *Br. Ceram. Trans.*, vol. 99, no. 6, pp. 270–273, Jun. 2000, doi: 10.1179/096797800681072.

[112] S. W. Kim, K. Park, S. H. Lee, K. H. Kang, and K. T. Lim, "Thermophysical properties of automotive metallic brake disk materials," *Int. J. Thermophys.*, vol. 29, no. 6, pp. 2179–2188, Dec. 2008, doi: 10.1007/s10765-008-0537-3.

[113] H. Nakanishi, K. Kakihara, A. Nakayama, and T. Murayama, "Development of aluminum metal matrix composites (Al-MMC) brake rotor and pad," *JSAE Rev.*, vol. 23, no. 3, pp. 365–370, 2002, doi: 10.1016/S0389-4304(02)00203-5.

[114] D. Wang *et al.*, "Enhanced thermal conductive 3D-SiC/Al-Si-Mg interpenetrating composites fabricated by pressureless infiltration," *Ceram. Int.*, vol. 43, no. 2, pp. 1755–1761, 2017, doi: 10.1016/j.ceramint.2016.10.104.

[115] R. Renz, G. Seifert, and W. Krenkel, "Integration of CMC brake disks in automotive brake systems," *Int. J. Appl. Ceram. Technol.*, vol. 9, no. 4, pp. 712–724, Jul. 2012, doi: 10.1111/j.1744-7402.2012.02812.x.

[116] Z. li, P. Xiao, B. Zhang, Y. Li, and Y. Lu, "Preparation and tribological properties of C/C-SiC brake composites modified by in situ grown carbon nanofibers," *Ceram. Int.*, vol. 41, Jun. 2015, doi: 10.1016/j.ceramint.2015.05.139.

[117] H. Nakanishi, K. Kakihara, A. Nakayama, and T. Murayama, "Development of aluminum metal matrix composites (Al-MMC) brake rotor and pad," *JSAE Rev.*, vol. 23, no. 3, pp. 365–370, 2002, doi: 10.1016/S0389-4304(02)00203-5.

[118] M. Rouhi, A. Angoshtari, and R. Naghdabadi, “Thermoelastic analysis of thick-walled finite-length cylinders of functionally graded materials,” *J. Therm. Stress. - J Therm. Stress.*, vol. 28, pp. 391–408, Mar. 2005, doi: 10.1080/01495730590916623.

[119] C.-M. Sonsino and H. Hanselka, “Fatigue life assessment of cast nodular iron disc brakes for railway vehicles,” *Rev. Metall. Cah. D’Informations Tech.*, vol. 104, no. 11, pp. 562–568, 2007, doi: 10.1051/metal:2007220.

[120] A. X. Pan, “Study on the casting defects of vermicular cast iron brake disc and the countermeasures,” in *Advanced Materials Research*, 2012, vol. 472–475, pp. 2645–2649, doi: 10.4028/www.scientific.net/amr.472-475.2645.

[121] G. Cueva, A. Sinatora, W. L. Guesser, and A. P. Tschiptschin, “Wear resistance of cast irons used in brake disc rotors,” *Wear*, vol. 255, no. 7–12, pp. 1256–1260, 2003, doi: 10.1016/S0043-1648(03)00146-7.

[122] ASM, *ASM Handbook , Volume 1 , Properties and Selection : Irons , Steels , and High Performance Alloys Section*, 10th ed. University of Illinois at Chicago: ASM International, 2005.

[123] B. C. Goo and C. H. Lim, “Thermal fatigue evaluation of cast iron discs for railway vehicles,” *Procedia Eng.*, vol. 2, no. 1, pp. 679–685, 2010, doi: 10.1016/j.proeng.2010.03.073.

[124] A. A. Yevtushenko and P. Grzes, “The FEM-Modeling of the frictional heating phenomenon in the pad/disc tribosystem (A Review),” *Numer. Heat Transf. Part A Appl.*, vol. 58, no. 3, pp. 207–226, 2010, doi: 10.1080/10407782.2010.497312.

[125] P. Dufrénoy and J. F. Brunel, “Thermal localizations in friction brakes,” *SAE Tech. Pap.*, 2008, doi: 10.4271/2008-01-2568.

[126] M. J. Han, C. H. Lee, T. W. Park, J. M. Park, and S. M. Son, “Coupled thermo-mechanical analysis and shape optimization for reducing uneven wear of brake pads,” *Int. J. Automot. Technol.*, vol. 18, no. 6, pp. 1027–1035, 2017, doi: 10.1007/s12239-017-0100-y.

[127] G. B. Kudal and M. R. Chopade, “Heat Transfer Characteristics of Ventilated Disc Brake Rotor with Diamond Pillars-A Review,” *Int. J. Curr. Eng. Technol.*, vol. 4, no. 4, pp. 219–222, 2011, doi: 10.14741/ijcet/22774106/spl.4.2016.45.

[128] A. Rashid and N. Strömberg, “An Efficient Sequential Approach for Simulation of Thermal Stresses in Disc Brakes,” pp. 1–6, 2012.

[129] D. Moher *et al.*, “Preferred reporting items for systematic reviews and meta-analyses: The PRISMA statement,” *Ann. Intern. Med.*, vol. 151, no. 4, pp. 264–269, Aug. 2009, doi: 10.7326/0003-4819-151-4-200908180-00135.

[130] J. Sokolska and P. Sokolski, *Thermal evaluation of operation of disc brakes made of selected materials*. 2019.

[131] M. Kim, J. G. Kim, and B. Goo, “Development of the Braking Performance Evaluation Technology for High-speed Brake Dynamometer,” *Int. J. Syst. Appl. Eng. Dev.*, vol. 6, no. 1, pp. 122–129, 2012.

[132] A. Roy, “Finite Element Analysis and Life Estimation of a Permanent Cylindrical Mold with ANSYS and Coffin-Manson Approach,” 2005.

[133] L. Wallis, E. Leonardi, B. Milton, and P. Joseph, “Air flow and heat transfer in ventilated disc brake rotors with diamond and tear-drop pillars,” *Numer. Heat Transf. Part A Appl.*, vol. 41, no. 6–7, pp. 643–655, May 2002, doi: 10.1080/104077802317418269.

[134] M. Renouf, F. Massi, N. Fillot, and A. Saulot, “Numerical tribology of a dry contact,” *Tribol. Int.*, vol. 44, no. 7–8, pp. 834–844, 2011, doi: 10.1016/j.triboint.2011.02.008.

[135] K. H. Huebner, D. L. Dewhirst, D. E. Smith, and T. G. Byrom, *The finite element method for engineers*, vol. 32, no. 10. John Wiley & Sons, 1995.

[136] E. Madenci, I. Guven, and B. Kilic, *Fatigue Life Prediction of Solder Joints in Electronic Packages with Ansys*®. 2003.

[137] A. Kumar and R. Sabarish, “Structural and thermal analysis of brake drum,” *Middle - East J. Sci. Res.*, vol. 20, no. 6, pp. 715–719, 2014, doi: 10.5829/idosi.mejsr.2014.20.06.11381.

[138] S. Prabhakar, S. Prakash, M. S. Kumar, and K. Annamalai, “Performance analysis of ventilated brake disc for its effective cooling,” *J. Chem. Pharm. Sci.*, vol. 7, no. March 2017, pp. 358–361, 2015.

[139] Ansys inc., *ANSYS Parametric Design Language*. Southpointe 2600 ANSYS Drive, PA 15317, 2018.

[140] R. A. G. León and E. P. Rojas, “Analysis of the amount of heat flow between cooling channels in three vented brake discs,” *Ing. y Univ.*, vol. 21, no. 1, 2017, doi: 10.11144/Javeriana.iyu21-1.aahf.

[141] M. Duzgun, “Investigation of thermo-structural behaviors of different ventilation applications on brake discs,” *J. Mech. Sci. Technol.*, vol. 26, no. 1, pp. 235–240, 2012, doi: 10.1007/s12206-011-0921-y.

[142] Ansys inc., “ANSYS Mechanical APDL Element Reference,” in *Chapter 2: Element Classifications*, Release 19., vol. 15317, no. November, Canonsburg: Southpointe 2600 ANSYS Drive, PA 15317, 2018, p. 9.

[143] S. Abbasi, S. Teimourimanesh, T. Vernersson, U. Sellgren, U. Olofsson, and R. Lundén, “Temperature and thermoelastic instability at tread braking using cast iron friction material,” *Wear*, vol. 314, no. 1–2, pp. 171–180, 2013, doi: 10.1016/j.wear.2013.11.028.

[144] A. Rashid, “Overview of disc brakes and related phenomena - A review,” *Int. J. Veh. Noise Vib.*, vol. 10, no. 4, pp. 257–301, 2014, doi: 10.1504/IJVNV.2014.065634.

[145] H. Ouyang, A. R. Abu-Bakar, and L. Li, “A combined analysis of heat conduction, contact pressure and transient vibration of a disk brake,” *Int. J. Veh. Des.*, vol. 51, no. 1–2, pp. 190–206, 2009, doi: 10.1504/ijvd.2009.027121.

[146] A. Belhocine and M. Bouchetara, “Thermal-mechanical coupled analysis of a brake disk rotor,” *J. Fail. Anal. Prev.*, vol. 13, no. 2, pp. 167–176, 2013, doi: 10.1007/s11668-012-9634-5.

[147] A. Belhocine, A. R. Abu Bakar, and M. Bouchetara, “Thermal and structural analysis of disc brake assembly during single stop braking event,” *Aust. J. Mech. Eng.*, vol. 14, no. 1, pp. 26–38, 2016, doi: 10.1080/14484846.2015.1093213.

[148] Ansys inc., “ANSYS Mechanical APDL Command reference,” in *N Commands*, Release 19., no. August, Canonsburg: Southpointe 2600 ANSYS Drive, PA 15317, 2018, p. 1022.

[149] Ansys inc., “ANSYS Mechanical APDL Basic Analysis Guide,” in *Chapter 3: Loading*, Release 19., vol. 15317, no. November, Canonsburg: Southpointe 2600 ANSYS Drive, PA 15317, 2018, p. 36.

[150] A. Belhocine and W. Z. Wan Omar, “Stres s analysis of automotive ventilate d disc

brake rotor and pads using finite element method," *Int. J. Multiphys.*, vol. 10, no. 1, pp. 75–97, 2016, doi: 10.21152/1750-9548.10.1.75.

[151] A. E. Sisson, "Thermal analysis of vented brake rotors," *SAE Tech. Pap.*, vol. 87, pp. 1685–1694, Mar. 1978, doi: 10.4271/780352.

[152] M. Fermér, "Brake Discs for Passenger Trains a Theoretical and Experimental Comparison of Temperatures and Stresses in Solid and Ventilated Discs," *Proc. Inst. Mech. Eng. Part F J. Rail Rapid Transit*, vol. 206, no. 1, pp. 37–46, Jan. 1992, doi: 10.1243/PIME_PROC_1992_206_215_02.

[153] S. Abbasi, S. Teimourimanesh, T. Vernersson, U. Sellgren, U. Olofsson, and R. Lundén, "Temperature and thermoelastic instability at tread braking using cast iron friction material," *Wear*, vol. 314, no. 1, pp. 171–180, 2013, doi: https://doi.org/10.1016/j.wear.2013.11.028.

[154] M. Petersson, "Two-dimensional finite element simulation of the thermal problem at railway block braking," *Proc. Inst. Mech. Eng. Part C J. Mech. Eng. Sci.*, vol. 216, no. 3, pp. 259–273, 2002, doi: 10.1243/0954406021524945.

[155] N. H. Kim, B. V Sankar, and A. V Kumar, *Introduction to Finite Element Analysis and Design*. Wiley, 2018.

[156] A. Adamowicz, "Finite element analysis of the 3d thermal stress state in a brake disk," *J. Theor. Appl. Mech.*, vol. 54, no. 1, pp. 205–218, 2016, doi: 10.15632/jtam-pl.54.1.205.

[157] T. Seifert, G. Maier, A. Uihlein, K.-H. Lang, and H. Riedel, "Mechanism-based thermomechanical fatigue life prediction of cast iron. Part II: Comparison of model predictions with experiments," *Int. J. Fatigue*, vol. 32, no. 8, pp. 1368–1377, 2010, doi: https://doi.org/10.1016/j.ijfatigue.2010.02.005.

[158] V. Tvergaard, "On localization in ductile materials containing spherical voids," *Int. J. Fract.*, vol. 18, no. 4, pp. 237–252, 1982, doi: 10.1007/BF00015686.

[159] M. Metzger, M. Knappe, and T. Seifert, "Models for Lifetime Estimation of Cast Iron Components," *MTZ Worldw.*, vol. 72, no. 10, pp. 70–77, 2011, doi: 10.1365/s38313-011-0101-6.

[160] M. Metzger, M. Leidenfrost, E. Werner, H. Riedel, and T. Seifert, "Lifetime Prediction

of EN-GJV 450 Cast Iron Cylinder Heads under Combined Thermo-Mechanical and High Cycle Fatigue Loading," *SAE Int. J. Engines*, vol. 7, no. 2, pp. 1073–1083, Mar. 2014, doi: 10.4271/2014-01-9047.

[161] S. Topouris, D. Stamenković, M. Olphe-Galliard, V. Popović, and M. Tirovic, "Heat dissipation from stationary passenger car brake discs," *Stroj. Vestnik/Journal Mech. Eng.*, vol. 66, no. 1, pp. 15–28, 2019, doi: 10.5545/SV-JME.2019.6002.

[162] M. H. Sabour and R. B. Bhat, "Lifetime prediction in creep-fatigue environment," *Mater. Sci. Pol.*, vol. 26, no. 3, pp. 563–584, 2008.

[163] C. Delprete and R. Sesana, "Proposal of a new low-cycle fatigue life model for cast iron with room temperature calibration involving mean stress and high-temperature effects," *Proc. Inst. Mech. Eng. Part C J. Mech. Eng. Sci.*, vol. 233, no. 14, pp. 5056–5073, 2019, doi: 10.1177/0954406219839089.

[164] E. Santecchia *et al.*, "A Review on Fatigue Life Prediction Methods for Metals," *Adv. Mater. Sci. Eng.*, vol. 2016, p. 9573524, 2016, doi: 10.1155/2016/9573524.

[165] M. Metzger and T. Seifert, "A mechanism-based model for LCF/HCF and TMF/HCF life prediction: Multiaxial formulation, finite-element implementation and application to cast iron," *Tech. Mech.*, vol. 32, no. 2, pp. 435–445, 2012.

[166] T. Seifert and H. Riedel, "Mechanism-based thermomechanical fatigue life prediction of cast iron. Part I: Models," *Int. J. Fatigue*, vol. 32, no. 8, pp. 1358–1367, 2010, doi: https://doi.org/10.1016/j.ijfatigue.2010.02.004.

[167] M. Metzger, K. Lee, and B. Nieweg, "On the thermo-mechanical fatigue behavior of the gray cast iron materials GJV-400 and GJL- 250 : Experiments , modelling and application to GJL-250 cylinder heads On the thermo-mechanical fatigue behavior of the gray cast iron materials GJV-400 and GJL-25," *Int. J. Fatigue*, vol. 53, no. August, pp. 58–66, Jul. 2013, doi: 10.13140/RG.2.1.4419.6968.

[168] K. T. Deressa and D. A. Ambie, "Non-Axisymmetric Modelling of Moving Heat Source for Spatial and Temporal Investigation of Temperature in Railway Vehicles Disc Brake," *Urban Rail Transit*, vol. 8, no. 3–4, pp. 198–216, 2022, doi: 10.1007/s40864-022-00176-9.

[169] A. Rashid and N. Strömberg, "Sequential simulation of thermal stresses in disc brakes

for repeated braking," *Proc. Inst. Mech. Eng. Part J J. Eng. Tribol.*, vol. 227, no. 8, pp. 919–929, 2013, doi: 10.1177/1350650113481701.

[170] W. Bena and G. Sirata, "Coupled Thermal Stress Analysis of Volvo Truck Disc Brake," *Adv. Mater. Sci. Eng.*, vol. 2022, 2022, doi: 10.1155/2022/7945264.

[171] N. Benhassine, A. Haiahem, and B. Bou-Said, "A comparative study of the transient thermomechanical behavior of friction of the ceramic brake discs: Temperature field effect," *J. Mech. Sci. Technol.*, vol. 33, no. 1, pp. 233–240, 2019, doi: 10.1007/s12206-018-1223-4.

[172] A. Kumar Shrivastava, R. Pandey, R. Kumar Gedam, N. Kumar, and T. Ravi Kiran, "Thermal analysis on car brake rotor using cast iron material with different geometries," *Mater. Today Proc.*, vol. 47, pp. 7019–7024, 2020, doi: 10.1016/j.matpr.2021.05.299.

[173] L. S. Lee J, "Thermal fracture endurance of cast irons with application study of pig iron ingot molds," *Metall. Mater. Trans. A*, pp. 1431–1440, 1995.

[174] W. J. F. Ruff G F, "Control of graphite structure and its effect on mechanical properties of gray iron," *Trans. Am. Foundry Soc.*, vol. 84, pp. 705–728, 1976.

[175] W. L. C. Lee S, "On thermal shock resistance of austenitic cast irons," *Metall. Mater. Trans. A*, vol. 22(8), pp. 1821–1831, 1991.

[176] H. Fredriksson, P. A. Sunnerkrantz, and P. Ljubinković, "Relationship between structure and thermal fatigue in cast iron," *Mater. Sci. Technol. (United Kingdom)*, vol. 4, no. 3, pp. 222–226, 1988, doi: 10.1179/mst.1988.4.3.222.

[177] J. A. Zieher F, Langmayr F, "Thermal mechanical fatigue simulation of cast iron cylinder heads," *SAE Tech. Pap.*, vol. 25(7), pp. 641–645.

[178] E. Nechtelberger, "Systematic Invenstigations to improve the quality of cylinder head cast iron with special reference to the tendency of crack formation," *Oesterreichishes Giesseti Inst.*, vol. 22, pp. 733–738, 1975.

[179] G. Wang, Z. Liu, Y. Li, and X. Chen, "Different thermal fatigue behaviors between gray cast iron and vermicular graphite cast iron," *China Foundry*, vol. 19, no. 3, pp. 245–252, 2022, doi: 10.1007/s41230-022-1204-1.

[180] G. hua Wang and Y. xiang Li, "Thermal conductivity of cast iron -A review," *China*

Foundry, vol. 17, no. 2, pp. 85–95, 2020, doi: 10.1007/s41230-020-9112-8.

[181] ISO 16112, "Compacted (vermicular) graphite cast irons - Classification," 2006.

[182] T. Seifert, G. Maier, A. Uihlein, K.-H. H. Lang, and H. Riedel, "Mechanism-based thermomechanical fatigue life prediction of cast iron. Part II: Comparison of model predictions with experiments," *Int. J. Fatigue*, vol. 32, no. 8, pp. 1368–1377, 2010, doi: https://doi.org/10.1016/j.ijfatigue.2010.02.005.

[183] G. Le Gigan and Chalmers tekniska högskola. Department of Applied Mechanics, "On improvement of cast iron brake discs for heavy vehicles : laboratory experiments, material modelling and fatigue life assessment," 2015.

[184] S. Biswas, C. Monroe, and T. Prucha, "Analysis of Published Cast Iron Experimental Data BT - Proceedings of the 3rd World Congress on Integrated Computational Materials Engineering (ICME 2015)," 2016, pp. 293–303.

[185] Sintercast, "Compacted Graphite Iron Compacted Graphite Iron -Material Data Sheet," *Supermetal CGI*, pp. 2–3.

[186] D. Holmgren and M. Selin, "Regression model describing the thermal conductivity of various cast irons," *Mater. Sci. Forum*, vol. 649, pp. 499–504, 2010, doi: 10.4028/www.scientific.net/MSF.649.499.

[187] R. Budynas and K. Nisbett, *Shigley's Mechanical Engineering Design*. McGraw-Hill Higher Education - VST E+p, 2014.

[188] Z. Zhan, W. Hu, B. Li, Y. Zhang, Q. Meng, and Z. Guan, "Continuum damage mechanics combined with the extended finite element method for the total life prediction of a metallic component," *Int. J. Mech. Sci.*, vol. 124–125, pp. 48–58, 2017, doi: 10.1016/j.ijmecsci.2017.03.002.

[189] F. Bagnoli, F. Dolce, and M. Bernabei, "Thermal fatigue cracks of fire fighting vehicles gray iron brake discs," *Eng. Fail. Anal.*, vol. 16, no. 1, pp. 152–163, 2009, doi: 10.1016/j.engfailanal.2008.01.009.

[190] M. Metzger and T. Seifert, "Computational assessment of the microstructure-dependent plasticity of lamellar gray cast iron—Part III: A new yield function derived from microstructure-based models," *Int. J. Solids Struct.*, vol. 87, pp. 102–109, 2016, doi: https://doi.org/10.1016/j.ijsolstr.2016.02.027.

[191] H. Sakamoto and K. Hirakawa, “Fracture analysis and material improvement of brake discs,” *JSME Int. Journal, Ser. A Solid Mech. Mater. Eng.*, vol. 48, no. 4, pp. 458–464, 2006, doi: 10.1299/jsmea.48.458.

[192] T. Seifert, P. von Hartrott, K. Boss, and P. Wynthein, “Lifetime Assessment of Cylinder Heads for Efficient Heavy Duty Engines Part I: A Discussion on Thermomechanical and High-Cycle Fatigue as Well as Thermophysical Properties of Lamellar Graphite Cast Iron GJL250 and Vermicular Graphite Cast Iron GJV450,” *SAE Int. J. Engines*, vol. 10, no. 2, pp. 359–365, 2017, doi: 10.4271/2017-01-0349.

APPENDIX A: ANSYS APDL PROGRAMS IMPLEMENTED TO EXECUTE THERMOMECHANICAL ANALYSIS ALGORITHMS

The Fortran algorithms applied are written here for original disc geometry, for service braking conditions, and for flake type cast iron material. It is assumed that for modified disc geometries and emergency braking, only input parameters are modified (disc geometries, braking conditions and material types). Besides, the commands are classified according to the sequence of actions to be executed.

- FE modeling: 3D disc geometry, material definition and meshing
- Heat input and boundary conditions calculations, and application
- Thermal analysis and
- Structural analysis

When these commands are implemented in ANSYS APDL, the left side commands and the right side commands preceded by exclamation mark (!), or "/com," should be inserted or read into the software.

Data Availability

The APDL programming commands used during the current study are available from the corresponding author on reasonable request.

APPENDIX D: LIST OF PUBLICATIONS

No.	References	Publisher
1	Deressa, K. T., & Ambie, D. A. (2022). Thermal Load Simulations in Railway Disc Brake: A Systematic Review of Modelling Temperature, Stress and Fatigue. Archives of Computational Methods in Engineering, 29(4), 2271–2283. https://doi.org/10.1007/s11831-021-09662-y	Springer
2	Deressa, K. T., & Ambie, D. A. (2022). Non-Axisymmetric Modelling of Moving Heat Source for Spatial and Temporal Investigation of Temperature in Railway Vehicles Disc Brake. Urban Rail Transit, 8(3–4), 198–216. https://doi.org/10.1007/s40864-022-00176-9	Springer
3	Deressa, K. T., & Ambie, D. A. (2022). Non-axisymmetric Modeling of a Moving Heat Source for Thermal Stress and Fatigue Analysis of Railway Vehicle Disc Brakes. Urban Rail Transit, 8(3–4), 198–216. https://doi.org/10.1007/s40864-023-00207-z	Springer
4	de Dieu, H. J., Deressa, K. T., Edison, T., & Rodger, M. (2023). A Review on Finite Element Method for Static Analysis of a Passenger Bogie Frame. AMERICAN JOURNAL OF ADVANCED SCIENTIFIC RESEARCH, 23.	Scienc Publishing group (Co-authored)
5	Deressa, K. T., & Ambie, D. A. (2024). Implementation of Non-Axisymmetric Moving Heat Source modeling in Railway Vehicles Disc Geometry and Material Selection. 3rd National Research symposium on "Emerging technologies for Building Green Economy", Adama Science and Technology University.	Coference

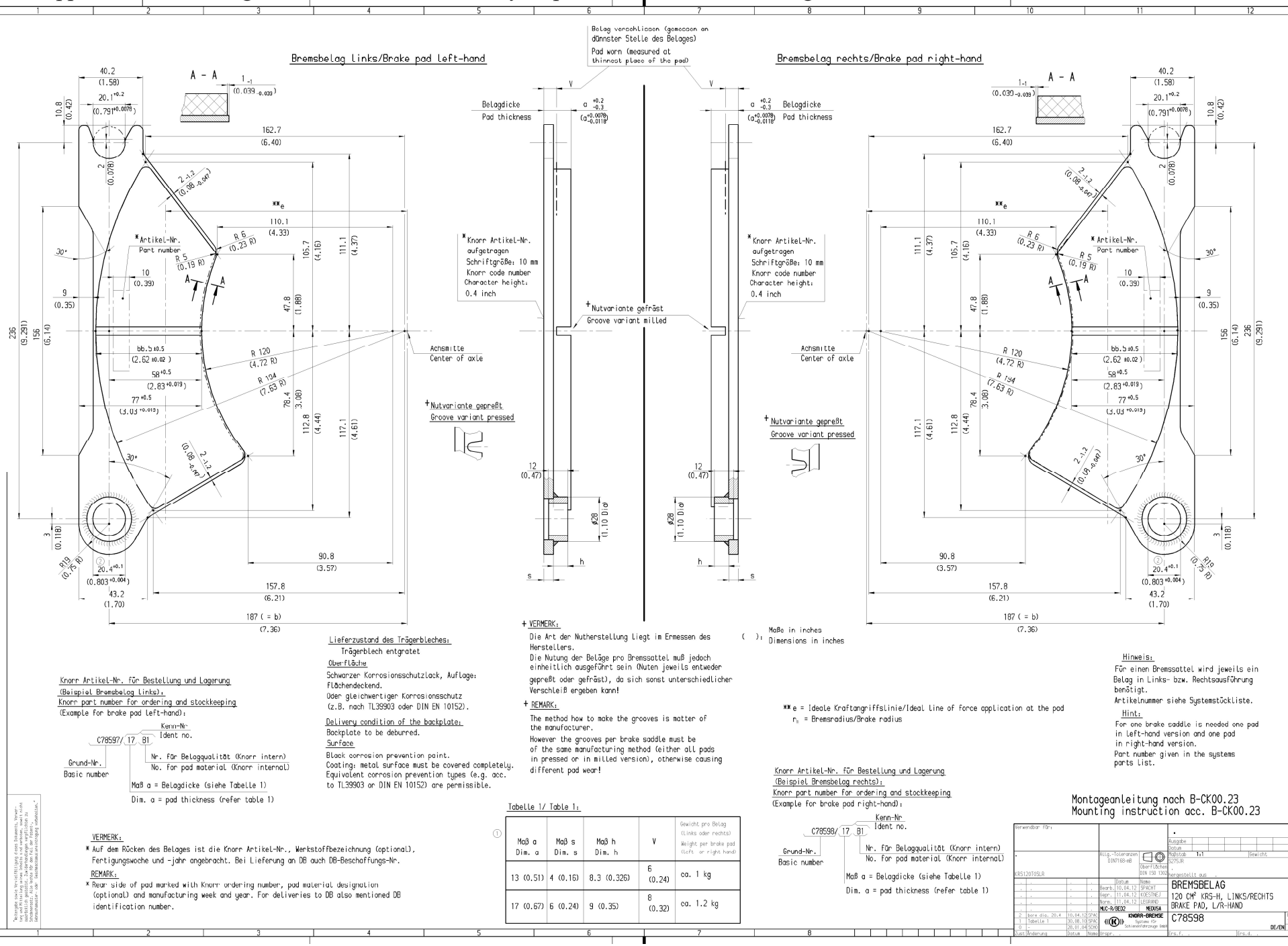

Knorr Artikel-Nr. für Bestellung und Lagerung
(Beispiel Bremsbelag links):
Knorr part number for ordering and stockkeeping
(Example for brake pad left-hand):

C78597/ 17 B1
- C78597: Grund-Nr. / Basic number
- 17: Maß a = Belagdicke (siehe Tabelle 1) / Dim. a = pad thickness (refer table 1)
- B1: Nr. für Belaggualität (Knorr intern) / No. for pad material (Knorr internal)
- Kenn-Nr. / Ident no.

Lieferzustand des Trägerbleches:
Trägerblech entgratet
Oberfläche
Schwarzer Korrosionsschutzlack, Auflage: flächendeckend.
Oder gleichwertiger Korrosionsschutz (z.B. nach TL39903 oder DIN EN 10152).

Delivery condition of the backplate:
Backplate to be deburred.
Surface
Black corrosion prevention paint.
Coating: metal surface must be covered completely. Equivalent corrosion prevention types (e.g. acc. to TL39903 or DIN EN 10152) are permissible.

+ VERMERK:
Die Art der Nutherstellung Liegt im Ermessen des Herstellers.
Die Nutung der Beläge pro Bremssattel muß jedoch einheitlich ausgeführt sein (Nuten jeweils entweder gepreßt oder gefräst), da sich sonst unterschiedlicher Verschleiß ergeben kann!

+ REMARK:
The method how to make the grooves is matter of the manufacturer.
However the grooves per brake saddle must be of the same manufacturing method (either all pads in pressed or in milled version), otherwise causing different pad wear!

** e = Ideale Kraftangriffslinie/Ideal Line of force application at the pad
r_s = Bremsradius/Brake radius

Hinweis:
Für einen Bremssattel wird jeweils ein Belag in Links- bzw. Rechtsausführung benötigt.
Artikelnummer siehe Systemstückliste.

Hint:
For one brake saddle is needed one pad in left-hand version and one pad in right-hand version.
Part number given in the systems parts list.

Knorr Artikel-Nr. für Bestellung und Lagerung
(Beispiel Bremsbelag rechts):
Knorr part number for ordering and stockkeeping
(Example for brake pad right-hand):

C78598/ 17 B1
- C78598: Grund-Nr. / Basic number
- 17: Maß a = Belagdicke (siehe Tabelle 1) / Dim. a = pad thickness (refer table 1)
- B1: Nr. für Belaggualität (Knorr intern) / No. for pad material (Knorr internal)
- Kenn-Nr. / Ident no.

VERMERK:
* Auf dem Rücken des Belages ist die Knorr Artikel-Nr., Werkstoffbezeichnung (optional), Fertigungswoche und -jahr angebracht. Bei Lieferung an DB auch DB-Beschaffungs-Nr.

REMARK:
* Rear side of pad marked with Knorr ordering number, pad material designation (optional) and manufacturing week and year. For deliveries to DB also mentioned DB identification number.

Tabelle 1/ Table 1:

① Maß a Dim. a	Maß s Dim. s	Maß h Dim. h	V	Gewicht pro Belag (Links oder rechts) Weight per brake pad (left or right hand)
13 (0.51)	4 (0.16)	8.3 (0.326)	6 (0.24)	ca. 1 kg
17 (0.67)	6 (0.24)	9 (0.35)	8 (0.32)	ca. 1.2 kg

Montageanleitung nach B-CK00.23
Mounting instruction acc. B-CK00.23

Verwendbar für:	KRS120TGSLR
Allg.-Toleranzen DIN7168-mB	Oberflächen DIN ISO 1302
Maßstab 1:1	Gewicht - kg
Ausgabe	
Datum	
Zeichnungsnummer	C2753R
Hergestellt aus	-
Bearb. 10.04.12 SPACHT	
Gepr. 11.04.12 KOESTNER	
Norm 11.04.12 LEGRAND	
MUC-S/BEQ2 MEDUSA	
KNORR-BREMSE Systeme für Schienenfahrzeuge GmbH	
Benennung	BREMSBELAG 120 CM² KRS-H, LINKS/RECHTS BRAKE PAD, L/R-HAND
Ersatz für: -	C78598
Ersetzt durch: -	Blatt 1 Bl.
Ers. f. -	DE/EN
Ers. d. -	

Zust.	Änderung	Datum	Name	Urspr.
2	bore dia. 20.4	10.04.12	SPAC	
1	Tabelle 1	30.08.10	SPAC	
0	-	28.01.04	SCHU	

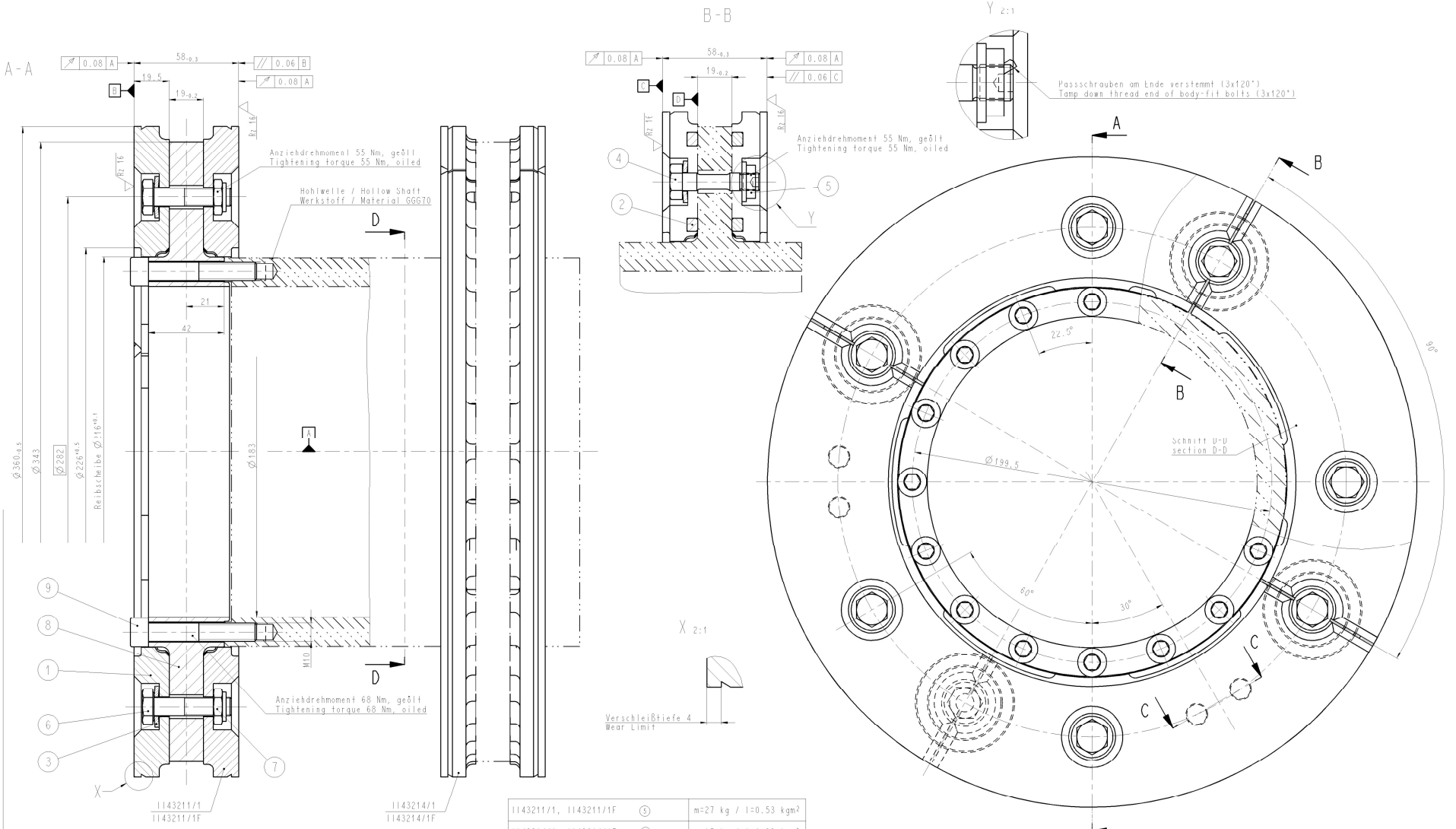

10	PIN	12
9	STUD BOLT	16
8	AXILE PLATE	1
7	LOCK NUT(HEX HEAD BOLT)	4
6	HEX HEAD BOLT	4
5	LOCK NUT (BODY-FIT)	2
4	BODY-FIT BOLT	2
3	SPRING WASHER	6
2	CONNECTING RING	8
1	DISC	2
PART NO	PART NAME	QUANTITY

Anschlußmaße an die Hohlwelle siehe Fertigungsanweisung C88376

Connecting dimensions of the hollow shaft see manufacturing instructions C88376

I143211/1, I143211/1F (5)	m=27 kg / I=0.53 kgm²
I143214/1, I143214/1F (5)	m=15 kg / I=0.32 kgm²
Max. Restunwucht bezügl. A Max. imbalance related to A	U = 16 gm
Zugehöriger Bremssattel Associated Brake Caliper	HC1P28N
Bremsbelag 120 cm² Brake Pad 120 cm²	C78597/17.. C78598/17..
Belageinbaumaß b Pad mounting distance b	b = 171 ±0.5
Richtwert für Kraftangriffslinie e Distance e for force application	e = 136 (3)
Bremsradius Brake Radius	rm = 147 (3)

I143211/1	Reibscheibe, Nabe und Verbindungselemente (Pos. 1 bis 10) Friction disc, hub and fixing elements (item 1 to 10)
I143214/1	Reibscheibe und Verbindungsteile (Pos. 1 bis 2, 10) Friction disc and fixing elements (item 1 to 2, 10)
I143211/1F, I143214/1F	Ausführung für SNCF SNCF version
Sachnummer	Ausführung

Verwendbar für: S70

Ausgabe . Datum . Maßstab 1:1 Gewicht 26.5 kg

I143211/1, I143214/1
I143211/1F, I143214/1F
W360B058XGGH

Allg. Toleranzen ISO 2768-mK
Oberflächen DIN ISO 1302

Reibscheibe aus Grauguss
Friction disc of grey-cast iron
hergestellt aus .

				Datum	Name
.	.	.	Bearb.	30.06.08	SPACHT
.	.	.	Gepr.	20.02.09	MOSBACH
5	SACH-NR. ERWEIT	30.06.08	SPAT	Norm.	23.02.09	LEGRAND
4	DETAIL 1	02.05.08	SEIT	MUC-R/BEEZ	Prof ENGINEER
3	RICHRADIUS 147	30.01.64	SEIT	KNORR-BREMSE Systeme für Schienenfahrzeuge GmbH	
2	SATTEL	11.06.92	SEIT		
1	NOTIZ	05.06.92	SEIT		
Zust.	Änderung	Datum	Name	Ursp.	

BREMSSCHEIBE
360/226X58-14H
BRAKE DISC

C88375/1 Blatt

Ers. f. . Ers. d. . DE/EN 1 Bl.

C88375.1 (A1) 5 8+ 3

"Weitergabe sowie Vervielfältigung dieses Dokuments, Verwertung und Mitteilung seines Inhalts sind verboten, soweit nicht ausdrücklich gestattet. Zuwiderhandlungen verpflichten zu Schadenersatz. Alle Rechte für den Fall der Patenterteilung oder Gebrauchsmuster-Eintragung vorbehalten."

Web of Science™

Web of Science CV
Prepared on June 28th 2024

Kejela Temesgen Deressa

https://www.webofscience.com/wos/author/rid/ABG-9203-2021
Web of Science ResearcherID: ABG-9203-2021
ORCiD: 0000-0002-6791-8751

Publication Metrics

For manuscripts published from date range June 2019 - June 2024

2	15
H-index	Sum of Times Cited
3	3
Total Publications	Web of Science Core Collection Publications

For all time

2	15
H-index	Sum of Times Cited
3	3
Total Publications	Web of Science Core Collection Publications

Publication Impact Over Time

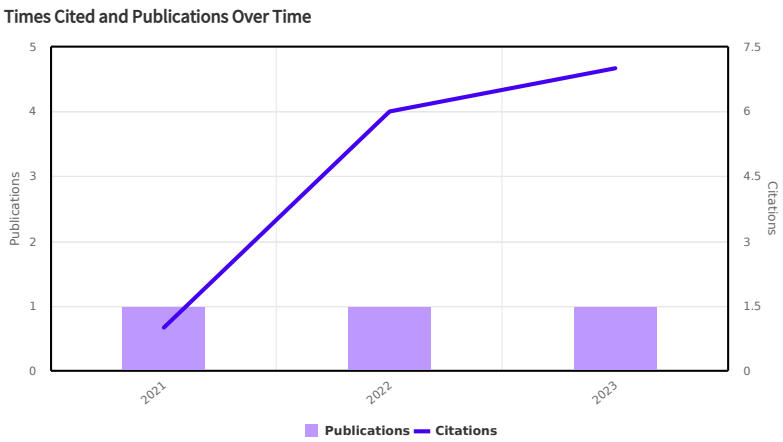

Publishing Summary

For manuscripts published from date range June 2019 - June 2024

(2) Urban Rail Transit	(1) Archives of Computational Meth…

Publications

For manuscripts published from date range June 2019 - June 2024 (3)	Times Cited (All time)
Non-axisymmetric Modeling of a Moving Heat Source for Thermal Stress and Fatigue Analysis of Railway Vehicle Disc Brakes Published: Dec 2023 in Urban Rail Transit DOI: 10.1007/S40864-023-00207-Z	0
Non-Axisymmetric Modelling of Moving Heat Source for Spatial and Temporal Investigation of Temperature in Railway Vehicles Disc Brake Published: Oct 2022 in Urban Rail Transit DOI: 10.1007/S40864-022-00176-9	3
Thermal Load Simulations in Railway Disc Brake: A Systematic Review of Modelling Temperature, Stress and Fatigue Published: 2021 in Archives of Computational Methods in Engineering DOI: 10.1007/S11831-021-09662-Y	12

Verified Reviews

Review Summary

Reviewer Summary

For manuscripts reviewed from date range June 2019 - June 2024

(2) Science Progress	(1) Metallurgical and Materials Engi...

3 REVIEWS OF 2 MANUSCRIPTS

For manuscripts published from date range June 2019 - June 2024

Numerical Simulation of Wear in Wind Turbine Brake Pads Reviewed: May 2022 for Metallurgical and Materials Engineering

Fatigue life prediction of brake discs for high-speed train via thermal stress
2 rounds from Jan 2022 to Mar 2022 for Science Progress

APPENDIX D: LIST OF PUBLICATIONS

No.	References	Publisher
1	Deressa, K. T., & Ambie, D. A. (2022). Thermal Load Simulations in Railway Disc Brake: A Systematic Review of Modelling Temperature, Stress and Fatigue. Archives of Computational Methods in Engineering, 29(4), 2271–2283. https://doi.org/10.1007/s11831-021-09662-y	Springer
2	Deressa, K. T., & Ambie, D. A. (2022). Non-Axisymmetric Modelling of Moving Heat Source for Spatial and Temporal Investigation of Temperature in Railway Vehicles Disc Brake. Urban Rail Transit, 8(3–4), 198–216. https://doi.org/10.1007/s40864-022-00176-9	Springer
3	Deressa, K. T., & Ambie, D. A. (2022). Non-axisymmetric Modeling of a Moving Heat Source for Thermal Stress and Fatigue Analysis of Railway Vehicle Disc Brakes. Urban Rail Transit, 8(3–4), 198–216. https://doi.org/10.1007/s40864-023-00207-z	Springer
4	de Dieu, H. J., Deressa, K. T., Edison, T., & Rodger, M. (2023). A Review on Finite Element Method for Static Analysis of a Passenger Bogie Frame. AMERICAN JOURNAL OF ADVANCED SCIENTIFIC RESEARCH, 23.	Scienc Publishing group (Co-authored)
5	Deressa, K. T., & Ambie, D. A. (2024). Implementation of Non-Axisymmetric Moving Heat Source modeling in Railway Vehicles Disc Geometry and Material Selection. 3rd National Research symposium on "Emerging technologies for Building Green Economy", Adama Science and Technology University.	Coference